Alma Mater Studiorum - Università di Bologna

DOTTORATO DI RICERCA IN

GEOFISICA

Ciclo 33

Settore Concorsuale: 04/A4 - GEOFISICA

Settore Scientifico Disciplinare: GEO/12 - OCEANOGRAFIA E FISICA DELL'ATMOSFERA

OCEAN-ATMOSPHERE INTERACTIONS: LINKING OCEANIC BIOLOGICAL ACTIVITY TO MARINE AEROSOL PHYSICO-CHEMICAL AND CLOUD PROPERTIES

Presentata da: Karam Abdelaal Mansour

Coordinatore Dottorato

Nadia Pinardi

Supervisore

Maria Cristina Facchini

Co-supervisore

Nadia Pinardi

Matteo Rinaldi

Esame finale anno 2021

Abstract

The ways in which oceanic biological activity affects climate, by modifying aerosol and cloud properties, are not completely understood. This contributes to the high uncertainties associated with climate predictions. In this work, in-situ measurements of aerosol chemical composition, particle number size distribution, cloud-relevant properties (cloud condensation nuclei and ice nucleating particle number concentrations) and ground-based cloud observations are combined with high-resolution satellite sea surface chlorophyll-a concentration maps and air mass back-trajectory data to investigate the impact of the marine biota on aerosol physico-chemical and cloud properties. Studies were performed over the North Eastern Atlantic Ocean, the central Mediterranean Sea and the Arctic Ocean, by deploying both multi-year datasets and short-time scale observations. This allowed to investigate the interaction processes between phytoplankton and aerosols occurring at different time scales. All the data were chosen to be representative of the marine atmosphere, reducing to a minimum anthropogenic input.

The present Dissertation evidences a relation between the time evolution of marine aerosol properties and the patterns of marine biological activity in all the investigated environments. Our studies show that the marine biota influences aerosol properties under a variety of aspects, from chemical composition to number concentration and size distribution, up to the most cloud-relevant properties. Both primary and secondary aerosol components are affected by the marine biota, which acts as a source of both surfactants, that can be incorporated into sea-spray particles, and volatile precursors, that can take part in gas-to-particle conversion processes in the atmosphere. The impact of oceanic biological activity on the microphysical properties of marine stratiform clouds is also evidenced by our analysis, over the Eastern North Atlantic Ocean. Such clouds tend to have a higher number of smaller droplets in periods of high biological activity than in winter, as a consequence of the higher number of cloud condensation nuclei provided by marine biogenic aerosol particles. This confirms the possibility of feedback interactions within the biota-aerosol-cloud climate system.

At short-time scales (1-2 months), we observed that aerosol properties tend to respond to biological activity variations (as tracked by Chlorophyll-a patterns) with a delay of about one to three weeks. This delay should be considered in model applications that make use of Chlorophyll-a to predict marine aerosol properties, at least when operating at time resolution of days to weeks.

As a final remark, this work contributes to filling the current knowledge gap on the dynamics of phytoplankton-aerosol-cloud interactions in different marine environments. Achieving a better characterization of the time and space relationships linking marine biological activity to marine aerosol composition and properties may significantly impact our future capability of predicting the chemical composition of the marine atmosphere, potentially contributing to reducing the uncertainty of future climate predictions, through a better understanding of the natural climate system.

Acknowledgements

“Chi non ringrazia le persone non ringrazia Dio”

After three years of research and practice, I would like to express my sincere gratitude to all those who have helped me to complete this work and has pushed me to be the best that I can be. First and foremost, I owe a special thanks to my supervisor Dr Maria Cristina Facchini, who continuously guided and supported me with endless patience, inspiration, and enthusiasm. I would like to acknowledge my co-supervisor Dr Matteo Rinaldi for his support during the thesis, showing me the way to do research, improving my skills and scientific experience. I am especially thankful to him for the time spent in meetings whenever I had something to discuss, especially in the difficult moments of Covid-19 pandemic, and the trust he has placed on me to produce scientific results from the first days of my PhD. Without their fruitful suggestions, the thesis would not be achieved in the present form.

The research leading to the Dissertation results has received funding from the European Union’s Seventh Framework Program (FP7–ENV-2013) project BACCHUS (grant n.603445), the CNR Joint Lab project (Air-Sea Lab), the EPA Ireland and the Department of the Environment, Climate and Communications; MaREI, the SFI Research Centre for Energy, Climate, and Marine, and the FORCeS (ID 821205) H2020 EU Project (Constrained aerosol forcing for improved climate projections).

I would like also to thank Prof Colin O'Dowd, Dr Darius Ceburnis and Dr Jurgita Ovadnevaite from School of Physics, Centre for Climate & Air Pollution Studies (C-CAPS), Ryan Institute, National University of Ireland Galway (NUIG), Galway, Ireland, for the warm hospitality during my visit to their university and the immense support in the analysis of the aerosol and cloud data. It has been a pleasure working with this great team and a wonderful experience and memories that I will not forget.

I am grateful to all the people of the CNR-ISAC group in Bologna including Dr Stefano Decesari and Dr Franco Belosi for their guidance, and fruitful discussions, Dr Marco Paglione for his collaboration and support. Many thanks to Dr Rosalia Santoleri, Dr Salvatore Marullo, and Dr Marco Bellacicco for their helpful technical support in the treatment of satellite Ocean colour data.

Finally, a huge thanks to my family and friends who have provided me with the love, support, and sacrifices during all those difficult times especially my wife and my son OMAR who lived his first years away from me while I was working on this thesis, beautifully he is sitting on my desk, playing with the keyboard, while I am writing these words, your love means the world for me.

Table of Contents

Abstract ---- I
Acknowledgements ---- II
Table of Contents ---- III
List of Figures ---- VI
List of Tables ---- X
List of Acronyms ---- XI

1. INTRODUCTION ---- 1
1.1 Definition of Marine Aerosol ---- 2
1.2 Marine Aerosol Generation ---- 3
1.3 Marine Aerosol Chemical Composition ---- 5
1.3.1 Sea-salt ---- 5
1.3.2 Organic Aerosol ---- 6
1.3.3 Non-sea-salt-Sulfate ---- 8
1.3.4 Nitrate ---- 9
1.3.5 Ammonium ---- 10
1.4 Marine Aerosols Particle Size Distributions ---- 10
1.5 Climate Relevance of Marine Aerosols ---- 13
1.5.1 Direct Effect ---- 15
1.5.2 Indirect Effect (Aerosol-Cloud Interaction) ---- 16
1.5.3 Marine aerosol and Ice Nucleating Particles ---- 19
1.6 The CLAW Hypothesis ---- 22
1.7 Final Considerations on Phytoplankton-Aerosol Interactions ---- 23
1.8 Aim and Objectives of the Present Study ---- 26

2. DATA AND METHODS OF ANALYSIS ---- 28
2.1 Sampling Locations ---- 28
2.1.1 MHD Atmospheric Research Station, NE Atlantic ---- 28
2.1.1.1 Long-term (2009-2017) In-situ Measurements ---- 30
2.1.1.2 Ground-based Remote Sensing Measurements ---- 31
2.1.1.3 BACCHUS Campaign ---- 33
2.1.2 CGR Climate Observatory, Central Mediterranean ---- 34
2.1.3 GVB observatory, Ny-Ålesund, Svalbard Islands ---- 35
2.2 Satellite Ocean Color Data ---- 36

2.3 Phytoplankton Carbon Estimation ---- 37
2.4 Air Mass Back-trajectories ---- 38
2.5 Meteorological Data ---- 39
2.6 Satellite Ground Type Maps ---- 39
2.7 Methods of Analysis ---- 40
2.7.1 Data Filtration ---- 41
2.7.2 Spatio-Temporal Correlation Analysis ---- 42
2.7.3 Source Regions Location ---- 44
2.7.3.1 PSCF ---- 44
2.7.3.2 CWT ---- 45

3. SEASONALITY OF MARINE AEROSOL CHEMICAL COMPONENTS OVER THE NE ATLANTIC OCEAN IN RELATION TO THE EVOLUTION OF THE OCEANIC BIOLOGICAL ACTIVITY ---- 46
3.1 Seasonal Trends of Marine Aerosol Chemical Composition ---- 46
3.2 Classification of Air Mass Back-Trajectories at MHD ---- 51
3.3 Marine Aerosol Seasonality According to BTs Clusters ---- 53
3.4 Spectral Analysis of CHL ---- 56
3.5 Seasonal Spatial Correlation Analysis ---- 58
3.6 Seasonally Dependent Marine Aerosol Source Region Attribution ---- 60
3.7 Discussion ---- 63

4. CHEMICAL COMPOSITION AND CLOUD-RELEVANT PROPERTIES IN THE NE ATLANTIC OCEAN DURING SUMMERTIME 2015 ---- 65
4.1 Overview of Marine Aerosol Properties during the Campaign ---- 65
4.2 Air Mass Back-Trajectories ---- 67
4.3 Spatio-Temporal Correlation with CHL ---- 68
4.3.1 Aerosol Chemical Composition ---- 68
4.3.2 Particle Number Concentration ---- 71
4.3.3 Cloud Condensation Nuclei ---- 72
4.3.4 Ice Nucleating Particles ---- 75
4.4 Potential Source Contribution Function ---- 76
4.5 Effect of Meteorology on Marine Aerosol ---- 79
4.6 Discussion ---- 81

5. CHL PATTERNS AND PARTICULATE MSA OVER THE CENTRAL MEDITERRANEAN SEA DURING SPRING 2016 ---- 87

5.1 Characterization of MSA at CGR in April 2016 ---------- 88

5.2 Air Mass Back-Trajectories ---------- 89

5.3 MSA Spatio-temporal Correlation with CHL ---------- 90

5.4 MSA Source Regions ---------- 96

5.5 MSA Spatio-temporal Correlation with PHYC ---------- 98

5.6 Discussion ---------- 99

6. IMPACT OF THE MARINE BIOTA ON THE INP CONCENTRATION OVER THE ARCTIC: THE CASE STUDY OF NY-ÅLESUND (SVALBARD) 2018 ---------- 103

6.1 Characterization of INP at GVB in 2018 ---------- 103

6.2 Back Trajectories and Influence of Ground Conditions ---------- 107

6.3 INP Spatio-temporal Correlation with CHL ---------- 110

6.4 INP Source Regions ---------- 113

6.5 Discussion ---------- 115

7. PHYTOPLANKTON IMPACT ON MARINE CLOUD MICROPHYSICAL PROPERTIES OVER THE NE ATLANTIC OCEAN ---------- 116

7.1 Cloud Properties Spatio-temporal Correlation with CHL ---------- 117

7.2 Aerosol-Cloud Interaction ---------- 122

7.3 Relating Cloud Properties to Meteorology ---------- 125

7.4 Discussion ---------- 129

8. GENERAL DISCUSSION AND CONCLUSIONS ---------- 132

Bibliography ---------- 139

APPENDIX ---------- 152

List of Figures

Figure 1.1: A schematic representation of the potential processes of marine aerosols formation and their impact on climate. Complex biological mechanisms regulate the composition of seawater, which in turn governs the composition of primary sea spray aerosol (SSA) and secondary aerosol formation through gas-phase emissions. The Physico-chemical properties of marine aerosol control its ability to interact with solar radiation directly (scattering and absorption) and indirectly (through the formation of cloud condensation nuclei (CCN) and ice nucleating particles (INP)). ---------- *2*

Figure 1.2: Left) Sources, transformation, and removal processes of aerosol particles in the major modes as a function of diameter (Saltzman, 2009). Right) Seasonal characteristics of marine aerosol number size distributions, Aitken and accumulation modes, over the NA Ocean, reproduced from O'Dowd et al. (2004). ---------- *11*

Figure 1.3: Average size-segregated chemical compositions and absolute mass concentrations of marine aerosol sampled at Mace Head in the Northeast Atlantic Ocean in a) winter, a season of LBA, and b) summer, a season of HBA, reproduced from O'Dowd et al. (2004). The size fractions from 0.125 to 0.5 µm cover the accumulation mode and the size fraction from 0.06 to 0.125 µm covers most of the Aitken mode. The concentrations of water-soluble organic carbon (WSOC), water-insoluble organic carbon (WIOC), and Black Carbon (BC) are reported as mass of organic matter (see Cavalli et al. (2004) for the full discussion). ----- *12*

Figure 1.4: The global average radiative forcing estimation in 2011 relative to 1750 for emitted chemical species (gases, aerosols, and their precursors) or other factors. The colors inset in the top part of the figure are used to represent RF from emitted species affecting several chemicals while red (positive forcing) and blue (negative forcing) are used for emitted components that affect fewer forcing agents. The vertical bars represent the relative uncertainty of the RF induced by each component. The net impact of the individual contributions is shown by a diamond symbol and its uncertainty (5 to 95% confidence range) is given by the horizontal error bar. Taken from Myhre et al. (2013). ---------- *14*

Figure 1.5: (a) Sea spray aerosol particles enriched with organic material are formed when bubbles burst at the air-sea interface. The surface-active organic material of biological origin is scavenged at the interface of the bubbles as they rise through the water column. This process enriches the air-sea interface with surface-active organic material forming the sea surface microlayer (green layers) as shown by Wilson et al. (2015). (b) Representation of the inference of INPs in upper tropospheric and supercooled clouds. For both high (ice) clouds and supercooled liquid clouds, heterogeneous ice nucleation produces few and large ice crystals that precipitate quicker, decreasing the lifetime of the clouds. Taken from Murray (2017). ---------- *21*

Figure 2.1: Sampling locations shown by the red, green, and blue squares and the borders of the studied oceanic domains delineated by the red, green, and blue boxes. WMED stands for Western Mediterranean and NA for North Atlantic. ---------- *29*

Figure 2.2: Simplified schematic diagram of the implemented multi-steps approach. ---------- *41*

Figure 2.3: Schematic representation of the time-lag method.---------- *43*

Figure 3.1: Monthly trend of CHL and marine aerosol chemical composition during 2009-2017. On each box that represents a month, the central line indicates the median, and the bottom and top edges of the box indicate the 25^{th} and 75^{th} percentiles, respectively. The connected line represents the monthly mean during maritime air masses. The monthly fractions of PM_1 chemical composition are shown in the stacked bar. MSA concentrations were excluded from OM in the fraction calculations. ---------- *47*

Figure 3.2: Spatial distributions of seasonal average CHL over the NA Ocean between 2009 and 2017. The black box is the oceanic area off the MHD coast exerted the most influence on marine aerosol properties. ----- *49*

Figure 3.3: Normalized monthly median of CHL, OM, nss-SO_4^{2-}, and MSA during 2009-2017. ---------- *50*

Figure 3.4: The 3-day air mass BTs (hourly time step) arriving at MHD (represented by a black square) sampling station every 6 hr (four times per day) at 100 m above the MSL during 2009-2017. The BTs were classified according to the origin of air mass into the marine Arctic (mA; red), marine Polar (mP; green), marine Tropical (mT; blue) and continental European (cP; magenta). The clusters of BTs are shown by the dark solid lines and the percentage of each cluster is inserted. The cP cluster was excluded from the analysis of clean marine aerosol. ---------- *52*

Figure 3.5: Monthly contribution of air mass BTs arriving at MHD in each cluster. ---------- *53*

Figure 3.6: Monthly trend of marine biogenic aerosol chemical composition at different air mass clusters as: top) mA, middle) mP, and bottom) mT. On each box that represents a month, the central line indicates the median, and the bottom and top edges of the box indicate the 25th and 75th percentiles, respectively. The connected line represents the monthly mean. ---------- 54

Figure 3.7: Spectral distribution of daily mean CHL at 24 pixels in the NA during 2009-2017. ---------- 57

Figure 3.8: Seasonal correlation coefficient spatial distribution between the main biogenic aerosol chemical composition measured at MHD and CHL over the NA Ocean during 2009-2017, considering clean marine air masses. Only significant correlation coefficients ($p < 0.01$) are presented. The black box is the broad oceanic region that is likely to exert the highest impact on aerosol properties at the sampling station, as it results from the analyses of this Chapter. ---------- 59

Figure 3.9: Correlation coefficient as a function of time-lag between mean CHL in the black box region and the main aerosol chemical components, in different seasons. ---------- 60

Figure 3.10: Seasonal PSCF distributions for clean marine aerosol arrived at MHD during 2009-2017. The sources of high concentrations are defined above the median values. ---------- 62

Figure 4.1: The 5-day air mass BTs (hourly time step) calculated by the NOAA HYSPLIT model arriving at MHD (represented by black square) sampling station four times per day (00, 06, 12, and 18 hr UTC) at 100 m above the MSL from 31 July to 21 September 2015. The blue box area comprises grid coordinates 44° – 50° N and 10° – 30° W (Region 1; O'Dowd et al. (2015)), the green box area comprises grid coordinates 47° – 57° N and 14° – 24° W (Region 2; Rinaldi et al. (2013)), while the red box area comprises grid coordinates 58° – 66° N and 30° – 44° W (region 3). These boxes delineate high correlation areas, discussed later. Only clean marine BTs (light blue) according to eBC threshold are used for PSCF calculations. ---------- 67

Figure 4.2: Examples of correlation coefficient spatial distribution between the main aerosol chemical composition measured at MHD and CHL over the NA Ocean for 9 days (left), 19 days (middle), and 21 days (right) time-lags, considering only clean marine air masses. In all correlation maps, the grey color represents non-significant correlation coefficients at 95% confidence level, the black square corresponds to MHD station and the regions of interests are shown as blue (Region 1), green (Region 2), and red (Region 3) boxes. ---------- 69

Figure 4.3: Correlation coefficient as a function of time-lag between mean CHL at different selected regions and the main aerosol chemical components. The black dashed lines represent the critical level of significant correlation at 95% confidence limit. ---------- 70

Figure 4.4: a) Examples of correlation coefficient spatial distribution between Aitken and Accumulation modes particle number concentration sampled at MHD and CHL over the NA Ocean for 10 days (left), 20 days (middle), and 22 days (right) time-lags, considering only clean marine air masses. b) Correlation coefficient as a function of time-lag between mean CHL at different selected regions and the different modes of particle number concentration. The black dashed lines represent the critical level of significant correlation at 95% confidence limit. ---------- 72

Figure 4.5: a) Examples of correlation coefficient spatial distribution between CCN number concentration at 0.25%, 0.50% and 0.75% supersaturation and CHL over the NA Ocean for different time-lags, considering only clean marine air masses. b) Correlation coefficient as a function of time-lag between mean CHL at different regions and CCN/ CCN fraction concentrations. The black dashed lines represent the critical level of significant correlation at 95% confidence limit. ---------- 74

Figure 4.6: a) Examples of correlation coefficient spatial distribution between the number concentration of INPs for particulate matter less than 1 µm/ 10 µm and CHL over the NA Ocean for 7 days (left), and 18 days (right) time-lag, considering only clean marine air masses. b) Correlation coefficient as a function of time-lag between mean CHL at different regions and the concentration of INPs. The black dashed lines represent the critical level of significant correlation at 95% confidence limit. ---------- 76

Figure 4.7: PSCF plots for clean marine a) SO_4^{2-}, b) MSA, c) OM, d) OM_{SS}, and e-f) particle member concentration in the Aitken and accumulation modes. The sources of high concentrations are defined above the median values during the period 31st August – 21st September 2015. The percent of grids that have high probability ≥ 0.5 inside each of the three marked regions are inserted. ---------- 78

Figure 4.8: Spatial distribution of the aerosol sources identified by merging the results of the spatio-temporal correlation with CHL and of PSCF for a) SO_4^{2-}, b) MSA, c) OM, d) OM_{SS}, and e-f) particle member concentration in the Aitken and accumulation modes. The color scale reflects how many times a given pixel has PSCF ≥ 0.5 and significant correlation coefficient by running time-lags from 8 to 25 days. ---------- 78

Figure 4.9: Scatter plot between daily mean aerosol chemical composition and particle number concentrations at Aiken/Accumulation modes. The color scale represents the average CHL in Region 2 with 19 day time-lag. ---------- *84*

Figure 4.10: Scatter plot between daily mean aerosol chemical composition and CCN number concentrations. The color scale represents the average CHL in Region 2 with 19 day time-lag. ---------- *85*

Figure 5.1: Scatter plot between online and offline daily MSA concentrations measured at CGR. ---------- *88*

Figure 5.2: Daily Pattern of MSA atmospheric concentration at CGR during 07-25 April 2016. On each box that represents a day, the central line indicates the median, and the bottom and top edges of the box indicate the 25th and 75th percentiles, respectively. The symbol "x" extends to the minimum and maximum data points (5-minute resolution) and the line connects the daily mean. ---------- *89*

Figure 5.3: The 3-day BTs (hourly time step) calculated by the NOAA HYSPLIT model arriving at CGR at 100 m above the MSL during 07-25 April 2016. The color scale represents the altitude of BT endpoints. The green color shows low BTs (altitude < 500 m). The black circle corresponds to CGR station. ---------- *90*

Figure 5.4: Spatial distribution of the correlation coefficient between MSA at CGR and CHL over the Mediterranean Sea for 8 days (left) and 16 days (right) time-lags. The grey color represents negative and non-significant correlation coefficients at 95% confidence level. The black star corresponds to CGR station. The blue box area comprises grid coordinates 37° − 39° N and 02° − 10° E (Region 1) while the red box area comprises grid coordinates 40° − 44.5° N and 03° − 10° E (Region 2). These boxes indicate the area selected to compute the curves presented in Figure 5.5 and the regression lines reported in Figure 5.6. ---------- *91*

Figure 5.5: ***a)*** *Correlation coefficient between CHL and MSA as a function of the time-lag, the black dashed line represent the critical level of significant correlation at 95% confidence limit;* ***b)*** *percentage of the number of pixels with positive and significant correlation in regions of interest;* ***c)*** *and* ***d)*** *correlation coefficient frequency distribution at areas of interest for time-lags of 0, 8, and 16 days.* ---------- *92*

Figure 5.6: Regression curves for CHL and MSA at lag = 8 days in Region 1 (left panel) and, at lag = 16 days in Region 2 (right panel). The correlation coefficients and the best fit line are reported. The cyan curves represent 95% confidence interval. Note that the scale of the x-axis (CHL) is not the same. ---------- *94*

Figure 5.7: Spatial distribution of monthly mean CHL over the Mediterranean Sea during March and April 2016. The spatial resolution of CHL is 1×1 km. ---------- *95*

Figure 5.8: Spatial distribution of the correlation coefficient between MSA at CGR and CHL over the Mediterranean Sea for 8 days (left) and 16 days (right) time-lags without uncertain point (16 April 2016). The grey color represents negative and non-significant correlation coefficients at 95% confidence level. ---------- *96*

Figure 5.9: PSCF plots for MSA in the period 07th-25th April 2016. The source of high MSA concentrations is defined as above the median (left) and the third quartile (right). The Mediterranean domain is divided into 1° × 1° latitude/longitude grid cells. The color scale represents the probability from 0 to 1. ---------- *97*

Figure 5.10: PSCF map by using low BTs (< 500m height) and the median of MSA as a threshold. ---------- *98*

Figure 5.11: Spatial distribution of the correlation coefficient between MSA at CGR and PHYC over the Mediterranean Sea for 9-days time-lag. The grey color represents negative and non-significant correlation coefficients at (p < 0.05). Regions 1 (blue box) and 2 (red box), as well as CGR station (black star) are shown. ---------- *99*

Figure 5.12: Daily time series of the average main meteorological data (ERA5) over Region 1 and Region 2 (boxes of interest). The green box represents the period of spring 2016 campaign. ---------- *101*

Figure 6.1: Time series of $nINP_{PM10}$ measured at GVB during spring and summer 2018. ---------- *104*

Figure 6.2: Atmospheric concentration of $nINP_{PM10}$ as a function of the activation temperature measured at GVB during spring and summer 2018. ---------- *105*

Figure 6.3: Activated fraction of INPs concentrations measured at GVB during 2018. ---------- *107*

Figure 6.4: The 120-hours air mass BTs (hourly time step) arriving at GVB sampling station at times corresponding to INPs samples during A) Spring and B) Summer 2018. The color scale represents the conditions of the ground crossed by the BTs. Air masses traveling at high altitude (> 500 m above MSL), which have been excluded in CWT calculations, are represented by the symbol "+". ---------- *108*

Figure 6.5: Ground type influence on low-travelling (< 500 m) air masses for INP measurements in spring and summer 2018. ---------- *109*

Figure 6.6: Influence of the "Land" ground type (fLand) during the summer campaign overlapped with the INP atmospheric concentrations at T = –15, –18 and –22 °C. ---------- *109*

Figure 6.7: Top): Examples of correlation coefficient spatial distribution between $nINP_{PM1}$ at T = –15 °C measured at GVB (represented by the black square) and CHL over the Arctic ocean for 6 days (left), 14 days (middle), and 16 days (right) time-lags. The color scale indicate the correlation coefficient. Regions of interest are shown as Olivo (Region 1), dark Purple (Region 2), and Orange (Region 3) boxes. Bottom): Correlation coefficient and percentage of the number of pixels with positive and significant correlation in the three evidenced regions, as a function of the time-lag. The black dashed line represents the critical level of significant (p < 0.05) correlation. ---------- *111*

Figure 6.8: A) CWT plots for $nINP_{PM1}$ at T = –15 °C. To facilitate the visual comparison, the same Regions evidenced in Figure 6.7 are reported. B) Spatial distribution of the fine INP sources identified by merging the results of the spatio-temporal correlation with CHL and of CWT. The color scale reflects how many times a given pixel has CWT ≥ median and significant correlation coefficient by running time-lags from 5 to 20 days. -------- *114*

Figure 7.1: The 3-day BTs arriving MHD at cloud base altitude above the ground-level during the clean marine conditions. The color scale represents the altitude of each endpoint of BTs. The black box is the main area of interest of the present study, discussed in detail later, and MHD station is shown by a black square. - *117*

Figure 7.2: Spatial distributions of correlation coefficients between left) R_{eff} and right) CDNC measured at MHD and CHL over the NA Ocean for 3-day time-lag. The grey color represents non-significant correlation coefficients at 95% confidence level, the black square corresponds to MHD station and the black box area comprises grid coordinates 45° − 60° N and 12° − 38° W that indicates high correlation area and is selected to compute the curves presented in Figure 7.3 and Figure 7.4. ---------- *118*

Figure 7.3: Correlation coefficients as a function of the time-lag between mean CHL within the identified box region and different cloud properties. The black dashed horizontal lines represent the critical level of significant correlation (p < 0.05). The sign || stands for normalized data. ---------- *119*

Figure 7.4: Correlation coefficient frequency distributions for R_{eff} and CDNC in the identified box at different time-lags from 0 to 21 days. The percentages of the number of pixels with negative (positive) significant correlation in that region for R_{eff} (CDNC) are inserted. ---------- *120*

Figure 7.5: ***Left)*** *Spatial distributions of correlation coefficients between N_a measured at MHD and CHL over the NA Ocean for 3-day time-lag.* ***Right)*** *Correlation coefficients as a function of the time-lag between mean CHL within the identified box region and N_a.* ---------- *122*

Figure 7.6: ***A)*** *Scatter plot between N_a and R_{eff} / CDNC,* ***B)*** *ACI_r derived from R_{eff} to N_a and* ***C)*** *ACI_n derived from CDNC to N_a at three LWC bins classified as LWC < third percentile (blue), one-third percentile < LWC < two-third percentile (green) and LWC > two-third percentile (red).* ---------- *124*

*Figure 7.7: Left) scatterplot showing the relation between CHL and R_{eff} at nearly homogenous T. Right) scatterplot showing the relation between T and R_{eff} at nearly homogenous CHL. * represents significant correlation at 95% confidence interval.* ---------- *129*

List of Tables

Table 1.1: Key properties of the main aerosol species in the marine troposphere. BC stands for Black Carbon, OA for organic aerosols and POA (SOA) for primary (secondary) organic aerosols. Adapted from Boucher et al. (2013). ---------- *6*

Table 2.1: Summary of the in-situ and ground-based remote sensing data used in the Dissertation. ---------- *29*

Table 3.1: Seasonal variations in PM_1 chemical composition [μg m^{-3}] of clean marine biogenic aerosol at different air mass clusters. The CHL [mg m^{-3}] seasonality during 2009-2017 were added. n is the number of clean hours (samples) in each category. ---------- *55*

Table 4.1: Summary of marine aerosol studied variables for the study (campaign) period. ---------- *66*

Table 4.2: Daily correlation coefficients between clean marine aerosol studied variables and meteorological variables over the evidenced source area (Region 2) in the NA Ocean. ---------- *80*

Table 4.3: Normalized Euclidean distance (0-1) between the "correlation vs. time-lag" profiles of the considered aerosol parameters for Region 2, deriving from a hierarchical cluster analysis. ---------- *83*

Table 4.4: Correlation coefficients between the considered hourly clean marine aerosol parameters. ---------- *83*

Table 5.1: Daily correlation coefficients between MSA measured at CGR and the atmospheric components over the interesting regions in the Mediterranean Sea. ---------- *101*

Table 6.1: Average (± standard deviation) and median (in brackets) INP concentrations measured at GVB during 2018. ---------- *106*

Table 7.1: Seasonal statistics of CHL, R_{eff} and CDNC. ---------- *121*

Table 7.2: Correlation coefficients between clean marine cloud data measured at MHD and meteorological variables over the coordinates (50° − 55° N and 10° − 15° W), 5° latitude/longitude around MHD. Correlations with CHL and N_a were added for comparison. ---------- *126*

Table 7.3: Two-dimensional linear regression of R_{eff} as a function of CHL and T spatial averages. ---------- *128*

List of Acronyms

ACI	Aerosol-Cloud Interaction
AF	Activated Fraction
AOD	Aerosol Optical Depth
APS	Aerodynamic Particle Sizer
ARL	Air Resources Laboratory
BC	Black Carbon
b_{bp}	Particulate backscattering
b_{bp}NAP	Background contribution of non-algal particles to b_{bp}
eBC	equivalent Black Carbon
BTs	Back-Trajectories
C3S	Copernicus climate change service
C-CAPS	Center for Climate & Air Pollution Studies
CCN	Cloud Condensation Nuclei
CDCE	Composition Dependent Collection Efficiency
CDNC	Cloud Droplet Number Concentration
CFSTG	Continuous-Flow Streamwise Thermal-Gradient
CGR	Capo Granitola
CHL	Chlorophyll-a concentration
CMEMS	Copernicus Marine Environment Monitoring Service
CNR	Italian National Research Council
COD	Cloud Optical Depth
cP	continental European
CWT	Concentration Weighted Trajectory
DFPC	Dynamic Filter Processing Chamber
DMS	Dimethylsulfide
DMSP	Dimethylsulphonium propionate
DOC	Dissolved Organic Carbon
ECMWF	European Centre for Medium-Range Weather Forecasts
ERF	Effective Radiative Forcing
ESA-CCI	European Space Agency Climate Change Initiative project
FIE	First Indirect Effect
GAW	Global Atmosphere Watch
GBRS	Ground Based Remote Sensing
GVB	Gruvebadet
HBA	High Biological Activity
H_{base}	Cloud base height
H_{thick}	Cloud thickness
H_{top}	Cloud top height
HR-Tof-AMS	High Resolution - Time of Flight - Aerosol Mass Spectrometer
HYSPLIT	Hybrid Single-Particle Lagrangian Integrated Trajectory
IMS	Ice Mapping System
INP	Ice nucleating particles
IPCC	Intergovernmental Panel on Climate Change

ISAC	Institute of Atmospheric Sciences and Climate
LBA	Low Biological Activity
LTS	Low Tropospheric Stability
LWC	Cloud liquid water content
mA	marine Arctic
MAAP	Multi-Angle Absorption Photometer
MBL	Marine Boundary Layer
MERIS	MEdium Resolution Imaging Spectrometer
MHD	Mace Head
MODIS	Moderate Resolution Imaging Spectroradiometer
mP	marine Polar
MSA	Methanesulfonic Acid
MSL	Mean Sea Level
mT	marine Tropical
MWR	Microwave radiometer
N_a	Aerosol number concentration
NA	North Atlantic
NESDIS	National Environmental Satellite Data and Information Service
NOAA	National Oceanic and Atmospheric Administration
NPF	New particle formation
NSIDC	National Snow & Ice Data center
nss	non-sea-salt
NUIG	National University of Ireland Galway
OA	Organic Aerosol
OC	Organic Carbon
OLCI-S3A	Ocean and Land Color Instrument-Sentinel 3A
OM	Organic Matter
OM_{SS}	Organic content of sea-spray aerosol
PHYC	Phytoplankton carbon biomass
PM_1	Particulate matter less than 1 µm diameter
PM_{10}	Particulate matter less than 10 µm diameter
PMA	Primary Marine aerosol
POA	Primary Organic aerosol
PSCF	Potential Source Contribution Function
PVV	Pressure Vertical Velocity
QAA	Quasi Analytical Algorithm
R	Correlation coefficient
R_{eff}	Cloud droplet effective radius
RF	Radiative Forcing
RH	Relative Humidity
SeaWiFS	Sea-viewing Wide Field of View
SMA	Secondary Marine Aerosol
SMPS	Scanning Mobility Particle Sizer
SOA	Secondary Organic Aerosol
SS	Sea Salt
SSA	Sea Spray Aerosol

SSR	Net surface solar radiation
SST	Sea Surface Temperature
S_w	Supersaturation with respect to water
SYRSOC	SYnergetic Remote Sensing Of Clouds
T	Air Temperature
T_A	Activation Temperature
VIIRS	Visible Infrared Imager/Radiometer Suite
WIOC	Water Insoluble Organic Carbon
WIOM	Water Insoluble Organic Matter
WMED	Western Mediterranean
WMO	World Meteorological Organization
WS	Wind Speed
WSOC	Water Soluble Organic Carbon
WSOM	Water Soluble Organic Matter

1. Introduction

Ocean-atmosphere interactions play a crucial role in the atmospheric system and in climate feedbacks, from the local to the global scale. Oceans, two-thirds of the Earth's surface, are the source of important natural aerosol components, collectively indicated as the marine aerosol. Marine aerosol dominates the atmospheric aerosol mass burden and particle number concentration over remote oceanic locations, far from continental outflows and can impact the Earth's radiation balance, directly, by interacting with incoming solar radiation, and/or indirectly, through aerosol-cloud interactions that modify cloud properties.

According to the 5th IPCC report (Stocker et al., 2013), the aerosol direct and indirect atmospheric radiative forcings are a major source of uncertainty in global climate predictions. Some of this uncertainty results from the poor characterization of the relation existing between oceanic biological activity and marine aerosol physico-chemical properties. Figure 1.1 shows a schematic representation of the potential processes of aerosol formation over the oceans and their impact on climate. Most of these pathways, from the ocean to clouds, are still poorly understood, leading to a lack of comprehension of both the direction and the magnitude of climate feedbacks. A more detailed investigation of the interactions between the ocean and the atmosphere, on different timescales, is vital to achieve a better understanding of the mechanisms that regulate the physico-chemical properties of marine aerosols and their role in climate regulation.

This Chapter reviews the current state of knowledge regarding the interaction between the oceanic biota and aerosol/cloud properties in the unperturbed marine boundary layer (MBL), explains the processes of cloud droplet activation and ice formation and, finally, illustrates the goals and objectives of the present study. An outline of the Dissertation is also presented.

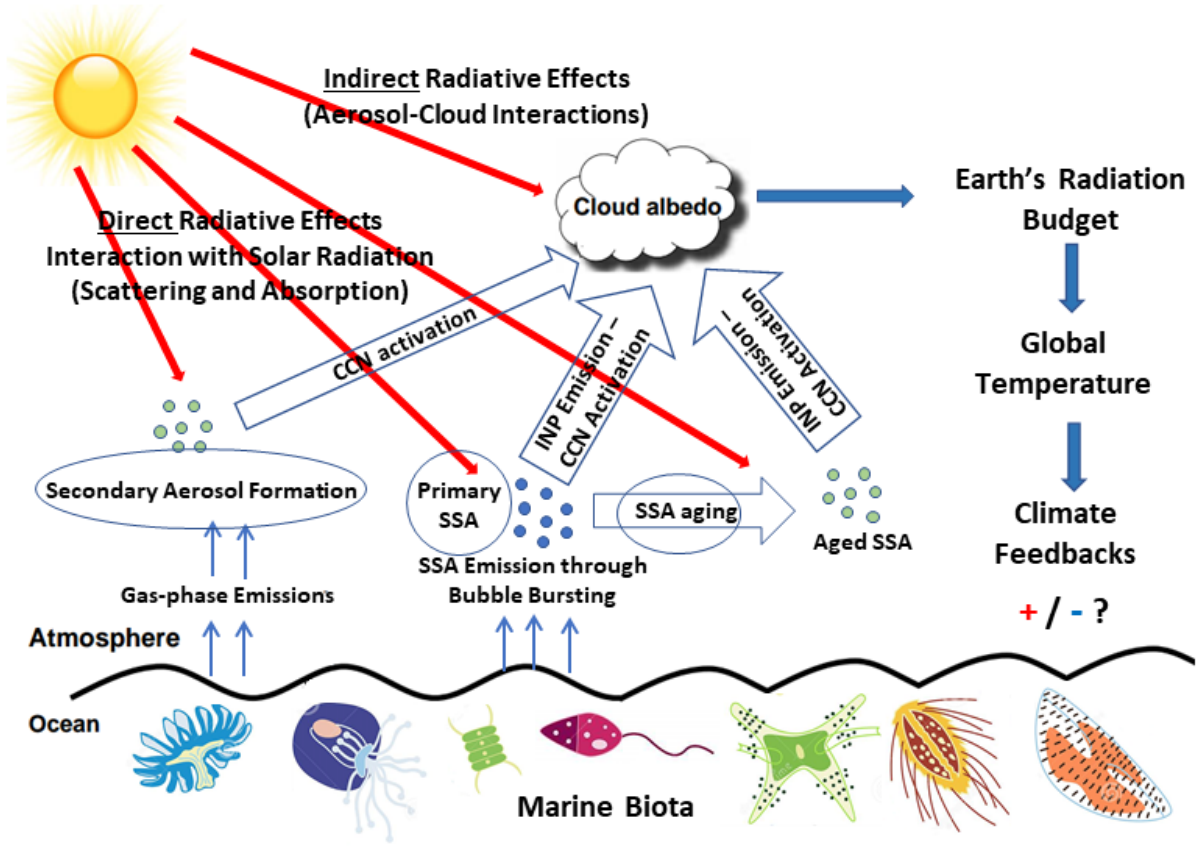

Figure 1.1: A schematic representation of the potential processes of marine aerosols formation and their impact on climate. Complex biological mechanisms regulate the composition of seawater, which in turn governs the composition of primary sea spray aerosol (SSA) and secondary aerosol formation through gas-phase emissions. The Physico-chemical properties of marine aerosol control its ability to interact with solar radiation directly (scattering and absorption) and indirectly (through the formation of cloud condensation nuclei (CCN) and ice nucleating particles (INP)).

1.1 Definition of Marine Aerosol

Marine aerosol is a suspension of solid and liquid particles (with diameters ranging between few nanometers and ten-twenty micrometers) in the atmosphere, originating from ocean-atmosphere interactions. The term "marine aerosol" comprises the various types of particles produced mechanically from the sea surface as well as chemically formed from the atmospheric chemical reactions involving gases emitted from the sea. The ocean contributes to the majority of the aerosol burden in the overlying atmosphere over remote oceanic locations (Cochran et al., 2017a; Cochran et al., 2017b; O'Dowd et al., 2008; Vignati et al., 2010). Continental aerosols, derived from fossil fuel combustion, biomass burning, mineral and soil dust, and terrestrial biogenic emissions, can be transferred across the ocean and

contribute to the aerosol burden in the MBL, since the atmospheric transport times involved are comparable to the aerosol lifetimes. Furthermore, ship emissions, especially in coastal regions, contribute to the aerosol burden over the oceans. Indeed, it is difficult to distinguish aerosols in marine and continental types, mainly because of the existence of many interactions between marine and continental gases and particulate matter (Saltzman, 2009). Nevertheless, in this Dissertation, the term marine aerosol will be used to indicate aerosols naturally produced because of ocean-atmosphere interactions, excluding contributions from continental or ship emissions.

1.2 Marine Aerosol Generation

Marine aerosol particles are emitted or injected directly into the atmosphere (primary marine aerosols, PMA, or sea spray aerosols, SSA) from the sea surface by wave breaking and bubble bursting processes (Gantt and Meskhidze, 2013; Quinn et al., 2015) or formed through photochemical oxidation and gas-to-particle conversion (secondary marine aerosols, SMA) of ocean-derived trace gases (Charlson et al., 1987; O'Dowd et al., 2002; Shaw, 1983), as displayed in Figure 1.1. The different production mechanisms result in a wide variety of particle sizes and chemical compositions that determine the impact of ocean-derived aerosols on climate.

Bubble bursting at the surface of the ocean results in the production of sea spray particles made up of inorganic sea salt and organic matter. Two distinct types of bubbles are produced by wave breaking: film drops and jet drops (Blanchard, 1963; Woolf et al., 1987), which generate different sizes of SSA particles. When wind speed exceeds about 5 m s^{-1}, breaking waves are formed, which entrain air bubbles into surface waters. Such bubbles rise to the surface and burst, creating up to hundreds of film drops with each bubble. Film drops are associated with small particles ranging in diameters from tens of nanometers up to 1 µm. The formation of jet drops occurs when a bubble bursts and allows water to rush into the freed space producing a large drop of similar chemistry to bulk seawater. Jet drops are larger sized primary particles, from about 1 to 25 µm. Sea spray particles resulting from film and jet drops can have lifetimes ranging from hours to days. At very high wind speeds (> 10 m s^{-1}), larger drops known as spume drops are torn directly from the crests of waves (Monahan et al., 1983). Those drops are so large (tens of micrometers to several millimeters) that they reside in the

atmosphere for only seconds to minutes before falling back to the sea surface (Andreas, 1992), and so they do not contribute significantly to the marine aerosol burden.

Particles can also be generated in the atmosphere via gas-to-particle conversion processes. The mechanisms for secondary particle formation in the MBL include: **(a)** new particle formation (NPF) via the nucleation of stable clusters (homogeneous nucleation) of the order of 0.5–1 nm in sizes (these clusters, once formed, can grow to larger sizes via condensation processes) and **(b)** clusters/particles growth through condensation of gas-phase species onto existing particles (heterogeneous nucleation), condensation of vapors, and aqueous-phase oxidation in cloud or particle-bound water. The most rapid mechanism for the formation of secondary aerosol in the marine environment is thought to be cloud processing, in which gas-phase species can undergo reactions into cloud droplets (O'Dowd et al., 2002). When the cloud evaporates, the size and composition of the residual particles left behind are changed.

The most investigated example of SMA formation process regards the emission of marine biogenic dimethylsulfide (DMS; CH_3SCH_3) from phytoplankton and successive oxidation in the atmosphere, by OH, NO_3 and possibly other radical species, to eventually yielding a variety of aerosol products like methanesulfonic acid (MSA; CH_3SO_3H) and sulfuric acid (H_2SO_4) (Becagli et al., 2013; Charlson et al., 1987; Chen et al., 2018; Facchini et al., 2008; Shaw, 1983; Watts et al., 1990). H_2SO_4 and MSA can react with other gas-phase species to form solid particles (homogeneous nucleation) or they can condense onto existing particles that lead to their growth (heterogeneous nucleation). The final product is a particulate phase containing biogenic non-sea-salt sulfate (nss-SO_4^{2-}) and MSA. The term nss-SO_4^{2-} is used to differentiate between seawater-derived aerosol sulfate (SS-SO_4^{2-}) and sulfate originating from gas-to-particle conversion processes (secondary sulfate). The SS-SO_4^{2-} and nss-SO_4^{2-} are somewhat distinguishable by their size distribution, with the marine-salt component typically in coarse aerosols and nss-SO_4^{2-} in the Aitken and accumulation aerosol modes (see further details in Section 1.4). Another and strong source of NPF, through secondary processes, is found in the coastal environments through the atmospheric reactions of iodine-oxide compounds (Allan et al., 2015; O'Dowd et al., 2002; Sellegri et al., 2016).

1.3 Marine Aerosol Chemical Composition

Aerosol particles are a highly variable mixtures of complex chemical components. A single atmospheric aerosol particle may consist of one mineral species or may contain dozens or even hundreds of separate chemical compounds (Saltzman, 2009). Marine aerosols consist primarily of a mixture of sea-salt (SS), non-sea-salt sulfate (nss-SO_4^{2-}), ammonium (NH_4^+), nitrate (NO_3^-) and water-soluble (WSOM) or insoluble (WIOM) organic compounds (Rinaldi et al., 2010). Marine aerosol's chemical properties reflect the original composition of particles injected or produced in the atmosphere and the chemical alteration of their components during atmospheric transport, by chemical reactions within the particle or with the surrounding gas phase. The general characteristics and role of the main aerosol components are summarized in Table 1.1.

1.3.1 Sea-salt

The generation of SS aerosols is caused by the action of wind on the sea surface which produces waves. Ocean waves break at sufficiently high wind speeds (typically > 5 m s^{-1}), generating bubbles into the water, which rise to the surface and burst. It is a challenging task to develop an algorithm for SS aerosol production across the oceans. It involves understanding and parametrizing the wave breakage, the formation of bubbles, the bursting of bubbles, the ejection of aerosols, deposition, and entrainment into the boundary layer. Observations of SS particle number over the ocean show a seasonal pattern, minimum in summer and maximum in winter, as a function of wind speed (Quinn and Bates, 2011; Yoon et al., 2007). In the North Atlantic (NA) Ocean, SS dominates all size fractions of SSA mass with a 74% contribution to the accumulation mode mass during winter (periods of low oceanic biological activity), while in summer (when biological activity is high), water-soluble organic carbon contributes between 60–90% of the submicron SSA mass (O'Dowd et al., 2004; O'Dowd et al., 2008).

SS can have a profound effect on cloud droplets activation, being the most hygroscopic aerosol component. In the Southern Ocean, SS was responsible for most of the aerosol-scattered light and comprised a significant fraction of CCN in the remote MBL (Murphy et al., 1998; Vallina et al., 2006). Most of cloud droplets can be formed upon SS nuclei (Twohy and Anderson, 2008), even under sulphate-rich conditions (O'Dowd et al., 1999).

Table 1.1: Key properties of the main aerosol species in the marine troposphere. BC stands for Black Carbon, OA for organic aerosols and POA (SOA) for primary (secondary) organic aerosols. Adapted from Boucher et al. (2013).

Aerosol Species	Size Distribution	Main Sources	Main Sinks	Tropospheric Lifetime	Key Climate Relevant Properties
Sea-salt	Coarse and accumulation modes	Breaking of air bubbles induced by wave breaking. Wind erosion	Sedimentation Wet deposition Dry deposition	1 day to 1 week depending on size	Light scattering. Very hygroscopic. CCN active.
Organic aerosol	POA: Aitken and accumulation modes. SOA: nucleation, Aitken and mostly accumulation modes. Aged OA: accumulation mode	POA: Emitted with sea spray in biologically active oceanic regions SOA: Gas-to-particle-conversion processes	Sedimentation Wet deposition Dry deposition	~ 1 week	Light scattering. Enhances absorption when deposited as a coating on BC. CCN active (depending on age, surface tension and chemistry). Can trigger heterogeneous ice formation.
Sulfate	Primary: coarse mode Secondary: Nucleation, Aitken, and accumulation modes	Primary: sea-spray. Secondary: oxidation of SO_2 and other S gases from natural and anthropogenic sources	Wet deposition Dry deposition	~ 1 week	Light scattering. Very hygroscopic. Enhances absorption when deposited as a coating on BC. CCN active
Nitrate	Accumulation and coarse modes	Oxidation of NO_x	Wet deposition Dry deposition	~ 1 week	Light scattering. Hygroscopic. CCN active
Ammonium	Nucleation, Aitken, and accumulation modes	Marine biota emissions. Reactions of gas-phase ammonia with sulfuric acid and nitric acid	Wet deposition Dry deposition	~ 1 week	Act as CCN

1.3.2 Organic Aerosol

Marine aerosol includes both organic matter (OM) compounds released from the surface of the ocean, within SSA, and the oxidation products of volatile or semi-volatile organics degassed from the sea surface. Sea surface waters contain large amounts of microscopic

particulates including phytoplankton, algae, bacteria, viruses, larger organism fragments, and organic detritus. Phytoplankton is the primary source of OM in the ocean. Phytoplankton releases OM during growth, predation by grazing organisms, and viral lysis. The characteristics of the OM in aerosols above the oceans are probably related to the underlying waters biogeochemistry. Surprisingly, little is understood about these processes and to what degree they affect the marine aerosol properties.

Since the 2000s, it has been known that OM makes up a significant fraction of the marine aerosol mass. O'Dowd et al. (2004) and Cavalli et al. (2004) reported a significant and dominating fraction of OM in sub-micrometer sizes of marine aerosol samples collected at Mace Head (Irish West Coast) in clean air masses. They found that the majority was WIOM and argued that this organic fraction and a significant portion of the WSOM were likely to be derived from bubble-mediated production. This hypothesis was based on the assumption that the dominant WIOM fraction cannot reasonably originate from in-cloud processes or from gas-phase oxidation processes, where products are more likely to be soluble. The mass concentration of OM was lower during the winter corresponding to limited biological activity. Similarly, the considerable concentration of WIOM found in marine aerosol samples obtained offshore of the Monterey coast (California) was attributed to natural primary marine emissions (Kaku et al., 2006). Measurements of aerosol OM in remote regions of the NA and Arctic Oceans reported that OM was made up of carbohydrate-like compounds containing organic hydroxyl groups derived from primary ocean emissions (Russell et al., 2010). Using isotopic carbon analysis, Ceburnis et al. (2011) showed unambiguously that over 80% of the marine aerosol organic carbon originated directly from marine plankton emissions.

The above-reported results were based on measurements of ambient aerosol in which it is hard to discriminate between primary and secondary organic compounds. Numerous studies have been undertaken concerning the production of nascent sea spray aerosols to overpass this limitation (Cochran et al., 2017a; Cochran et al., 2017b; Collins et al., 2013a; Facchini et al., 2008; Hasenecz et al., 2020; Keene et al., 2007; Lee et al., 2015; Prather et al., 2013). From these laboratory experiments, it was discovered that nascent SSA comprises a complex population of particles with a varying chemical composition that is specifically affected by complex physical and biological processes occurring in the ocean (see Section 1.8: “Final Considerations on Phytoplankton-Aerosol Interactions” for more details).

In addition to primary organic aerosol (POA), multiple evidence elucidates the phytoplankton regulation of secondary organic aerosol (SOA). For instance, Facchini et al. (2008) observed elevated concentrations of dimethyl- and diethyl- ammonium salts in atmospheric aerosols in regions of phytoplankton blooms, mainly in the sub-micrometer size range, indicating a secondary production mechanism. MSA, oxalic acid and dicarbonyls have been observed in atmospheric aerosols over many ocean regions remote from continental sources (Miyazaki et al., 2010; Rinaldi et al., 2011). MSA is the most studied and well understood SMA compound (Facchini et al., 2008; Li et al., 1996; Mukai et al., 1995; Savoie and Prospero, 1989; Watts et al., 1990; Yoon et al., 2007); apart from this, a clear understanding of the physico-chemical processes leading to SOA formation over the ocean is still missing.

1.3.3 Non-sea-salt-Sulfate

Sulfates are among the most important, and well characterized, secondary aerosol components in the marine atmosphere. Marine phytoplankton produces dimethylsulphonium propionate (DMSP) that breaks down to DMS, the primary precursors for sulfate aerosols, and several other products. The production of DMSP, the biochemical precursor of DMS, depends not only on the different phytoplankton classes (Keller et al., 1989; Orellana et al., 2011) but also on the physiological state of the cells within each group (Becagli et al., 2013; Matrai and Vernet, 1997). Furthermore, DMS release in the water column is highly related to phytoplankton senescence/demise rather than growth (Kwint and Kramer, 1995; Laroche et al., 1999; Zhuang et al., 2011) which means that healthy and exponentially growing cells release little amounts of DMSP. Biogenic DMS is the dominant volatile sulfur compound in ocean surface waters which constitutes approximately 50% of the global natural sulfur emissions (Andreae, 1990) to the remote marine troposphere. After emission to the atmosphere, the oxidation of DMS results in the producing of a large variety of sulfur-containing compounds, including, for example, sulfur dioxide (SO_2), sulfuric acid (H_2SO_4), dimethylsulfone ($CH_3S(O)_2CH_3$, $DMSO_2$), methanesulfinic acid ($CH_3S(O)OH$, MSIA), dimethylsulfoxide ($CH_3S(O)CH_3$, DMSO), and methanesulfonic acid (CH_3SO_3H, MSA) (Arsene et al., 1999; Barnes et al., 1996; Barnes et al., 2006; Urbanski et al., 1998). SO_2 can be taken up by particles directly to form nss-SO_4^{2-} or can undergo aqueous-phase oxidation in cloud droplets to form nss-SO_4^{2-}.

Toole and Siegel (2004) suggested that the net biological production and concentration of DMS in the upper oceanic mixed layer is directly proportional to the ultraviolet radiation dose at the sea surface and to seasonally varying parameters such as sea surface temperature (SST) and solar flux. This assumption is supported by Becagli et al. (2013) and Vallina and Simo (2007) who showed a strong correlation between DMS concentrations and the solar radiation dose in the upper mixed layer of the open ocean regardless of latitude, phytoplankton biomass and temperature. In the Eastern Mediterranean atmosphere, the monthly DMS measurements showed a seasonal variability that is highly correlated to SST (Kouvarakis and Mihalopoulos, 2002).

1.3.4 Nitrate

Nitrate aerosol (NO_3^-) is a particulate matter component formed chemically from the oxidation of nitrous oxides (NO_x) in the atmosphere. Typical sources of nitric oxides are the burning of fossil fuels, soils, biomass, and lightning. Due to the expected increase in nitrate precursor emissions, nitrate aerosols are expected to become more significant in the future atmosphere (Bauer et al., 2007) as an air pollutant, with rising the annual mean near-surface air concentrations. Given its major anthropogenic origin, nitrate is only a minor component of marine aerosol, which presence usually indicates contamination of the air mass by anthropogenic emissions.

Nitric acid is contained mainly in the coarse mode of marine aerosol rather than in the fine particle mode because of the reaction between gaseous nitric acid and sodium chloride present in SSA particles, which results in the formation of particulate phase sodium nitrate ($NaNO_3$) and the release of gaseous chloridric acid (HCl). Redistribution of nitrate to aerosols in the coarse mode has a major impact on its role in the climate system. If nitrate is deposited in the fine particle fraction, the aerosol and cloud radiative properties would be influenced by enhancing the scattering of incoming shortwave solar radiation and increasing the CCN level. Nevertheless, nitrate has far less radiative effects on the coarse mode aerosols. The coarse distribution of nitrate also ensures that their atmospheric residence time in the MBL is shorter than that of sulfate aerosols, resulting in quicker removal from the atmosphere by gravitational settlement. Deposition of aerosol nitrate (and other compounds containing

aerosol-borne nitrogen) can have a significant impact on ocean productivity, particularly in oligotrophic regions with limited upwelling or riverine inputs.

1.3.5 Ammonium

In the remote marine troposphere, NH_4^+ is the dominant base interacting with acidic species, given its presence in the gas and particle phases and in cloud, rain and seawater (Quinn et al., 1987). Ammonium sulfate ($(NH_4)_2SO_4$) and ammonium nitrate (NH_4NO_3) are formed by reactions of gas-phase ammonia with sulfuric acid (H_2SO_4) and nitric acid (HNO_3) respectively (Huntzicker et al., 1980; Marti et al., 1997; Stockwell et al., 2003). The formation of these hygroscopic secondary salts strongly depends on several chemical and micro-meteorological factors, such as the levels of gaseous precursors, the concentrations of atmospheric oxidants, the characteristics of preexisting aerosols, the air temperature and humidity (Baek et al., 2004; Pathak et al., 2009).

1.4 Marine Aerosols Particle Size Distributions

Marine aerosol particles in the atmosphere have widely variable diameters ranging from few nanometers to tens of µm. Particle size is one of the most important parameters for describing the behavior of aerosols, affecting both physical and chemical properties and, ultimately, their lifetime. Aerosol size distributions are usually plotted against the logarithm of the particle diameter (Dp) and are generally defined by their number, surface, or volume.

A typical example of marine aerosol number size distribution is shown in Figure 1.2. The number size distribution is expressed as $dN/d(log\ Dp)$, or the number of particles per cm^3 of air in a size bin $1\ log\ Dp$ wide. Because $log\ Dp$ is unitless, the number distribution has units of numbers of particles per cm^3. The integrated area under the size distribution, therefore, represents the total number of particles. In general, the number concentration is dominated by particles less than about 0.3 µm in diameter.

The size distribution of marine atmospheric aerosol particles is characterized by three modes: the Aitken mode ($Dp < 0.1\ \mu m$), the accumulation mode ($0.1 < Dp < 0.5\ \mu m$), and the coarse mode ($Dp > 0.5\ \mu m$) (Fitzgerald, 1991). These limits of each mode are subjective since both concentrations and mean size ranges have hemispheric variations and latitudinal trends (Heintzenberg et al., 2000). Nucleation mode is sometimes observed, containing very

small particles ($Dp < 0.01\ \mu m$). Each aerosol mode has different mechanisms of formation and removal, and often very different chemical characteristics.

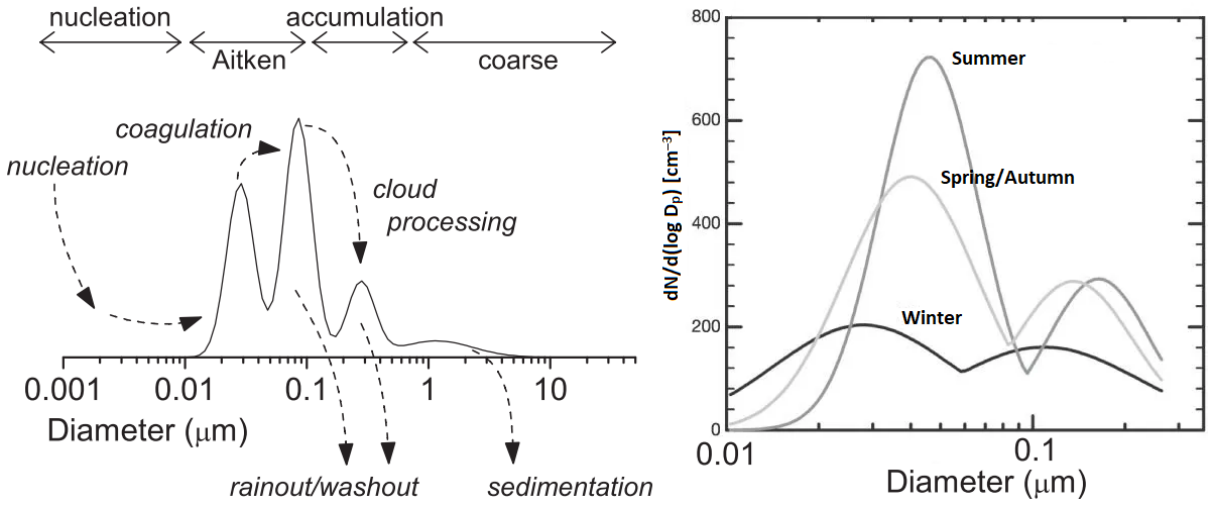

Figure 1.2: Left) Sources, transformation, and removal processes of aerosol particles in the major modes as a function of diameter (Saltzman, 2009). Right) Seasonal characteristics of marine aerosol number size distributions, Aitken and accumulation modes, over the NA Ocean, reproduced from O'Dowd et al. (2004).

Figure 1.3 illustrates the average relative chemical compositions and mass distributions of remote marine aerosol for the periods of low biological activity (LBA) and periods of high biological activity (HBA) in the NA ocean (O'Dowd et al., 2004). In winter, LBA, the SS dominates all the size fractions with a 74% (0.3 μg m^{-3}) contribution to the accumulation mode mass. The remainder of the mass in this mode comprised 10% (0.045 μg m^{-3}) nss-SO_4^{2-} and 15% (0.070 μg m^{-3}) OM. By contrast, during algal/phytoplankton blooming periods (HBA), from spring to autumn, the OM fraction increased markedly, particularly for the sub-micrometric sizes, and this fraction increased with decreasing size. The OM in the accumulation mode contributed 65% (0.619 μg m^{-3}) of the mass, whereas SS contributed 10% (0.097 μg m^{-3}) and nss-SO_4^{2-} dominated 23% (0.216 μg m^{-3}). The largest percentage contribution (83%) of OM occurred in the fine mode (0.06–0.125 μm). Across the size range from 0.06 to 0.5 μm, the average contributions of water-insoluble and water-soluble organics were 45% and 18%, respectively. These seasonal trends can have large impacts on aerosol chemistry, ultimately impacting how marine aerosol affects the regional and global climate (Brooks and Thornton, 2018; Cochran et al., 2017b; McCoy et al., 2015; Meskhidze and Nenes, 2006, 2010; Sciare et al., 2009; Yoon et al., 2007).

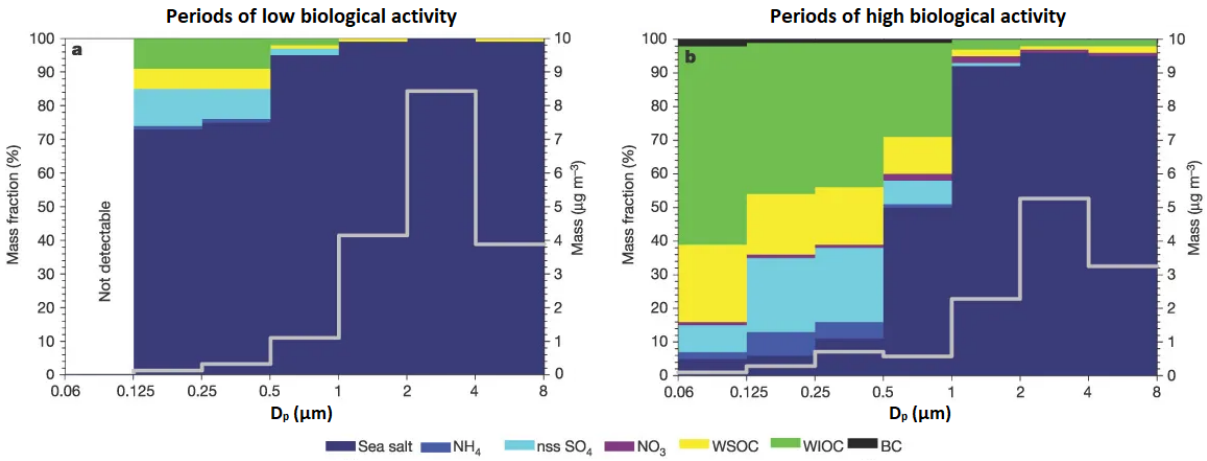

Figure 1.3: Average size-segregated chemical compositions and absolute mass concentrations of marine aerosol sampled at Mace Head in the Northeast Atlantic Ocean in a) winter, a season of LBA, and b) summer, a season of HBA, reproduced from O'Dowd et al. (2004). The size fractions from 0.125 to 0.5 µm cover the accumulation mode and the size fraction from 0.06 to 0.125 µm covers most of the Aitken mode. The concentrations of water-soluble organic carbon (WSOC), water-insoluble organic carbon (WIOC), and Black Carbon (BC) are reported as mass of organic matter (see Cavalli et al. (2004) for the full discussion).

Cloud processing is believed to be responsible for the transition of material from the gas-to-particle phase and the growth of particles from the Aitken to the accumulation mode in marine non-precipitating clouds (Hoppel et al., 1986), known as "Hoppel theory". The number-size-distributions of marine aerosol are mostly bimodal with two dominant peaks, the Aitken and accumulation modes. Exposed to non-precipitating clouds, marine aerosol shows increased mass associated with CCN particles consistent with the aqueous-phase processing of SO_2 to SO_4^{2-} (Hoppel et al., 1994), which supports the fact that cloud droplet activation is a mechanism of particle growth. Hoppel theory implies that in a well-mixed MBL, an initial (monomodal) number-size distribution will be exposed to MBL cloud supersaturation which will activate all particles with critical diameters (chemistry dependent) greater than that associated with the cloud supersaturation. These particles then expand in mass by aqueous-phase processing with the addition of SO_4^{2-}, and once evaporated they behave as a secondary mode of larger particles.

1.5 Climate Relevance of Marine Aerosols

The chemical composition, number concentration and size distribution of marine aerosols determine their ability to influence climate (Brooks and Thornton, 2018; Charlson et al., 1987; Langmann et al., 2008) by either absorbing and scattering incoming solar radiation (the direct radiative effect) (Murphy et al., 1998; Zhang and Du, 2017) or serving as CCN and INPs, whereby modifying the microphysical and macrophysical properties of clouds (the cloud-albedo or aerosol indirect effect) (DeMott et al., 2016; McCluskey et al., 2018c; O'Dowd et al., 2004; Ovadnevaite et al., 2017).

Radiative forcing (RF) provides a tool for quantifying how the transfer of energy, into and out of the climate system, is influenced by natural and anthropogenic emissions (Myhre et al., 2013). The IPCC defines RF as the change in net downward radiative flux at the tropopause after allowing for stratospheric temperatures to readjust to radiative equilibrium while holding surface and tropospheric temperatures and state variables fixed at the unperturbed values. Another estimate is the effective radiative forcing (ERF) which is defined as the change in net downward radiative flux at the top of the atmosphere after allowing for atmospheric temperatures, water vapor, clouds and land albedo to adjust, but with global mean surface temperature or ocean and sea ice conditions unchanged. Both RF and ERF are expressed in watts per square meter averaged over a particular time and quantifies the energy imbalance that occurs when the imposed change takes place.

Figure 1.4 shows the RF bar chart for the period 1750–2011 based on emitted compounds (well-mixed and short-lived gases, aerosols, and their precursors) or other changes (Myhre et al., 2013). The proposed emission-based RF estimates provide substantially different relative importance to different considered emissions. The radiatively active short-lived trace gases, aerosols and their precursors are often commonly referred to as short-lived climate forcers because their atmospheric effect is mainly felt during the first one to three decades of their emissions (Fiore et al., 2015; Myhre et al., 2013) as opposed to long-lived greenhouse gases.

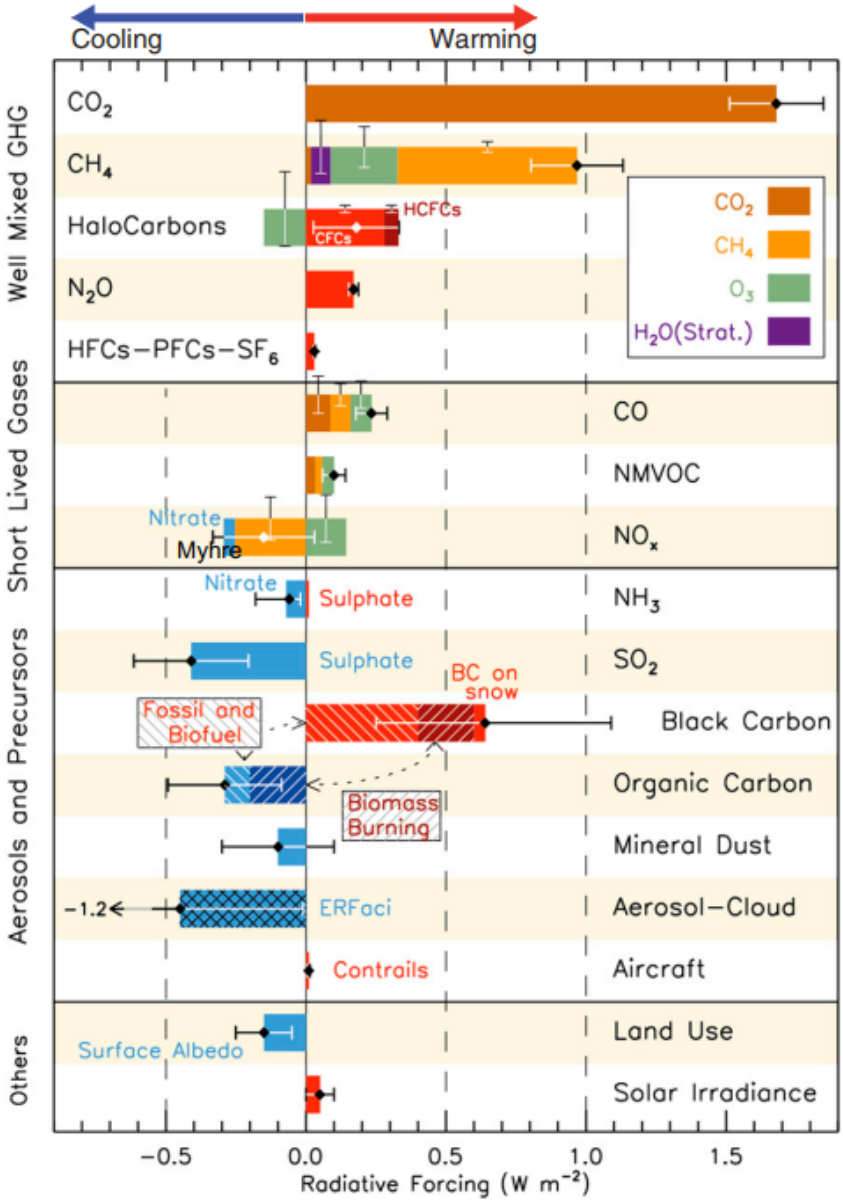

Figure 1.4: The global average radiative forcing estimation in 2011 relative to 1750 for emitted chemical species (gases, aerosols, and their precursors) or other factors. The colors inset in the top part of the figure are used to represent RF from emitted species affecting several chemicals while red (positive forcing) and blue (negative forcing) are used for emitted components that affect fewer forcing agents. The vertical bars represent the relative uncertainty of the RF induced by each component. The net impact of the individual contributions is shown by a diamond symbol and its uncertainty (5 to 95% confidence range) is given by the horizontal error bar. Taken from Myhre et al. (2013).

The short lifetime of aerosols and their precursors results in spatially inhomogeneous abundances and related forcings highly sensitive to the location of emissions. Consequently, their climate influence may be more important on a regional scale (Aamaas et al., 2017; Collins et al., 2013b), as opposed to the more homogeneous spatial effect of well-mixed greenhouse

gases. In general, the impacts of aerosol on clouds might have a profound negative forcing impact and partially offset a substantial part of the global mean forcing of the greenhouse gases (Breon, 2006; Slingo, 1990). However, the estimation of climate forcings still has a high degree of uncertainty, particularly concerning aerosol-cloud interactions. A large fraction of the uncertainty is due to lack of knowledge of the unperturbed natural aerosol-cloud-climate system (Carslaw et al., 2013; Rap et al., 2013), partially due to the complex nature of aerosol-cloud interactions, and also due to the difficulties in performing measurements in pristine conditions. It has been shown that 45% of the aerosol forcing variance results from uncertainties in natural emissions, while 34% of the variance is related to anthropogenic emissions (Carslaw et al., 2013). This reflects the importance of understanding unperturbed, pre-industrial, marine environments, dominated by natural aerosols. The RF estimates for aerosol direct effect and the aerosol-cloud interaction (cloud albedo effect) are discussed in the following Sections.

1.5.1 Direct Effect

The RF due to direct aerosol effect (aerosol-radiation interactions) results from scattering and absorption of shortwave and longwave radiation by atmospheric aerosol particles. The direct scattering effect of a particle is based on its refractive index, shape, and diameter, although, the scattering properties of a population of aerosols are also dependent on the number-size distribution of their particles. The greater the impact of scattering, the greater the aerosol optical depth (AOD). The global ERF estimate due to aerosol-radiation interactions (ERF_{ari}) is assessed to be –0.45 (–0.95 to +0.05) W m^{-2} between 1750 and 2011.

The most effective particle size range for the scattering of sunlight is between 0.2 and 1 µm for a wavelength of 0.55 µm, which corresponds to mid-visible solar radiation. As a result, the nss-SO_4^{2-} aerosol can be a significant contributor to aerosol light scattering (see Figure 1.3). The SS is among the most significant natural aerosol chemical component in the atmosphere as regards direct aerosol effects and solar radiation scattering in the MBL for both sub- and super-micrometer size ranges (Bates et al., 2006; Kleefeld et al., 2002; Murphy et al., 1998). The majority of SS aerosol mass occurs in particles larger than 1 µm in diameter, low scattering efficiency, but the abundance of SS mass concentration is enough to compensate the low scattering efficiency of this size range.

Scattering properties in the NA Ocean are proportional to the square of the wind speed independently of season. However, periods of HBA often result in half the scattering of LBA seasons (Vaishya et al., 2012). Vaishya et al. (2012) attributed this scattering discrepancy to the presence of a large fraction of sub-micrometric OM particles which reduces the refractive index of the particles, explaining 70% of the reduction in scattering alone. When considering the modified size distribution during HBA combined with the lowered refractive index of the OM particles, another 22% of the reduction in scattering could be explained.

1.5.2 Indirect Effect (Aerosol-Cloud Interaction)

The aerosol-cloud interaction is quantified in terms of the ERF (ERF_{aci}) with an estimate of –0.45 (–1.2 to 0.0) W m^{-2} (Figure 1.4). The total ERF due to aerosols ($ERF_{ari+aci}$, excluding the effect of absorbing aerosol on snow and ice) is assessed to be –0.9 (–1.9 to –0.1) W m^{-2} with medium confidence. The effects of marine aerosols on micro- and macro-physical properties of clouds are largely determined by the number concentration and composition of particles less than 300 nm since this diameter range large enough to take up water vapor and serve as nuclei for cloud droplet formation in MBL (Quinn and Bates, 2011).

The indirect effect of aerosols occurs through radiation interaction with droplet particles in the cloud, which exist in a super-saturated regime in the atmosphere. When an air parcel experiences an adiabatic updraft into the higher altitude of the atmosphere, its temperature begins to dip below the dew point and water vapor becomes super-saturated (Relative humidity (RH) > 100%). RH, expressed as a percentage, is a measure of the amount of water vapor that air can retain at a given temperature and pressure. If the relative humidity is < 100 %, we refer to the air as sub-saturated, while we refer it as super-saturated when RH > 100 %. Once supersaturation is reached, water condenses on the aerosol particles, which are sufficiently large and soluble enough to take up water, grow, and act as CCN and cloud droplets start to form. The aerosol characteristics that are important in cloud droplet activation are size, concentration, and chemical composition. A dynamic equilibrium between adiabatic cooling (increasing supersaturation) and condensation on existing droplets (that reduces supersaturation) sets the supersaturation which develops in clouds. Cooling occurs during the initial phases of cloud formation, and supersaturation rises, which induces droplet formation. Nevertheless, a stage is achieved where condensation of water vapor is dominant,

supersaturation is minimized, and nucleation of droplets stops. Hence the point of maximum supersaturation is the quantity which defines how many particles will function as a CCN.

Aerosol particles greater than 300 nm in diameter can activate irrespective of chemical composition, but due to their limited number, they do not make a major contribution to the concentration of CCN numbers. For particles smaller than 300 nm, chemical composition influences the activation critical diameter into cloud droplet by assessing the solute molecular weight of the droplet, density, solubility, degree of dissociation, and surface tension. Köhler theory (Köhler, 1936) estimated the activation critical diameter values between 40 and 300 nm for soluble compounds that do not greatly impact droplet surface tension at about 0.1–0.4% supersaturation range. Such a range has been investigated as the effective supersaturation of MBL clouds (Hoppel et al., 1996; Leaitch et al., 1996; Roberts et al., 2006), although effective supersaturations up to 0.75 % for marine stratocumulus clouds (Martucci and O'Dowd, 2011) and 1% for clean stratus clouds (Hudson et al., 2000) have been reported. At 1% supersaturation, the activation critical diameter decreases to 20–30 nm. In summary, particles smaller than 300 nm in diameter decide the CCN concentration in the remote MBL and have the potential to modify cloud properties. The number and size of cloud droplets depend on how many particles can serve as CCN (Fanourgakis et al., 2019; Lance et al., 2004) and it is controlled by updraft velocity (Jones et al., 2009; Liu et al., 2020a), aerosol size distribution (Hegg, 1999), and chemical composition (Twohy and Anderson, 2008). The CCN population differs significantly with space and time due to the short atmospheric lifetimes of aerosol particles as well as to the inhomogeneous distribution of its local sources and sinks.

Clouds in the Earth system have considerable climatic impacts. They play a significant role in the Earth's radiative balance by reflecting and absorbing both shortwave solar and longwave infrared radiation. Cloud reflectivity (albedo) is controlled by microphysical properties, such as cloud droplet number concentration (CDNC), cloud droplet effective radius (R_{eff}), and importantly cloud liquid water content (LWC) (Frey et al., 2017; Liu et al., 2020b). For the same amount of LWC, an increase in the aerosol/CCN concentrations in the atmosphere will produce more CDNC and a decrease in R_{eff} (Twomey, 1974; Twomey et al., 1984). Enhancement of cloud droplet number concentration and diminishing of cloud droplet size contribute to an increase in brightening (more reflectivity) of the cloud as more solar

radiation is scattered upward and less is transmitted through the cloud, which is called the first indirect effect (Twomey effect) of aerosol in clouds.

The second indirect effect refers to increasing cloud lifetime in the atmosphere through precipitation suppression. This leaves more water in liquid-phase clouds for longer periods due to reducing cloud droplet sizes (Albrecht, 1989; Liou and Ou, 1989; Rosenfeld et al., 2019; Toll et al., 2019), which makes them less likely to become rain droplets. Precipitation is considered as strongly suppressed when R_{eff} does not exceed 12–14 μm in marine low clouds (Fan et al., 2020; Freud and Rosenfeld, 2012). Cloud lifetime is a measure of how long the clouds reflectance will last. The cloud lifetime is sensitive to both synoptic meteorological conditions and dynamical cloud microphysical interactions. The collision-coalescence of droplets becomes less efficient with increased CDNC and decreased R_{eff} which leads to an increase in cloud cover fraction with cloud optical depth (COD) for a long-time (Myhre et al., 2007). Marine clouds are susceptible to perturbation in marine aerosol flux associated with natural emissions through processes driving CCN activation. Global models have shown that biogeochemical changes in the surface seawater can account for a change in marine CCN number concentrations between 5% and +50% (Meskhidze et al., 2011; Tsigaridis et al., 2013; Westervelt et al., 2012).

The aerosol physico-chemical properties play a key role in the cloud nucleation capability of aerosol particles. While recent studies introduced observational and theoretical evidence indicating that surface tension reduction by organics can lead to significant increases in cloud droplet concentrations (Ovadnevaite et al., 2017; Ruehl et al., 2016), other studies have shown that CCN concentrations are mainly controlled by the aerosol number size distribution (Dusek et al., 2006). The increase in aerosol concentration leads to an increase in CDNC, which implies a decrease in R_{eff}, with stronger effect under more stable conditions, while cloud fraction and LWC are not sensitive to the aerosols load (Li et al., 2016; Liu and Li, 2019; Liu et al., 2016). Indeed, Lowe et al. (2019) showed that the susceptibility to the particle surface phase of cloud microphysics, optical properties, and shortwave radiative effects is determined by an interplay between the aerosol particle size distribution, chemical composition, water availability and atmospheric dynamics, and so, the surface phase is important primarily in clean environments where ultrafine particulate sources occur.

The aerosol-cloud interactions are difficult to study because it is hard to break up the aerosol and meteorological effects (Sato and Suzuki, 2019; Stevens and Feingold, 2009). Clouds are liable to meteorological conditions that complicate their responses to changes in aerosol concentration and composition (Loeb and Schuster, 2008). In the MBL, cloud cover is considerably associated with lower troposphere stability (LTS) (Janssen et al., 2011; Wood and Bretherton, 2006), a measure of convection strength. The LTS, defined as the difference in potential temperature between 700 hPa and the surface, explains most of the seasonal variability of marine stratiform cloud coverages at five oceanic regions (Klein and Hartmann, 1993). An increase of 1 K of LTS produces a 6% increase in cloud fraction. Employing artificial neural networks, Andersen et al. (2017) proved that monthly LTS was the main determinant of cloud fraction and droplet size. The transport and mixing of the aerosols from the surface to the cloud base determines the fraction of aerosols activated into cloud droplets (Janssen et al., 2011). When the meteorological effects are excluded, Rosenfeld et al. (2019) concluded that aerosol-driven droplet concentrations account for 75% of the radiative cooling effect variability mainly due to their effects on the coverage of low-level ocean clouds.

Marine aerosols may be involved also in the process of ice formation in clouds, which has severe and not well characterized climate effects (Murray et al., 2021). These aspects will be treated in the following Paragraph.

1.5.3 Marine aerosol and Ice Nucleating Particles

Ice in tropospheric clouds can form via homogeneous freezing at temperatures below –38 °C and relative humidity with respect to ice (RH_i) above 140%. Outside these conditions, ice formation can occur by heterogeneous nucleation, at higher temperatures, aided by aerosol particles known as ice nucleating particles (INPs). Heterogenous ice formation occurs through four different mechanisms: deposition, condensation, immersion, and contact freezing (Vali et al., 2015). Ice formation by deposition occurs when the ambient is super-saturated with respect to ice and sub-saturated with respect to liquid water: water molecules can pass from the vapor phase directly to the ice phase on a solid substrate (INP). In condensation freezing, ice forms as water vapor condenses on a CCN at $T < 0$ °C, while in immersion freezing a supercooled water droplet freezes thanks to a nucleus suspended in the body of water. In

contact freezing, an external INP promotes freezing coming into contact with a supercooled droplet.

Cloud glaciation can quickly and strongly alter the radiative properties of clouds, cloud extent, lifetime and precipitation rate (Figure 1.5b) (Kanji et al., 2017; Murray, 2017). In mixed-phase clouds the role of ice crystals is particularly important because ice can influence the supercooled liquid water content through the Wegener–Bergeron–Findeisen process (Korolev, 2007; Korolev and Field, 2008). Most precipitation in clouds initiates via the ice phase (Lau and Wu, 2003; Lohmann and Feichter, 2005). Therefore, atmospheric processes involving INPs can have a strong impact on climate.

INPs may be of natural origin (*e.g.*, mineral dust, volcanic ashes, terrestrial biogenic material, etc.) or anthropogenic (*e.g.*, industrial processes, biomass burning, etc.) (Hoose and Mohler, 2012; Murray et al., 2012). Because of their generally efficient ice nucleating ability and their large emission rates, mineral dust particles are recognized as the most significant INP type at the global scale (Hoose and Mohler, 2012; Murray et al., 2012). The main sources of dust particles are arid soils or deserts, volcanoes, and agriculture soils.

Nevertheless, many studies demonstrated that SSA can be a significant source of INPs over remote oceanic locations (Bigg, 1973; Bigg and Leck, 2001; Schnell and Vali, 1976). Recently, the interest of the scientific community has been fostered by publications confirming the potential climate relevance of the marine primary biogenic aerosols from phytoplankton exudates as a source of INPs (Burrows et al., 2013; DeMott et al., 2016; Hartmann et al., 2019; McCluskey et al., 2018a; McCluskey et al., 2017; McCluskey et al., 2018b; McCluskey et al., 2018c; Vergara-Temprado et al., 2017; Wilson et al., 2015). Organic material emitted by marine organisms was found to nucleate ice well below the homogeneous freezing threshold, and for activation temperature (T_A) as warm as –10 °C in immersion mode (Wilson et al., 2015). By contrast, ice-nucleating properties have rarely been associated with secondary organic aerosol in any environment (Kanji et al., 2017; Si et al., 2018; Wilbourn et al., 2020).

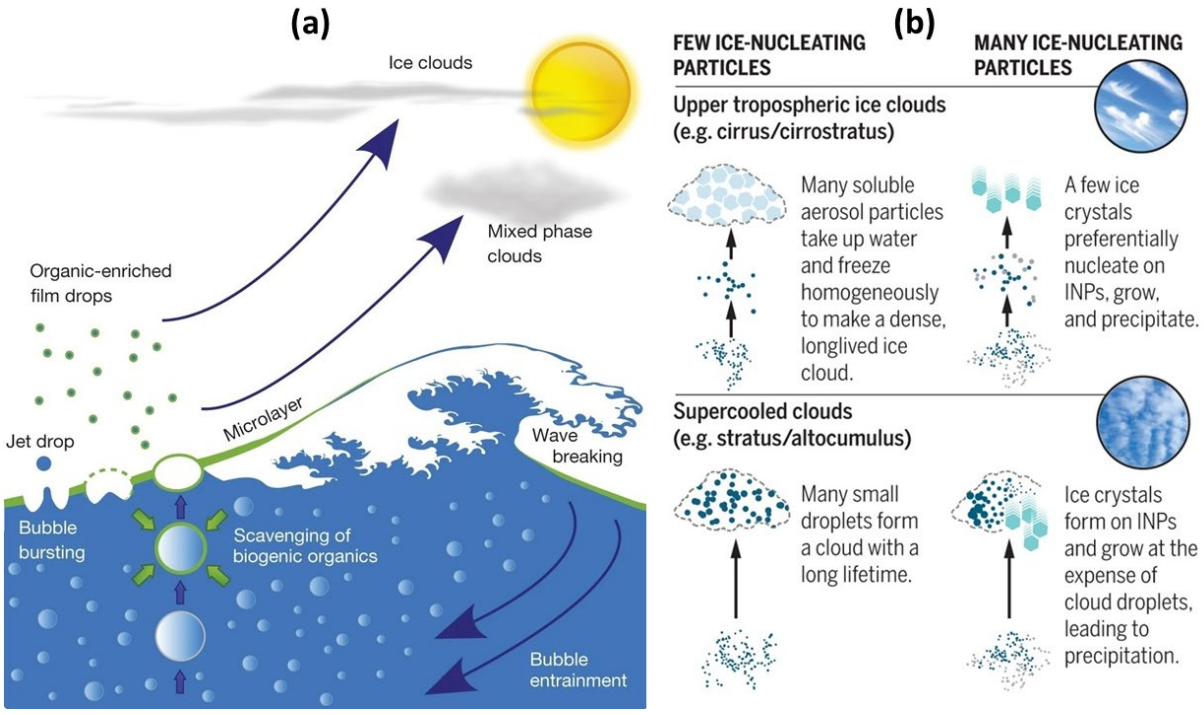

Figure 1.5: (a) Sea spray aerosol particles enriched with organic material are formed when bubbles burst at the air-sea interface. The surface-active organic material of biological origin is scavenged at the interface of the bubbles as they rise through the water column. This process enriches the air-sea interface with surface-active organic material forming the sea surface microlayer (green layers) as shown by Wilson et al. (2015). (b) Representation of the inference of INPs in upper tropospheric and supercooled clouds. For both high (ice) clouds and supercooled liquid clouds, heterogeneous ice nucleation produces few and large ice crystals that precipitate quicker, decreasing the lifetime of the clouds. Taken from Murray (2017).

The mechanism of ice formation in clouds from SSA is shown in Figure 1.5a. SSA may contain significant quantities of organic material that is ejected into the atmosphere during bubble bursting; these organics are thought to be the key factor for SSA ice activation (McCluskey et al., 2018b; Wilson et al., 2015). It has been documented that the ice-nucleating properties of SSA evolve during the time extent of an algal bloom (McCluskey et al., 2017), following the evolution of the algal population. This leads to the hypothesis of a phytoplankton-driven seasonality of the INP properties of marine aerosol, which may be another piece of the phytoplankton-aerosol-cloud puzzle. However, long term marine INP measurement studies are currently lacking, providing little information on INP seasonality and spatial source distribution in the marine environment.

1.6 The CLAW Hypothesis

The CLAW (Charlson, Lovelock, Andreae, Warren) hypothesis (Charlson et al., 1987) proposed the first mechanism by which phytoplankton regulates the Earth's climate. It can be described by the following negative feedback loop: 1. Increased seawater phytoplankton blooms, due to increased world temperature, will raise oceanic DMS concentrations and subsequently raise DMS releasing into the atmosphere, 2. DMS, that undergoes oxidation in the atmosphere, form sulfate aerosols, and 3. Such aerosols participate in the regulation of marine atmospheric CCN populations and thus increase the planetary albedo. The consequent reduction in Earth's temperature or in the amount of solar radiation entering the surface will, in turn, reduces phytoplankton abundance, and therefore DMS production, thereby closing the feedback loop.

Many studies support the CLAW hypothesis. For example, during seasons of high biological productivity, the increase in biogenic DMS was associated to raise in CCN numbers (Korhonen et al., 2008; Lana et al., 2012; Meskhidze and Nenes, 2010; Sanchez et al., 2018; Toole and Siegel, 2004; Vallina et al., 2006) and consequently cloud albedo (Charlson et al., 1987; Langmann et al., 2008; Sanchez et al., 2018; Thomas et al., 2010), resulting in negative climate feedback (Kim et al., 2018; Kogan et al., 1996; Lohmann and Leck, 2005; Mahmood et al., 2019) that stabilizes the Earth's atmosphere. At Cape Grim, Tasmania, a remote sampling site in the Southern Ocean, the atmospheric concentration of DMS, MSA, nss-SO_4^{2-}, and CCN were maximized in Summer, as is predicted for biologically controlled parameters (Ayers et al., 1997; Ayers and Gras, 1991). The DMS and CCN measurements made in the MBL over the tropical South Atlantic (Andreae et al., 1995) and the northeastern Pacific Ocean (Hegg et al., 1991) showed that DMS could describe up to 50 percent of the variation in CCN concentrations. The observations of the South Atlantic also showed significant correlations between MSA/nss-SO_4^{2-}, and CCN. A recent study by Fossum et al. (2018) concluded that SMA (mainly sulfate) dominates the number fraction of activated cloud droplets in the Antarctic MBL. Further, over yearly timescales, secondary biogenic aerosol particles dominate the sub-micrometer number concentration and CCN population during summer in the Arctic atmosphere (Lange et al., 2019). Such DMS and CCN seasonality coherence were viewed as a support for the hypothesis of MBL CCN regulation by DMS emissions. Experimentally, SMA

was linked to phytoplankton abundance and increases CCN activity, implying that SMA is the most important factor influencing marine cloud properties (Mayer et al., 2020).

Despite the various observations which put in relation the different actors of the phytoplankton-DMS-CCN-cloud albedo climate feedback loop, global models have shown that the predicted changes in DMS flux have a low impact on the CCN concentration due to the abundance of MBL CCN from non-DMS sources (Carslaw et al., 2010; Woodhouse et al., 2010). This suggests that the response of clouds to changes in the aerosol may be much more complex than hypothesized by CLAW: for instance, Quinn and Bates (2011) hypothesized a role of SSA in the marine biota-aerosol-cloud feedback. Indeed, Ovadnevaite et al. (2011a) revealed that SSA enriched with POA enhance the CCN activation efficiency and that high CDNC concentrations can be explained by SSA enriched by primary organics. Further, biogenic marine SOA can influence cloud activation (Croft et al., 2021; Ovadnevaite et al., 2017), which makes the climate system even more complex. In addition to various sources of ocean derived CCN in the MBL, the continental emissions can travel thousands of kilometers to distant ocean areas and contribute to particle nucleation in the MBL troposphere, providing an additional CCN source (Korhonen et al., 2008). Nonetheless, the lack of a global climate feedback loop dependent on oceanic phytoplankton sulfur emissions does not rule out the link between ocean-related CCN and climate, which may have been dominant in the pre-industrial period and may still regulate the regional climate over unperturbed oceanic regions (*e.g.*, the Southern Ocean) (McCoy et al., 2015). It is worth mentioning that the link between marine biota and INP concentration, mediated by SSA (DeMott et al., 2016; McCluskey et al., 2017; Ruehl et al., 2016; Vergara-Temprado et al., 2017; Wang et al., 2015; Wilson et al., 2015), was not known when the CLAW hypothesis was developed. This adds further complexity to ocean-atmosphere-climate interactions.

1.7 Final Considerations on Phytoplankton-Aerosol Interactions

There is a general consensus in literature that the characteristics of marine aerosol are dependent on the properties of the seawaters from which they are generated and, particularly, on the ongoing biological activity (Cochran et al., 2017a; Crocker et al., 2020; Facchini et al., 2008; Mayer et al., 2020; O'Dowd et al., 2004; Sellegri et al., 2021). Significant efforts have been made worldwide to explain how marine biological activity affects

atmospheric aerosol properties and their seasonality since the 1980s, when the (secondary) sulfate-driven phytoplankton-cloud-climate feedback was postulated (Charlson et al., 1987). For instance, Meskhidze and Nenes (2006) reported CDNC over a blooming ocean area twice as high as away from the bloom, with a resulting 30% reduction in R_{eff}. A clear seasonal pattern was observed for organic aerosols in the southern Indian Ocean by Sciare et al. (2009) which was related to the ocean biological productivity. Miyazaki et al. (2010) observed average concentrations of organic carbon and oxalic acid two to three times higher in marine biologically more influenced aerosols, than in less influenced aerosols. More recently, McCoy et al. (2015) reported enhanced aerosol number concentrations that are spatially correlated with regions of high chlorophyll-a concentration (CHL), over the Southern Ocean. As a final example, the research by Dall'Osto et al. (2017b), Dall'Osto et al. (2019), Decesari et al. (2020), and Rinaldi et al. (2020) showed that the chemical composition of marine aerosol over the Weddell sea, is highly influenced by the life cycle of algal communities living at the interface between sea-water and sea-ice. At the beginning of the Antarctic summer, when sea-ice melts, these micro-organisms produce important amount of exudates to defend themselves from the abrupt change of their environment (strong salinity delta, solar radiation, etc…) and such osmolytes (and their degradation products) impact the chemical composition of marine aerosol particles, possibly triggering also new particle formation.

In the NA, where the majority of the data used for the present study were collected, the physical and chemical properties of marine aerosol and their link to oceanic biological activity have been extensively studied (Cavalli et al., 2004; Facchini et al., 2008; O'Dowd et al., 2004; O'Dowd et al., 2008; Rinaldi et al., 2010). Yoon et al. (2007) reported a clear seasonal trend, resembling that of oceanic biological activity, for several aerosol chemical components, size distribution modal diameters and optical properties. Contextually, the CCN fraction over the NA Ocean has been associated with the organic enrichment of sea-spray aerosol (Ovadnevaite et al., 2011a), potentially introducing new biosphere-climate feedbacks (Quinn and Bates, 2011). Sanchez et al. (2018) pointed out a clear seasonality in the CCN budget over the NA Ocean, related to phytoplankton induced DMS emissions. Finally, the recent work by Sinclair et al. (2020) showed that cloud microphysical properties correlate with marine biogenic aerosol concentrations, while cloud macrophysical properties correlate more with atmospheric state parameters than changes in CCN concentrations.

Some specific works suggest a direct coupling between phytoplankton biomass and the production of organic-rich marine primary aerosols over the NA Ocean (Gantt et al., 2011; O'Dowd et al., 2015; Rinaldi et al., 2013), indicating that biological activity has an active role in primary aerosol formation. In details, Rinaldi et al. (2013) reported that an eight-day time-lagged correlation exists between satellite retrieved CHL and organic enrichment in the SSA measured at MHD, analyzing a dataset of marine aerosol samples collected from 2002 to 2009. Said paper improved previous works by Langmann et al. (2008) and Vignati et al. (2010) and was the first one to introduce the spatio-temporal correlation approach for investigating the relationship between marine aerosol properties and biological activity. O'Dowd et al. (2015) illustrated a clear dependency of the organic fraction of SSA on biological activity with a 24-day time-lag by using high-resolution aerosol chemical composition measurements from 2009 to 2011. The interpretation of the time-lag that exists between the peaks of phytoplankton activity and SSA emission (or SMA formation) is a big challenge for marine aerosol science (Lee et al., 2015; McCluskey et al., 2017; Wang et al., 2015) and may have implication on future marine aerosol parametrizations for regional and global models.

Similarly, a number of other papers evidenced the influence of freshly produced OM, by blooming algal species, on the SSA chemical composition and sometimes cloud-relevant properties. These works comprise a vast literature of laboratory studies, including the ones performed at the world's largest lab facility of this kind, at NSF-CAICE in San Diego (Cochran et al., 2017a; Cochran et al., 2017b; Collins et al., 2013a; Lee et al., 2015; Prather et al., 2013) and laboratory studies by Fuentes et al. (2011) and O'Dowd et al. (2015). Field observations by Ovadnevaite et al. (2011a) suggested that hygroscopicity and CCN properties of SSA may change significantly when it originates from highly biologically productive seawaters. More recently, open sea field observations of primary biological particles showed specific spatio-temporal distributions as compared to total aerosols, over the NA Ocean, with a significant relationship with seawater CHL (Kasparian et al., 2017). Finally, the model simulations (Burrows et al., 2014) suggested that SSA organics can be contributed by different types of seawater organic compounds, from both fresh and refractory organic carbon, in varying proportions according to the region and season.

On the other hand, results contrasting the above cited literature have been reported in the last years. Publications reporting observations taken in the Western NA Ocean (Bates et

al., 2020; Keene et al., 2017; Kieber et al., 2016; Quinn et al., 2014; Russell et al., 2010) show a constant chemical composition of SSA independently on the season and the algal blooming stage. These studies concluded that the organic fraction of SSA comes from the large pool of refractory dissolved organic carbon (DOC) in the ocean and that fresh algal exudates plays no role in modifying SSA physico-chemical and cloud relevant properties. Consequently, chemical transport and climate models could treat the ocean as a uniform organic SSA source, affected only by sea surface temperature.

Overall, we can only acknowledge the contrasting results reported in the scientific literature on this subject, aware that future studies may be able to settle this issue. In conclusion, the actual effect of phytoplankton activity on SSA chemical composition remains controversial, while a more general consensus can be found regarding the impact of the marine biota on secondary marine aerosols.

1.8 Aim and Objectives of the Present Study

The above discussion shows how far the scientific community is from understanding in detail the interactions between the marine biota and the aerosol-cloud-climate system. Systematic studies, elucidating the relationship between marine biological activity temporal patterns and the main properties of marine aerosol, deconvolving the role of meteorology from that of biology, are still missing. Only a small fraction of the marine boundary layer is covered by measurements, which, for obvious reasons, tend to be short term observations. Most of all, only a few studies have tackled this issue from a multidisciplinary perspective, merging information from aerosol physics and aerosol chemistry with oceanography and marine biology.

The present Thesis aims at understanding to which extent phytoplankton activity have the potential to affect climate, by modifying aerosol physico-chemical and cloud properties. Specific objectives of this study are:

- Understanding the relationship between the atmospheric concentration of the main marine aerosol chemical components and phytoplankton activity, at different time scales and at different locations.

- Elucidating how cloud-relevant (CCN & INP) aerosol properties and cloud properties themselves are influenced by phytoplankton activity, in comparison to the role of meteorology.
- Investigating the space and time evolution of marine biogenic aerosol sources over different ocean domains.
- Quantifying the time-lag between surface CHL patterns and marine aerosol properties evolution, at different time scales and oceanic domains, in order to improve our current capability of deriving CHL-based parameterizations of marine aerosols for regional and global models.

The final goal of the present study is to contribute to increase the actual knowledge of the interactions between the marine biota and the aerosol-cloud system, potentially helping to improve the current understanding of the natural climate system. Considering this, the present study provides an important piece of information that may contribute to the development of an improved generation of climate and Earth System Models.

The Thesis is structured as follows: Chapter 1 overviews the current literature and the objectives of the Thesis. Chapter 2 presents the main data sources and methods of analysis. Chapter 3 displays the results of long-term marine aerosol measurements at MHD. Chapter 4, Chapter 5, and Chapter 6 show the results of short-term campaigns carried out at MHD, CGR, and GVB, respectively. In Chapter 7, we discuss the long-term in-situ measurements of cloud properties measured at MHD. Finally, Chapter 8 summarizes the major findings and the conclusions of the Thesis.

2. Data and Methods of Analysis

The focus of this Chapter is to describe the in-situ aerosol and ground-based measurements at the different sampling stations object of the present study. In addition, the remotely sensed ocean color data as well as the methods of analysis employed in this Dissertation will be described. It also details several other complementary data like meteorological data, satellite ground type maps and air mass back-trajectories. The following sub-sections describe the specific instrumentation, acquisitions settings, and techniques used to gather the main chemical and physical parameters of interest, including aerosol chemical composition, aerosol size distribution, cloud condensation nuclei (CCN) and ice nucleating particle (INP) concentrations, and cloud microphysical, macrophysical, and optical properties.

2.1 Sampling Locations

The data used in this study were taken from field measurements at three sampling sites, representative of the North East Atlantic Ocean (Mace Head [MHD] Global Atmosphere Watch (GAW) research station), the central Mediterranean Sea (Capo Granitola [CGR] Climate Observatory) and the Arctic Ocean (Gruvebadet observatory [GVB]), as shown in Figure 2.1. All the sites are described in detail in the following Sections, while Table 2.1 presents a summary of the available measurements and sampling periods at each site.

2.1.1 MHD Atmospheric Research Station, NE Atlantic

The first measurement location is the MHD (http://www.macehead.org/) GAW research station. The station is located on the west coast of Ireland (53.33° N, 09.90° W), westerly exposed to the NA ocean, at about 300 m from the waterline and 21 m above the mean sea level (MSL). The MHD station is operated by the National University of Ireland Galway (NUIG), School of Physics and the University's Ryan Institute Center for Climate & Air Pollution Studies (C-CAPS).

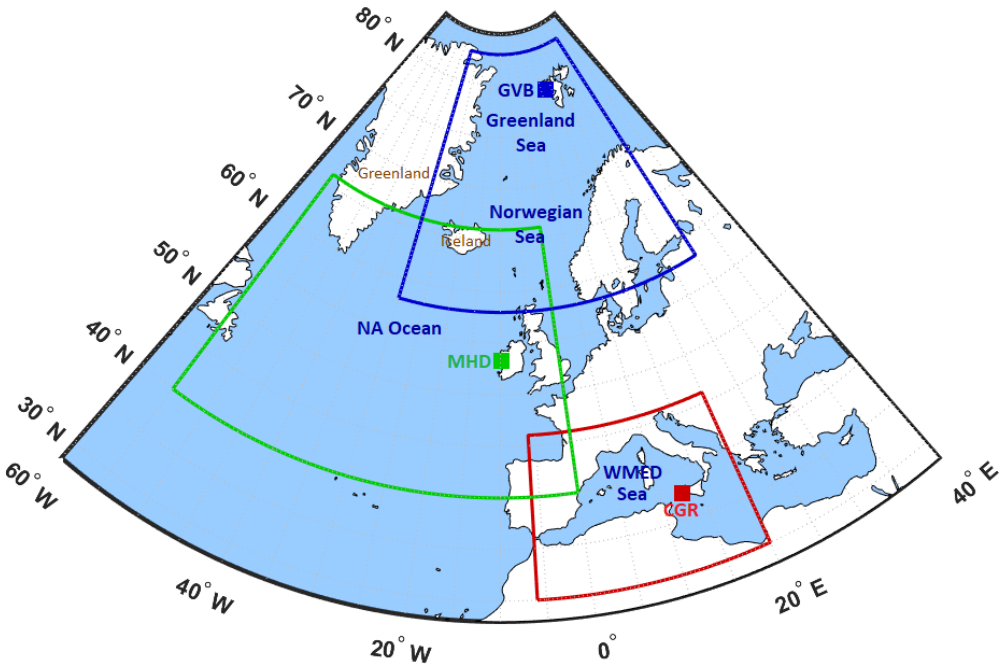

Figure 2.1: Sampling locations shown by the red, green, and blue squares and the borders of the studied oceanic domains delineated by the red, green, and blue boxes. WMED stands for Western Mediterranean and NA for North Atlantic.

Table 2.1: Summary of the in-situ and ground-based remote sensing data used in the Dissertation.

Timescale	Location	Parameter	Instrument(s)	Sampling Period
Long-term Measurements	MHD	Aerosol chemical composition Equivalent black carbon Particle number concentration Cloud Microphysical Properties	HR-Tof-AMS MAAP SMPS Cloud radar, Ceilometer, and MWR	2009 – 2017 52 Cases: From February 2009 to January 2015
Short-term Campaigns	MHD	Aerosol chemical composition Equivalent black carbon Particle number concentration CCN number concentration INP number concentration	HR-Tof-AMS MAAP SMPS CFSTG-CCN-Chamber DFPC	31/07 – 21/09/2015 31/07 – 31/08/2015 30/07 – 28/08/2015
	CGR	MSA Concentration	HR-Tof-AMS	07 – 25/04/2016
	GVB	INP number concentration	DFPC	17/04 – 02/05/2018 11 – 27/07/2018

MHD has been a site for aerosol measurements since 1958 when condensation nuclei were measured at a small coastal lookout. In 1985, the site was refurbished for use as a laboratory and a standard meteorological recording system was installed there. In 1989, a further laboratory was constructed close to the shoreline. A 20 m sampling tower was also built up. The Irish Government constructed a second shoreline laboratory and an extension to the original cottage, later in 1989. In 1994, the World Meteorological Organization (WMO) designated MHD site as one of the most important GAW stations in the Northern hemisphere. MHD is the only GAW station in the eastern Atlantic region and is the globally acknowledged clean background western European station, providing key baseline input for intercomparing with levels elsewhere in Europe. More than 600 publications in refereed journals and over 25,000 citations that have some connection either with the MHD research station or with members, both present and past, of the atmospheric physics research at NUIG.

2.1.1.1 Long-term (2009-2017) In-situ Measurements

Nine years of aerosol chemical composition were measured continuously by an Aerodyne High Resolution - Time of Flight - Aerosol Mass Spectrometer (HR-ToF-AMS) which provides a real-time size-resolved composition of volatile and semi-volatile particulate matter (DeCarlo et al., 2006). The aerosol measurements were performed through the station central aerosol sampling system which inlet is set at 10 m above ground level. The HR-ToF-AMS measurements were performed at a time resolution of 10 minutes and it was calibrated according to the recommendations by Jimenez et al. (2003) and Allan et al. (2003). A Nafion drier was installed in front of the HR-ToF-AMS sampling inlet to reduce the relative humidity (RH) of the sample to < 20%. The HR-ToF-AMS Composition Dependent Collection Efficiency (CDCE) was calculated based on aerosol composition, according to Middlebrook et al. (2012). The measurement uncertainty, mainly determined by the applied CDCE, is approximately 30-40% in AMS mass concentration (Bahreini et al., 2009; Middlebrook et al., 2012).

The HR-ToF-AMS measures the aerosol chemical composition (PM_1), by providing the atmospheric concentration of the major inorganic species, such as sulfate (SO_4^{2-}), ammonium (NH_4^+) and nitrate (NO_3^-), and organic matter (OM) in the submicron size range (Canagaratna et al., 2007). The sea-salt (SS) concentrations can also be derived following the method described by Ovadnevaite et al. (2012). The measured SO_4^{2-} concentrations include both non-sea-salt sulfate (nss-SO_4^{2-}) and sea-salt sulfate (ss-SO_4^{2-}). The contribution of the nss-SO_4^{2-}

was determined by subtracting the ss-SO_4^{2-} concentration (7.7% of total SS) from the total SO_4^{2-} concentration (Ovadnevaite et al., 2012; Ovadnevaite et al., 2014). The methanesulfonic acid (MSA) concentration was derived from the concentration of mass fragment $CH_3SO_2^+$, following the procedure by Ovadnevaite et al. (2014). All data were analyzed using the standard ToF-AMS analysis software SQUIRREL v1.51 and PIKA v1.10 (D. Sueper, available at: http://cires.colorado.edu/jimenez-group/ToFAMSResources/ToFSoftware/index.html) within Igor Pro 6.2.1 (WaveMetrics, Lake Oswego, OR).

Furthermore, equivalent black carbon (eBC) concentrations were measured in-situ by a multi-angle absorption photometer (MAAP), through the same central inlet as AMS measurements (O'Dowd et al., 2014). eBC concentrations were used to discriminate anthropogenically impacted air masses, as detailed in Section 2.7.1.

The submicron aerosol size distributions were measured by a Scanning Mobility Particle Sizer (SMPS, 0.02 < particle diameter (Dp) < 0.5 µm), where aerosols are neutralized (aerosol neutralizer: Kr-85, TSI Model 3077) and size-discriminated based on their mobility diameter (differential mobility analyzer: TSI Model 3071) and counted by a condensation particle counter (TSI Model 3010). Aerosol sizing instruments were located downstream of Nafion driers (RH < 20%) (Ovadnevaite et al., 2017), and thus, size distributions refer to the aerosol dry diameter (Sanchez et al., 2017). The MHD SMPS system is in line within the general uncertainties derived for this type of instrument (Ovadnevaite et al., 2017). The uncertainties are around ±10% for the size range between 20 and 200 nm in particle size (Wiedensohler et al., 2012), and about ±20% for the particle size range 200–800 nm (Wiedensohler et al., 2018).

2.1.1.2 Ground-based Remote Sensing Measurements

The ground-based remote sensing (GBRS) division at MHD has been a Cloudnet station since 2009 (Illingworth et al., 2007) and comprises a cloud radar, ceilometer, and microwave radiometer (MWR), and since 2015 a Doppler wind lidar. GBRS provides continuous monitoring of the atmosphere at one location, with high vertical and temporal resolutions. This provides useful detailed insights into highly complex cloud processes, which can be a powerful tool for the detection and quantification of cloud indirect effects (Feingold et al., 2003).

The radar is a MIRA36, a 35.5 GHz Ka-band Doppler cloud radar (Melchionna et al., 2008) that measures in-cloud reflectivity, linear depolarization ratio, and vertical speed of cloud droplets at 30 m and 10 sec vertical and temporal resolutions. The radar was also used to track the top level of clouds. Further description of the calibration offset of the radar reflectivity can be found in Preissler et al. (2016).

The ceilometer is a CHM15k measuring 1064 nm (Heese et al., 2010; Martucci et al., 2010). It detects photons backscattered from atmospheric targets at vertical and temporal resolutions of 15 m and 30 sec, such as cloud droplets or aerosol particles. Based on the optical depth of the atmosphere, it can detect aerosol particles, as well as clouds up to a certain penetration point. The ceilometer was used to detect the cloud base altitude.

The MWR is a multichannel microwave profiler RPG-HATPRO (Crewell and Lohnert, 2003; Lohnert and Crewell, 2003; Lohnert et al., 2009) measuring near water vapour and oxygen absorption lines (Martucci and O'Dowd, 2011).

The SYnergetic Remote Sensing Of Clouds (SYRSOC) retrieval method uses GBRS data from the three mentioned instruments as a primary input. It allows for vertically resolved determination of cloud properties from the ground. Using the SYRSOC algorithm (Martucci and O'Dowd, 2011; Preissler et al., 2016), the microphysical cloud properties such as R_{eff}, CDNC, and LWC and cloud optical properties like cloud optical depth (COD) and cloud albedo are retrieved. The vertical and temporal resolutions of the output are 15 m and 10 sec.

The present study focuses on a subset of the cloud cases introduced and discussed by Preissler et al. (2016), that are cases which could be attributed to clean marine conditions, with negligible to null continental influences. From 6 years of cloud observations (February 2009 to January 2015), homogeneous sections of less than 1-hour duration have been selected of all non-precipitating single-layer water clouds. These criteria are necessary to match the monomodal droplet size distribution assumption of SYRSOC.

A total of 52 clean marine stratiform clouds were analyzed. The cloud cases roughly span 24.2 h of observations distributed over 47 days. A prevalent marine origin is dominant in the formation of stratiform clouds at MHD, while air masses from Europe are typically drier, leading to suppressing cloud formation. Although cloud-free conditions are rare at MHD, the

downtime of each instrument (radar, ceilometer, and MWR) was 20 to 25% making them rarely coincidental (Preissler et al., 2016) which limits cloud microphysics data accessibility.

The cloud microphysics retrievals from SYRSOC were compared with in-situ aircraft measurements from two-day field experiment conducted at MHD (Martucci et al., 2013), showing a very good agreement in the SYRSOC full profiles. In that experiment, the retrieved CDNC were compared to the CCN concentrations and the best agreement was occurred at a supersaturation between 0.1 – 0.75 % for the marine stratocumulus. Preissler et al. (2016) compared SYRSOC results with satellite MODIS observations, concluding a large difference for liquid water path (LWP) and COD and a good agreement for R_{eff} with a linear fit of nearly unity slope, for the whole dataset. Nevertheless, CDNC retrievals were not extensively validated against an independent method and so their level of uncertainty is so far undefined. However, we decided to include CDNC in the analysis as the CDNC dataset shows consistency with the rest of the cloud parameters, as for example a clear anticorrelation with R_{eff} (R^2 = 0.72) and correlation with the normalized albedo (R^2 = 0.29), which are consistent with the theory (Twomey, 1974; Twomey et al., 1984).

2.1.1.3 BACCHUS Campaign

An intensive short-term campaign was carried out between 30 July and 21 September 2015 at MHD station in the framework of the EU project BACCHUS, with the support of the CNR project "Air-Sea Lab". The submicron aerosol chemical compositions and aerosol size distributions were collected online by the HR-ToF-AMS and SMPS installed at MHD. The details were described above in Section 2.1.1.1.

In addition, CCN measurements were performed with a miniature Continuous-Flow Streamwise Thermal-Gradient CCN Chamber (CFSTG-CCN-Chamber), which measures the concentration of activated CCN over a range of supersaturations (Roberts and Nenes, 2005). The supersaturation range spanned 0.2 to 0.82 %. Further details on SMPS and CCN measurements are reported in Sanchez et al. (2017).

The atmospheric INP concentrations were quantified in the lab by the membrane filter technique (Bigg et al., 1963; Vali, 1975). Aerosol samples were collected on nitrocellulose membrane filters (Millipore HABG04700, nominal porosity 0.45 µm) by deploying two parallel sampling systems, one equipped with a PM_1 inlet and the other with a PM_{10} (cut-point-

Standard EN 12341, TCR Tecora). The operative sampling flow was 38.3 lpm in each sampling line and was generated by two independent pumps (Bravo H Plus, TCR Tecora). The INP number concentration (*n*INP) was measured offline on said filters by using the Dynamic Filter Processing Chamber (DFPC) developed at the CNR-ISAC laboratories in Bologna (Italy), following the procedure described in Santachiara et al. (2010) and Belosi et al. (2017).

The quantification of INPs occurred at an activation temperature (T_A) of –22 °C and in conditions of supersaturation with respect to water (S_w) equal to 1.01. Uncertainties for T_A and S_w are about 0.1 °C and 0.02, respectively. Consequently, the estimated, INP measurement uncertainty of the DFPC is ±30% (DeMott et al., 2018). Examples of inter-comparisons between the DFPC and other INP quantification techniques can be found in DeMott et al. (2018), McCluskey et al. (2018c) and Hiranuma et al. (2019). The *n*INP, expressed in units of m^{-3}, was calculated by dividing the number of INP quantified for each sample by the total volume of air passed through the corresponding filter.

At MHD, sampling for INP analyses occurred only in clean marine conditions, to avoid continental influences, as detailed in McCluskey et al. (2018c). Briefly, the sampler received power from the clean sector sampling system only when eBC is less than 15 ng/m^3 and wind direction is between 190° to 300°. This ensures sampling of air masses mostly representative of clean marine conditions, minimizing anthropogenic influences, as demonstrated in a number of previous works (*e.g.*, Ceburnis et al. (2011) and O'Dowd et al. (2014)).

2.1.2 CGR Climate Observatory, Central Mediterranean

The second measurement location is the I-AMICA Capo Granitola (CGR) Climate Observatory (37.6667° N, 12.6500° E; 5m above MSL), located 12 Km to the SE from Mazara del Vallo (Cristofanelli et al., 2017) and facing the Sicily Channel. The station, run by CNR-ISAC, is a regional GAW station and is considered representative of the Mediterranean background atmosphere. An intensive aerosol characterization campaign was carried out between 07 and 25 April 2016 in the framework of the CNR project Air-Sea Lab and the EU project BACCHUS. A more detailed description of the campaign can be found in Rinaldi et al. (2019).

The atmospheric concentration of submicron MSA was measured online by an Aerodyne HR-ToF-AMS (DeCarlo et al., 2006), following the recommendations of Jimenez et al. (2003), Allan et al. (2003) and Canagaratna et al. (2007). Briefly, the measurements were performed

by alternating between "V" and "W" ion path modes every 2.5 min. The concentrations reported here correspond to the data collected in V mode. The resolving power of the V-ion mode was about 2000-2200 during the whole campaign. Ionization efficiency (IE) calibrations were performed at the beginning, in the middle and after the campaign. Filter blank acquisitions during the campaign were performed once a day, at randomly chosen moments, to evaluate the background and correct for the gas-phase contribution.

The mass spectrometer was connected to the station main aerosol sampling system (Cristofanelli et al., 2018) and the aerosol was dried to about 40% RH by means of a Nafion drier before sampling. As done for MHD measurements, the HR-ToF-AMS CDCE was calculated based on aerosol composition, according to Middlebrook et al. (2012).

As at MHD, the MSA concentration was derived from the concentration of mass fragment $CH_3SO_2^+$, following the procedure by Ovadnevaite et al. (2014). Since the MSA quantification method has not been standardized in the AMS, and its fragmentation pattern could be instrument dependent (Zorn et al., 2008), the obtained concentrations were validated against offline measurements. MSA concentration was determined by ion chromatography analysis of PM_1 filter samples (24 hour time-resolution) collected in parallel to the mass spectrometry measurements (Rinaldi et al., 2019).

2.1.3 GVB observatory, Ny-Ålesund, Svalbard Islands

The third measurement location was the Gruvebadet observatory (GVB), located in proximity of the village of Ny-Ålesund (78.9167° N, 11.9333° E) on the Spitsbergen Island, Svalbard. The observatory is about 70 m above MSL, located about 1 Km SW of the village. This position guarantees that the aerosol samples are not affected by local sources of pollution, being the main wind flow from southeast (Udisti et al., 2016). The aerosol sampling for INP quantification analysis was collected at an inlet located about 1 m above the building roof.

The *n*INP were determined by using the DFPC method, as detailed in Section 2.1.1.3. Samples were collected during two intensive field campaigns. The spring campaign occurred between 17 April and 2 May 2018, while the summer campaign covered the period between 11 and 27 July 2018. One couple of samples (PM_1 & PM_{10}) was collected per day, with a sampling duration between 3 and 4 hours, to avoid filter overloading. The sampling generally

started in the morning, during the spring campaign, while it started typically in the afternoon during the summer campaign. Samples were stored at room temperature until analysis. Differently from the INP samples at MHD, measurements were performed at T_A of −15 °C, −18 °C and −22 °C.

The aerosol particle number size distribution is continuously monitored at GVB since 2010 using a SMPS model TSI 3034 for the diameter range between 10 and 500 nm (54 channels) and an Aerodynamic Particle Sizer (APS) model TSI 3321 for the diameters above 500 nm (same number of channels as the SMPS). Both instruments are connected to a common multiple inlet with laminar flow and record data averaged over 10 minutes (Giardi et al., 2016; Lupi et al., 2016). The aerodynamic diameters reported by the APS were corrected to real physical diameters using a particle mass density equal to 1.95 g cm^{-3} and the number concentration in the resulting overlapping range was taken equal to that from the SMPS.

Meteorological parameters (air temperature, T; pressure, P; relative humidity, RH; wind speed, WS) were taken from those continuously provided by the Amundsen-Nobile Climate Change Tower, positioned less than 1 Km N-E of GVB (Mazzola et al., 2016), while precipitation data (type and amount) from the eKlima database, provided by the Norwegian Meteorological Institute (https://seklima.met.no/observations/).

2.2 Satellite Ocean Color Data

The present study is based on different satellite ocean-color data products. The best estimates “Level-4; Cloud Free” sea surface chlorophyll-a concentrations (CHL; mg m^{-3}) were obtained from the EU Copernicus Marine Environment Monitoring Service (CMEMS) through the website http://marine.copernicus.eu/. These ocean-color data products are the result of merging Sea-viewing Wide Field of View (SeaWiFS), Moderate Resolution Imaging Spectroradiometer (MODIS-Aqua), MEdium Resolution Imaging Spectrometer (MERIS), Visible and Infrared Imager/Radiometer Suite (VIIRS) and Ocean and Land Color Instrument-Sentinel 3A (OLCI-S3A) sensors. These sensors measure the average CHL content over the first optical depth. A detailed description of all ocean color products is given in the Product User Manual (http://resources.marine.copernicus.eu/documents/PUM/CMEMS-OC-PUM-009-ALL.pdf).

The surface CHL is chosen as the reference surrogate for tracing the evaluation of marine biological activity (Yoon et al., 2007) because it is the most widely available and validated

ocean color parameter. Moreover, in a previous approach, Rinaldi et al. (2013) concluded that there is no need to substitute CHL with other biological surrogates, which are generally affected by larger and less quantified uncertainties, considering that they do not produce better results than CHL in tracing marine aerosol properties.

For the NE Atlantic Ocean domain (period 2009-2017) and the Arctic Ocean (summer 2018), CHL fields were extracted from the global Level-4 product (Identifier: OCEANCOLOUR_GLO_CHL_L4_REP_OBSERVATIONS_009_082), available at 1/24 degree (about 4 km) spatial-resolution and daily time-resolution.

In the Mediterranean domain, another CHL product was used: the daily 1 km spatial-resolution (Identifier: OCEANCOLOUR_MED_CHL_L4_NRT_OBSERVATIONS_009_041) which has been estimated by the application of the Mediterranean Ocean Color 4 bands (MedOC4) algorithm (D'Alimonte et al., 2003; Volpe et al., 2007).

2.3 Phytoplankton Carbon Estimation

A second satellite parameter used in this study is the optical particulate backscattering (b_{bp}) at 443 nm wavelength, which is an important parameter to study ocean biology and oceanic carbon estimations. The $b_{bp}(443)$ data over the Mediterranean Sea, as generated by the ocean color component of the European Space Agency Climate Change Initiative project (ESA-CCI; available at: https://www.oceancolour.org/), is available with daily composites of merged sensors (*i.e.* MERIS, MODIS Aqua, SeaWiFS LAC & GAC, VIIRS) and a spatial resolution roughly 4.63 km. The b_{bp} is obtained by the application of the Quasi Analytical Algorithm (QAA; Lee et al. (2002) and Lee (2014)). The b_{bp} retrieval by the QAA was assessed using in-situ data of matched b_{bp} (Pitarch et al., 2020). The results showed a negligible bias when QAA-derived b_{bp} was compared to in-situ b_{bp}, confirming high efficiency of QAA in the b_{bp} detection.

The daily phytoplankton carbon biomass (PHYC) data were computed using the equation of Behrenfeld et al. (2005) based on the light backscattering coefficient in seawater due to particles, b_{bp} (λ) as:

$$PHYC = [b_{bp}(443) - b_{bp}NAP(443)] \times SF \qquad [\text{mg C m}^{-3}],$$

where $b_{bp}(443)$ is the particulate backscattering coefficient (m^{-1}) at 443 nm and it is used as a measure of the particle concentration in seawater (Dall'Olmo et al., 2012; Dall'Olmo et al., 2009; Westberry et al., 2008; Westberry et al., 2010). The $b_{bp}NAP(443)$ is the background contribution of non-algal particles to $b_{bp}(443)$ and it is equal to the constant value of 0.00035 m^{-1}, following Behrenfeld et al. (2005). This constant background value was estimated as the intercept of the least-square linear regression fit between CHL and b_{bp} by using global SeaWiFS monthly ocean color data (1997–2002). The $b_{bp}NAP$ represents a global estimate of b_{bp} by the stable heterotrophic and detrital components of the surface particle population. The scaling factor ($SF = 13000$ mg C m^{-2}) is a constant to convert b_{bp} (m^{-1}) into $PHYC$ (Behrenfeld et al., 2005; Bellacicco et al., 2018; Bellacicco et al., 2016; Westberry et al., 2008) which is consistent with field estimates from different oceanic regions.

2.4 Air Mass Back-trajectories

The air mass back-trajectories (BTs) were calculated using the Hybrid Single-Particle Lagrangian Integrated Trajectory (HYSPLIT4; https://ready.arl.noaa.gov/HYSPLIT.php) model, a transport and dispersion model developed by the National Oceanic and Atmospheric Administration (NOAA), Air Resources Laboratory (ARL) (Rolph et al., 2017; Stein et al., 2015).

For the short-term campaign at MHD, five-day BTs (hourly time step) arriving 100 m above the MSL were calculated four times per day (00, 06, 12, and 18 hr UTC) during the sampling period, while at CGR, three-day BTs were calculated with the same conditions of time step, altitude, and times per day as MHD. At GVB sampling station, the BTs arrival time was set simultaneous to the INP samples and five-day backward time was used. Such backward time, 72 or 120 hours is in line with fine aerosol (PM_1) atmospheric residence time and cover the oceanic domains in the studied environments.

In order to cover the long-term (9 years) of the data sampled at MHD, three-day BTs (hourly time step) were considered four times per day, by specifying a new trajectory starts from the source location every 6 hours. Each run of the HYSPLIT model was selected to cover 1 week of the data. Using this procedure, the maximum trajectory duration is restricted by 72 backward hours for each trajectory.

For the SYRSOC data, the BTs were calculated simultaneously to each cloud case, arriving at the cloud base altitude of the MHD sampling station to define the marine source areas, coming from the Atlantic Ocean.

2.5 Meteorological Data

The European Centre for Medium-Range Weather Forecasts (ECMWF) fifth generation reanalysis ERA5 (C3S, 2017) data provides estimates for the hourly state of the atmosphere, worldwide, with spatial resolution 0.25° × 0.25° at the surface and at different pressure levels. The ERA5 data are available by the ESA Ocean Color-Climate Change Initiative (ESA OC-CCI) team (http://www.esaoceancolour-cci.org) and the Copernicus climate change service (C3S). From the global domain, we extracted multiple atmospheric components like air temperature (T), sea surface temperature (SST), net surface solar radiation (SSR), wind speed (WS), relative humidity (RH), pressure vertical velocity (PVV), and potential temperature at 1000 hPa (surface) and at 850 hPa time series in order to evaluate the relationship between marine aerosol/cloud properties and the main meteorological variables, in comparison with the importance of the oceanic biological activity in different marine environments.

2.6 Satellite Ground Type Maps

In the arctic ocean, since the ocean (and land) can be covered by ice for part of the year, the ground types over which air masses travelled in the 5 day before arrival at the sampling station (GVB, see Section 2.1.3) were identified, following Wex et al. (2019). The considered ground types were “seawater”, “sea-ice”, “land”, and “snow” (over land). The ground condition maps were obtained from the National Ice Center's Interactive Multisensor Snow and Ice Mapping System (IMS) (Helfrich et al., 2007; National Ice-Center, 2008), National Snow & Ice Data center (NSIDC; https://nsidc.org/). IMS maps are a composite product by NOAA/NESDIS (National Environmental Satellite Data and Information Service), combining information on both sea ice and snow cover. Information from 15 different sources of input are included in the production of these maps (Helfrich et al., 2007).

We used the daily Northern Hemisphere maps with a resolution of 4 km. For each BT time step corresponding to INP sample, we applied nearest-neighbour interpolation in space and

time to find the corresponding satellite coordinate along the BT. Consequently, the ground type conditions during air mass passage were determined.

2.7 Methods of Analysis

To investigate the relationship between phytoplankton activity and marine aerosol properties, we applied a multi-step data analysis approach (Figure 2.2). The approach aims at identifying the most probable source regions of the marine aerosols observed at the sampling stations and at evidencing any eventually present correlation between aerosol properties and CHL patterns within said regions. The steps are briefly described below and with more details in the following Sections:

- **a-** **Air mass back-trajectory analysis**: the aim of this step is to identify the ocean regions located upwind to the sampling stations (borders of the studied domains), with respect to the main wind circulation patterns during the study periods. Any correlation resulting from the following step (**b**) outside the domain evidenced in step (**a**) is automatically excluded as considered a spurious correlation (i.e., not motivated by a physical mechanism).
- **b-** **Spatio-temporal correlation analysis**: under the assumption that marine aerosol properties should follow the evolution of marine biological activity (traced by CHL), we looked for sea regions showing a positive and significant correlation between the aerosol (or cloud) properties and CHL patterns.
- **c-** **Source regions location**: the potential sources of marine aerosol are spatially identified by evidencing the BTs associated to the highest concentrations. These was done by applying either the potential source contribution function (PSCF) algorithm or the concentration weighted trajectory (CWT) model, according to the time-resolution of the available data.

Only source regions that are plausible according to all the above three steps have been considered as reliably identified sources of marine aerosol. Consequently, the evidenced correlations between aerosol parameters and CHL, within the identified source regions, have been considered as resulting from a physical mechanism (*i.e.,* the correlation is causal, not casual) and representing an actual link between phytoplankton activity and marine aerosol properties. It is worth highlighting that the spatio-temporal correlation (step **b**) and the source

regions location (step **c**) methods are totally independent and based on different principles. The fact that a source region is identified by two independent methods strongly supports the reliability of the discussed results.

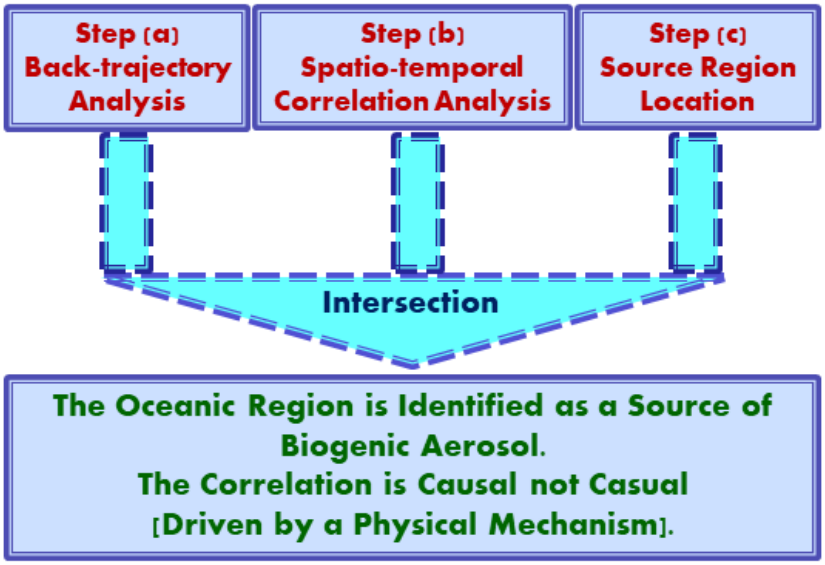

Figure 2.2: Simplified schematic diagram of the implemented multi-steps approach.

2.7.1 Data Filtration

Before applying the spatio-temporal correlation and source regions location analyses, the aerosol/cloud data in this study were strictly filtered to select only the cleanest marine air masses. This was done to avoid any interference from anthropogenic aerosols from land or ship emissions. The filtration was achieved in the different studied marine environments using the following means:

i. The North Atlantic

The online high-resolution aerosol data have been averaged to hourly mean and filtered against hourly eBC mass concentration as an anthropogenic tracer, to ensure the cleanliness of the marine air masses. The hourly averages corresponding to eBC not exceeding 15 ng m^{-3} was used to reliably exclude anthropogenically impacted air masses (Grigas et al., 2017; O'Dowd et al., 2015; Ovadnevaite et al., 2014; Preissler et al., 2016). The offline samples for INP analyses were sampled using the MHD Clean Sector Sampling System (Rinaldi et al., 2009), as detailed in Section 2.1.1.3.

i. The Mediterranean

Given that MSA is considered the best tracer of biogenic marine aerosol, not significantly influenced by anthropogenic emissions, no filtration was performed.

ii. The Arctic

No clean sector system was deployed during the collection of the filters at the Arctic station. The INPs dataset at GVB have been subjected to ground type contribution analysis to exclude the air masses impacted by the land influences, as explained in Chapter 6. Land sources are potentially a major source of INPs in the Arctic (Tobo et al., 2019), therefore samples corresponding to air masses that travelled extensively over snow-free land were excluded, in order to select only samples potentially dominated by marine INPs.

2.7.2 Spatio-Temporal Correlation Analysis

To explore the relationship between marine aerosol/ cloud properties and phytoplankton activity (represented by CHL), we computed, by standard least squares regression, the correlation coefficients between in-situ aerosol (or ground based cloud) parameters, measured at the sampling station, and satellite-derived ocean color data, at each grid point of the studied domains. Furthermore, we also explored the effect on the correlation of considering a time-lag between the CHL and aerosol/cloud parameters time series.

Rinaldi et al. (2013) and O'Dowd et al. (2015) showed that the correlation between marine aerosol properties and satellite tracers of oceanic biological activity is maximized when an appropriate time-lag is considered. The time-lag was attributed, in that case, to the time scale of the processes responsible for the production and release of organic matter that could be transferred within sea-spray. Similar results were reported by Lee et al. (2015) and Wang et al. (2015), who observed a delay time (4 to 10 days) between changes in sea-spray chemical composition and CHL peaks in controlled laboratory experiments. Also, McCluskey et al. (2017) demonstrated 4-days time-lag between INPs activation in SSA and CHL peaks, with the same experimental setup.

Based on the above findings, we tested the effect of considering a delay time between the CHL time series and in-situ aerosol properties in all the probed datasets. This approach is also justified by the fact that surface CHL tracks the growing phase of algal blooms, while the

release of phytoplankton exudates, likely involved in the production of biogenic marine aerosols, occurs mainly at a later stage, during the senescence/demise phase (Kwint and Kramer, 1995; Laroche et al., 1999; Miyazaki et al., 2020; Zhuang et al., 2011). This was done by shifting back in time the considered time window along the CHL time-series, while keeping constant the in-situ aerosol time series (Rinaldi et al., 2013).

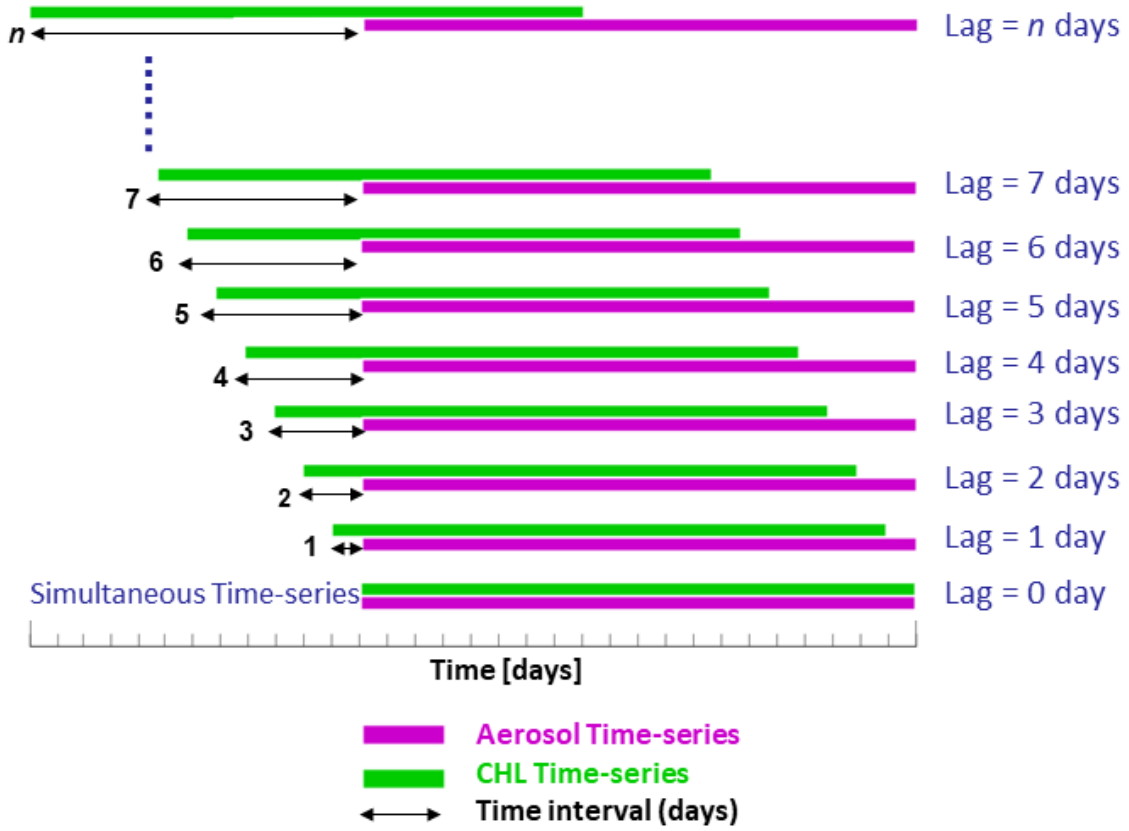

Figure 2.3: Schematic representation of the time-lag method.

The graphical representation of the time-lag method is shown in Figure 2.3. Basically, the effect of different time-lags on the "aerosol vs. CHL" correlation is tested, starting from simultaneous time-series, corresponding to "Lag = 0", then by sliding CHL backwards day by day to get the time-lag which maximizes the correlation coefficient between the two considered time series. Such process is conducted for each pixel of the studied domain, to obtain the "Lag = *n*" map where "*n*" is the number of days by which the CHL time-series is shifted back.

2.7.3 Source Regions Location

Two approaches were carried out to operate the geographical source attribution, evidencing the regions associated with high aerosol/cloud droplet concentrations in the studied environments, which evidences the most probable source regions. The approaches, PSCF and CWT, combine the aerosol/cloud data with air mass BT data.

2.7.3.1 PSCF

The possible source regions of marine aerosol which have high concentration at a receptor site are identified by the PSCF algorithm using the spatial probability distribution of pathways of air masses that arrived at the sampling site over a time period (Chang et al., 2011; Dall'Osto et al., 2017b; Karaca et al., 2009; Polissar et al., 2001). It combines the BTs information with the measured data to produce probability fields for potential source regions.

The studied domains (NA, Mediterranean) were divided into $i° \times j°$ latitude/longitude grid cells covering the limits of BTs. The conditional probability that the air passing through the ij-th cell has a high aerosol concentration when arriving at the sampling station is given by:

$$PSCF_{ij} = (m_{ij}/n_{ij}) \times W_{ij}$$

Where n_{ij} is the number of trajectories with segment endpoints in a cell ij and m_{ij} is the subclass ($m_{ij} < n_{ij}$) of trajectories connected to aerosol concentrations above a threshold defined as concentrations above the median.

The PSCF values may be affected by grid cells containing a low number of endpoints that may be overestimated so that it is multiplied by a weighting factor, W_{ij}, (Masiol et al., 2019) as indicated below.

$$W_{ij} = 1 \quad \text{if } n_{ij} \geq 2\bar{N}$$
$$W_{ij} = 0.75 \quad \text{if } \bar{N} \leq n_{ij} < 2\bar{N}$$
$$W_{ij} = 0.50 \quad \text{if } \bar{N}/2 \leq n_{ij} < \bar{N}$$
$$W_{ij} = 0.25 \quad \text{if } n_{ij} < \bar{N}/2$$

Where $\bar{N}$ is the average number of endpoints over the grid cells with at least one endpoint.

2.7.3.2 CWT

Due to the limited time-resolution of INPs collected at GVB, the allocation of regional source areas potentially affecting INP concentrations was achieved by applying the CWT model (Bycenkiene et al., 2014; Hsu et al., 2003; Jeong et al., 2011), instead of PSCF. In this procedure, each grid cell within the studied domain is associated to a weighted concentration, which is a measure of the source strength of a grid cell with respect to concentrations observed at the sampling site. The average weighted concentration in the grid cell (i, j) is determined as follows:

$$CWT_{ij} = \frac{\sum_{t=1}^{L} C_t D_{ijt}}{\sum_{t=1}^{L} D_{ijt}} \times W_{ij}$$

Where t is the index of the trajectory (arrival time simultaneous to INP samples), L is the total number of trajectories (5 days – hourly time step), C_t is the INP concentration observed at sampling location (receptor site) on arrival of trajectory t, and D_{ijt} is the residence time (time spent) of trajectory t in the grid cell (i, j). Given C_t for INP, D_{ijt} can be determined by counting the number of hourly trajectory segment endpoints in each grid cell for each trajectory. This was repeated for all the back trajectories L. A high value for CWT_{ij} means that air parcels traveling over the grid cell (i, j) would be, on average, associated with elevated concentrations at the receptor site.

The CWT values were subjected to a weighting factor, W_{ij}, to minimize the effect of grid cells containing a low number of endpoints. The W_{ij} was based on the 1st quartile and median of the number of endpoints over the grid cells with at least one endpoint, as indicated below.

$W_{ij} = 1$ if $D_{ij} \geq median$

$W_{ij} = 0.8$ if $1^{st} quartile < D_{ij} < median$

$W_{ij} = 0.0$ if $D_{ij} \leq 1^{st} quartile$

3. Seasonality of Marine Aerosol Chemical Components over the NE Atlantic Ocean in Relation to the Evolution of the Oceanic Biological Activity

In this Chapter, a continuous record of submicron (PM_1) marine aerosol chemical composition data was used to investigate the relation between oceanic biological activity and marine aerosol properties over the NE Atlantic Ocean. The submicron fraction is the most climate relevant aerosol size range as it dominates the number distribution and comprises the majority of the CCN. We examined the results of nine years (2009-2017) of in-situ aerosol measurements (by HR-ToF-AMS, see Section 2.1.1.1) collected at the MHD GAW research station (Ireland). The dataset, which is presently the longest record of unperturbed marine aerosol chemical composition worldwide, provides the atmospheric concentrations of the main biogenic aerosol components, such as nss-SO_4^{2-}, MSA, OM and NH_4^+ as well as NO_3^- and sea salt (SS).

3.1 Seasonal Trends of Marine Aerosol Chemical Composition

The submicron marine aerosol data were analyzed examining only the cleanest air masses characterized by virtually no continental and/or anthropogenic contamination. This was achieved by selecting only air masses of marine origin, crossing the NA ocean region, according to the BTs classification (Section 3.2). Furthermore, the high-resolution aerosol chemical composition data, averaged to hourly resolution, were filtered against hourly eBC mass concentration. Only the hourly averages corresponding to eBC concentrations not exceeding 15 ng m^{-3} were used to exclude anthropogenically impacted air masses. These criteria have been demonstrated to minimize anthropogenic inputs deriving both from long-range transport across the NA Ocean, from the North American continent, and eventually present ship emissions (O'Dowd et al., 2015; Ovadnevaite et al., 2014). The clean marine hourly aerosol data have been averaged daily, to be compared with the satellite retrieved CHL data, which are available at the highest time resolution of 24 hours. Days with less than 6 continuous hours of clean measurements were excluded from the analyzed dataset.

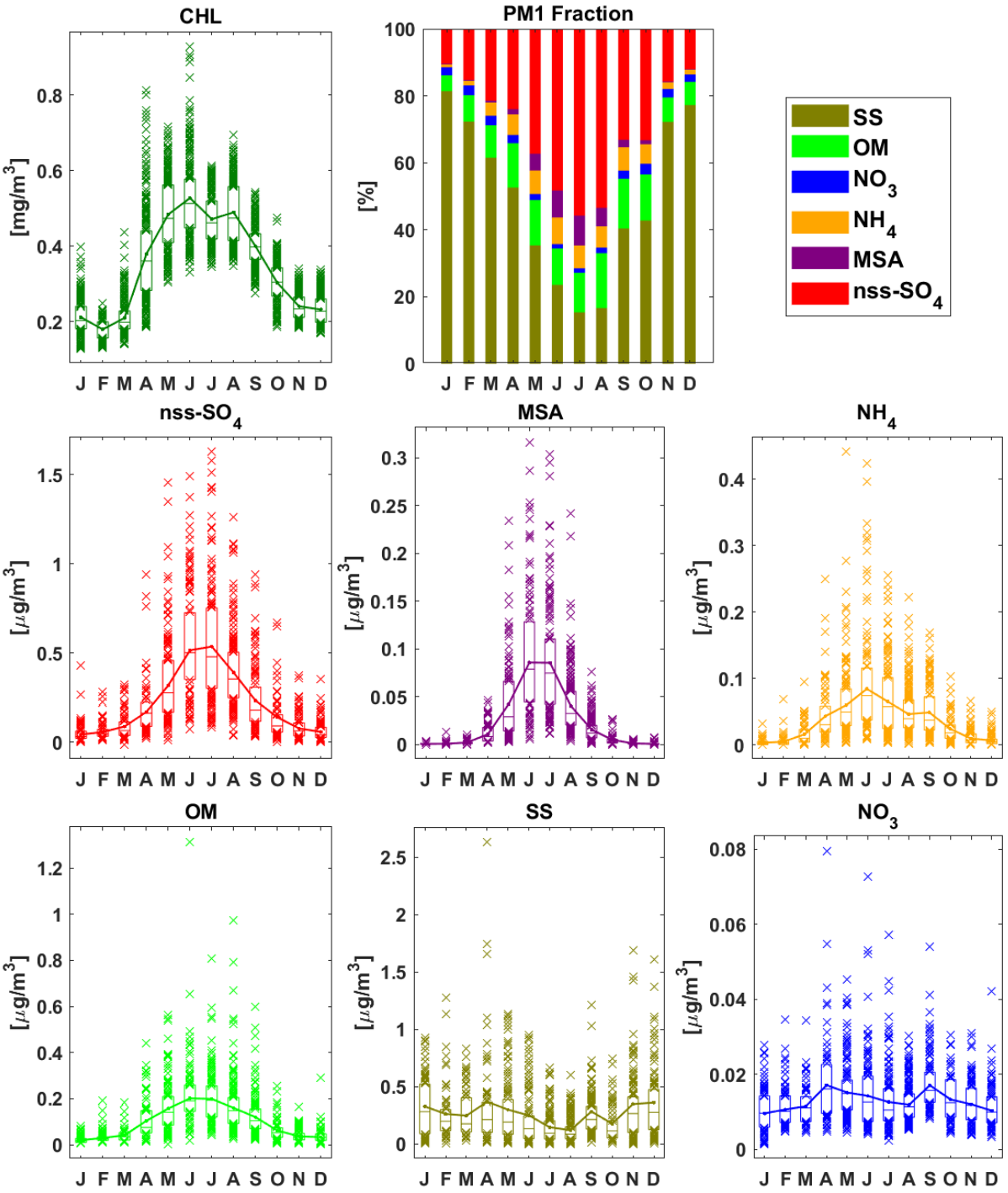

Figure 3.1: Monthly trend of CHL and marine aerosol chemical composition during 2009-2017. On each box that represents a month, the central line indicates the median, and the bottom and top edges of the box indicate the 25th and 75th percentiles, respectively. The connected line represents the monthly mean during maritime air masses. The monthly fractions of PM_1 chemical composition are shown in the stacked bar. MSA concentrations were excluded from OM in the fraction calculations.

The seasonal trends (monthly resolution) of marine aerosol component concentrations and their fractional contributions, as well as the average CHL over the oceanic region directly

facing MHD, are shown in Figure 3.1. This region (black box in Figure 3.8) comprises the most probable biogenic marine aerosol sources as investigated by the source region identification analysis presented in Section 3.6.

The seasonal trend of nss-SO_4^{2-}, MSA, NH_4^+, and OM concentrations exhibits maxima in summer (HBA) and minima during winter (LBA), in consistent with previous studies performed at MHD (Cavalli et al., 2004; O'Dowd et al., 2004; Ovadnevaite et al., 2014; Yoon et al., 2007) with less extensive dataset. This trend coincides with the marine biological activity seasonal variations as indicated by CHL, a proxy of phytoplankton productivity, suggesting a significant impact of marine biological activity on the chemical composition of aerosol observed at MHD. CHL during HBA is of the order of 0.50 ± 0.09 mg m^{-3} (summer) while it goes down to 0.21 ± 0.04 mg m^{-3} in winter, as presented in Table 3.1. An almost equal concentration of CHL during the transition seasons, autumn and spring. The reported correlation coefficients between CHL, within the black box, and nss-SO_4^{2-}, MSA and OM are 0.61, 0.60, and 0.57, respectively. It is worth highlighting that SS and NO_3^-, the only marine aerosol components not related to biological precursors, do not follow the above concentration seasonal trend.

As known from the literature, the NA ocean is spatially characterized by diverse types of phytoplankton generating a distinct bloom occurring mainly in spring and going on through the summer (Friedland et al., 2016; Lacour et al., 2015; McKinley et al., 2018). Figure 3.2 displays the climatic seasonality of CHL during the study period, between 2009 and 2017 over the NA Ocean. The outlined black box (45° − 60° N and 12° − 38° W) corresponds to the spatial domain in which ocean biota emissions have the largest influence on aerosol properties sampled at MHD (see further details in Sections 3.5 and 3.6).

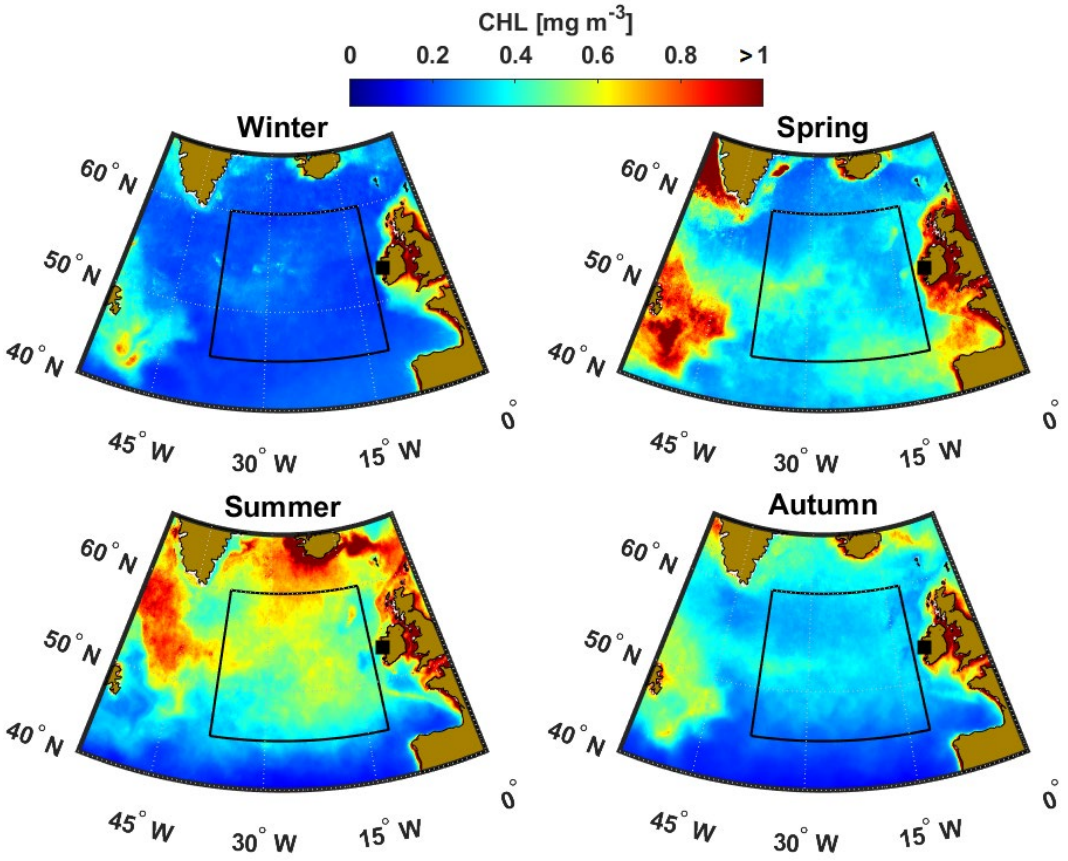

Figure 3.2: Spatial distributions of seasonal average CHL over the NA Ocean between 2009 and 2017. The black box is the oceanic area off the MHD coast exerted the most influence on marine aerosol properties.

Nss-SO_4^{2-} and MSA show the most pronounced seasonality as a result of the increase in DMS emission (gaseous precursors of both aerosol components), produced by the marine biota during the HBA period (Andreae, 1990; Charlson et al., 1987) and to the concurrent enhanced photochemical activity of the atmosphere (Barnes et al., 2006). By comparing the monthly trend of median CHL and marine biogenic aerosol chemical composition (Figure 3.3) in a normalized scale, the CHL peak appeared wider than the marine aerosol one, indicating that biomass concentration starts to grow earlier, and aerosol chemical composition follows accordingly. Furthermore, OM is characterized by a broader seasonal trend (Figure 3.3) than nss-SO_4^{2-} and MSA. This is probably due to the number of different processes (primary and secondary) contributing to generate marine organic aerosol. Rinaldi et al. (2010) pointed out that the peak in primary OM concentration at MHD is likely to occur in spring, when seawater is enriched in biogenic organic components and wind speed has not reached yet the summer minimum. Conversely, OM is more likely to be contributed by secondary sources during summer, when the photochemistry reaches its maximum, even though Ovadnevaite et al.

(2011b) demonstrated the occurrence of occasional plumes of highly concentrated primary OM in that season. This variety of processes may explain the broader shape of OM seasonal trend.

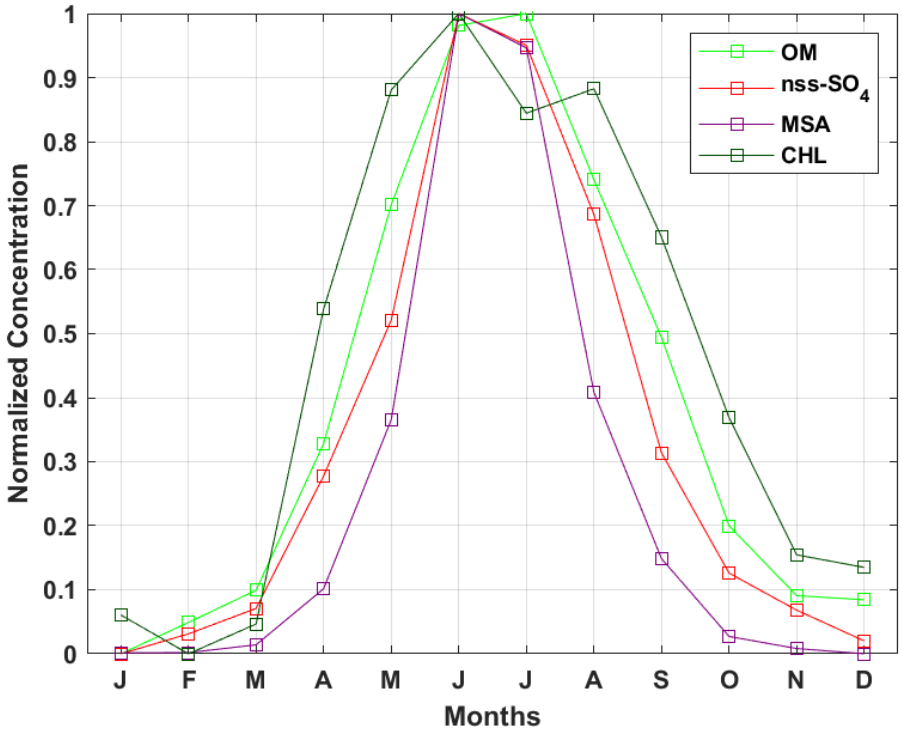

Figure 3.3: Normalized monthly median of CHL, OM, nss-SO_4^{2-}, and MSA during 2009-2017.

The clean marine average (median) nss-SO_4^{2-} concentration at MHD in the 9 years of the study ranges from 0.05 (0.03) µg m^{-3} in winter to 0.46 (0.38) µg m^{-3} in summer; the MSA concentration in summer is 0.07 (0.04) µg m^{-3}, while it goes down to less than 1 ng m^{-3} in winter (further comparisons are presented in Table 3.1). OM exhibits seasonal variations from winter to summer between 0.03 (0.02) and 0.18 (0.15) µg m^{-3}. Conversely, the SS mass concentration increases during winter (mean 0.33; median 0.22) months, with the minimum concentrations (0.16; 0.09) observed in summer. Higher wind speeds are common for the NA Ocean during the winter (Rinaldi et al., 2013) and result in higher amounts of sea spray due to the power-law relationship between spray and wind speed (Monahan et al., 1983; Ovadnevaite et al., 2012). No clear seasonal pattern is exhibited for NO_3^- which is only a minor component in submicron marine aerosol.

In agreement with Ovadnevaite et al. (2014), standard deviations are often larger than the average aerosol mass concentrations, demonstrating that mass concentrations were not

normally distributed. Seasonality in the submicron marine aerosol (2009-2017) is in good agreement with MHD aerosol climatology for the 2002–2004 (Yoon et al., 2007) and 2009-2011 (Ovadnevaite et al., 2014) periods. The coincident seasonalities between aerosol components and CHL suggest a relationship between biological processes and the formation of marine aerosol. But it could be explained also by the different origin of the air masses reaching MHD in different seasons. In other words, this seasonality could be driven by either the dependence of aerosol chemical composition on the seasonal cycle of the NA biological activity or from the different contribution of different air mass types per season. This last aspect will be addressed below.

3.2 Classification of Air Mass Back-Trajectories at MHD

To classify the origin of air masses arriving at MHD for the period 2009-20117, 3-day back-trajectories (BTs) were calculated every 6 hr (4 times a day) with an arrival height of 100 m above MSL of the sampling station. By applying the non-hierarchical clustering algorithm (Dorling et al., 1992; Tripathi et al., 2010), using squared Euclidean distance as a similarity measure, the BTs were grouped into 4 main clusters showing the long-term general circulation of air masses arriving MHD (Figure 3.4). Cluster analysis is a multivariate statistical method that involves separating a collection of statistics into a variety of clusters that are distinct regarding standard group values of the variables. The goal is to maximize the variance between groups and to minimize variance within each group.

The BTs representing air masses during 2009-2017 are shown in Figure 3.4. Three air mass clusters, encountered at MHD, have a maritime origin, namely marine Arctic (mA), marine Polar (mP), and marine Tropical (mT), according to the classification by Dall'Osto et al. (2010). An air mass cluster, labelled as continental European (cP), represents air masses reaching the sampling station after passing over Northern Europe. This cluster and associated air masses were excluded by any further analysis, in this study, representing conditions of anthropogenic pollution at MHD.

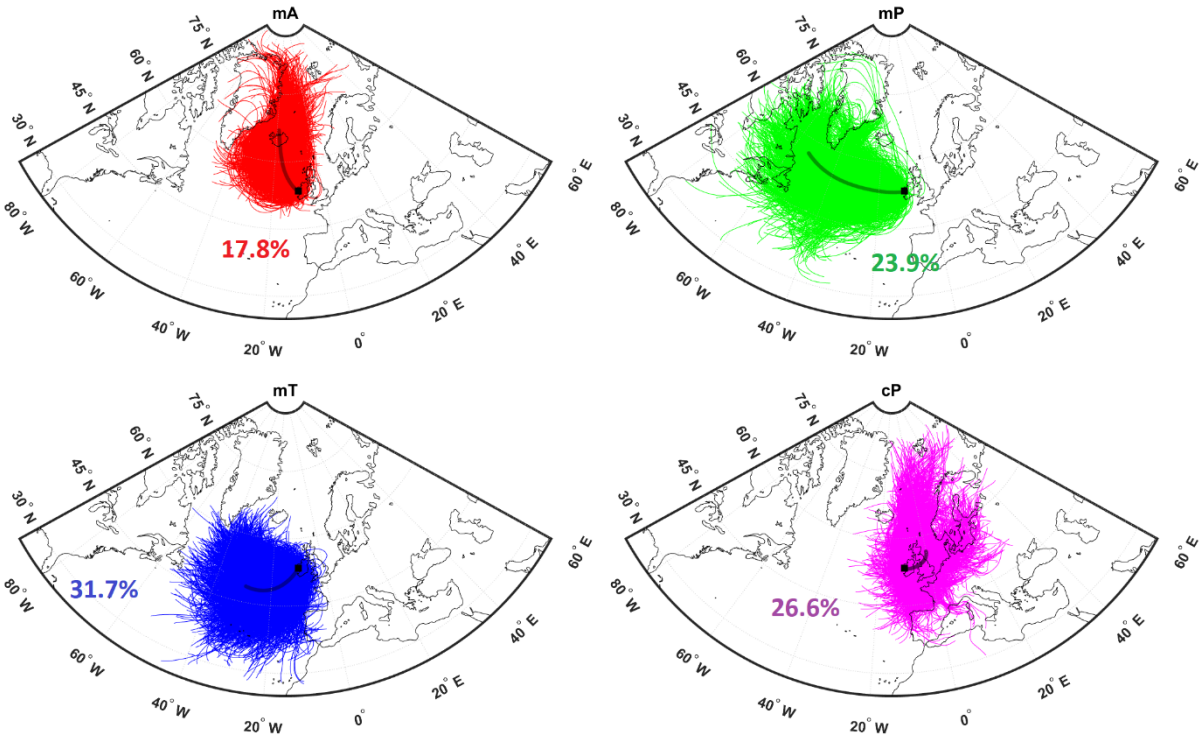

Figure 3.4: The 3-day air mass BTs (hourly time step) arriving at MHD (represented by a black square) sampling station every 6 hr (four times per day) at 100 m above the MSL during 2009-2017. The BTs were classified according to the origin of air mass into the marine Arctic (mA; red), marine Polar (mP; green), marine Tropical (mT; blue) and continental European (cP; magenta). The clusters of BTs are shown by the dark solid lines and the percentage of each cluster is inserted. The cP cluster was excluded from the analysis of clean marine aerosol.

Figure 3.5 shows the seasonality of BTs reaching MHD during the investigation period (2009-2017). In the 9 years of the calculated BTs (4 times per day; Total = 13148 times), the mT is the dominant air mass type (4169 times; 31.7%), followed by mP (3145; 23.9%) and mA (2338; 17.8%). Totally, maritime air masses account for around 73.4%. Of the marine air masses, mT are more abundant in summer (June to August). The mA has a major contribution from late spring (April and May) to the summer, while mP prevails in winter, November to February.

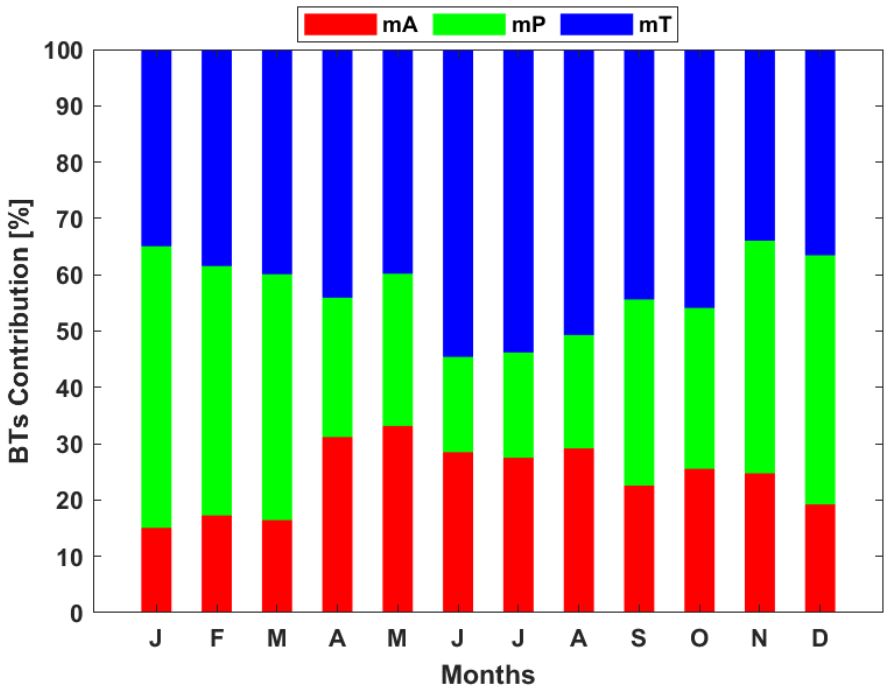

Figure 3.5: Monthly contribution of air mass BTs arriving at MHD in each cluster.

3.3 Marine Aerosol Seasonality According to BTs Clusters

Considering that the air mass BTs arriving at MHD display seasonal variations, one can hypothesize that seasonality in marine aerosol chemical components may be driven by the origins of air masses. To check this hypothesis, the aerosol measurements were classified according to the marine air mass clusters. To treat all the measurements over the day, since BTs have been calculated 4 times a day, we supposed that each BT has the same origin over 6 hours around its time. This assumption is based on the fact that BTs do not change much within a few hours since they are calculated with models at low time resolution. The data was subjected to eBC filtration after this classification, as discussed above.

Even when clean marine aerosol data were divided into homogeneous BT clusters, the concentration seasonal trends are evident within each type of air mass. Figure 3.6 shows the general seasonal pattern in each marine air mass cluster, separately. The largest median (mean) concentrations for nss-SO_4^{2-}, MSA and OM (selected as tracers of marine biogenic aerosol) are observed in June and July for all three marine air masses, in consistence with the marine biological activity trend.

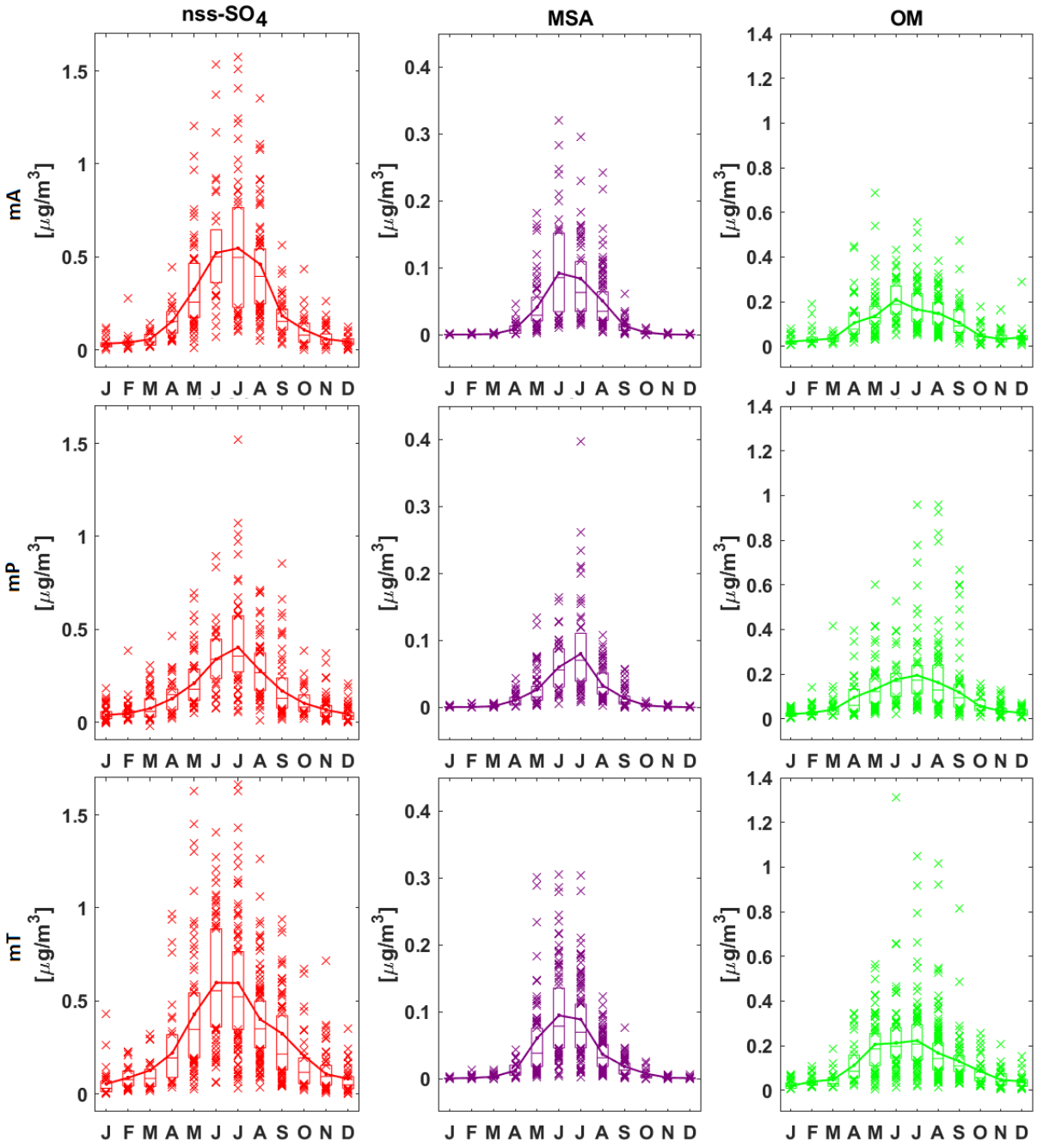

Figure 3.6: Monthly trend of marine biogenic aerosol chemical composition at different air mass clusters as: top) mA, middle) mP, and bottom) mT. On each box that represents a month, the central line indicates the median, and the bottom and top edges of the box indicate the 25th and 75th percentiles, respectively. The connected line represents the monthly mean.

Table 3.1 quantifies the aerosol mass concentrations in two distinct seasons: winter (December, January, and February) and summer (June, July, and August). The mP air mass has the lowest contribution of nss-SO_4^{2-} and MSA during summer while OM is almost constant between the three air masses. The highest nss-SO_4^{2-} concentration is advected in the mT air

mass in consistent with the previous study by Dall'Osto et al. (2010) and Ovadnevaite et al. (2014). Passing from low to high biological activity conditions causes an average increase in nss-SO_4^{2-} and OM of ~ 8 and 5 times respectively, while MSA concentration increases of almost two orders of magnitude, given the sub-nanogram-per-cubic-meter winter-time concentration. The marine aerosol mass fractional contributions to the total aerosol mass concentration were 12.2%, 0.2%, and 6.4% for nss-SO_4^{2-}, MSA, and OM, respectively, in winter. Throughout the summer, these percentages were raised to 52.6%, 7.4%, and 13.2%. It is worth noting that in the fractional estimates MSA concentrations were subtracted from OM. In conclusion, the air mass origin does not explain the seasonality in marine aerosol chemical composition since the seasonality is evident also by selecting homogeneous air mass types, in agreement with Ovadnevaite et al. (2014).

Table 3.1: Seasonal variations in PM_1 chemical composition [μg m^{-3}] of clean marine biogenic aerosol at different air mass clusters. The CHL [mg m^{-3}] seasonality during 2009-2017 were added. *n* is the number of clean hours (samples) in each category.

	Winter (LBA)				**Summer (HBA)**			
	All Marine *n* = 4179	**mA** *n* = 689	**mP** *n* = 2403	**mT** *n* = 1087	**All Marine** *n* = 7199	**mA** *n* = 2074	**mP** *n* = 1755	**mT** *n* = 3370
	Mean S.Dev Median				Mean S.Dev Median			
CHL	0.21 0.04 0.20				0.50 0.09 0.49			
nss-SO_4^{2-}	0.05 0.06 0.03	0.04 0.04 0.03	0.04 0.04 0.03	0.07 0.09 0.05	0.46 0.33 0.38	0.50 0.34 0.43	0.33 0.23 0.29	0.51 0.36 0.42
MSA	< 0.001 – < 0.001	< 0.001 – < 0.001	< 0.001 – < 0.001	≈ 0.001 – < 0.001	0.07 0.06 0.04	0.07 0.06 0.05	0.05 0.05 0.04	0.07 0.07 0.05
OM	0.03 0.03 0.02	0.03 0.04 0.03	0.02 0.02 0.02	0.03 0.03 0.03	0.18 0.15 0.15	0.17 0.09 0.15	0.18 0.16 0.14	0.20 0.16 0.16

3.4 Spectral Analysis of CHL

In order to better characterize the seasonal patterns of surface CHL over the NE Atlantic Ocean, which appears to be a major driver of marine aerosol chemical composition, we performed the spectral analysis of the daily CHL time-series (2009-2017), using Fourier transformation. The spectral analysis is a technique used to estimate the power spectrum of a signal from its time-domain representation. The spectrum decomposes the signal into different frequencies and identifies periodicities. Highest power peaks are located at the most critical frequencies influencing the time series analyzed. With this method, it is possible to understand the important features that regulate the systematic variations over time of a signal.

The results of 24 pixels distributed homogenously over the area of the NA ocean facing directly MHD (black box) are shown in Figure 3.7, as an example. The dominant cycles of phytoplankton activity in the NA are the annual and semi-annual cycles. The annual cycle (one crest and one trough in a year) has the highest power spectrum which means that the most notable changes in CHL (amplitude) occurred passing from winter to summer. This cycle contributes 13–36% of the total spectrum depending on the location. The second significant variations happen from season to season by the semi-annual cycle. Cycles occurring at smaller frequencies (*e.g.,* monthly, weekly) are also evidenced by this analysis; nevertheless, they contribute to smaller CHL variations and their impact on aerosol properties cannot be easily quantified.

In a previous work, Rinaldi et al. (2013) tried to deconvolute the different time-scales of the signals generating the correlation observed at MHD between sea-spray organics and CHL. In agreement with the above analysis, they concluded that, although the seasonal signal (variability over one year) played a major role, the observed correlation was also contributed by both short-term fluctuations (i.e., sub-seasonal scale) and interannual variability (i.e., time scale larger than one year). The former was demonstrated to contribute for timescales of 60 and 90 days, while no statistically robust conclusion could be derived for faster fluctuations (one month or less).

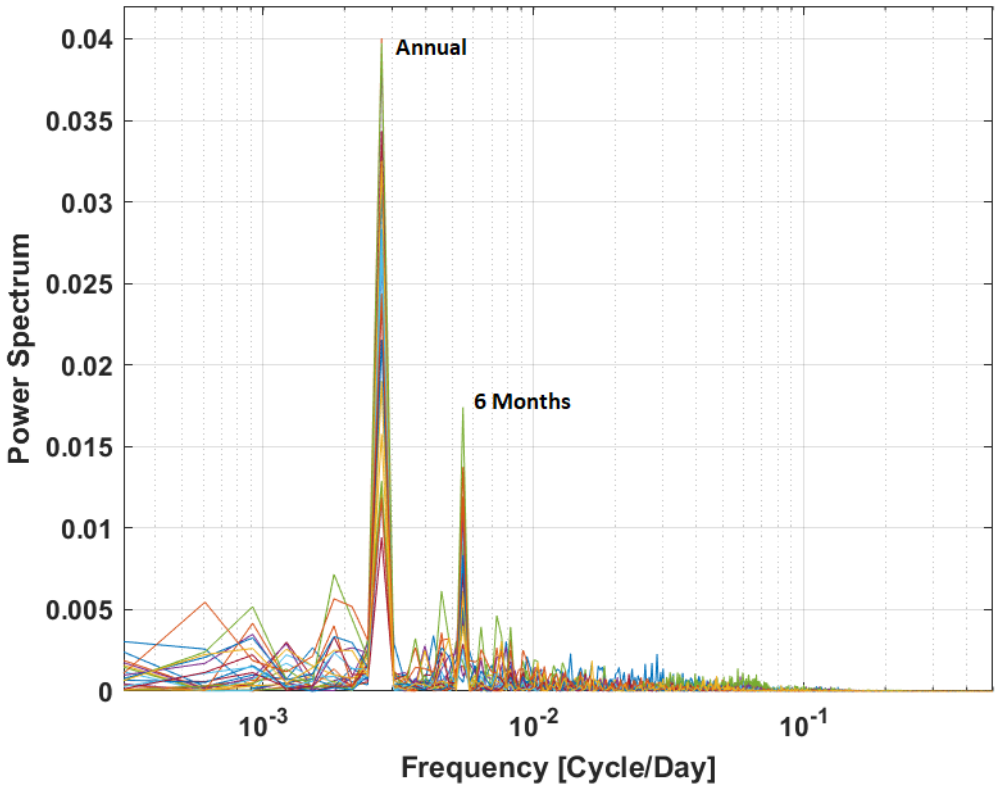

Figure 3.7: Spectral distribution of daily mean CHL at 24 pixels in the NA during 2009-2017.

Investigating the correlation at time scales shorter than one year is important to understand the impact of oceanic biological activity on marine aerosol properties in detail. It is worth highlighting that all the variables considered in this study, CHL and aerosol component concentrations, are potentially influenced by the same meteorological parameters, on the yearly time scale. The annual cycle of the CHL is controlled primarily by solar radiation, which also impacts the sea surface temperature (Friedland et al., 2016; Martinez et al., 2011). Contextually, meteorology also affects concentrations of the biogenic aerosol components: nss-SO_4^{2-} and MSA are linked to the emission of DMS from the sea surface, which depends on biotic factors (phytoplankton activity) but also on abiotic ones (sea temperature, wind speed). Most importantly, the atmospheric capacity of oxidizing DMS, producing nss-SO_4^{2-} and MSA, depends on meteorological parameters (solar radiation, air temperature, relative humidity) (Becagli et al., 2013; Kouvarakis and Mihalopoulos, 2002; Toole and Siegel, 2004; Vallina and Simo, 2007), which mostly share the same seasonality as CHL. Similarly, OM formation is potentially influenced by the same factors, at least for the secondary fraction, even though the current level of understanding of the physico-chemical processes involved is much lower. In other words, the observed correlation between aerosol

composition and CHL over multi-year time scales is certainly an indication that phytoplankton activity has an impact on marine aerosol concentration and composition. Nevertheless, it is difficult to distinguish how much of the variability of aerosol composition is due to the phytoplankton itself and how much depends on the seasonality of meteorological parameters. For this reason, in the following Sections we will investigate the relationship between aerosol properties (chemical composition) and oceanic biological activity on a shorter time scale, dividing the dataset into seasons.

3.5 Seasonal Spatial Correlation Analysis

To evaluate the effect of marine biological activity on aerosol chemical composition, over a wide oceanic region located upwind of MHD, the spatial distributions of the correlation coefficient between aerosol chemical properties measured at MHD and surface CHL, at each grid point of the NA domain were investigated, following the approach introduced by Rinaldi et al. (2013), and further used by O'Dowd et al. (2015). A standard least squares regression was used for this purpose.

Figure 3.8 displays the correlation coefficient spatial distribution between the clean marine biogenic aerosol chemical composition measured at MHD and CHL over the NA Ocean during 2009-2017. In the presented correlation maps, only significant correlation coefficients ($p < 0.01$) are shown. The datasets were divided into four seasons: winter (December, January, and February), spring (March, April, and May), summer (June, July, and August), and autumn (September, October, and November).

In winter, when the biological activity is at its minimum, the correlation coefficients are generally weak, indicating that there is not a strong driver of marine aerosol properties from oceanic biological activity or simply that the variability in CHL is too low to evidence any trends when compared with aerosol properties. In summer, the correlation coefficients are significant mainly toward the south of the East Atlantic, in agreement with dominant mT air mass during that period. Areas of significant correlation are more widespread in spring and autumn (transition seasons) and tend to the North, consistently with a higher contribution from mP and mA air masses.

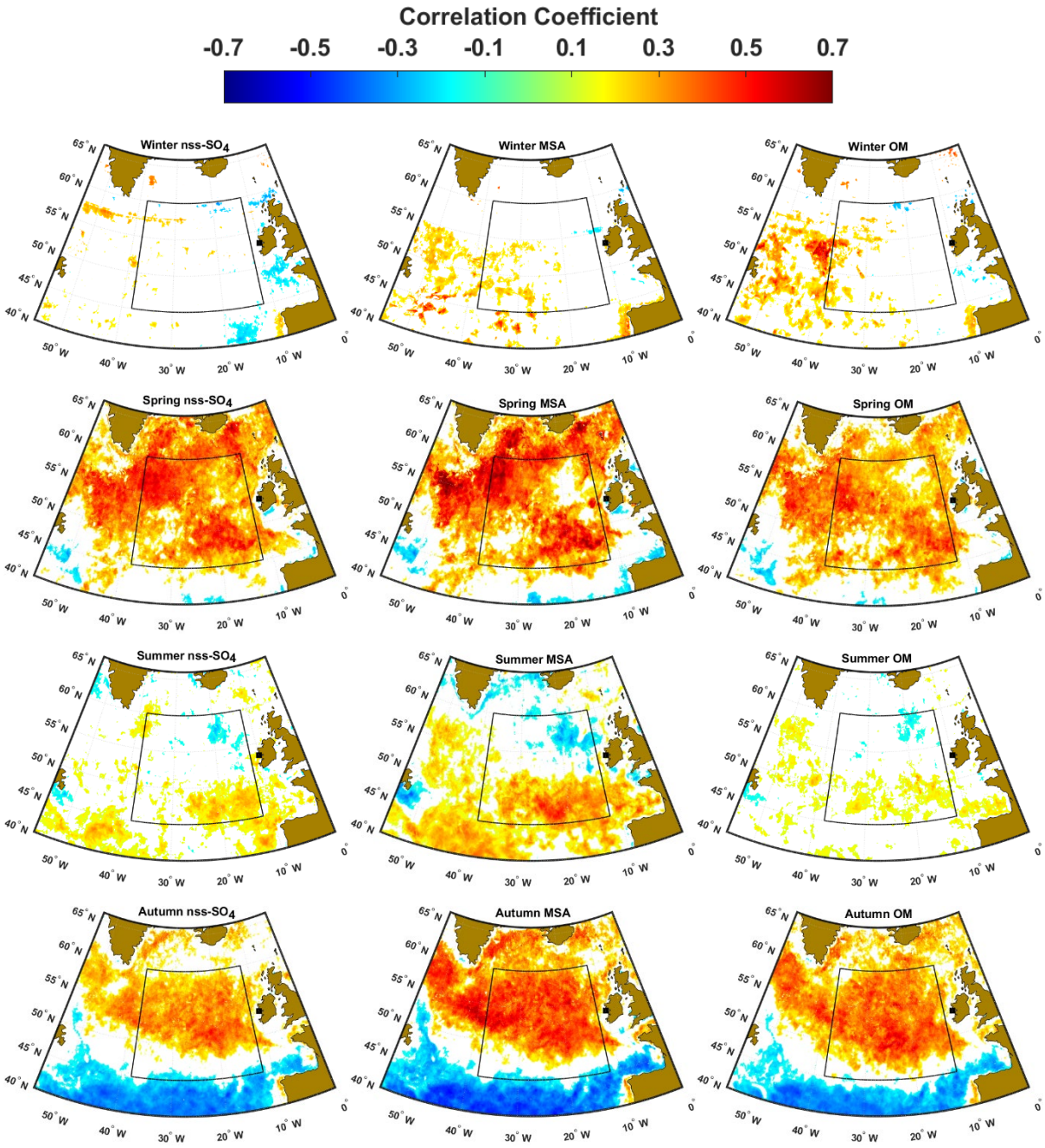

Figure 3.8: Seasonal correlation coefficient spatial distribution between the main biogenic aerosol chemical composition measured at MHD and CHL over the NA Ocean during 2009-2017, considering clean marine air masses. Only significant correlation coefficients ($p < 0.01$) are presented. The black box is the broad oceanic region that is likely to exert the highest impact on aerosol properties at the sampling station, as it results from the analyses of this Chapter.

These results show that the correlation between aerosol chemical composition and CHL can be observed also at sub-yearly scale for large areas of the NE Atlantic Ocean, excluding wintertime, when the biological activity is probably too low to affect marine aerosol

properties significantly. For the studied long-term data, we noticed no major effect of the considered delay time (see Chapter 2) on the correlation between aerosol composition and CHL in the different seasons; a scant, generally decreasing, variations of the correlation coefficient as a function of the delay time, as shown in Figure 3.9. For this reason, we have presented the result obtained considering a time-lag of 0 days. Considerations on the importance of the time-lag in multi-year datasets are discussed at the end of this Chapter.

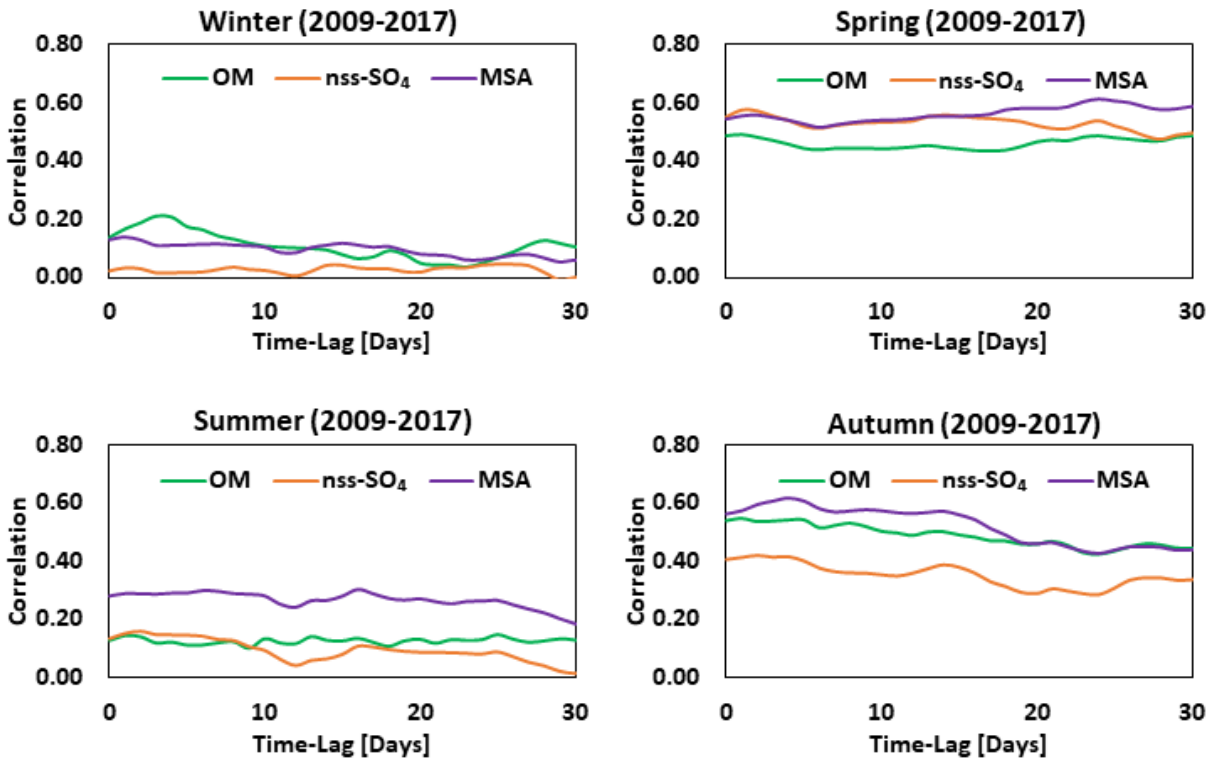

Figure 3.9: Correlation coefficient as a function of time-lag between mean CHL in the black box region and the main aerosol chemical components, in different seasons.

In order to ascertain that the observed correlations are due to a real physical mechanism linking phytoplankton activity to aerosol chemical composition and are not only due to casually coincident time trends, in the next Section we will cross these results with the spatial source attribution analysis (PSCF), following the approach described in Section 2.7.3.1.

3.6 Seasonally Dependent Marine Aerosol Source Region Attribution

The identification of the clean marine aerosol source regions, for each season, was carried out by combining the high-resolution aerosol chemical composition data (2009-2017) with the

3-day air mass BTs, following the PSCF approach (Chang et al., 2011). PSCF allows a probabilistic geographical source attribution for high-resolution aerosol data, showing the pixels associated with the highest concentrations (defined as above the median), which evidence the most probable source regions. In this analysis, only maritime air masses (mA, mP, and mT) have been considered. Since the air mass BTs were obtained every 6 hr, the aerosol chemical composition data were selected as follows: 1-hour average around the arrival time of the air mass BT was calculated, for each aerosol chemical component, and associated to the corresponding BT. Further, the aerosol data were filtered to select only the cleanest marine air masses (Section 2.7.1).

The PSCF maps (Figure 3.10) show generally consistent features between the aerosol chemical components of biogenic origin like nss-SO_4^{2-}, MSA and OM. The results show a shifting of the potential biogenic aerosol sources according to the season, likely due to the changing atmospheric circulation and to the spatial evolution of phytoplankton blooms over the year in the NE Atlantic Ocean. All the potential source regions identified by PSCF fall within the area highlighted by the black box of Figure 3.8 (45° – 60° N and 12° – 38° W) immediately to the west of Ireland.

It is worth noting that the source regions of SS (Figure S1; APPENDIX), which is not a biogenic aerosol component, clearly do not overlap with the biogenic aerosol sources, evidencing different formation processes unrelated with the trends of biological activity.

Comparing the PSCF maps with the correlation maps presented in Section 3.5, a broad overlapping of the regions characterized by significant and positive correlation with potential biogenic aerosol sources can be observed for all the seasons, apart winter, for which we cannot evidence any significantly correlating region. In spring, an extensive overlapping region can be identified to the Eastern part of the domain, while in Autumn the overlapping area coincides more with the central part of the black box, up to its western boundaries. In summer, PSCF evidences two potential major source regions, one to the South and one to the North-East of the domain, the latter not captured by the CHL correlation analysis. This may indicate a source that, although strong enough to affect the PSCF maps, it is not systematically present every year or not with the same magnitude, which can determine the loss of correlation in that area using the nine years of summer data. This would be an interesting topic of investigation for future works.

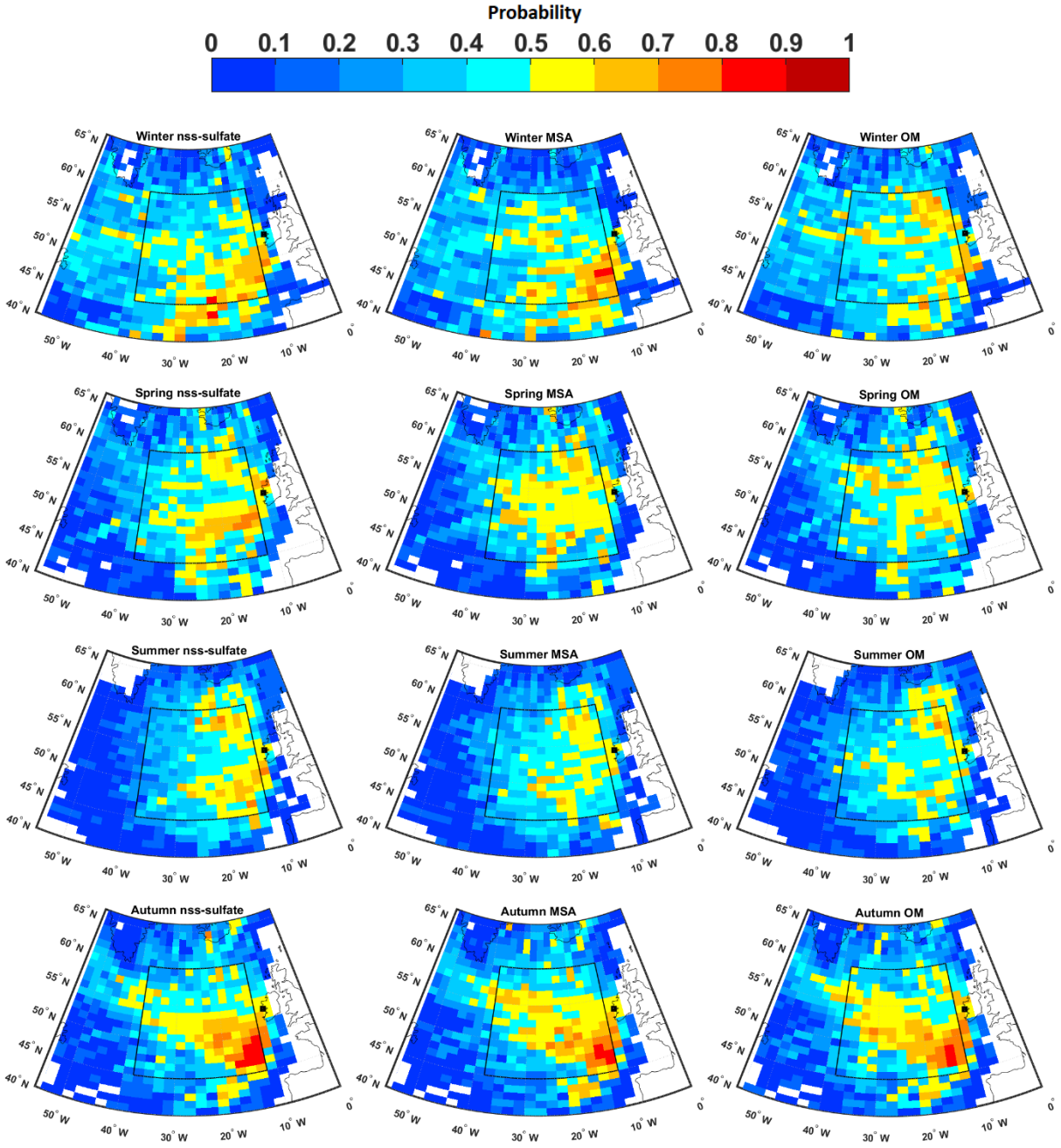

Figure 3.10: Seasonal PSCF distributions for clean marine aerosol arrived at MHD during 2009-2017. The sources of high concentrations are defined above the median values.

These results evidence that a relation between the oceanic biological activity and marine aerosol chemical composition can be observed also at sub-yearly time scale. It is worth highlighting that the existence of such relation was not deduced only from correlation with CHL, which do not necessary imply a cause-effect relation. As detailed in Chapter 2, our conclusions are based on the consistency of results between two totally independent approaches (spatio-temporal correlation with CHL and potential source attribution by PSCF),

showing that the correlation occurs mostly in regions associated with high production of biogenic marine aerosol components. This strongly supports a causal link between phytoplankton patterns in surface oceanic waters and the variability of marine aerosol chemical composition in the overlying atmosphere.

3.7 Discussion

In this Chapter, the link between marine aerosol properties (chemical composition) and oceanic biological activity patterns over the NA Ocean has been evidenced for a multi-year dataset, but also at the sub-yearly (i.e., seasonal) time scale. In a multi-year dataset from offline observations, Rinaldi et al. (2013) observed a significant correlation between the organic content of sea-spray aerosol (OM_{SS}), measured at MHD, and oceanic CHL. Interestingly, they reported significant correlation coefficients starting from 0 to 15 day time-lag (see Chapter 2 for details) with slightly higher correlation observed at 8 days. Similarly, O'Dowd et al. (2015) reported a peak in the correlation at 24 days delay time for the same parameter from online measurements and weekly marine net primary productivity, but with a correlation coefficient frequency distribution that was very similar between time-lags of 8, 16 and 24 days. The correlation was significant also simultaneously at time-lag of 0 day. In the present Chapter, we noticed that the seasonal correlation coefficient between marine biogenic aerosol concentration and CHL, in the identified black box region, is significant and rather constant from 0 to 25 days of delay time (max between 1 and 4 days).

When considering long-term data (multi-year datasets), the correlation is mainly driven by the annual cycle of CHL as discussed above. In that case, we do not expect a sharp dependency of the correlation coefficient with the delay time as the time resolution of the processes governing the correlation is much larger than the few considered weeks of delay time, as observed in the above reported examples. Conversely, when considering short-time data (sub-seasonal), processes occurring at lower time scales are likely dominant in determining the correlation between aerosol properties and oceanic biological activity patterns and, for this reason, considering a delay time between CHL and aerosol parameters may significantly change the observed correlation, as we will show and discuss in the next Chapters.

In the next Chapters (4, 5, and 6), we will focus on shorter time scales, close to single algal bloom evolution times (Lehahn et al., 2014), to further investigate the relation linking marine

aerosol properties to phytoplankton activity. This will be achieved by using in-situ aerosol measurements collected during three intensive field campaigns conducted in late Summer 2015 at the Mace Head Research Station (MHD), in Spring 2016 at the Capo Granitola (CGR) Mediterranean Climate Observatory and in Summer 2018 at the Gruvebadet (GVB) Arctic observatory. These intensive campaigns will allow extending the range of observed aerosol parameters to other climate relevant properties, as number size distribution, CCN and INP concentrations, which are not all available as long-term records. These measurements will be used to investigate the relationship between oceanic biological activity and physico-chemical/cloud-relevant properties of atmospheric aerosol particles over three different marine environments (NA ocean, the Mediterranean Sea, and the Arctic ocean) on short (sub-seasonal) time scales (~ 1-2 months). An advantage of the short time-scale case studies is that it can be easier to discriminate the effect of meteorology from that of biology, facilitating a process-level understanding of the relation linking phytoplankton activity to marine aerosol properties.

A better knowledge of the short time-scale phytoplankton-aerosol interactions may lead to a significant improvement in the current understanding of the physical and biochemical processes responsible for the formation of biogenic marine aerosol over the oceans and ultimately to a better comprehension of the ocean-atmosphere-cloud system, with potentially important impacts on climate science.

4. Chemical Composition and Cloud-Relevant Properties in the NE Atlantic Ocean during Summertime 2015

In this Chapter, we elucidate the relationship between oceanic biological activity and physico-chemical/cloud-relevant properties of atmospheric aerosol particles over the NA ocean, on a short time scale (~ 1-2 months). The in-situ aerosol data at MHD were performed during an intensive field campaign conducted in late summer (August-September) 2015 as a part of BACCHUS (Impact of Biogenic versus Anthropogenic emissions on Clouds and Climate: towards a Holistic UnderStanding) research project. The data comprise in-situ aerosol chemical composition, particle number size distribution, cloud condensation nuclei (CCN) and ice nucleating particle (INP) number concentrations. Specific objectives for this Chapter are to: **(a)** characterize the relationship between the main aerosol chemical components and plankton activity during an intensive observation period representative of summer conditions; **(b)** identify the source regions of biogenic aerosol components of marine origin, active during the campaign, in comparison to those evidenced in previous works using multi-year datasets, and **(c)** resolve how cloud-relevant properties of marine aerosol are influenced by phytoplankton activity.

4.1 Overview of Marine Aerosol Properties during the Campaign

The aerosol chemical composition, particle number, CCN and INP concentrations in clean marine and all sectors, are summarized in Table 4.1. Figure S2, Figure S3, Figure S4 and Figure S5 (APPENDIX) display the time-series plots of all the studied aerosol variables in clean conditions during the campaign, paired with CHL data. The OM mass-fraction enrichment (OM_{SS}) in marine aerosol was calculated as the contribution of OM mass relative to the total OM plus SS mass. In general, except SS, the concentrations of aerosol components were lower in clean marine conditions, consistent with a previous comparison by Dall'Osto et al. (2010).

According to the particle size distribution during the campaign, we have selected two dominant modes of particle number concentration: Aitken ($20 < Dp < 100$ nm) and accumulation ($100 < Dp < 500$ nm) for this study. In clean marine air, aerosol size distributions display bimodality (Dall'Osto et al., 2010; Hoppel et al., 1990) with an Aitken and accumulation

mode. In the Aitken mode size range, the average particle number concentration was 401±323 cm^{-3}, while it was 96±43 cm^{-3} in the accumulation mode range.

From the size scanned CCN measurements, CCN concentrations were selected at three supersaturations (0.25, 0.5, 0.75 ± 10% supersaturation at each level). The number concentration of CCN ranged from 112±43 cm^{-3}, at 0.25% supersaturation, to 252±119 cm^{-3}, at 0.75% supersaturation. CCN concentrations in the different sectors are in agreement with long term measurements by Reade et al. (2006). The study average number of INPs (T_A = –22 °C, S_W = 1.01) was 2.7±2.8 (10.1±8.8) m^{-3} in PM_1 (PM_{10}) fractions, respectively, as already reported by McCluskey et al. (2018c).

Table 4.1: Summary of marine aerosol studied variables for the study (campaign) period.

Parameter	Clean Marine	All Data	Sampling Period
	mean ± s.dev (median)		
Aerosol chemical composition			
SS [µg m^{-3}]	0.16 ± 0.14 (0.12)	0.14 ± 0.14 (0.09)	From 31/07/2015 to 21/09/2015
OM [µg m^{-3}]	0.15 ± 0.14 (0.11)	0.54 ± 0.88 (0.20)	
NO_3^- [µg m^{-3}]	0.02 ± 0.01 (0.01)	0.08 ± 0.23 (0.02)	
SO_4^{2-} [µg m^{-3}]	0.25 ± 0.18 (0.22)	0.44 ± 0.51 (0.28)	
NH_4^+ [µg m^{-3}]	0.03 ± 0.02 (0.02)	0.11 ± 0.21 (0.04)	
MSA [µg m^{-3}]	0.02 ± 0.02 (0.02)	0.03 ± 0.02 (0.02)	
OM_{SS}	0.51 ± 0.23 (0.51)	0.65 ± 0.26 (0.70)	
eBC [ng m^{-3}]	7.19 ± 4.42 (7.19)	50 ± 105 (13)	
Particle number concentration			
Aitken: $N_{20\text{-}100nm}$ [cm^{-3}]	401 ± 323 (336)	572 ± 555 (401)	From 31/07/2015 to 21/09/2015
Accumulation: $N_{100\text{-}500nm}$ [cm^{-3}]	96 ± 43 (91)	209 ± 261 (122)	
Total: $N_{20\text{-}500nm}$ [cm^{-3}]	497 ± 334 (432)	780 ± 778 (531)	
CCN number concentration (supersaturation)			
$nCCN_{0.25}$ [cm^{-3}]	112 ± 43 (108)	150 ± 99 (121)	From 31/07/2015 to 31/08/2015
$nCCN_{0.50}$ [cm^{-3}]	161 ± 72 (144)	220 ± 162 (165)	
$nCCN_{0.75}$ [cm^{-3}]	252 ± 119 (222)	312 ± 202 (253)	
INP number concentration (T_A = –22 °C, S_w = 1.01)			
$nINP_{PM1}$ [m^{-3}]	2.7 ± 2.8 (2.3)		25 samples from 30/07/2015 to 28/08/2015
$nINP_{PM10}$ [m^{-3}]	10.1 ± 8.8 (7.8)		

Note. Cases with hourly eBC concentrations < 15 ng m^{-3} were classified as clean marine that are likely not influenced by anthropogenic sources. PM_1 and PM_{10} correspond to total particulate matter less than 1 µm and 10 µm diameter, respectively.

4.2 Air Mass Back-Trajectories

Five-day BTs were calculated four times (00, 06, 12, and 18 hour UTC) a day during the sampling period from 31 July to 21 September 2015, arriving at 100 m above the MSL of the MHD sampling station were utilized to define the source areas. The aerosol data were averaged over a 1 hour (half an hour before and after the arrival time of each back-trajectory) to be filtered for hourly eBC (< 15 ng m^{-3}) to consider only pristine clean marine cases (Figure 4.1).

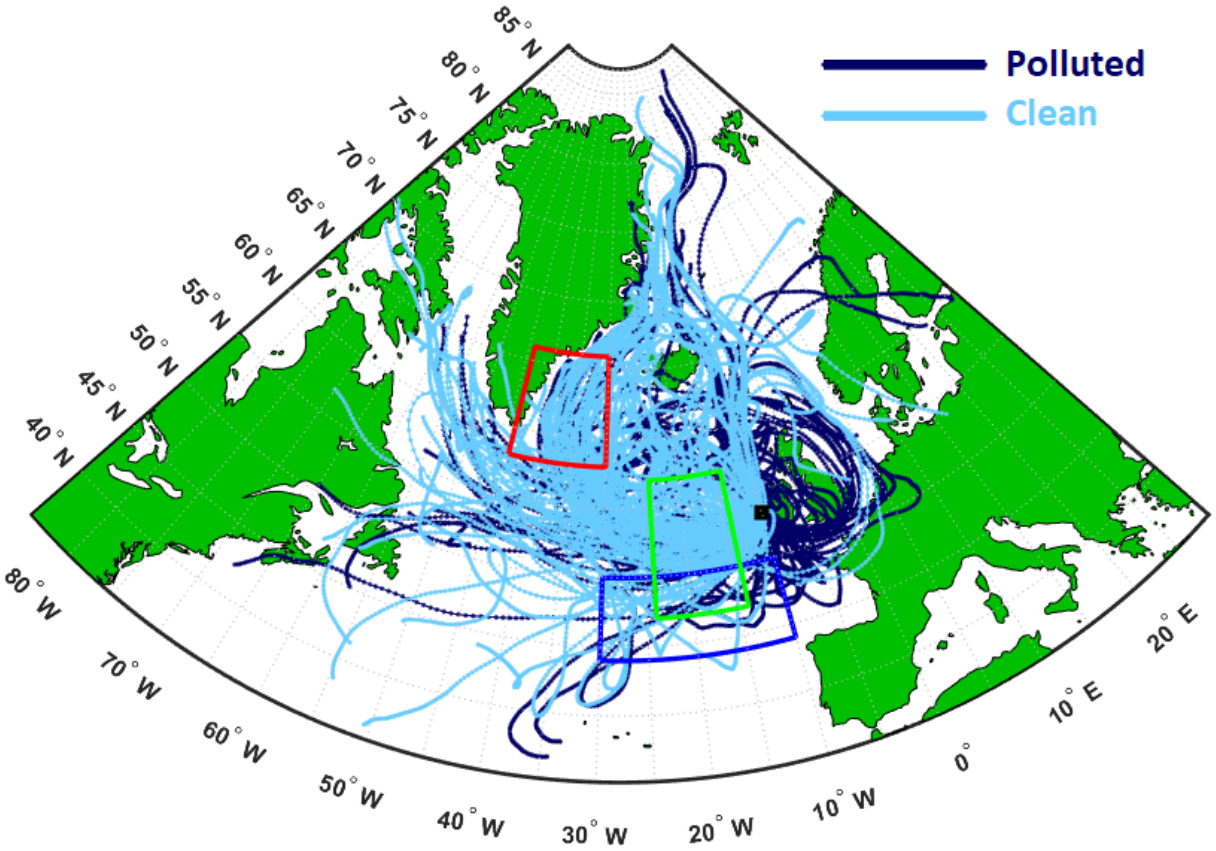

Figure 4.1: The 5-day air mass BTs (hourly time step) calculated by the NOAA HYSPLIT model arriving at MHD (represented by black square) sampling station four times per day (00, 06, 12, and 18 hr UTC) at 100 m above the MSL from 31 July to 21 September 2015. The blue box area comprises grid coordinates 44° – 50° N and 10° – 30° W (Region 1; O'Dowd et al. (2015)), the green box area comprises grid coordinates 47° – 57° N and 14° – 24° W (Region 2; Rinaldi et al. (2013)), while the red box area comprises grid coordinates 58° – 66° N and 30° – 44° W (region 3). These boxes delineate high correlation areas, discussed later. Only clean marine BTs (light blue) according to eBC threshold are used for PSCF calculations.

4.3 Spatio-Temporal Correlation with CHL

Following the approach implemented on long-term data (Chapter 3), the spatial distributions of the correlation coefficient between aerosol physico-chemical properties measured at MHD and surface CHL, at each grid point of the NA domain were investigated considering different time-lags. The time-lag between the CHL time series and aerosol properties has to be considered, on short time-scales (sub-seasonally), in order to take into account the time scale of the biochemical processes responsible for the production of transferable organic matter (in case of PMA) or gaseous precursors (for SMA) in the seawater, after the phytoplankton growing phase. In the latter case, the time-lag comprises also the atmospheric processing time necessary to convert gaseous precursors into particulate matter.

The basic assumption for the time-lagged correlation approach is that marine biological aerosol should follow the evolution of marine biological activity (traced by CHL). For this reason, we looked for positively correlating sea regions: in our interpretation, these regions have a higher probability of being related to the observed aerosol properties.

A general analysis of the obtained results evidenced three specifics positively correlating oceanic regions. Two broadly coincides with those evidenced by O'Dowd et al. (2015), between 44° − 50° N and 10° − 30° W (hereafter Region 1; blue box), and by Rinaldi et al. (2013), between 47° − 57° N and 14° − 24° W (Region 2; green box), as shown in Figure 4.1. These two regions were described as the ocean regions exerting the maximum influence on the chemical composition of SSA sampled at MHD by two distinct multi-year datasets and they already approximate the regions of maximum correlation observed in the present study. Another area of high correlation is found comprising the grid coordinates 58° − 66° N and 30° − 44° W (Region 3; red box). These three regions of high correlation are consistently located upwind of MHD as illustrated from 5-days air mass BT in Figure 4.1, even though it is clear that Region 1 is less interested than the other two from air masses reaching MHD during the study period.

4.3.1 Aerosol Chemical Composition

The spatial distributions of the correlation coefficient (*R*) obtained with different time-lags between CHL and daily averaged nss-SO_4^{2-}, MSA, OM, and OM_{SS} data are shown in Figure 4.2. In all the presented correlation maps, the yellow/red (blue) colors represent positive

(negative) significant correlation coefficients at 95% confidence level while the grey color represents the non-significant ones.

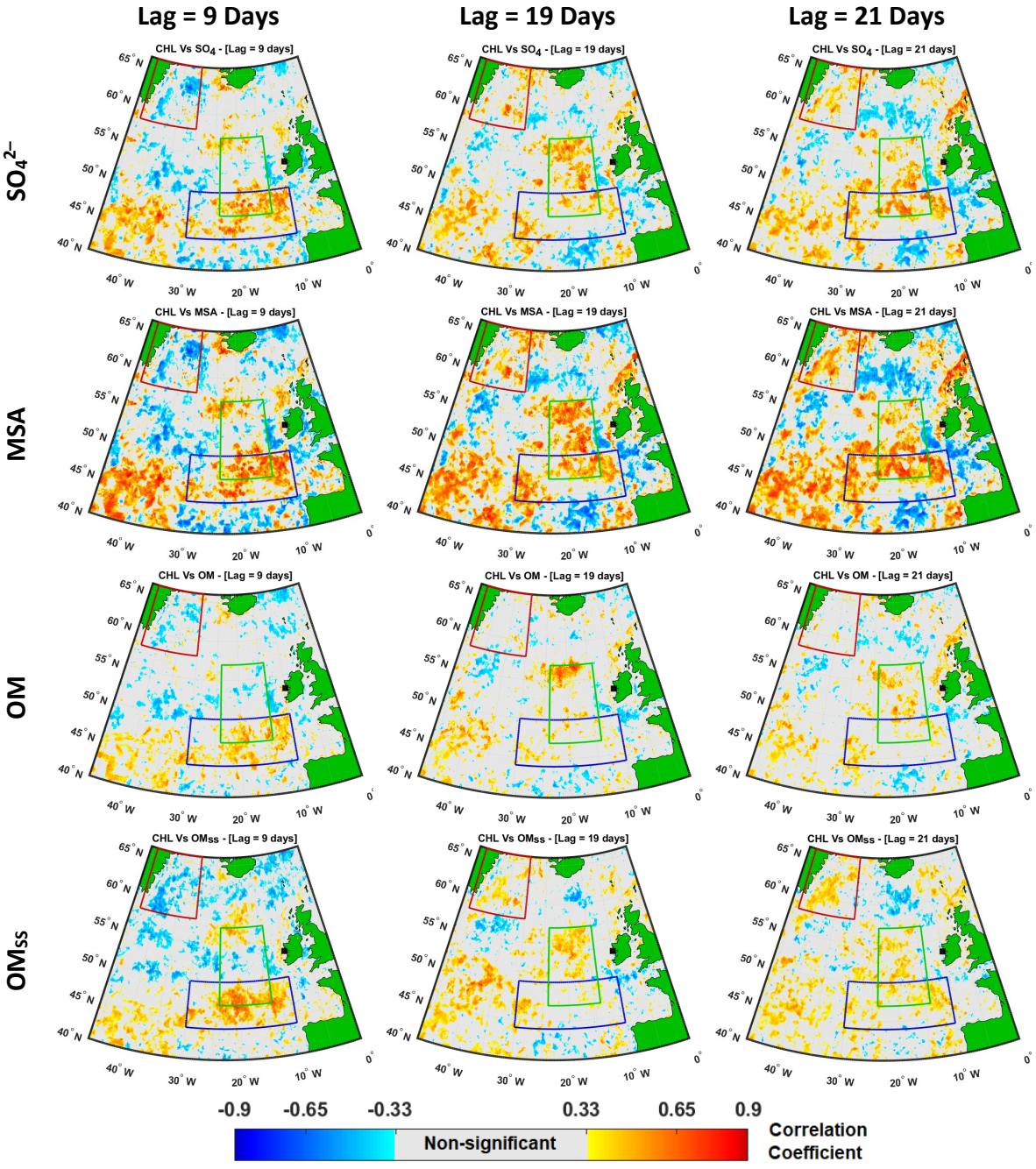

Figure 4.2: Examples of correlation coefficient spatial distribution between the main aerosol chemical composition measured at MHD and CHL over the NA Ocean for 9 days (left), 19 days (middle), and 21 days (right) time-lags, considering only clean marine air masses. In all correlation maps, the grey color represents non-significant correlation coefficients at 95% confidence level, the black square corresponds to MHD station and the regions of interests are shown as blue (Region 1), green (Region 2), and red (Region 3) boxes.

The maps (Figure 4.2) show a significant correlation in the three specific regions in the NA with different time delays. The number of pixels that have significant negative correlation within those regions is negligible, indicating an overall positive correlation for the evidenced areas. The southwestern belt of high correlations in the bottom left corner of the maps is not considered in this study as it is not supported by the BTs pattern (Figure 4.1) and, therefore, a relationship with aerosol measurements at MHD is not to be expected. In that area, high correlations may be due to the similarity of CHL seasonal cycles (Lacour et al., 2015) with Region 1, which could produce a false-positive result because of non-causal correlations, as shown by the spatial distribution of weekly mean CHL (Figure S6; APPENDIX).

Figure 4.3 illustrates the behavior of the correlations, within the three regions, as a function of the considered time-lag between the CHL and the aerosol properties time series. In general, over the three regions, there is an increase in correlation coefficient as a function of the time-lag, generally after about one week towards 20-25 days. Region 1 shows two maxima (bimodal shape) with the first one after 8-9 days and the second maximum between 20 and 25 days. In the second region (green box), the correlation becomes significant after 8-10 day lag for MSA and SO_4^{2-}, but the best correlation occurs at 19-day time-lag for all other chemical components. In the third region (red box), significant correlations were observed for all components after a time-lag of about 18-20 days, except for OM.

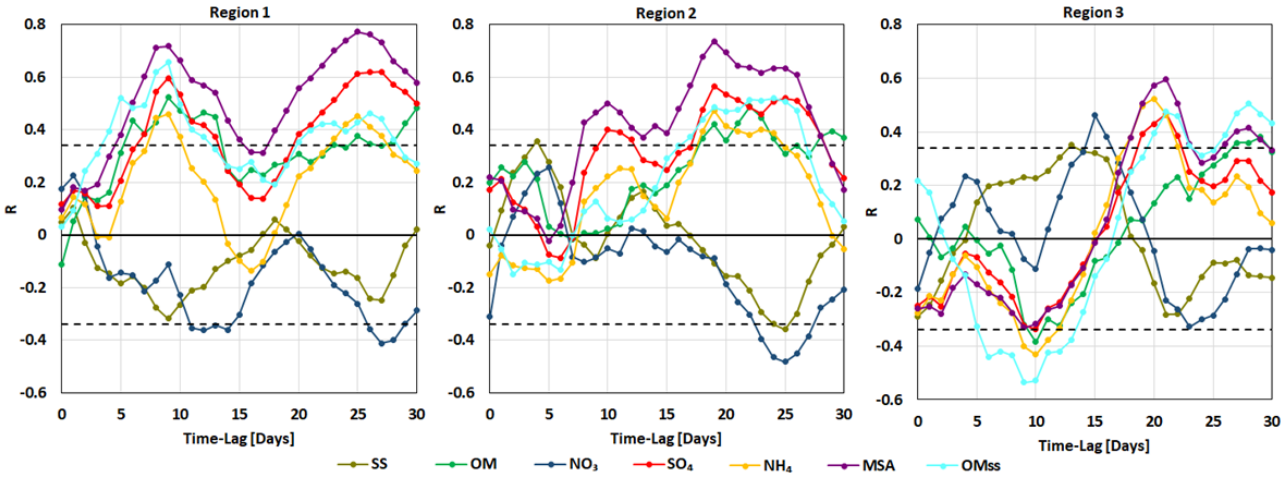

Figure 4.3: Correlation coefficient as a function of time-lag between mean CHL at different selected regions and the main aerosol chemical components. The black dashed lines represent the critical level of significant correlation at 95% confidence limit.

Figure 4.3 also shows that NH_4^+ follows the profile of SO_4^{2-}, although with lower correlation values (NH_4^+, NO_3^-, and SS correlation maps are provided in Figure S7; APPENDIX). This result is consistent with the fact that NH_4^+ is the main ion to neutralize sulfuric acid in the MBL (Huntzicker et al., 1980; Marti et al., 1997). No significant correlation was observed for NO_3^-, which is reasonable since NO_3^- is almost negligible in the sub-micrometer clean marine aerosol (Watts et al., 1990). As expected, SS also does not correlate with CHL in none of the regions.

4.3.2 Particle Number Concentration

A significant correlation between particle number concentration, in both Aitken and accumulation modes, and surface CHL has been found, as presented in Figure 4.4a. Generally, the shape of the correlation as a function of the delay time for particle number concentration follows the one already presented for the chemical composition (Figure 4.4b). In Region 1, the correlation increased to significant levels ($p < 0.05$) after about one week, with the first maximum at time-lag 10 days and a second between 20 and 25 days. Over Region 2, the correlation reaches its maximum value after 20 days, with a reduction in the number of pixels in accumulation mode. As already discussed for the chemical composition, the correlation is lower in Region 3, with significant values after 20 days, but only for the Aitken mode.

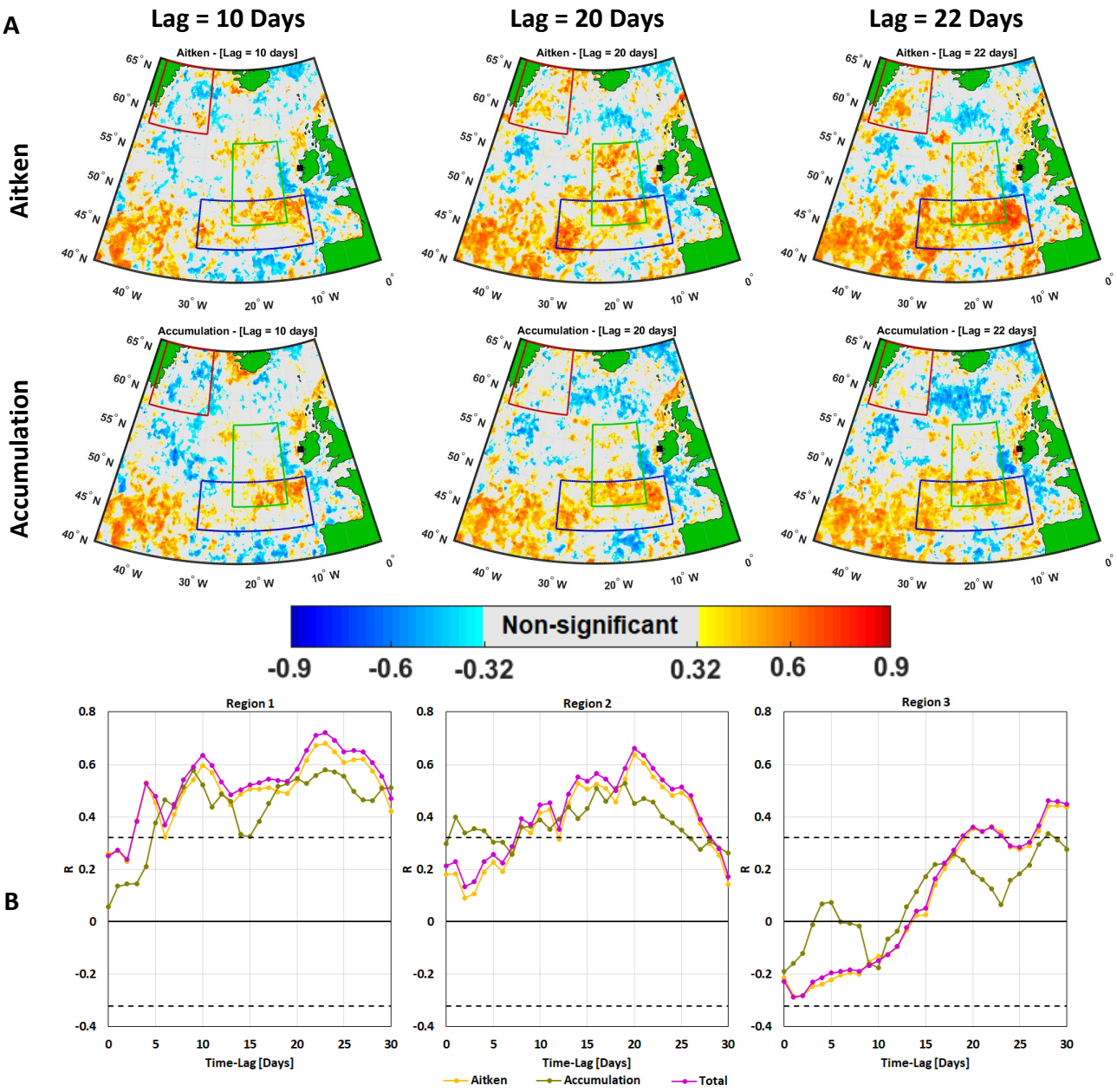

Figure 4.4: a) Examples of correlation coefficient spatial distribution between Aitken and Accumulation modes particle number concentration sampled at MHD and CHL over the NA Ocean for 10 days (left), 20 days (middle), and 22 days (right) time-lags, considering only clean marine air masses. b) Correlation coefficient as a function of time-lag between mean CHL at different selected regions and the different modes of particle number concentration. The black dashed lines represent the critical level of significant correlation at 95% confidence limit.

4.3.3 Cloud Condensation Nuclei

In agreement with aerosol chemistry and particle number concentration, there is a significant correlation between the number of CCN and CHL in the three regions (Figure 4.5a),

with a correlation vs. delay time shape broadly similar to the ones already described in the previous Paragraphs (Figure 4.5b). The correlation is stronger with increasing supersaturation level which agrees with the higher correlation observed between CHL and Aitken mode particle concentration, as smaller particles require higher supersaturation to be activated.

Differently from what observed for CCN concentration, the CCN fraction (CCN/N), calculated as the ratio between CCN and total particle number concentration (20 < Dp < 500 nm), shows no significant dependency on CHL over the NA (Figure 4.5b). This result agrees with Quinn et al. (2014) who showed that the fraction of total particles that activate to form CCN at a given supersaturation is independent of CHL. This lack of correlation suggests that, during the study period, phytoplankton activity influenced the CCN pool more by controlling the particle number concentration than by affecting the CCN properties of single marine aerosol particles. Ovadnevaite et al. (2011a) showed that the CCN fraction of SSA increases as a function of organic enrichment. Consequently, the present results suggest that phytoplankton-regulated new particle production was more important than sea-spray primary production, for the CCN budget, during the observation period. This is reasonable considering that the campaign was performed in late summer when photochemistry is maximized by high solar radiation and sea-spray production is at its yearly minimum, due to the seasonal minimum of wind speed (Ovadnevaite et al., 2014; Rinaldi et al., 2010).

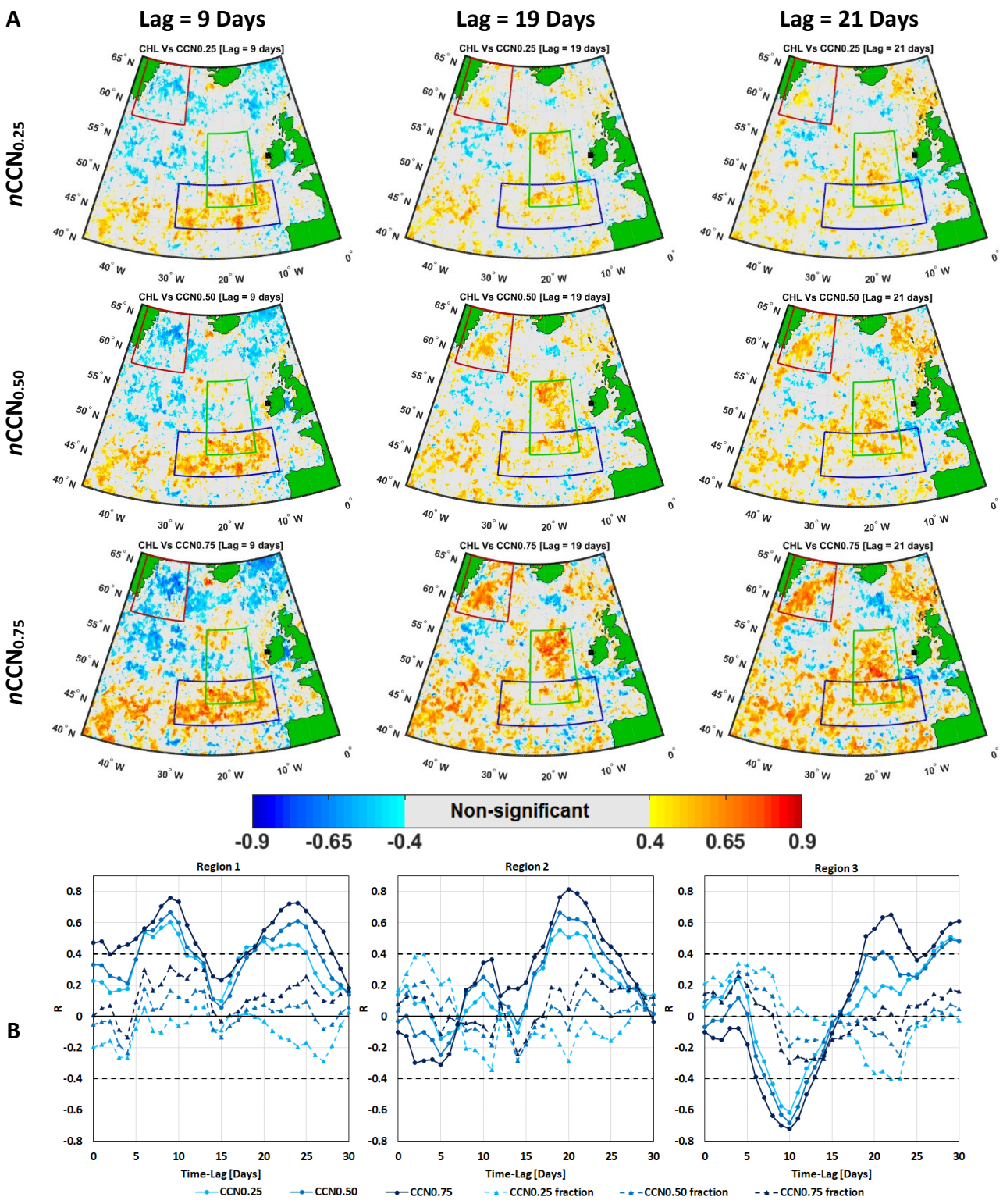

Figure 4.5: a) Examples of correlation coefficient spatial distribution between CCN number concentration at 0.25%, 0.50% and 0.75% supersaturation and CHL over the NA Ocean for different time-lags, considering only clean marine air masses. b) Correlation coefficient as a function of time-lag between mean CHL at different regions and CCN/ CCN fraction concentrations. The black dashed lines represent the critical level of significant correlation at 95% confidence limit.

4.3.4 Ice Nucleating Particles

SSA particles can act as ice nucleating particles (INPs) in clouds. In particular, the attention of the scientific community is oriented toward the organic fraction as responsible for the ice nucleation ability of SSA (McCluskey et al., 2018c; Wilson et al., 2015). The correlations between CHL and *n*INP measured by the DFPC (T_A = –22 °C, S_W = 1.01) were investigated (Figure 4.6) for both the PM_1 and PM_{10} size intervals, revealing that $nINP_{PM1}$ was positively correlated with CHL by applying the time-lag approach.

$nINP_{PM1}$ was statistically significantly correlated after 17 (16) days for Region 1 (2) and at 18 days for Region 3. A lack of a clear relationship between $nINP_{PM10}$ and CHL is found in this study. This suggests that different particle types, with different relations with CHL, are responsible for the INP properties of fine and coarse marine aerosols, as already pointed out by McCluskey et al. (2017). In detail, submicron INPs are linked to phytoplankton exudates enriching sub-micrometer SSA particles, while the ice nucleation properties of the coarse fraction depend on the presence of cells or cell fragments.

It is worth pointing out that a previous publication (McCluskey et al., 2018c) already discussed the relation of the present INP dataset and surface CHL. Said paper concluded that there was no evidence of a significant correlation between *n*INP and CHL over a region roughly resembling Region 2, up to 14 days of delay time. The choice of the delay time interval (0-14 days) was based on Rinaldi et al. (2013) which showed the best correlation between CHL and OM_{SS} occurring with a lag of 8 days. The present work extends the delay time interval up to 30 days and shows how $nIPN_{PM1}$ correlates with CHL with broadly the same behavior as all the previously considered marine aerosol properties.

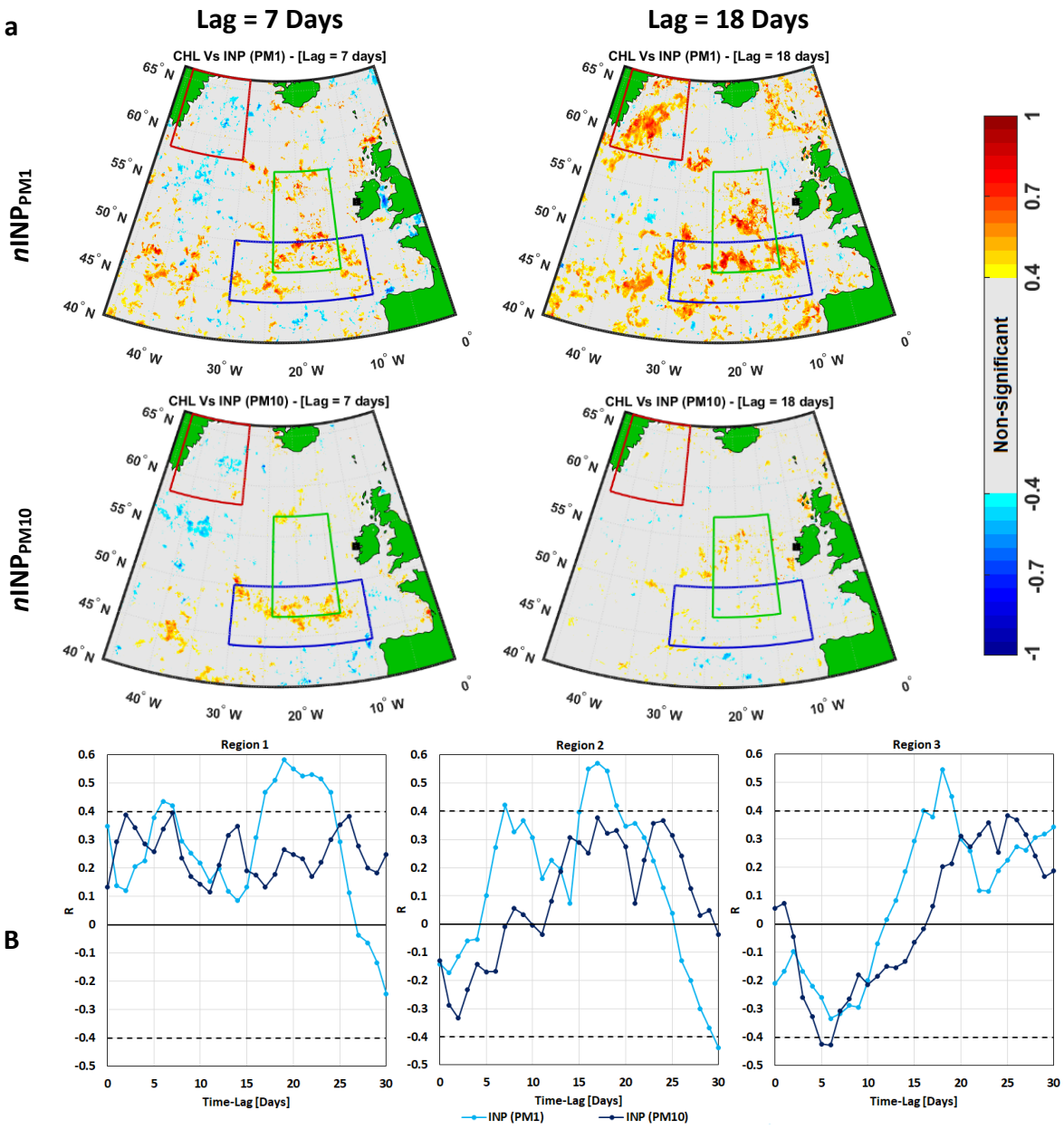

Figure 4.6: a) Examples of correlation coefficient spatial distribution between the number concentration of INPs for particulate matter less than 1 μm/ 10 μm and CHL over the NA Ocean for 7 days (left), and 18 days (right) time-lag, considering only clean marine air masses. b) Correlation coefficient as a function of time-lag between mean CHL at different regions and the concentration of INPs. The black dashed lines represent the critical level of significant correlation at 95% confidence limit.

4.4 Potential Source Contribution Function

An independent attempt at aerosol source identification was carried out by combining the high-resolution aerosol chemical composition and particle number concentration data with 5 days air-mass BTs, following the PSCF approach (Chang et al., 2011). The PSCF maps (Figure

4.7) showed generally consistent features between all the considered aerosol chemical components and number size distribution modes. The most probable source regions of the biogenic aerosol species measured at MHD during the campaign, according to PSCF, were the oceanic region immediately to the west of Ireland and the Northwest oceanic region between Greenland and Iceland. The results of the PSCF analysis are generally in agreement with those of the previously presented spatio-temporal correlation analysis (Sections 4.3.1 and 4.3.2).

In order to facilitate the comparison between correlation maps and PSCF ones, in Figure 4.8, we have evidenced each pixel that has both a PSCF value higher than 0.5, and a significant and positive correlation between aerosol properties and surface CHL, considering every delay time between 8 and 25 days. The ocean region broadly corresponding to Region 2 is clearly indicated as the main source region of the biogenic marine aerosol sampled during the campaign.

The combined analysis also suggests that the region between Greenland and Iceland (matching broadly Region 3) likely exerts some influence on marine aerosol sampled at MHD, in particular for SO_4^{2-}, MSA, OM and Aitken mode particles, while this is less evident for accumulation mode sized particles. We can argue that the contribution of this source region on the aerosol population sampled at MHD is lower than that of Region 2, likely because of the long distance from the receptor site.

PSCF only evidences spots of high probability for Region 1 and, accordingly, only a few sparse spots are evidence by the combined analysis (Figure 4.8), apart for accumulation mode sized particles. This agrees with the previously evidenced low number of BTs connecting Region 1 to MHD, suggesting that the generally well-spread correlation between marine aerosol properties and CHL observed for this Region is likely not entirely due to a cause-effect relation. For this reason, Region 1 will not be considered further on in the text. This does not exclude that Region 1 may have an effect on marine aerosol reaching MHD in other periods/seasons or over different time scales, as pointed out by O'Dowd et al. (2015).

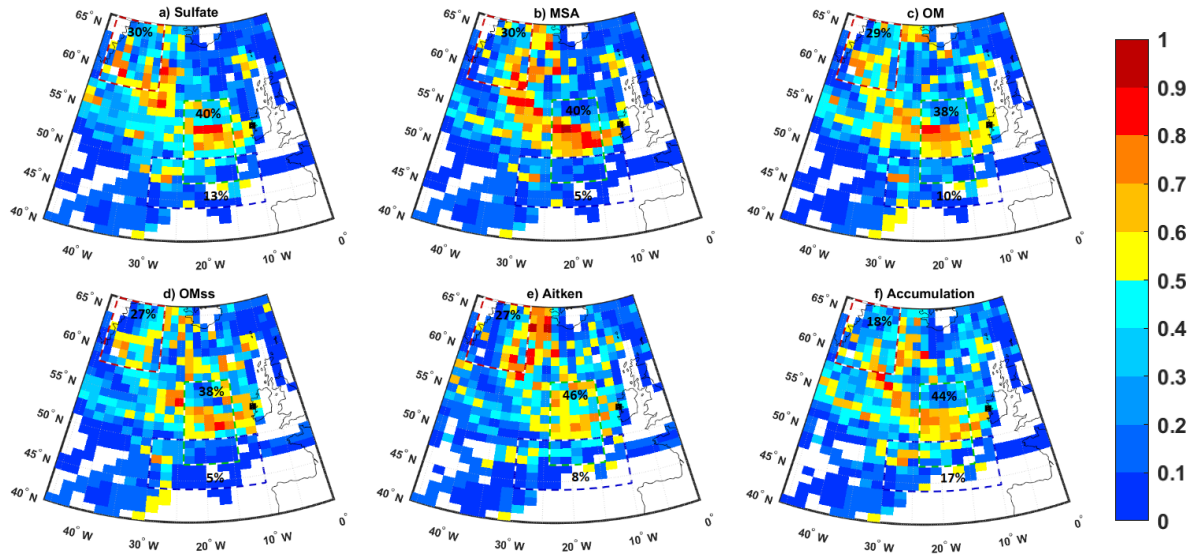

Figure 4.7: PSCF plots for clean marine a) SO_4^{2-}, b) MSA, c) OM, d) OM_{SS}, and e-f) particle member concentration in the Aitken and accumulation modes. The sources of high concentrations are defined above the median values during the period 31st August – 21st September 2015. The percent of grids that have high probability ≥ 0.5 inside each of the three marked regions are inserted.

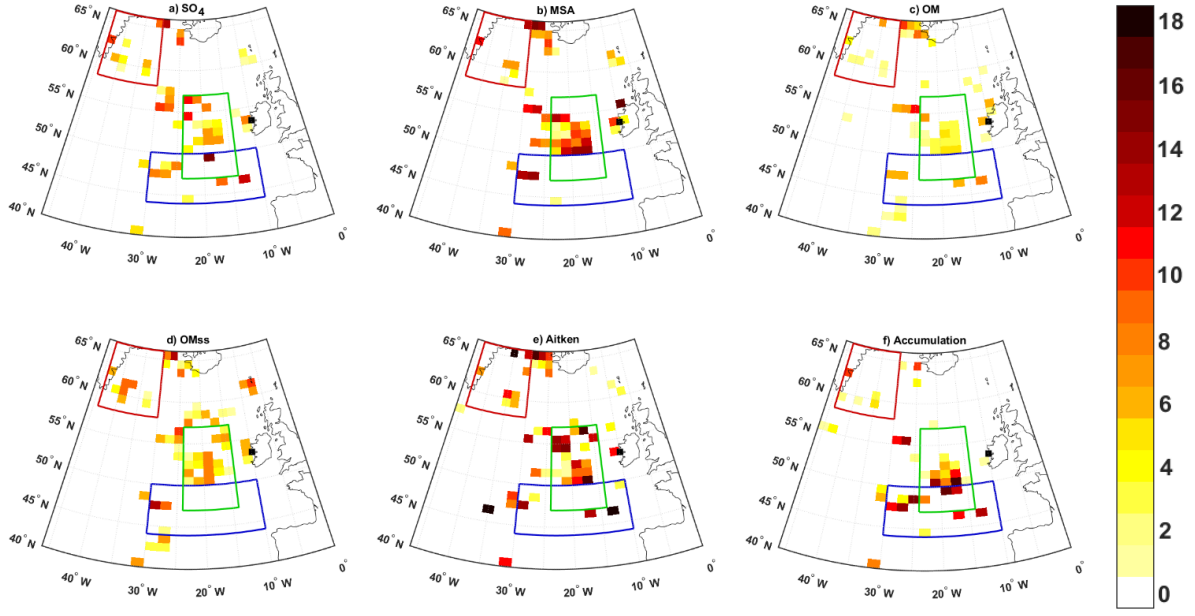

Figure 4.8: Spatial distribution of the aerosol sources identified by merging the results of the spatio-temporal correlation with CHL and of PSCF for a) SO_4^{2-}, b) MSA, c) OM, d) OM_{SS}, and e-f) particle member concentration in the Aitken and accumulation modes. The color scale reflects how many times a given pixel has PSCF ≥ 0.5 and significant correlation coefficient by running time-lags from 8 to 25 days.

4.5 Effect of Meteorology on Marine Aerosol

In order to evaluate the importance of oceanic biochemistry in determining the observed marine aerosol properties with respect to other relevant atmospheric parameters, we evaluated the relationship between aerosol properties and the main meteorological variables over the NA ocean. The fifth generation of ECMWF- ERA5 atmospheric reanalysis data were analyzed to perform a spatio-temporal correlation analysis between in-situ aerosol properties and meteorological parameters over the Eastern NA Ocean domain, similar to that done with CHL. A maximum delay time of 5 days was considered in this case, as no meteorological effect can reasonably go back more than 5 days before aerosol sampling time.

The correlation coefficients between clean marine aerosol properties and the daily mean time series of sea surface temperature (SST), net surface solar radiation (SSR) and wind speed (WS) over Region 2 are listed in Table 4.2, together with the correlation coefficients observed between aerosol properties and CHL in that region to facilitate the comparison.

Over Region 2, the main identified source of biogenic aerosol during the campaign, no meteorological parameter correlated with aerosol parameters better than CHL (apart SS and $n\mathrm{INP}_{\mathrm{PM10}}$ that do not correlate with CHL). In other words, although meteorological conditions can affect the atmospheric concentrations of marine aerosols (both in terms of mass and number), which will ultimately control the number of CCN and INPs, the strongest driver of the aerosol properties during the study period was marine biological activity traced by CHL.

In detail, our results show a significant positive correlation between solar irradiance and both MSA and SO_4^{2-}, as expected for DMS photo-oxidation products. Toole and Siegel (2004) suggested that the net biological production and concentration of DMS in the upper mixed layer is directly proportional to the ultraviolet radiation dose at the surface and to seasonally varying variables such as temperature and solar flux. Our results are supported by Becagli et al. (2013) and Vallina and Simo (2007) who showed a strong correlation between DMS concentrations and the solar radiation dose in the upper mixed layer of the open ocean.

A significant negative correlation was observed between $\mathrm{OM}_{\mathrm{SS}}$ and WS. Previous studies, focused on SSA, interpreted the inverse $\mathrm{OM}_{\mathrm{SS}}$–WS relationship as a result of the surface microlayer disruption occurring at high WS, leading to reduced organic-enrichment in SSA (Gantt et al., 2011; Rinaldi et al., 2013). Considering that we cannot apportion the observed

OM, which may also be contributed by secondary sources (see Section 4.6), we recognize that this correlation may also represent the increase of SS emissions with increasing WS.

The concentration of particle numbers in various modes is positively associated with solar irradiance, thereby demonstrating the significance of processes of secondary aerosol formation during the campaign period.

Table 4.2: Daily correlation coefficients between clean marine aerosol studied variables and meteorological variables over the evidenced source area (Region 2) in the NA Ocean.

Parameter	Sample Number	SST (°C)	SSR (J m^{-2})	WS (m sec^{-1})	CHL (mg m^{-3})
SO_4^{2-}	*n* = 35 *Rc* = 0.33		0.45		0.57
MSA			0.49		0.74
OM			0.35		0.42
OM_{SS}			0.39	–0.35	0.49
NH_4^+		0.36			0.47
SS				0.40	
$N_{20\text{-}100nm}$	*n* = 38 *Rc* = 0.32		0.45		0.64
$N_{100\text{-}500nm}$			0.40		0.45
$N_{20\text{-}500nm}$			0.46		0.66
$nCCN_{0.25}$	*n* = 25 *Rc* = 0.40				0.55
$nCCN_{0.50}$		–0.41			0.67
$nCCN_{0.75}$		–0.40			0.77
$nINP_{PM1}$	*n* = 25 *Rc* = 0.4	0.43			0.54
$nINP_{PM10}$			0.56	0.52	

Note. Consideration is given to the time-lag which maximizes the correlation within 5-days corresponding to the aerosol transport duration. Correlations with CHL are also shown at the same time-lag in spatial correlation maps for comparison with meteorological data. Only significant values ($p < 0.05$) are presented. *Rc* is the critical correlation coefficient and *n* is the number of samples.

4.6 Discussion

Following the combined approach based on back-trajectory analysis, spatio-temporal correlation analysis between in-situ aerosol data and high-resolution satellite ocean color data, and PSCF on the NA Ocean domain allows us to identify the marine regions with the highest probability of being a source of the biogenic aerosol measured at MHD, during summer 2015. The results of spatio-temporal correlation analysis and PSCF are consistent for at least one region within the considered domain. The main source of marine aerosol was the oceanic region facing directly MHD station, roughly within the grids 47° – 57° N and 14° – 30° W (broadly corresponding to Region 2), as pointed out in previous works. Within this oceanic region, the influence of phytoplankton patterns on marine aerosol properties is evident.

The region between the Eastern coast of Greenland and Iceland can probably be considered as a second source region, clearly of minor impact on the sampling site. This latter source region was never evidenced in previous studies based on multi-year CHL correlation, suggesting that the influence of this region may be lower in other periods of the year.

The two considered marine regions are characterized by different patterns in the seasonal cycle of surface CHL as indicated by Lacour et al. (2015) who bio-regionalized the NA Ocean into six clusters based on 17 years of ocean color data. Region 2, in our study, represents the overall subpolar gyre with high phytoplankton biomass during June to September while Region 3 is represented by two clusters characterized by less spatial coherence than the others and with blooming starting early in May. Allan et al. (2015) evidenced that the Eastern coast of Greenland is a hotspot for new particle formation during summer (July and August) due to emissions of iodine from sea-ice associated algal species. The above results may suggest that such particle source can affect the aerosol population also at high distance and at lower latitudes. This may be an interesting topic for future studies.

Analyzing the "correlation vs. time-lag" profiles presented in Figure 4.3, Figure 4.4b, and Figure 4.5b by hierarchical cluster analysis to highlight similarities and differences between them (Table 4.3), it is evident that MSA and SO_4^{2-} (in this order) are the aerosol components with the highest similarity with the total particle and Aitken mode trends. This evidences that secondary marine aerosol components are the most important contributors to the total particle number during the investigated period. This finding is also supported by the

correlation analysis reported in Table 4.4, Figure 4.9 and Figure 4.10. The analysis shows that particle number, in the two considered modes, correlates best with the main tracers of SMA (MSA and SO_4^{2-}), while no correlation is observed with SS (tracer of PMA). The fact that CHL tracks better the atmospheric concentration of smaller particles than accumulation mode sized ones suggests that biological activity emissions have an important impact on new particle formation. This has been already pointed out, for different marine environments, by other studies (Dall'Osto et al., 2017a; Dall'Osto et al., 2018). Wex et al. (2016), Quinn et al. (2017) and Sanchez et al. (2018) obtained similar results over different ocean regions, linking marine CCN to SMA production. In the present campaign, we are not able to partition OM into its primary and secondary components, however, the correlation with SO_4^{2-} (Table 4.4) suggests a significant secondary contribution during the studied period.

Table 4.3 shows that the profile similarity between accumulation mode particle and CCN concentrations decreases with increasing supersaturation. As already discussed, this reflects the major role of Aitken particles to the CCN pool at higher supersaturation, when also smaller particles can activate and is also reflected by the results of the correlation analysis (Table 4.4). Contextually, the CCN correlation profile follows quite well the general profile of OM at low supersaturations, while the similarity with OM decreases with increasing supersaturation. The same is true also for SO_4^{2-}, even though with a lower dependency on the supersaturation. This reflects the major role that chemistry can play in particle activation at low supersaturation, indicating that also the OM fraction can play a potential role in cloud formation, particularly at low supersaturation.

The evidenced link between surface CHL and sub-micrometer INPs proves the potential climate relevance of SSA, even during periods dominated by secondary aerosols. Indeed, the ice nucleation activity of marine aerosol has been related to the organic content of SSA (DeMott et al., 2016; McCluskey et al., 2018a; McCluskey et al., 2018b; McCluskey et al., 2018c; Wilson et al., 2015), while no ice nucleation ability is attributed in literature to secondary (organic or inorganic) particles. Supporting our findings, a relation between algal blooming and ice nucleating properties of SSA has already been reported in the literature (McCluskey et al., 2017; Wilbourn et al., 2020).

Table 4.3: Normalized Euclidean distance (0-1) between the "correlation vs. time-lag" profiles of the considered aerosol parameters for Region 2, deriving from a hierarchical cluster analysis.

	OM	SO_4^{2-}	MSA	NH_4^+	SS	NO_3^-	N Aitken	N Accu.	N Total	CCN 0.25	CCN 0.50
SO_4^{2-}	0.28										
MSA	0.42	0.19									
NH_4^+	0.39	0.29	0.41								
SS	0.60	0.73	0.87	0.62							
NO_3^-	0.76	0.86	1.00	0.69	0.23						
N Aitken	0.39	0.22	0.18	0.39	0.77	0.90					
N Accu.	0.31	0.29	0.30	0.48	0.68	0.85	0.24				
N Total	0.40	0.24	0.17	0.43	0.80	0.94	0.05	0.23			
CCN0.25	0.29	0.29	0.42	0.22	0.61	0.70	0.39	0.43	0.43		
CCN0.50	0.43	0.31	0.40	0.17	0.73	0.79	0.39	0.51	0.44	0.19	
CCN0.75	0.59	0.41	0.43	0.31	0.89	0.94	0.44	0.62	0.47	0.38	0.20

Note. "Zero" indicates coincident profiles, while "One" indicates the maximum observed dissimilarity.

Table 4.4: Correlation coefficients between the considered hourly clean marine aerosol parameters.

	OM	SO_4^{2-}	MSA	NH_4^+	SS	NO_3^-	N Aitken	N Accu.	N Total	CCN 0.25	CCN 0.50
SO_4^{2-}	0.52										
MSA	0.48	0.87									
NH_4^+	0.55	0.87	0.73								
SS				0.13							
NO_3^-	0.30	0.23		0.36	0.43						
N Aitken		0.24	0.37		–0.21	–0.14					
N Accu.	0.72	0.75	0.63	0.67	0.20	0.41	0.20				
N Total		0.33	0.44	0.15	–0.18	–0.08	0.99	0.32			
CCN0.25	0.66	0.67	0.54	0.64	0.13	0.40		0.97	0.11		
CCN0.50	0.62	0.73	0.67	0.71		0.33	0.17	0.90	0.27	0.92	
CCN0.75	0.35	0.58	0.64	0.49	–0.20	0.09	0.74	0.56	0.81	0.60	0.77

Note. All presented values are significant at 95% confidence level.

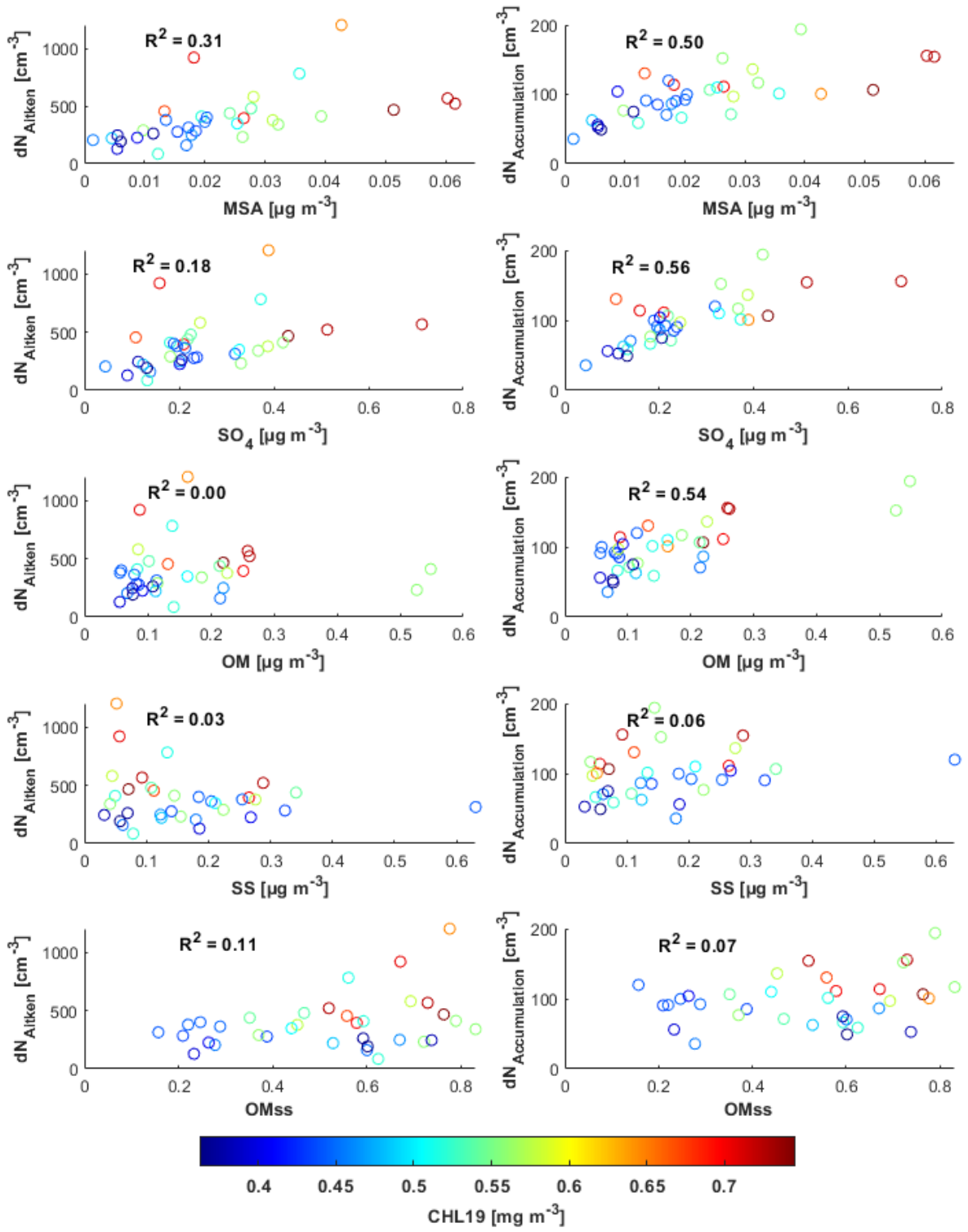

Figure 4.9: Scatter plot between daily mean aerosol chemical composition and particle number concentrations at Aiken/Accumulation modes. The color scale represents the average CHL in Region 2 with 19 day time-lag.

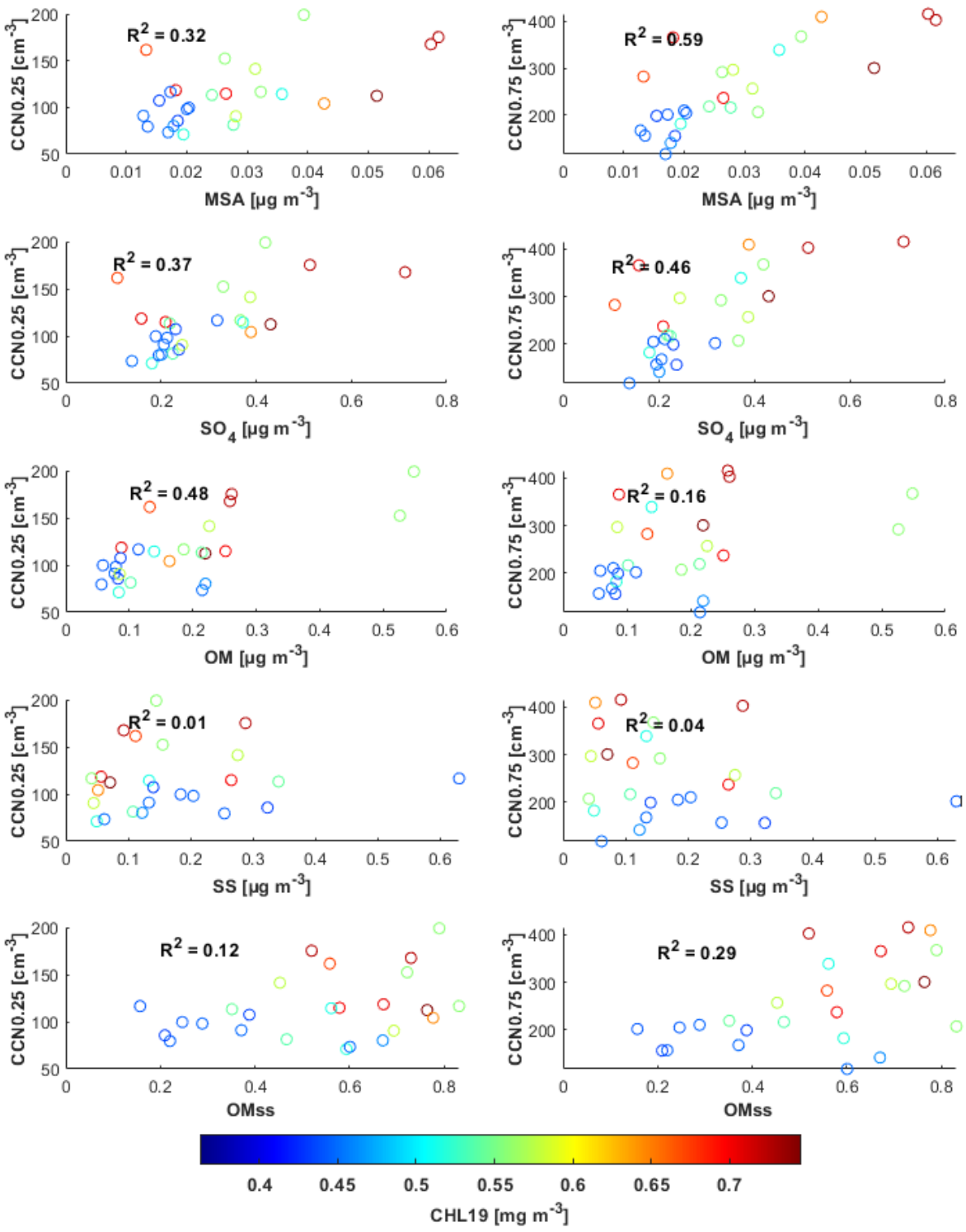

Figure 4.10: Scatter plot between daily mean aerosol chemical composition and CCN number concentrations. The color scale represents the average CHL in Region 2 with 19 day time-lag.

Previous studies pointed out the relationship between the yearly cycle of marine biological activity, as observed by CHL and net primary productivity, and marine aerosol properties over

the NA Ocean (Cavalli et al., 2004; O'Dowd et al., 2015; O'Dowd et al., 2004; Rinaldi et al., 2013; Yoon et al., 2007). In particular, Rinaldi et al. (2013) tried to deconvolute the different time-scales of the signals generating the OM_{SS} vs. CHL correlation over the eastern NA Ocean. They concluded that, although the seasonal signal (variability over one year) played a major role, the observed correlation was also contributed by both short-term fluctuations (*i.e.,* sub-seasonal scale) and interannual variability (*i.e.,* time scale greater than one year). The former was demonstrated to contribute for timescales of 60 and 90 days, while no statistically robust conclusion could be derived for faster fluctuations (one month or less). The present Chapter demonstrates that a relationship between phytoplankton activity and the main aerosol physico-chemical and cloud-relevant properties can be observed also on a short time scale (1-2 months). This correlation is not driven by the seasonal pattern and shows that short time-scale variations in the oceanic biological activity affect aerosol properties quickly, with a delayed response of the order of 10-20 days. This delay coincides roughly with the time necessary to pass from the blooming to the decaying phase of an algal bloom (Lehahn et al., 2014), and has been previously related to the release of SSA-transferable organic matter in surface seawater (O'Dowd et al., 2015; Prather et al., 2013).

These results are broadly similar to those by O'Dowd et al. (2015) which reported a peak in the correlation at 24 days delay time for OM_{SS}, but with a correlation coefficient frequency distribution that was very similar between time-lags of 8, 16 and 24 days. It may also be worth considering that O'Dowd et al. (2015) used a multi-year dataset, while the present Chapter is focused on two months of intensive measurements, representative of late summer. This can explain some of the observed discrepancies as it can be expected that biological and biochemical processes at the sea surface occur at different velocities, in different seasons, depending on biotic (*e.g.,* type of phytoplankton, stress conditions) and abiotic (*e.g.,* sea surface temperature, radiation, wind speed...) conditions. On the other hand, the discrepancy with the results of Rinaldi et al. (2013), which reported maximized correlation at 8 days time-lag, can mainly be explained by the different time resolution of the data: 8-day integrated offline samples against daily observations. In fact, the time resolution of the observations has an impact on the results of the correlation analysis, as shown by O'Dowd et al. (2015).

5. CHL Patterns and Particulate MSA over the Central Mediterranean Sea during Spring 2016

The Mediterranean Sea, surrounded at its northern margin by the highly populated areas of southern Europe and at its southern margin by the African continent, is characterized by high aerosol levels by different sources. It is subjected to a continuous flux of anthropogenic and natural emissions from the ocean and the land. The Mediterranean region is one of the most vulnerable areas to climate change, therefore, it is an interesting area for the study of aerosol processes and aerosol-climate interactions.

Many efforts have been dedicated toward understanding the role of biogenic sulfur particles as a climate regulator. The formation and seasonality of sulfur compounds in both gaseous and particulate phases have been extensively studied in the Mediterranean region (Bardouki et al., 2003; Kouvarakis and Mihalopoulos, 2002; Mihalopoulos et al., 2007; Mihalopoulos et al., 1997). The first measurements of aerosol sulfur species in the Eastern Mediterranean (Crete island) reported that the contribution of biogenic sulfate was between 0.6% and 28.3% with the highest values during summer (Mihalopoulos et al., 1997). Kocak et al. (2004) measured 610 daily aerosol samples on the northeastern Mediterranean coast of Turkey, covering four years (1996-1999) to define the chemical composition of aerosol and its potential source regions. They showed that the MSA displays a seasonal variability, ranging from 0.02±0.03 μg m^{-3} in wet winter (November-February) to 0.05±0.05 μg m^{-3} in dry summer (June-September). In the Western Mediterranean (WMED), two intensive campaigns in the summers of 2009 and 2010 (Schembari et al., 2014) and one campaign in summer 2011 (Bove et al., 2016) were carried out, reporting MSA concentrations of the order of 54 ± 28 ng m^{-3}. These works quantified the biogenic sulfate contribution, based on MSA concentrations, to be more important (26%) than that from dust and sea salt.

The present Chapter aims at investigating the relationship between marine biological activity and the production of biogenic aerosol in the Central Mediterranean Sea by identifying the source regions of MSA, tracer of secondary organic aerosol, observed at a semi-remote coastal location.

5.1 Characterization of MSA at CGR in April 2016

The atmospheric concentration of submicron MSA was measured online by an Aerodyne HR-ToF-AMS during an intensive field campaign carried out between 07 and 25 April 2016 at the Capo Granitola (CGR) Climate Observatory (southern Sicily). Since the MSA fragmentation pattern can be instrument dependent and its quantification method has not been standardized in the HR-ToF-AMS, the online MSA concentrations were validated against offline measurements. Daily MSA concentrations were determined by ion chromatography analysis of PM_1 filter samples, collected in parallel to the mass spectrometry measurements. As presented in Figure 5.1, the online method agreed quite well with the offline MSA filter measurements and any discrepancy was within instrument uncertainties. In this analysis, we have chosen to use online MSA data, instead of the more standard offline ones, as the former provides a higher time-resolution during the campaign.

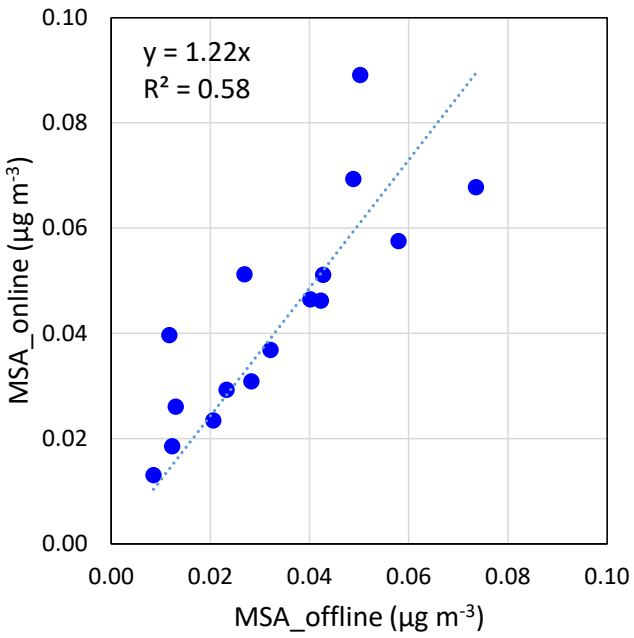

Figure 5.1: Scatter plot between online and offline daily MSA concentrations measured at CGR.

The daily pattern of MSA concentration measured at CGR during the campaign, obtained from 5-minutes time resolution AMS measurements, is presented in Figure 5.2. The mean (± standard deviation) and median of MSA for the entire study period were 0.04 ± 0.02 and 0.033 µg m^{-3}, respectively. The highest MSA concentration was observed on 16 April, while

generally, the first and last parts of the campaign were characterized by lower concentrations. The above MSA concentrations are consistent with those reported by Kouvarakis and Mihalopoulos (2002) and Kocak et al. (2004), for Eastern Mediterranean sites, and within the range of variability for the April month presented by Becagli et al. (2013), in Sicilian Channel.

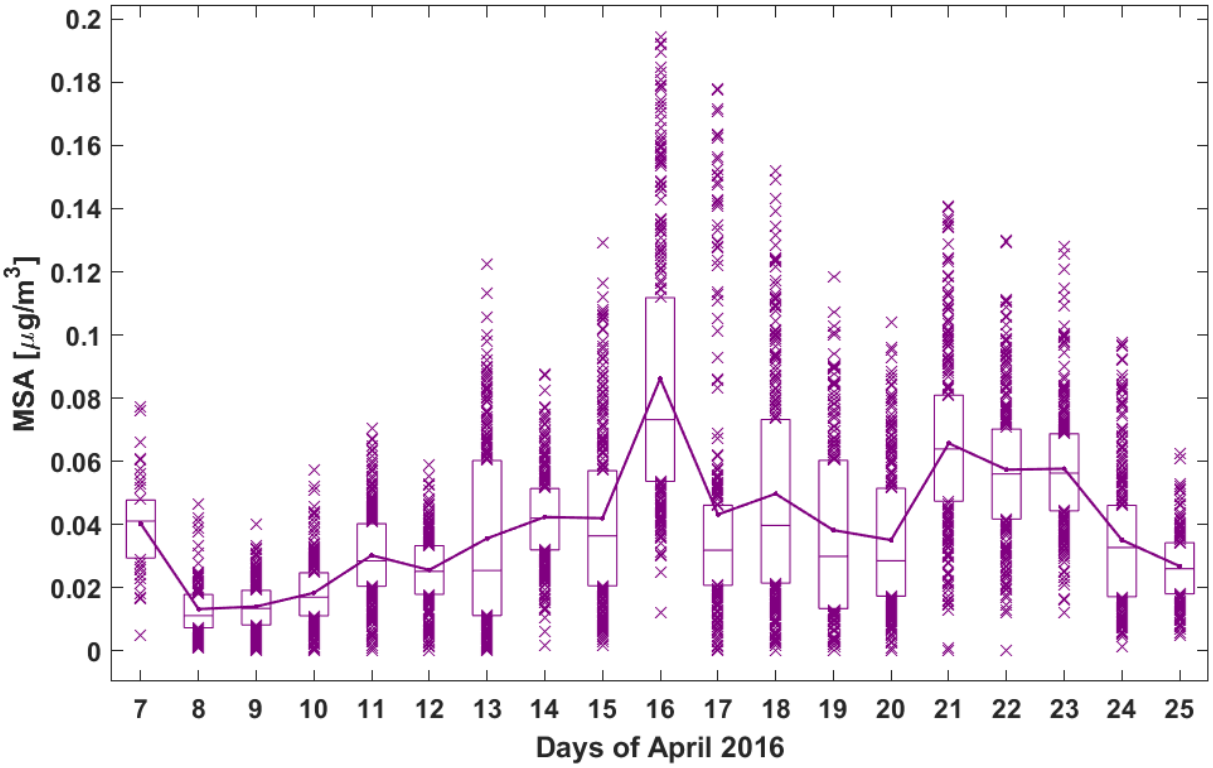

Figure 5.2: Daily Pattern of MSA atmospheric concentration at CGR during 07-25 April 2016. On each box that represents a day, the central line indicates the median, and the bottom and top edges of the box indicate the 25th and 75th percentiles, respectively. The symbol "x" extends to the minimum and maximum data points (5-minute resolution) and the line connects the daily mean.

5.2 Air Mass Back-Trajectories

At CGR sampling station, three-days BTs were calculated four times (00, 06, 12, and 18 hour UTC) a day during the measurement period from 07 to 25 April 2016, arriving at 100 m above the MSL. The BTs (Figure 5.3) show the general circulation of air masses arriving at CGR during the investigated period. Generally, the air masses from either arid regions (Sahara Desert) or from the populated areas of the north and eastern Europe influence the atmospheric environment above the Mediterranean.

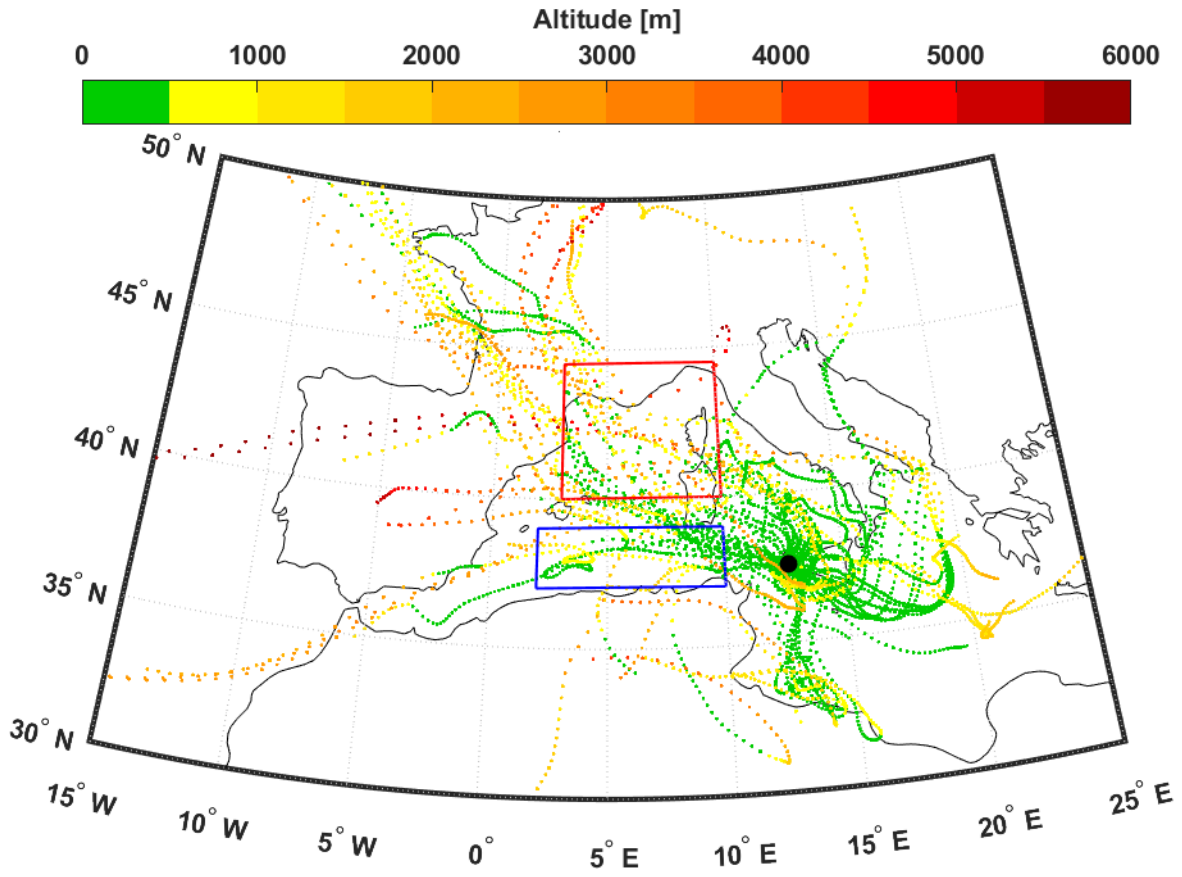

Figure 5.3: The 3-day BTs (hourly time step) calculated by the NOAA HYSPLIT model arriving at CGR at 100 m above the MSL during 07-25 April 2016. The color scale represents the altitude of BT endpoints. The green color shows low BTs (altitude < 500 m). The black circle corresponds to CGR station.

In the following Paragraphs, we will investigate the source regions of the MSA measured at CGR, within the Mediterranean Basin, with the aim of shedding light on the relationship between marine biological activity and secondary organic aerosol production. This will be done by the multi-step approach discussed in Chapter 2.

5.3 MSA Spatio-temporal Correlation with CHL

The spatial distributions of the correlation coefficient (*R*) between MSA atmospheric concentration (daily averages) at CGR and satellite derived CHL seawater concentration, at each grid point of the WMED Sea domain, was calculated, with different time-lags between the two time-series (from 0 to 27 days), as explained in Chapter 2. Examples for two specific time-lags, are shown in Figure 5.4 (full set of maps with all the tested time-lags are presented in Figure S8; APPENDIX). In the maps, the colors represent only positive and significant correlation coefficients ($p < 0.05$). The analysis of the correlation maps obtained with different

time-lags (from 0 to 27 days) between CHL and MSA shows that the maximum correlation is found at two regions in the WMED with different time delays. These regions are consistently located upwind to the sampling point with respect to the main wind direction during the measurement period, as shown by the BTs analysis (Figure 5.3). The two regions are potentially the main sources of DMS that is converted to the MSA observed at CGR during April 2016.

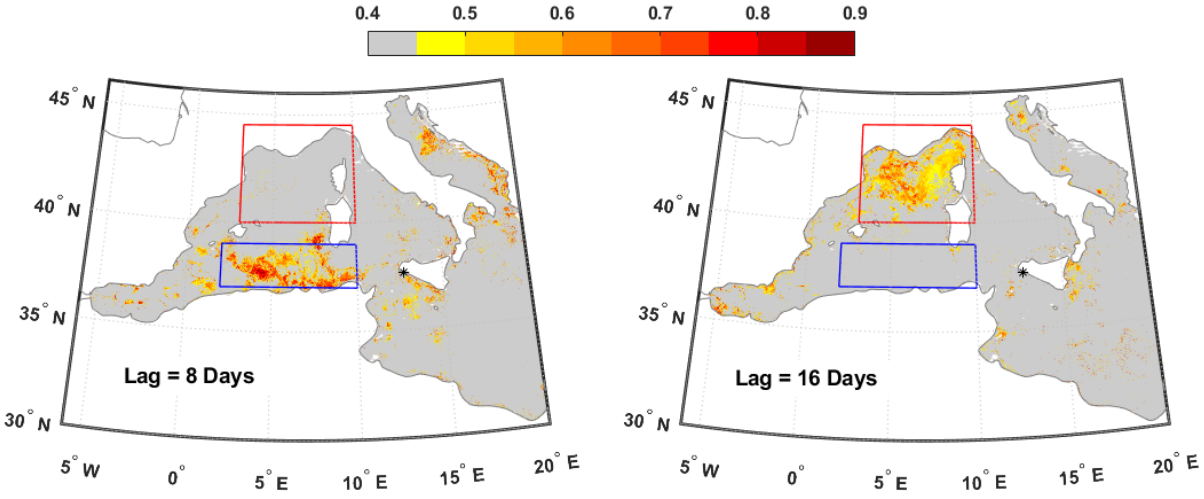

Figure 5.4: Spatial distribution of the correlation coefficient between MSA at CGR and CHL over the Mediterranean Sea for 8 days (left) and 16 days (right) time-lags. The grey color represents negative and non-significant correlation coefficients at 95% confidence level. The black star corresponds to CGR station. The blue box area comprises grid coordinates 37° – 39° N and 02° – 10° E (Region 1) while the red box area comprises grid coordinates 40° – 44.5° N and 03° – 10° E (Region 2). These boxes indicate the area selected to compute the curves presented in Figure 5.5 and the regression lines reported in Figure 5.6.

The first region, in the South WMED (blue box, hereafter denoted as Region 1), comprises the area between 37° – 39° N and 02° – 10° E and shows a maximum correlation at a time-lag of 8 days. About 43% of the pixels within this region show a positive and significant correlation (Figure 5.5b). In the second region (North WMED: 40° – 44.5° N and 03° – 10° E; red box, hereafter denoted as Region 2), the best correlation occurred at 16 days time-lag with approximately the same percentage of significant positive pixels at Region 1. The significantly negative pixels within both regions are very low, approximately 4%, indicating an overall significant positive correlation.

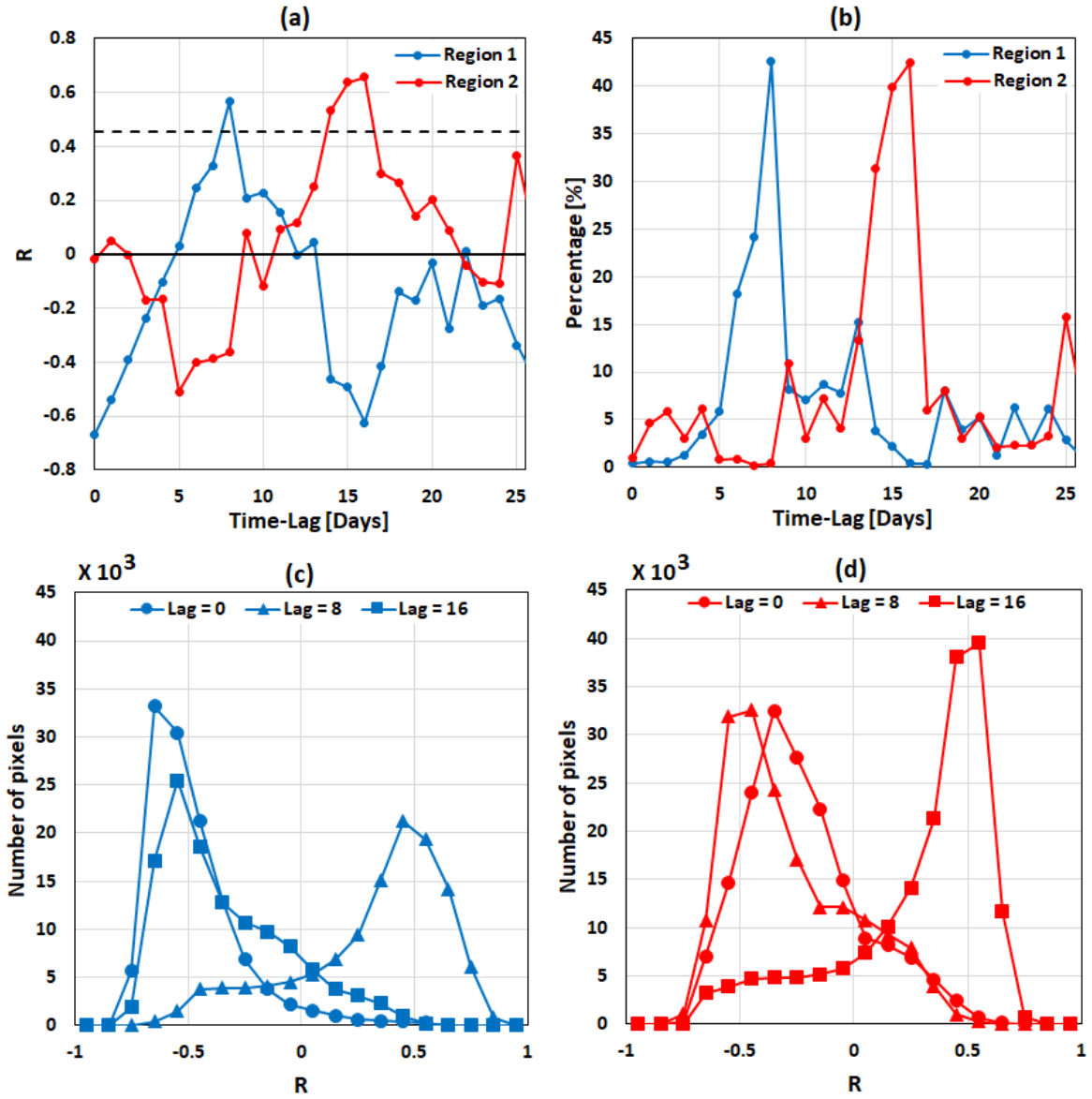

Figure 5.5: **a)** Correlation coefficient between CHL and MSA as a function of the time-lag, the black dashed line represent the critical level of significant correlation at 95% confidence limit; **b)** percentage of the number of pixels with positive and significant correlation in regions of interest; **c)** and **d)** correlation coefficient frequency distribution at areas of interest for time-lags of 0, 8, and 16 days.

The correlation coefficient frequency distributions over both regions separately (Figure 5.5 c & d) for time-lags of 0, 8, and 16 days clearly show the increase in the correlation between CHL and MSA as a function of the considered delay time. The correlation between MSA and CHL over Region 1 increases toward positive correlation from the peak at R = 0.45 up to nearly R = 0.95 at time-lag 8 days. While in Region 2, both amplitude and peak distribution value increases as the time-lag is increased from 0 to 16 days.

In our interpretation, the time-lag between CHL and MSA represents the time scale of the biological processes responsible for the production of DMS in the seawater, together with the physico-chemical processes leading to the atmospheric formation of MSA from DMS. This latter can be estimated in 1-2 days (Barnes et al., 2006; Boucher et al., 2003; Hezel et al., 2011; Kloster et al., 2006). Indeed, it is known from the literature that the release of DMSP (precursor of DMS) is limited for healthy and exponentially growing cells, while high quantities of DMSP are released by stressed or senescent cells (Laroche et al., 1999; Zhuang et al., 2011) and by phytoplankton subjected to grazing (Wolfe and Steinke, 1996) or infected by viruses (Hill et al., 1998). All these processes occur at a later stage than the exponential growth phase and can contribute to the observed time-lag between the CHL time series and in-situ measured aerosol properties. A related point to consider is that the average travel time from the two selected regions to the sampling point is of the order of one day, based on the BTs analysis. Therefore, aerosol transport alone, nor DMS oxidation time, cannot explain the observed delay between the CHL and MSA time series.

Becagli et al. (2013) reported an inverse relationship between monthly CHL and MSA concentrations around Lampedusa Island (Sicily Channel), in the central Mediterranean Sea, studying four years of observations (2005-2008). A similar inverse relationship between DMS and CHL is reported by Toole and Siegel (2004) in the Sargasso Sea and by Vallina and Simo (2007) in the northwestern coastal Mediterranean Sea. These findings are not in contradiction with our hypothesis: the anti-correlation between monthly CHL and MSA (Becagli et al., 2013) was observed in long time scales (multi-years) and it is clearly driven by the different seasonality of the two correlated variables over the Mediterranean Sea. On long time scales (6 months to multi-year) changes in nutrients, light, SST, etc... induce physiological changes in the phytoplankton (so-called photoacclimation, which is particularly strong in the Mediterranean Sea (Bellacicco et al., 2016)), that may modify the relation between CHL and DMS emission. This means that the same value of surface CHL, in two different seasons, can be associated with significantly different DMS fluxes to the atmosphere, making CHL unsuitable as a MSA tracer on the long-term, over the Mediterranean Sea. On sub-monthly time scales, as in this experiment, the variability of oceanic physical parameters is minimized and DMS emissions are primarily modulated by biological productivity. Consequently, we

assume that MSA atmospheric concentrations can be traced back to variations in the sea surface CHL.

The scatter plots between the average CHL (the mean value of all cells) in the maximum correlation areas (Region 1 and Region 2) and MSA reveal a linear relationship as shown in Figure 5.6. The relationships are as follows:

$$MSA = 0.56 \times CHL - 0.032, \quad \text{for Region 1}$$

$$MSA = 0.11 \times CHL - 0.001, \quad \text{for Region 2}$$

The time-lags 8 and 16 days have been considered, respectively for Region 1 and Region 2, for consistency with the above-described results. The inferred regression implies that CHL over Region 1 (Region 2) can describe 32% (43%) of MSA variance observed at CGR.

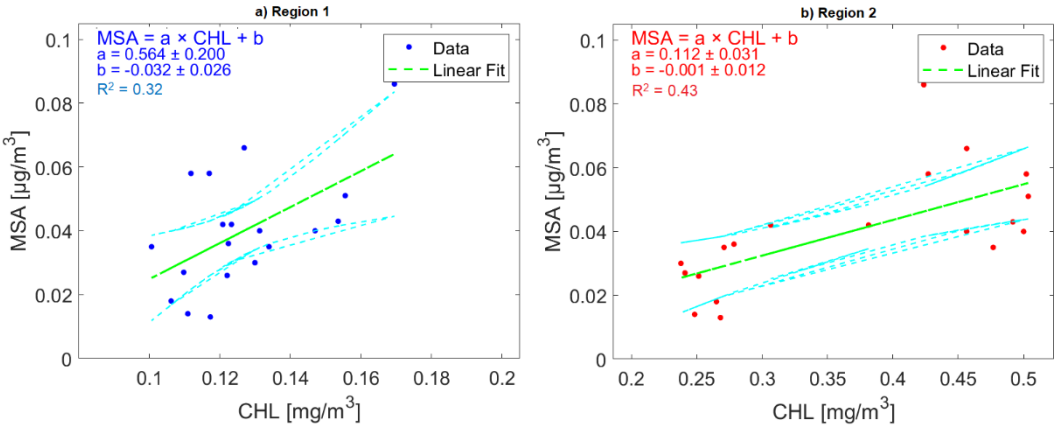

Figure 5.6: Regression curves for CHL and MSA at lag = 8 days in Region 1 (left panel) and, at lag = 16 days in Region 2 (right panel). The correlation coefficients and the best fit line are reported. The cyan curves represent 95% confidence interval. Note that the scale of the x-axis (CHL) is not the same.

In Region 1, the minimum MSA observed value was 0.013 µg m^{-3} corresponding to a CHL of 0.12 mg m^{-3}, while the maximum observed MSA was 0.086 µg m^{-3} corresponding to a CHL of 0.17 mg m^{-3}. In Region 2, more biologically productive than Region 1, the minimum (maximum) observed MSA is equivalent to a CHL of 0.27 (0.42) mg m^{-3}. Region 2 is considered the most productive region over the Mediterranean Sea (Figure 5.7) away from coasts and river discharge input and thus plays a crucial role in controlling the space-time extent of the phytoplankton spring bloom in the Gulf of Lions–Ligurian Sea region (D'Ortenzio and d'Alcala, 2009; Salgado-Hernanz et al., 2019; Volpe et al., 2012; Volpe et al., 2007).

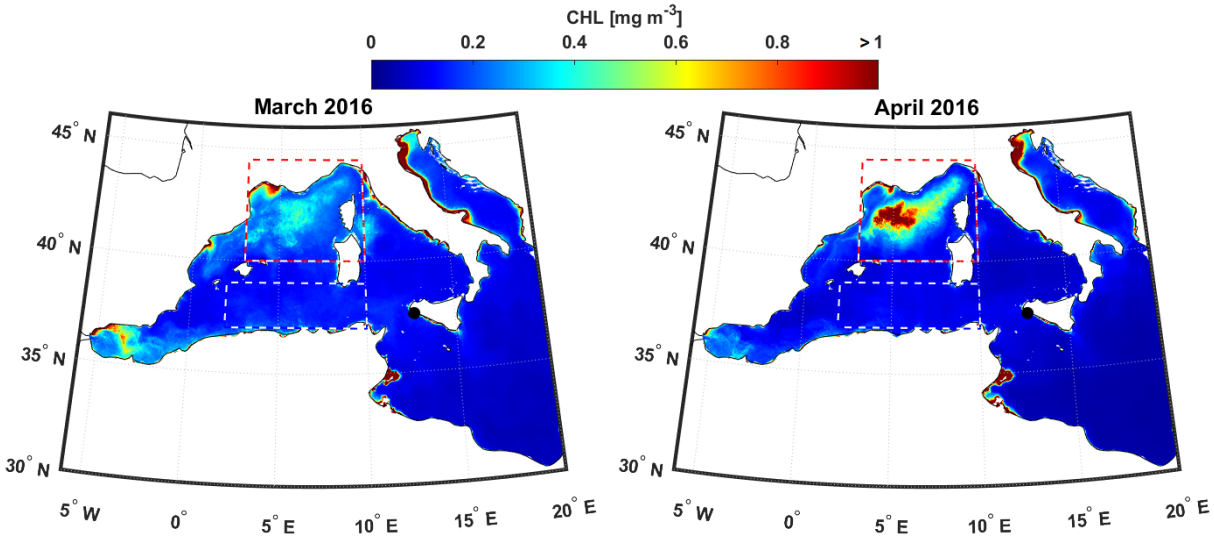

Figure 5.7: Spatial distribution of monthly mean CHL over the Mediterranean Sea during March and April 2016. The spatial resolution of CHL is 1×1 km.

The regression curves presented in Figure 5.6 are only indicative of the general correlation trends over the two Regions (which includes correlating and not-correlating pixels due to the natural variability of the CHL over space), nevertheless the correlation maps (Figure 5.4) are obtained by correlating MSA atmospheric concentration and CHL surface concentration in each single pixel of the domain. These single-pixel correlations do not necessarily reflect the shape of the correlation in Figure 5.6. From the scatter plot (Figure 5.6), it could be assumed that one point (point 10, corresponding to 16 April 2016, hereafter P10) of the dataset is characterized by high MSA and high CHL, drives in some way the correlation and helps to obtain a high and significant correlation coefficient over Region 1. To check this, we run again the correlation analysis over the domain, excluding P10. The resulting correlation maps (Figure 5.8) still identify Region 1 as a potential source region, even though with a lower magnitude of the correlation. This demonstrates that, although the high MSA concentration observed on 16 April (P10) improves the correlation with CHL when considering a delay time of 8 days, the general correlation trend between the two variables is evident also without this point.

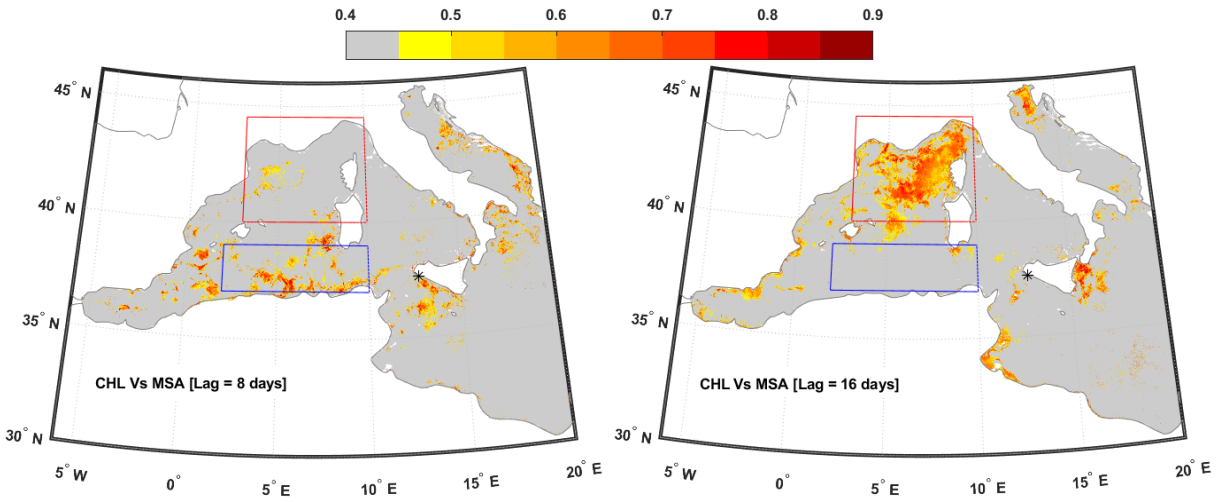

Figure 5.8: Spatial distribution of the correlation coefficient between MSA at CGR and CHL over the Mediterranean Sea for 8 days (left) and 16 days (right) time-lags without uncertain point (16 April 2016). The grey color represents negative and non-significant correlation coefficients at 95% confidence level.

5.4 MSA Source Regions

The high time-resolution MSA data were combined with air-mass BTs calculated four times per day during the sampling period (Figure 5.3), following the PSCF method (Chang et al., 2011). The MSA data were averaged over 6 hours periods (3 hours before and after the arrival time of each back trajectory) to associate one MSA concentration value to each trajectory. PSCF allows a geographical source attribution for high-resolution aerosol data, showing the pixels associated with the highest concentrations (defined in this Chapter as above the median and the third quartile), that correspond to the probable source regions. In other words, PSCF provides another way of assessing MSA sources over the Mediterranean basin for the investigated period, alternative to and completely independent from the statistical analysis presented in the previous Section.

We point out here that PSCF was run by considering 3-days BTs, which is a time frame adequate to track air mass transport across the Mediterranean basin, as demonstrated by Figure 5.3. This three-days' time frame is not related to the time-lag considered in the "MSA vs. CHL" correlation analysis. As already addressed, in the regression analysis, the time-lag serves to phase the CHL time series with the MSA one. In other words, the time-lag in the correlation approach refers mainly to processes occurring before the formation of MSA from

its precursor DMS, while the three days considered in the PSCF approach regard the transport of MSA (after its formation) to the receptor point.

The analysis (Figure 5.9) shows that the most probable homogeneous source region for the measured MSA is the south WMED Sea, along with some spots around Sicily, mainly due to coastal production. When looking at concentrations above the third quartile (Figure 5.9b), source areas tend to concentrate over the sea region between Sardinia and the Algerian coast, which corresponds to Region 1. This result confirms that Region1 is likely the most important source area of MSA observed at CGR during the campaign, while Region 2 is not confirmed as a source region by PSCF.

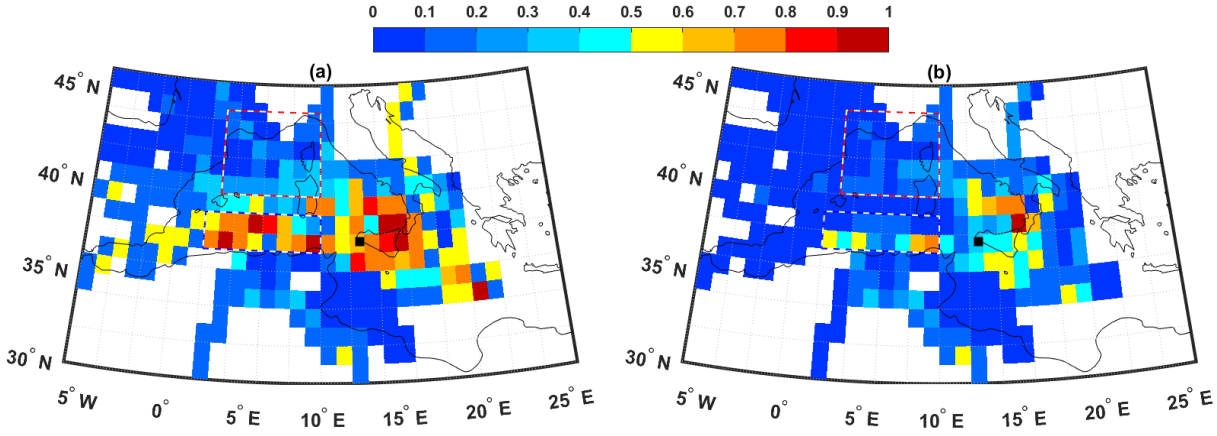

Figure 5.9: PSCF plots for MSA in the period 07th-25th April 2016. The source of high MSA concentrations is defined as above the median (left) and the third quartile (right). The Mediterranean domain is divided into 1° × 1° latitude/longitude grid cells. The color scale represents the probability from 0 to 1.

The altitude of the BTs passing over Regions 1 and 2 was analyzed, in order to assess if this can explain the discrepancy of results between PSCF and CHL correlation analysis regarding Region 2. Indeed, BTs over Region 2 tend to pass at a higher altitude compared to Region 1 (50% of BTs pass lower than 1000 m over Region 2, compared to 89% over Region 1; as shown in Figure 5.3), even though low-passing BTs are not negligible in Region 2. The PSCF run only on low BTs (< 500 m height) shows that most of the BT endpoints in Region 2 do not ever associate with MSA concentrations above the median (Figure 5.10), confirming that Region 2 was not a hotspot for MSA production during the campaign. It is clear that a few low BTs passing through Region 2, most of them do not coincide with high MSA measured at CGR during the campaign.

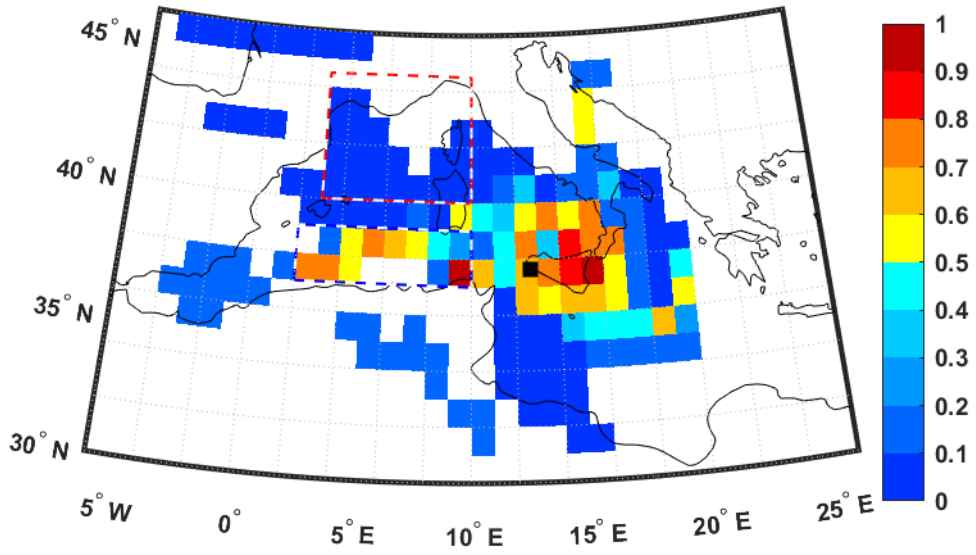

Figure 5.10: PSCF map by using low BTs (< 500m height) and the median of MSA as a threshold.

5.5 MSA Spatio-temporal Correlation with PHYC

Although CHL is the most widespread proxy of the algal biomass concentration in seawater, its retrieval does not take into account the physiological adjustments that phytoplankton undergoes in response to changes in light and nutrient conditions (Bellacicco et al., 2016; Halsey and Jones, 2015), leading to potential biases in the estimation of the biomass trends. For this reason, Behrenfeld et al. (2005) developed an alternative algal biomass concentration index, in terms of total phytoplankton carbon (PHYC).

PHYC data (Calculations details are presented in Section 2.3) over the Mediterranean Sea are combined with MSA data at CGR, following the same approach as for CHL data, to check if a different proxy for algal activity could lead to different results. It is worth highlighting that here we use the PHYC-MSA correlation only in a qualitative sense, to compare with the above results, as the low quality of PHYC data is a limiting factor in studying its relationship with MSA. The estimation of PHYC biomass and its physiological status with a high resolution from space has remained so far, an elusive target (Behrenfeld et al., 2005; Bellacicco et al., 2016).

A significant correlation between PHYC and MSA has been found, with time-lag about 6-9 days, mainly over Region 1, as shown in Figure 5.11. These results support those obtained by CHL-MSA correlation maps and PSCF algorithm, which point to Region 1 as potentially the main source of MSA observed at CGR during the Spring campaign.

Despite the results of Becagli et al. (2013), which showed a better correlation between the P^B index (ratio of algal Carbon and CHL) and MSA than CHL vs. MSA, the corresponding derived phytoplankton physiology index PHYC:CHL ratio, from satellite data, does not show a significant correlation with MSA in the evidenced two Regions as shown from correlation maps in the APPENDIX (Figure S9). We cannot, however, exclude that, with future improvements in ocean color remote sensing and algorithm development, PHYC and PHYC:CHL ratio may become a better surrogate of algal activity in this kind of approach.

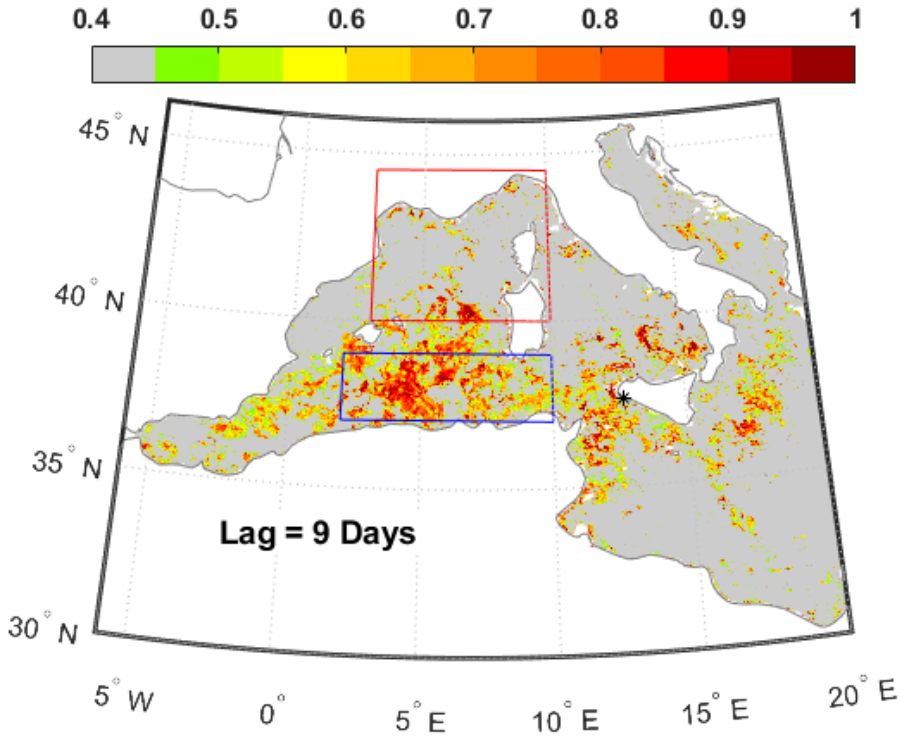

Figure 5.11: Spatial distribution of the correlation coefficient between MSA at CGR and PHYC over the Mediterranean Sea for 9-days time-lag. The grey color represents negative and non-significant correlation coefficients at ($p < 0.05$). Regions 1 (blue box) and 2 (red box), as well as CGR station (black star) are shown.

5.6 Discussion

The results of the combined approach (BTs analysis, spatio-temporal correlation analysis, and PSCF) point to the south WMED Sea, particularly the region between Sardinia and the Algerian coast, as the most likely source of MSA measured at CGR during April 2016. This source is at a greater distance upwind the Sicilian Channel from the sampling location than previously estimated (Becagli et al., 2013). Considering that a significant fraction of aerosol

MSA can be found in the sub-micrometer size range (Rinaldi et al., 2010; Watts et al., 1990), long-range transport of MSA within the Mediterranean basin is clearly possible. The removal of MSA from the atmosphere is carried out mainly through wet and/or dry deposition with a lifetime estimated to be about one week (Gondwe et al., 2003; Hezel et al., 2011).

The role of Region 2 as MSA source, evidenced by the correlation with CHL, is clearly not supported by the PSCF approach nor by the correlation with PHYC. Interestingly, Region 2, roughly corresponding to the Gulf of Lion–Ligurian Sea region, is considered the most biologically productive region of the Mediterranean Sea (Figure 5.7), away from coasts and river discharge (D'Ortenzio and d'Alcala, 2009; Salgado-Hernanz et al., 2019; Volpe et al., 2012; Volpe et al., 2007) and it is characterized by an intense phytoplankton bloom in springtime.

In order to assess the reasons why this highly biologically productive region is not contributing significantly to the MSA atmospheric burden as observed at the sampling location, reanalysis meteorology data (ERA5; (C3S, 2017)) were analyzed to evidence the main differences between Region 1 and Region2. The daily mean time series (Figure 5.12) of wind speed (WS), sea surface temperature (SST), net surface solar radiation (SSR) and relative humidity (RH) in Region 1 and Region 2 show that all the parameters are basically identical between the two regions, with the exception of SST. On the time scale of our study, a positive and significant correlation is found between MSA concentration and SST (together with SSR and RH, as presented in Table 5.1. This agrees with the fact that warmer SST leads to enhanced phytoplankton growth and consequently enhances DMS emission (Kim et al., 2018). In addition, warmer SST may enhance the degassing of DMS to the atmosphere. Indeed, the difference in SST could explain why Region 1 emits significant amounts of DMS (acting as MSA source) while Region 2 does not. This would also suggest that Region 2 may become more important for the Mediterranean aerosol MSA budget later on in the summer when SST increases at higher latitudes.

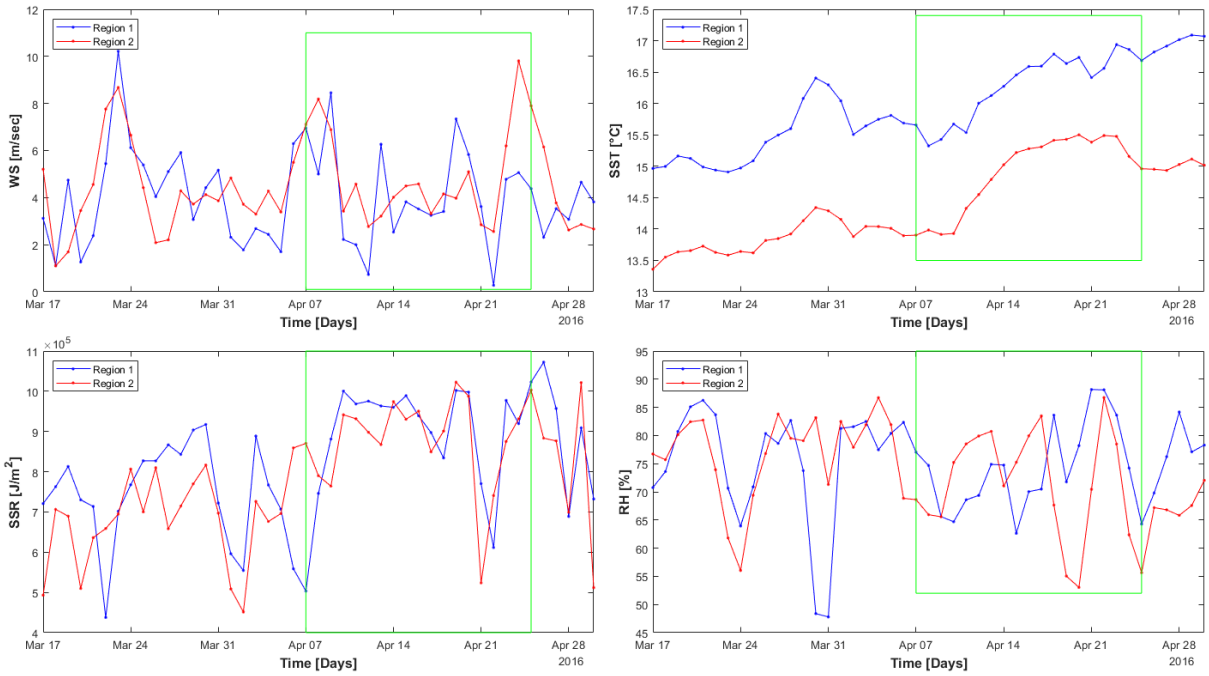

Figure 5.12: Daily time series of the average main meteorological data (ERA5) over Region 1 and Region 2 (boxes of interest). The green box represents the period of spring 2016 campaign.

Table 5.1: Daily correlation coefficients between MSA measured at CGR and the atmospheric components over the interesting regions in the Mediterranean Sea.

	Samples Number	WS	SST	SSR	RH	CHL
Region 1	***Daily***	–0.28*	0.6	0.64	0.52	0.56
Region 2	***n* = 19; R_c = 0.45**	–0.51	0.67	0.58	0.36	0.66

Note. R_c is the critical correlation coefficient and *n* is the number of samples. *represents non-significant values at 95% confidence level. The meteorological data are extracted from global ERA5 with spatial resolution 0.25° × 0.25°.

The significant correlation observed between MSA concentration and net surface solar radiation is in line with previous observations by Toole and Siegel (2004), Becagli et al. (2013) and Vallina and Simo (2007) who showed a strong positive correlation between DMS and the solar radiation dose in the upper mixed layer of the open ocean. Nevertheless, given the lack of significant differences in this parameter between the two Regions, SSR cannot explain the difference in DMS/MSA production.

Apart from physical (abiotic) parameters, the different DMS/MSA productivity of the two considered regions may be due also to differences in the biological communities and biochemical conditions characterizing the two marine areas. There is plenty of evidence in the recent literature that the Mediterranean Sea can be divided into different bioregions (Basterretxea et al., 2018; D'Ortenzio and d'Alcala, 2009; Lavigne et al., 2013; Navarro et al., 2014; Salgado-Hernanz et al., 2019; Sammartino et al., 2015) characterized by different CHL seasonality, phytoplankton population and ecological succession. The analysis performed by Basterretxea et al. (2018), based on neural network classification of 17 years of ocean color data, clearly shows that Regions 1 and 2 belong to different bioregions, with consequent diversity in the phytoplankton community composition. Based on the monthly maps of phytoplankton functional type distribution over the Mediterranean Sea by El Hourany et al. (2019), during April, the dominant phytoplankton functional type is Synechococcus, with a minor contribution from Haptophytes in Region 1 and Diatoms in Region 2. The DMSP content of phytoplankton cells, related to DMS emissions from the sea surface after DMSP excretion and processing, differs markedly between different phytoplankton types (Gali et al., 2013; Keller et al., 1989; McParland and Levine, 2019) and may also vary significantly depending on the stress level. The above evidence suggests a possible biotic reason at the base of the observed diversity in DMS/MSA production between the two considered sea regions.

6. Impact of the Marine Biota on the INP Concentration over the Arctic: The Case Study of Ny-Ålesund (Svalbard) 2018

Not many measurements of Ice Nucleating Particle (INP) concentration exist in the Arctic at present; however, these particles play a fundamental role in the lifetime and radiative effects of Arctic stratiform clouds (Prenni et al., 2007; Wex et al., 2019). These clouds are often mix-phase and structured in persistent layers (Choi et al., 2010; Costa et al., 2017; Shupe et al., 2006; Shupe et al., 2011) and play a key role in the "Arctic amplification", i.e., the phenomenon by which the Arctic is warming much faster than the global average. A better knowledge of INP sources and dynamics over the Arctic is necessary for a better understanding of northern high latitudes climate and of the "Arctic amplification" itself.

An INP measurement program was started by CNR-ISAC at the Gruvebadet observatory (GVB), located in proximity of the village of Ny-Ålesund (78° 55' N, 11° 56' E) on the Spitsbergen Island in 2018. Here, we analyse the results of the spring and summer campaigns performed during the first year of activity, to investigate the potential impact of the marine biota on the INP concentration (*n*INP) in the Arctic atmosphere. Details on sampling and on the INP measurement technique can be found in Chapter 2.

6.1 Characterization of INP at GVB in 2018

Sampling for the Dynamic Filter Processing Chamber (DFPC) occurred on an intensive campaign basis. The spring campaign occurred between 17 April and 2 May 2018, while the summer campaign covered the period between 11 and 27 July 2018. Considering the whole investigated size range (PM_{10}), INP concentrations measured at Ny-Ålesund by DFPC, in conditions of supersaturation with respect to water (immersion plus condensation freezing), during the spring campaign, ranged 55-185 (median 115), 5-90 (53) and 3-37 (20) m^{-3}, for activation temperature (T_A) equal to –22, –18 and –15 °C, respectively. During the summer campaign, the concentration ranges were 33-135 (median 77), 18-107 (45) and 6-66 (20) m^{-3}, for the same activation temperatures (Figure 6.1).

INP concentrations reported in literature from ground-based observations are roughly comprised between 10^{-2} m^{-3} and 10^{3} m^{-3} (Bigg, 1996; Bigg and Leck, 2001; Borys, 1983; Conen

et al., 2016; Creamean et al., 2018; Irish et al., 2019; Mason et al., 2016; Si et al., 2018; Wex et al., 2019). Given this variability of results, certainly related to the great variability of parameters that can influence the results of INP measurements (different instruments, locations, seasons, weather conditions, ice nucleation modality, etc.), we can conclude that the results of the present study are generally consistent with literature.

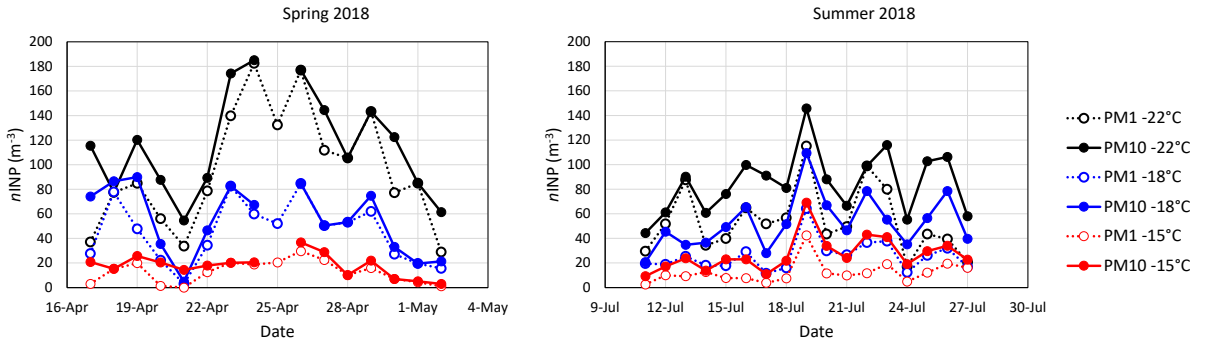

Figure 6.1: Time series of $n\text{INP}_{PM10}$ measured at GVB during spring and summer 2018.

INP concentrations observed at GVB present the typical dependency on T_A, with concentrations raising with reducing the activation temperature. Figure 6.2 shows that spring samples have a steeper temperature dependency with respect to summer ones. This suggests that the INP populations may consist of particles with different characteristics in the two seasons. This is reasonable as typically the Arctic atmosphere is influenced by long range transport of aerosol particles from lower latitudes during springtime, the so-called Arctic haze (Heidam et al., 1999; Shaw, 1995; Stohl, 2006). Conversely, local sources tend to be more important in summer, especially after snow and ice melting, which allows more interactions between glacial soils and seawater with the atmosphere (Tobo et al., 2019).

The sampling strategy adopted for DFPC measurements (parallel PM_1 and PM_{10} sampling) allowed a basic investigation of the INP size dependency. Table 6.1 reports the number concentrations of INPs measured in the two different size ranges, together with the average contribution of super-micrometer (coarse) INPs, derived by difference. A small contribution from coarse INPs characterized the spring campaign (~ 20%), suggesting that the dominant INP sources may be located at long distances (scale of the order of 100s-1000s km), with consequent depletion of the largest particles during transport, due to their higher gravitational deposition velocities. This result is consistent with previous works highlighting

the contribution of long-range transport from lower latitudes during the Arctic spring (Heidam et al., 1999; Shaw, 1995; Stohl, 2006).

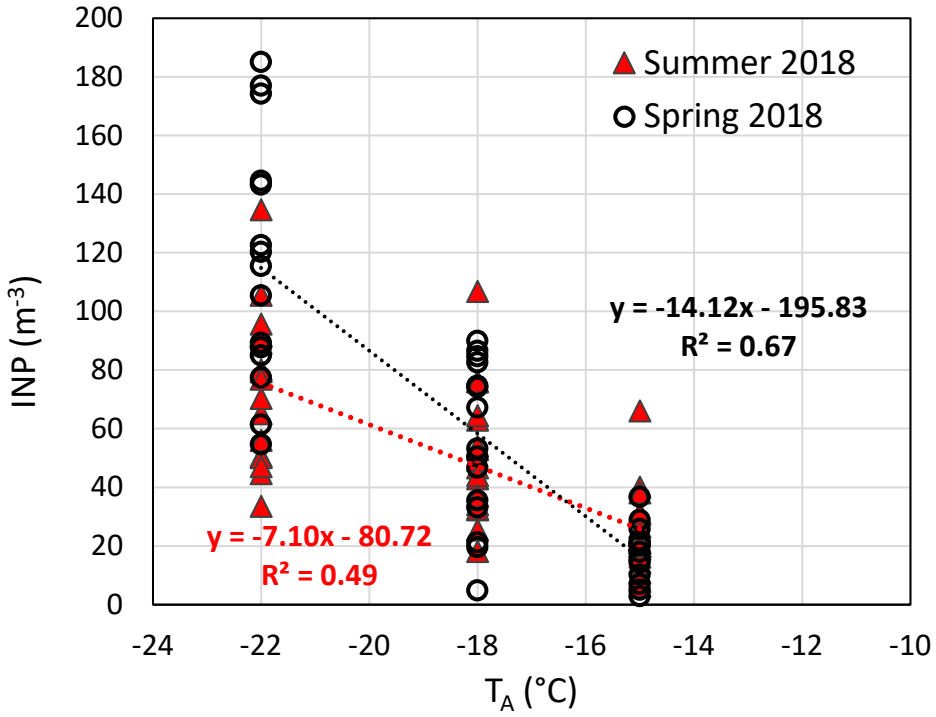

Figure 6.2: Atmospheric concentration of nINP$_{PM10}$ as a function of the activation temperature measured at GVB during spring and summer 2018.

During the summer campaign, a significant ($p < 0.05$) increase of the contribution of coarse INPs was observed (from ~ 50% at T_A = –22 °C to ~ 70% at T_A = –15 °C), likely resulting from the activation of local sources after snow and ice melting. Furthermore, the increase of coarse INP contribution, from spring to summertime, is progressively more pronounced with increasing activation temperature, which may suggest a significant contribution of biological coarse particles during summer. Indeed, bioaerosol are usually associated to ice nucleation at relatively warm temperature [–15 °C or higher] (Conen et al., 2011; Frohlich-Nowoisky et al., 2015; Hoose and Mohler, 2012; Murray et al., 2012; O'Sullivan et al., 2014; O'Sullivan et al., 2015; Tesson and Santl-Temkiv, 2018) and a prove that bio-materials can contribute to the Arctic INP population was recently presented by Santl-Temkiv et al. (2019). On the other hand, mineral particles tend to be efficient ice nucleators at lower temperature [–22 °C or lower] (DeMott et al., 2010; Hoose and Mohler, 2012; Kanji et al., 2017; Murray et al., 2012). Similar

results were reported by Mason et al. (2016) for Alert Arctic station, including the increasing coarse INPs contribution as a function of the activation temperature.

Table 6.1: Average (± standard deviation) and median (in brackets) INP concentrations measured at GVB during 2018.

T_A		Spring	Summer
–22 °C	PM_1 [m^{-3}]	97±48 (85)	43±27 (38)
	PM_{10} [m^{-3}]	116±42 (115)	74±26 (77)
	Coarse contribution [%]	21±22 (20)	45±24 (48)
–18 °C	PM_1 [m^{-3}]	45±25 (49)	23±13 (23)
	PM_{10} [m^{-3}]	55±28 (53)	50±22 (47)
	Coarse contribution [%]	20±20 (17)	53±17 (58)
–15 °C	PM_1 [m^{-3}]	13±9 (14)	9±9 (7)
	PM_{10} [m^{-3}]	18±9 (20)	24±14 (20)
	Coarse contribution [%]	32±36 (22)	65±23 (72)

An important parameter to be considered when analysing INP data is the activated fraction (AF), calculated as the number of INPs divided by the total particle number. In this case, we selected particles with aerodynamic diameters larger than 500 nm, as this range is thought to be more influential for ice formation in the atmosphere (DeMott et al., 2010). Although the INP concentrations do not differ much between the two campaigns, a significant increase of the AF can be observed passing from spring to summer (Figure 6.3). Furthermore, the spring-to-summer AF increase is progressively more evident at T_A = –15 °C (4 times, as median ratio) than at T_A = –22 °C (2 times). This result shows that local aerosol particles are particularly efficient in nucleating ice at warm temperatures and that Arctic Haze (anthropogenic) aerosol has a lower ability to nucleate ice than local particles. This conclusion was first derived by Borys (1983, 1989) and was recently confirmed by Hartmann et al. (2019), which showed a low impact of anthropogenic emissions over the INP concentration with respect to the preindustrial period, through the analysis of ice core records.

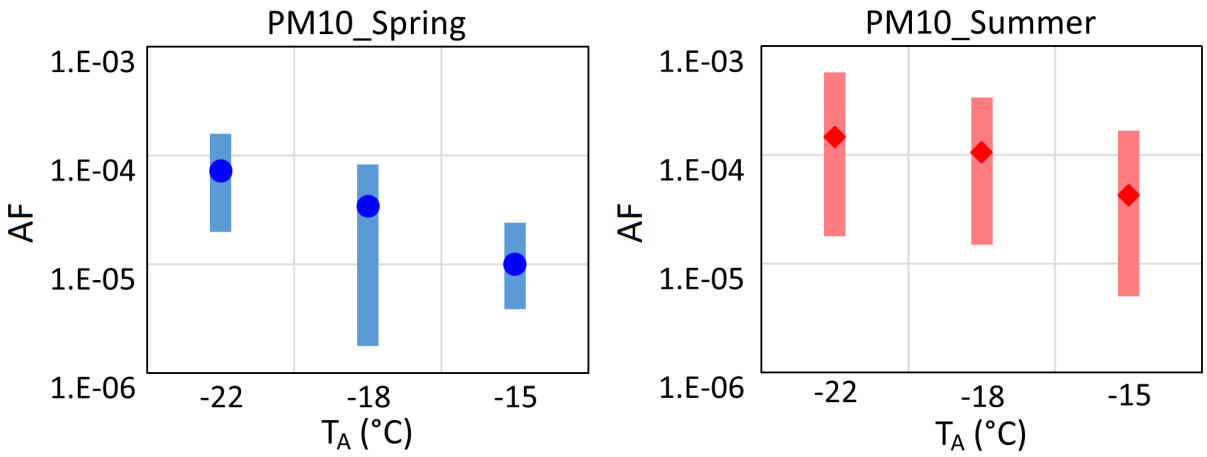

Figure 6.3: Activated fraction of INPs concentrations measured at GVB during 2018.

Analysing the patterns of the main meteorological parameters (T, P, RH and WS) in relation to *n*INP, no clear relation emerges. We note anyways that precipitation events were sometimes associated to a reduction of the INP concentration, without resulting in a significant correlation.

The above collection of results suggests that two distinct aerosol populations contribute to the INP burden over the sampling site in spring and in summer. Springtime aerosol is mainly influenced by long range transport of particles from lower latitudes, including anthropogenic aerosols, while summertime INPs are probably emitted by local sources with a potentially important contribution by biological materials. Among the possible summertime local sources of INPs, recent works evidenced both terrestrial (Creamean et al., 2018; Irish et al., 2019; Si et al., 2018; Tobo et al., 2019) and marine sources (Bigg, 1996; Bigg and Leck, 2001; Creamean et al., 2018), even though a clear proof that biogenic materials associated to sea-spray particles may contribute to the INP properties of Arctic aerosol is still missing.

6.2 Back Trajectories and Influence of Ground Conditions

The ground types over which air masses travelled in the 5 days before arrival at GVB station were identified, following Wex et al. (2019). Ground conditions (seawater, sea-ice, land and snow) corresponding to the collected INP samples were evaluated by merging 5-day BTs, as shown in Figure 6.4, and satellite snow and ice coverage data (Section 2.6). Only low crossing air masses, up to an altitude of 500 m above MSL were considered for this analysis.

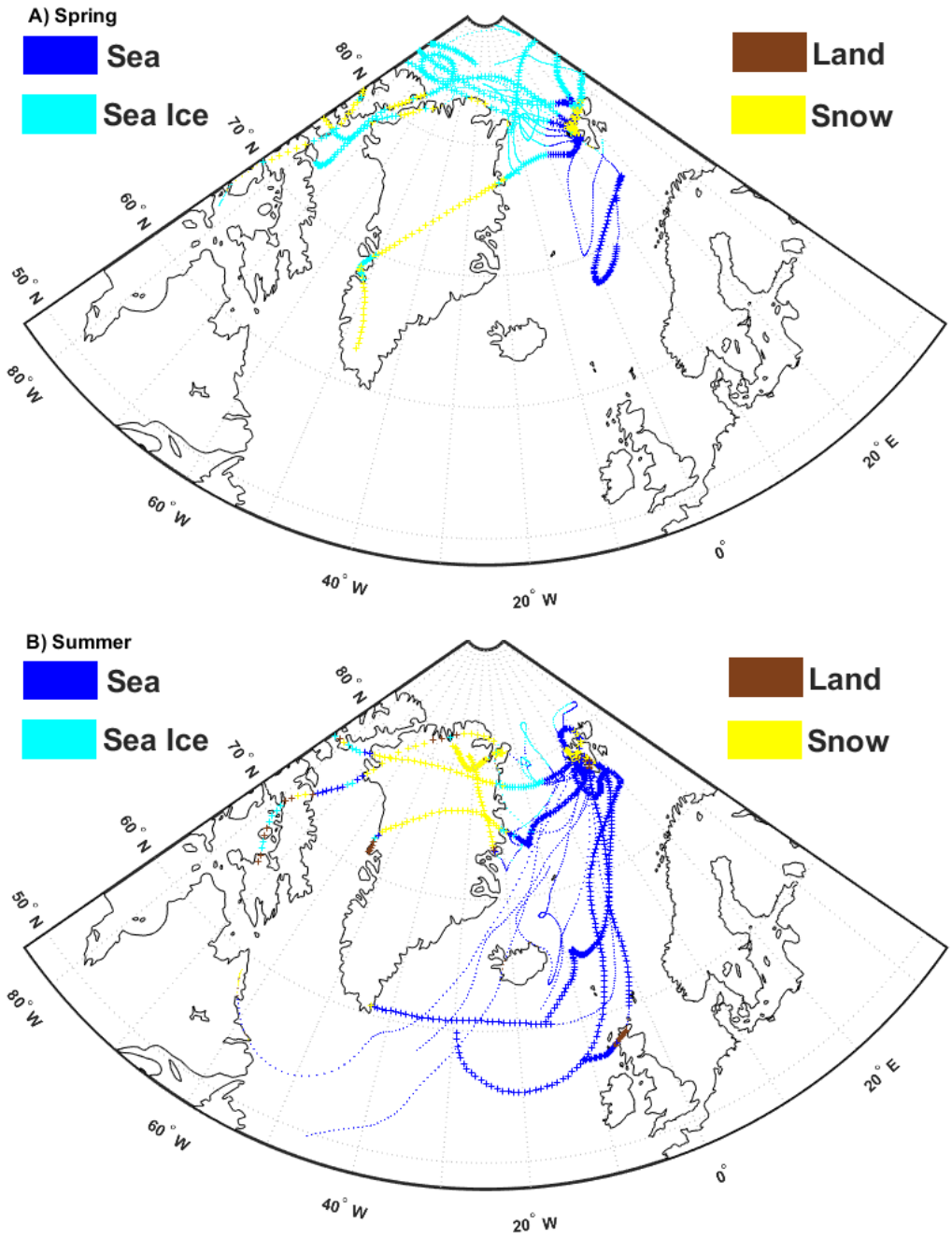

Figure 6.4: The 120-hours air mass BTs (hourly time step) arriving at GVB sampling station at times corresponding to INPs samples during A) Spring and B) Summer 2018. The color scale represents the conditions of the ground crossed by the BTs. Air masses traveling at high altitude (> 500 m above MSL), which have been excluded in CWT calculations, are represented by the symbol "+".

Figure 6.5 shows that the contribution of the four considered ground types varies with the season. In spring, most contacts occurred with sea-ice or snow-covered land, while in summer low air masses were more influenced by ice-free seawaters. The land (snow-free) contribution was the lowest in every season.

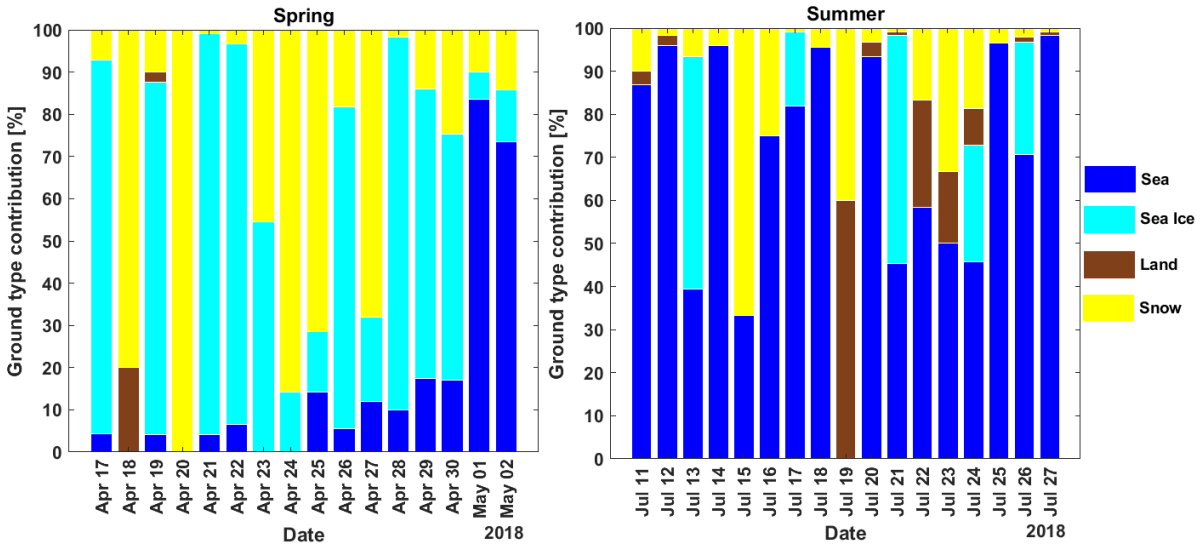

Figure 6.5: Ground type influence on low-travelling (< 500 m) air masses for INP measurements in spring and summer 2018.

Nevertheless, the influence of land sources on the INP concentrations emerges clearly from Figure 6.6; air masses with a higher terrestrial influence were always associated with *n*INP peaks in summer, while land influence is almost absent in springtime. This may be due to the higher ice nucleation efficiency of mineral dust and soil particles compared to marine biological particles (McCluskey et al., 2018b; McCluskey et al., 2018c; Wilson et al., 2015) or to higher abundance of particles in land influenced air masses. In summer, contacts with snow-free land occurred mainly within the Svalbard archipelago (local sources) or over Greenland and Iceland (regional sources), as shown by Figure 6.4. This outcome agrees with recent works pointing to both local and regional soils as important INP sources over the Arctic (Tobo et al., 2019).

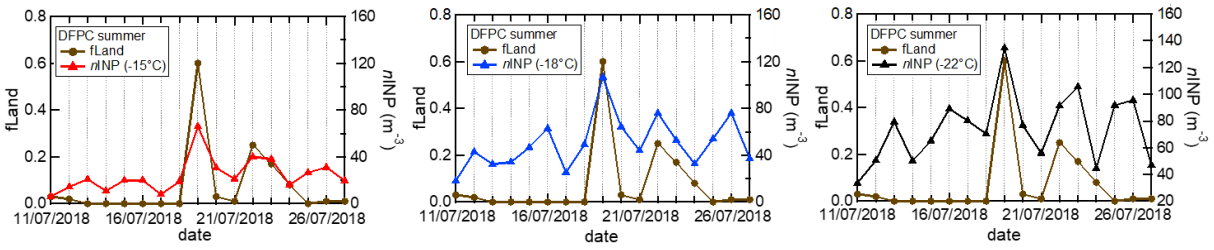

Figure 6.6: Influence of the "Land" ground type (fLand) during the summer campaign overlapped with the INP atmospheric concentrations at T = –15, –18 and –22 °C.

Considering that the sampled air masses had ground contacts mainly over seawater in summer (about 70%), one can hypothesize that marine biological sources may dominate the INP concentration at GVB, outside the periods of elevated terrestrial influence. In the following Sections, we will investigate the relation between the marine biota and INP atmospheric concentration during the summer season, by complementing the above data with satellite ocean color data.

6.3 INP Spatio-temporal Correlation with CHL

To check the hypothesis of marine biological activity may dominate the INP concentration in summer, we investigated the spatio-temporal correlation of the INP datasets with satellite retrieved surface CHL, following the time-lag approach implemented in Chapter 4 and Chapter 5. To exclude interferences from land sources, we removed from the dataset the samples corresponding to BTs that have been in contact with land for more than 10% of the time (3 samples). Furthermore, we focused on INP data obtained at T = –15 °C, which are the most representative of ice nucleation by biological particles and the less subject to influences from mineral particles.

The results of the correlation analysis are reported in Figure 6.7, in the form of correlation maps, resulting from the linear regression between the CHL at each grid point of the Arctic domain and $n\mathrm{INP}_{\mathrm{PM1}}$ at T = –15 °C measured at GVB. Different maps were obtained by considering different time-lags between the two correlated time series, *i.e.*, by considering CHL values shifted back in times of 1 to 27 days with respect to the INP filter sampling times (the maps are shown in Figure S10; APPENDIX). As discussed in previous Chapters, the time-lag approach has been demonstrated to maximize the correlation between in-situ measurements of aerosol properties and CHL fields.

The spatial distributions of the correlation coefficient (R) in example maps, as well as the behavior of the correlations, within three evidenced regions, as a function of the considered time-lag between CHL and $n\mathrm{INP}_{\mathrm{PM1}}$ at T = –15 °C, are shown in Figure 6.7. The maps (Figure 6.7) show a positive and significant correlation in three specific oceanic regions in the Arctic with different time-lags. These regions, characterized by high correlation (red dots in the maps), were consistently located upwind of GVB during the sampling period (Figure 6.4), and may be related to the emission of biological particles acting as INPs in our samples.

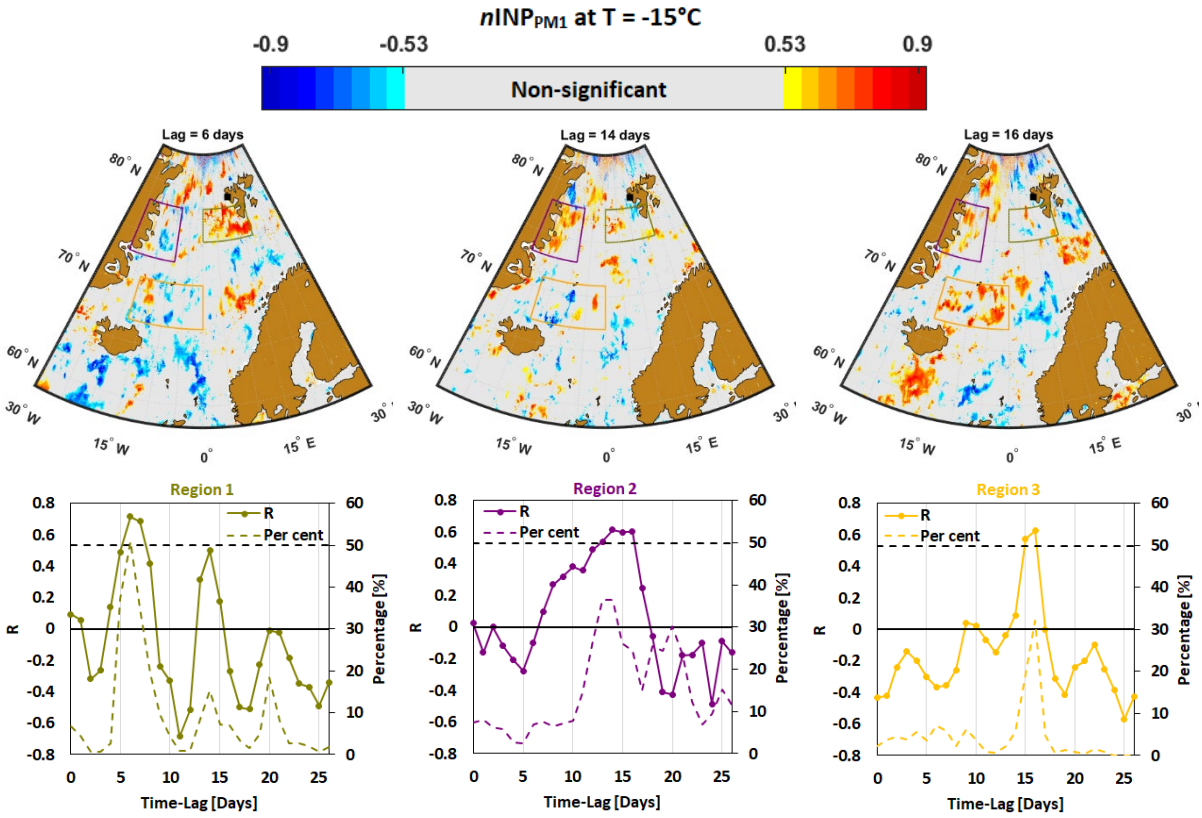

Figure 6.7: Top): Examples of correlation coefficient spatial distribution between *n*INP$_{PM1}$ at T = –15 °C measured at GVB (represented by the black square) and CHL over the Arctic ocean for 6 days (left), 14 days (middle), and 16 days (right) time-lags. The color scale indicate the correlation coefficient. Regions of interest are shown as Olivo (Region 1), dark Purple (Region 2), and Orange (Region 3) boxes. Bottom): Correlation coefficient and percentage of the number of pixels with positive and significant correlation in the three evidenced regions, as a function of the time-lag. The black dashed line represents the critical level of significant ($p < 0.05$) correlation.

The first region surrounds the Svalbard archipelago (hereafter denoted as Region 1), comprises the area between 75° – 78° N and 0° – 18° E (outlined box in Figure 6.7) and shows a maximum correlation at a time-lag of 6 days. Approximately 51% of the pixels display a positive and significant correlation within this region. In the second region (close to the Greenland coast: 73° – 78° N and 9° – 24° W), the best correlation occurred at 14-day time-lag. The third region (Region 3) is located to the northeast of Iceland and extends from 67° to 71° N and from 18° W to the prime meridian (Greenwich). Within this region, the correlation is maximized at 16-day time-lag. The percentage of significant and positive grids in region 2 and region 3 are 37% and 32%, respectively. The "correlation vs. time-lag" plots presented in Figure 6.7 have only the aim of showing the overall dependency of the correlation with the delay time in each region. The average R reported in these plots are often below the

significance threshold, as to plot them, the CHL has been averaged over the whole region, regardless the non-significant pixels contained in each region. Few positive correlation clusters tend to be in the south of Iceland and in the north of region 2, but have not been illustrated in the above analysis, they are not supported by the main circulation pattern of low BTs during the summer campaign.

Conversely to fine INP, $n\text{INP}_{PM10}$ do not evidence any significant correlation with CHL (Figure S11; APPENDIX). This is consistent with the results obtained at MHD (Chapter 4), where correlation with CHL was observed only for sub-micrometer INPs. In our interpretation, the lack of a correlation between surface CHL and coarse INPs does not imply that coarse INPs are not emitted from the ocean surface, it may simply evidence that CHL is not the appropriate proxy to track the emission of large biological INP from the oceans. Indeed, CHL has been previously observed to correlate with the enrichment of organic matter in sub-micron sea spray (O'Dowd et al., 2015; Rinaldi et al., 2013) but no investigation was ever attempted with super-micrometer particles. McCluskey et al. (2017) clearly evidenced the production of both sub- and super-micrometer INPs during laboratory experiments with controlled algal blooms, pointing out that different particle type and production mechanisms are involved.

Considering the limited number of data points used in this analysis (14 samples), we carefully evaluated the robustness of the correlations that originate the obtained correlation maps (Figure 6.7). It is impossible to check visually all the regressions that form the correlation maps discussed here as each map is composed of 651,508 pixels, of which between 30,724 (~ 5%) and 85,829 (~ 13%) present a positive and significant correlation, according to the considered delay time from 0 to 27 day. Therefore, we focused on the three evidenced sea regions characterized by systematic high correlation between INP and CHL and we divided, within each region, the significant and positively correlating pixels into three categories: High, Medium, and Low correlating, according to the distribution of the correlation coefficient. Then we selected randomly 6 pixels within each category, per each region, of which we plotted the results of the INP vs. CHL regression analysis, for a total of 54 scatter plots (Figure S12, Figure S13 and Figure S14; APPENDIX). Careful investigation of the randomly selected scatter plots shows a variety of conditions regarding the robustness of the investigated correlation, with generally robust correlations, in the majority of the cases not distorted (or influenced) by one

single (or a few) points, which we consider a prove of the robustness of the obtained correlation maps.

6.4 INP Source Regions

Aware that the evidenced correlations alone cannot imply unambiguously a cause-effect relation, we also run the CWT spatial source attribution model on the same INP dataset (DFPC; PM_1; T = –15 °C; no land influenced samples). In this analysis, 5-day BTs arriving 100 m above GVB sampling station were calculated. For each INP sample, BTs were calculated twice per each day corresponding to an INP sample, during the summer campaign. The Arctic domain was divided into 1° × 3° latitude/longitude grid cells (1,443 cells, 308 cells with at least one endpoint) between the limits of low BTs (75° W – 42° E & 48° – 85° N), Figure 6.4.

The resulting map (Figure 6.8A), composed of 203 cells over the selected domain, evidences that potential sub-micron INP sources at GVB, during the summer period, were broadly located in the same sea regions previously evidenced by the spatio-temporal correlation with CHL. In order to facilitate the comparison between spatio-temporal correlation maps and the CWT results, we have evidenced each pixel that has both a high CWT value (defined above the median), and a significant and positive correlation between $n\mathrm{INP}_{PM1}$ and surface CHL, considering every delay time between 5 and 20 days (Figure 6.8B). Sea areas corresponding to Region 1 and Region 2 are clearly evidenced by this analysis, suggesting that they may have been involved in the emission of biogenic INPs sampled at GVB, outside the major evidenced episodes of terrestrial influence. The combined analysis also suggests that the region in the northeast of Iceland (Region 3) may also be a potential bio INP source area, even though the spatial distribution of the evidenced pixels is more scattered and, therefore, less convincing.

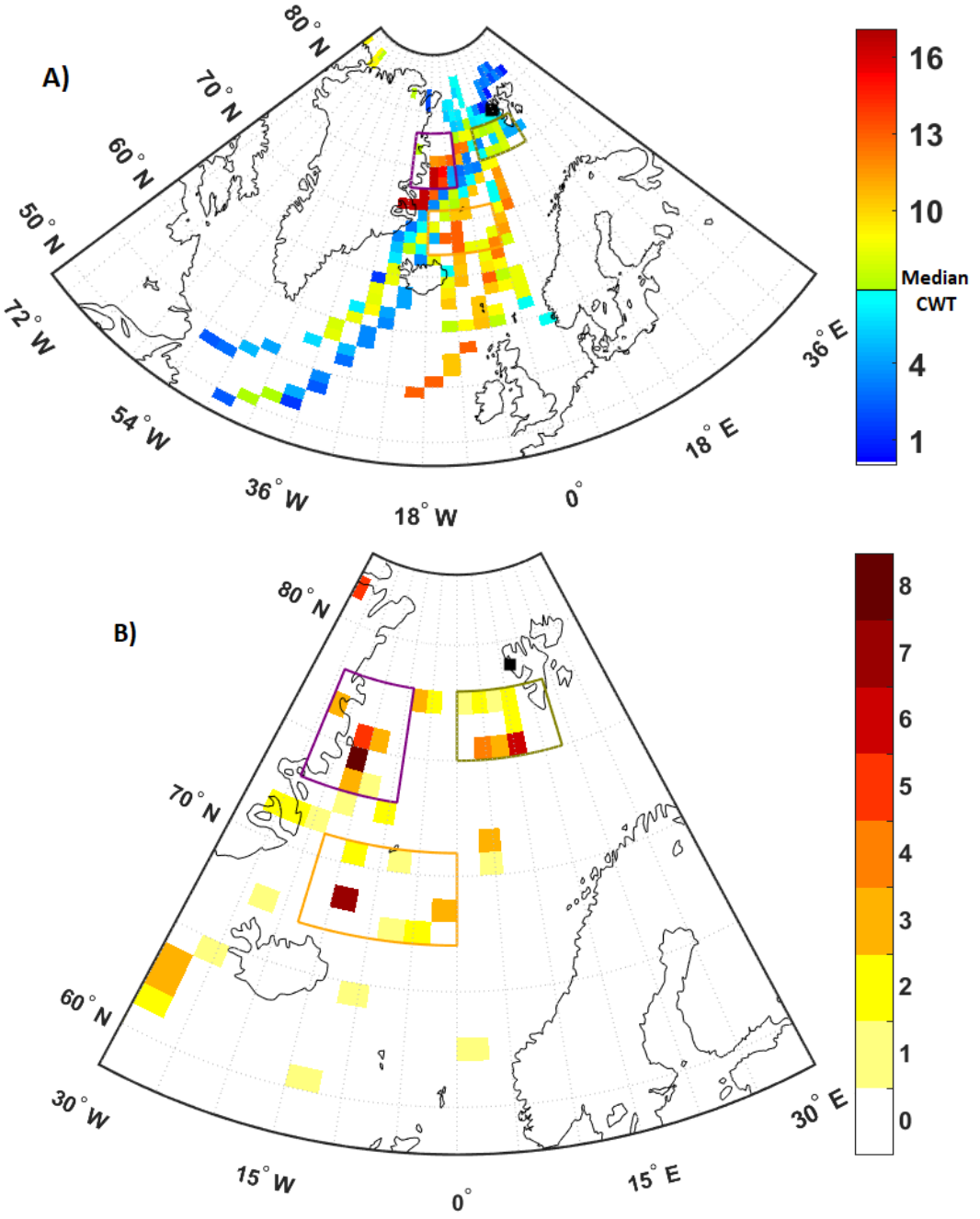

Figure 6.8: A) CWT plots for $n\mathrm{INP}_{PM1}$ at T = –15 °C. To facilitate the visual comparison, the same Regions evidenced in Figure 6.7 are reported. B) Spatial distribution of the fine INP sources identified by merging the results of the spatio-temporal correlation with CHL and of CWT. The color scale reflects how many times a given pixel has CWT ≥ median and significant correlation coefficient by running time-lags from 5 to 20 days.

6.5 Discussion

Concentrations of INPs measured at Ny-Ålesund, during spring-summer 2018, were presented in this Chapter and discussed in order to assess the impact of the Arctic marine biota on the INP concentration in the Arctic atmosphere.

Analysis of INP concentrations, low-travelling BTs, and ground conditions during the passage of the air mass suggest that the summertime INP population may be contributed both by terrestrial and marine sources. When the sampled air masses were influenced by contact with snow-free land, the INP concentration tended to peak, likely reflecting the higher nucleation ability of terrestrial particles. Our analysis suggests that outside the major terrestrial inputs, the Arctic marine biota may have a role in regulating the atmospheric concentration of INPs, during the summer season.

The major limit of the analysis presented in this Chapter is the low number of samples available, which limits the time representativity of the dataset and necessarily increases the uncertainty of the outputs of both the spatio-temporal correlation analysis and of the CWT algorithm. Nevertheless, the consistency of the two independent approaches (spatio-temporal correlation analysis and CWT source location) provides a certain measure of credibility to the presented results. For this reason, we consider the above as a convincing hint that the marine biota may be a source of INPs in the Arctic, well aware that further studies, based on more robust datasets, are necessary to confirm this result and to achieve a more quantitative understanding of the role of the marine biota as a source of INPs to the Arctic atmosphere and of the relative importance of marine vs. terrestrial INP sources over the Arctic.

7. Phytoplankton Impact on Marine Cloud Microphysical Properties over the NE Atlantic Ocean

Stratiform clouds, formed mainly over the oceans, have a profound impact on the Earth's radiation budget (Falkowski et al., 1992; Klein and Hartmann, 1993) by reflecting the incoming solar radiation to space. This results in a substantial net cooling of the Earth's atmosphere (Albrecht, 1989). Cloud reflectivity (albedo) is controlled by microphysical properties, such as cloud droplet number concentration (CDNC), cloud droplet effective radius (R_{eff}), and liquid water content (LWC). The increase in cloud cover fraction with cloud optical depth (COD) is a result of aerosol-cloud interactions (Myhre et al., 2007) through increasing cloud lifetime by precipitation suppression (the second aerosol indirect effect), that leaves more water in liquid-phase clouds for longer periods due to reducing cloud droplet size (Albrecht, 1989; Liou and Ou, 1989; Rosenfeld et al., 2019; Toll et al., 2019).

In this Chapter, we assess the relationship between phytoplankton activity and cloud properties in background clean marine conditions, over the eastern NA Ocean. A unique dataset of multi-year cloud observations (from February 2009 to January 2015) was measured by ground-based remote sensing instruments at the Mace Head Atmospheric Research Station (MHD), on the west coast of Ireland (see Section 2.1.1.2 for details). The data include cloud microphysics (CDNC, R_{eff}, LWC), cloud macrophysical (cloud base height [H_{base}], cloud top height [H_{top}], and cloud thickness [H_{thick}]) and optical properties (albedo and COD). Cloud observations were analyzed together with ocean color data and in-situ aerosol measurements. Moreover, using ECMWF ERA 5 reanalysis atmospheric data, the influence of different meteorological conditions on the relationships of ocean biochemistry and cloud properties are studied.

Based on back-trajectories (BTs), starting from the dataset of cloud observations presented by Preissler et al. (2016), 52 cloud cases were classified as marine, coming from the Atlantic Ocean (Figure 7.1) and used in this study. The average equivalent black carbon (eBC) for the considered 52 cases is 7.5 ng/m^3, proving negligible anthropogenic contribution (Grigas et al., 2017; Ovadnevaite et al., 2014; Preissler et al., 2016).

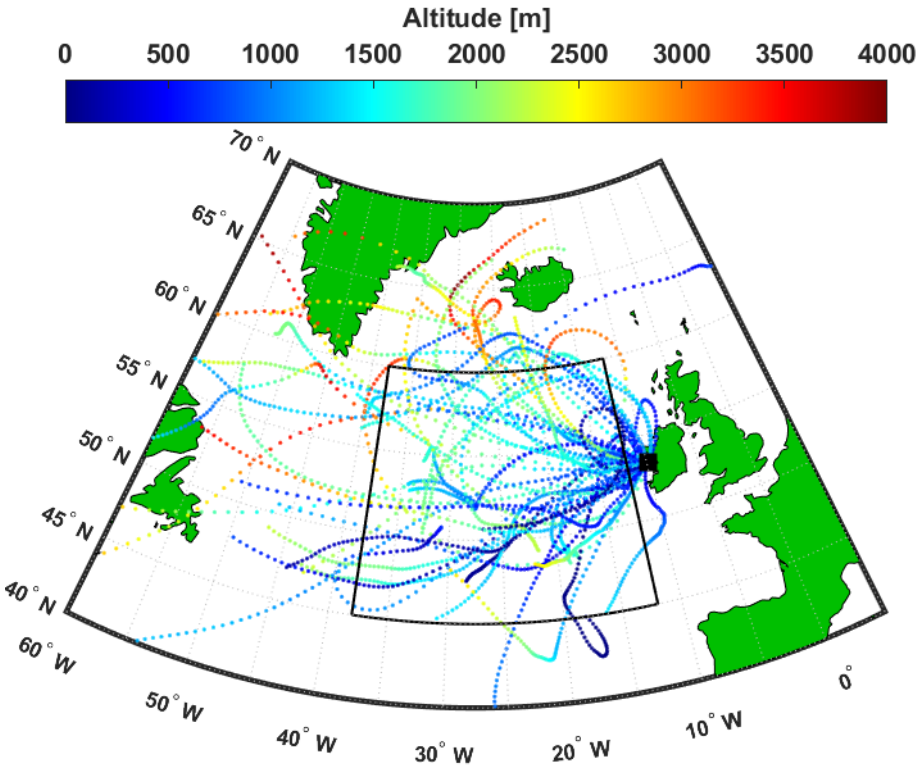

Figure 7.1: The 3-day BTs arriving MHD at cloud base altitude above the ground-level during the clean marine conditions. The color scale represents the altitude of each endpoint of BTs. The black box is the main area of interest of the present study, discussed in detail later, and MHD station is shown by a black square.

7.1 Cloud Properties Spatio-temporal Correlation with CHL

Following the approach presented in the previous Chapters, the spatial distribution of the correlation coefficient between daily CHL and both R_{eff} and CDNC of clouds passing above MHD was calculated considering different time-lags (Chapter 2). Figure 7.2 shows the correlation maps resulting with a time-lag of 3 days, as an example. In general, all the maps revealed a systematic correlation within a specific oceanic region (45° − 60° N and 12° − 38° W: black box in Figure 7.2) of the Eastern NA domain. Such a region was already identified as the main source of biogenic marine aerosol at MHD by long-term aerosol measurements, as discussed in Chapter 3, supporting the hypothesis that the observed correlation may represent a causal link between the evolution of the oceanic productivity and marine stratiform cloud properties. A negative overall correlation was observed for R_{eff} and a positive one for CDNC, justified by the inverse relationship which links these two cloud microphysical variables (Twomey, 1974; Twomey et al., 1984).

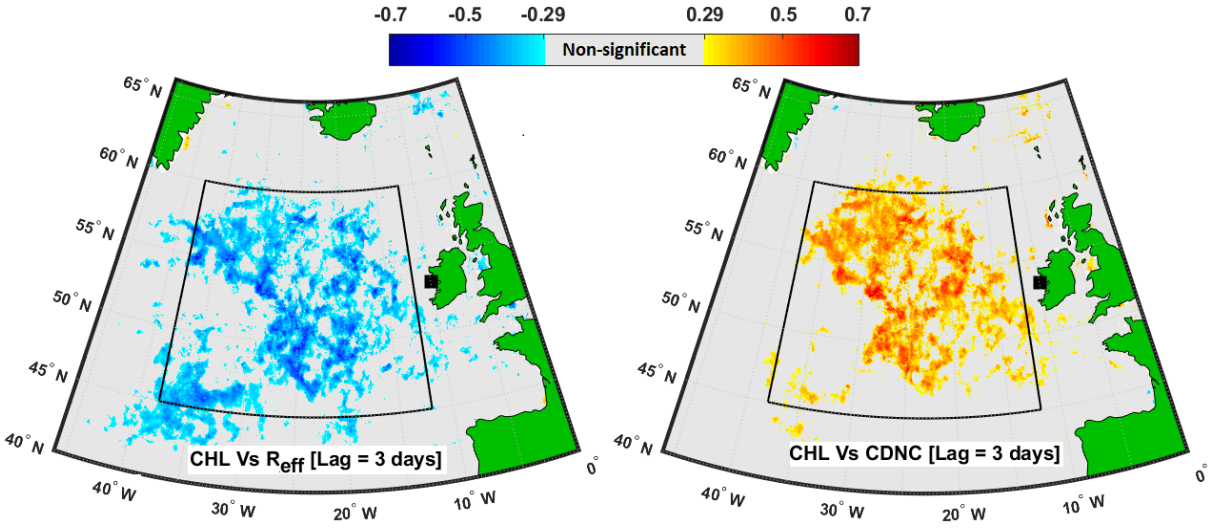

Figure 7.2: Spatial distributions of correlation coefficients between left) R_{eff} and right) CDNC measured at MHD and CHL over the NA Ocean for 3-day time-lag. The grey color represents non-significant correlation coefficients at 95% confidence level, the black square corresponds to MHD station and the black box area comprises grid coordinates 45° – 60° N and 12° – 38° W that indicates high correlation area and is selected to compute the curves presented in Figure 7.3 and Figure 7.4.

Considering the selected region (black box in Figure 7.2), the correlation as a function of the considered time-lag (Figure 7.3) shows significant values from 0 up to 7 days time-lag, with maximum correlations achieved at 3 days, only for CDNC and R_{eff}. Among the parameters provided by SYRSOC, no other cloud properties (*e.g.*, LWC, Albedo, and COD) show similar significant correlations with CHL. The correlations presented in Figure 7.3 are only indicative of the general correlation trends over the whole box region which includes correlating and non-correlating pixels due to the spatial natural variability of CHL. Anyways, localized patches of correlation can be observed for both R_{eff} and CDNC, up to 15 day time-lag (Figure S15 and Figure S16; APPENDIX), as it is evident from the percentage of negative and positive correlating pixels in Figure 7.4.

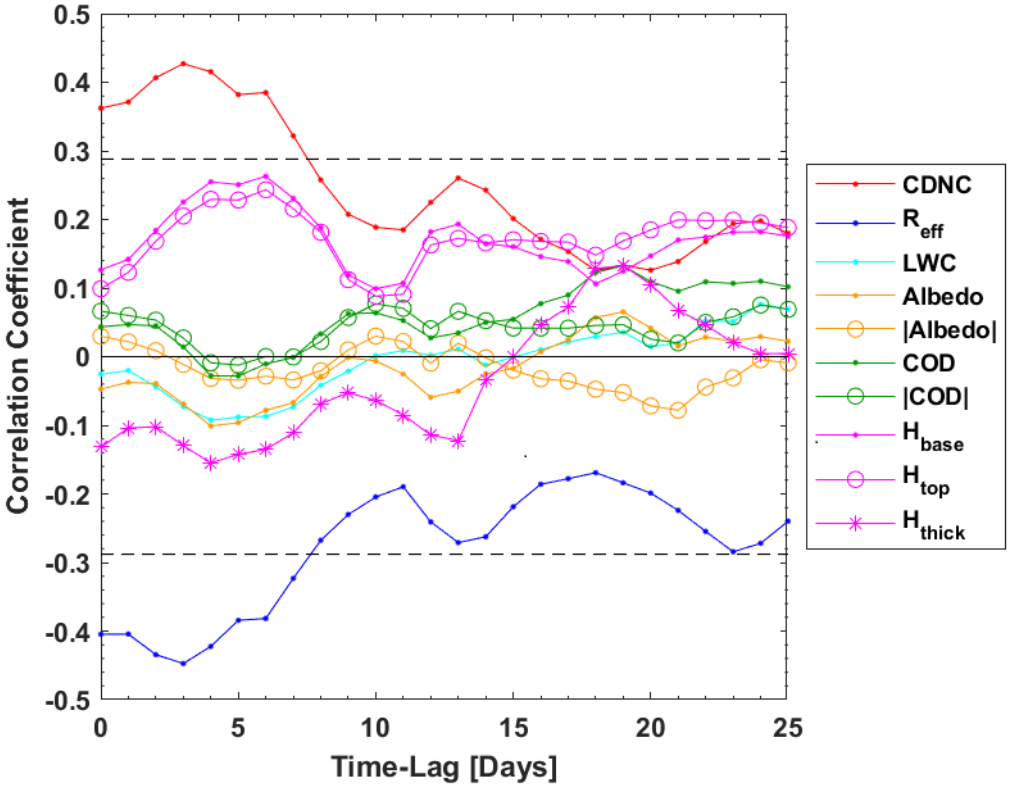

Figure 7.3: Correlation coefficients as a function of the time-lag between mean CHL within the identified box region and different cloud properties. The black dashed horizontal lines represent the critical level of significant correlation ($p < 0.05$). The sign || stands for normalized data.

The correlation coefficient frequency distributions (Figure 7.4), taken over the same box region, for time-lags of 0, 3, 6, 9, 12, 15, 18 and 21 days show that the correlation between CHL and R_{eff} (CDNC) is oriented toward negative (positive) values as the time-lag is increased from 0 to 4–12 days. In general, a significant correlation could be observed between aerosol/ cloud properties and CHL patterns, with a time-lag between zero and 25 days. The discrepancy in the obtained max-correlation time-lags with respect to other datasets discussed in this Dissertation is likely the result of the different time resolution and time coverage of the datasets, as discussed in Chapters 3, 4 and 5. Indeed, the time-lag dependency of the correlation in the present case is more similar to that presented in Chapter 3 for a similarly multi-year dataset, than to the short-term case studies presented in Chapters 4, 5 and 6. This reflects the importance of considering the time-lag between CHL and aerosol parameters in case of short-term scale experiments, where biological processes occurring at sub-seasonal time scales are likely to prevail. For long-term data (multi-year datasets), where the association between biological activity and aerosol properties is primarily driven by the annual

cycle of CHL, a less sharp dependency of the correlation coefficient on the delay time is generally observed.

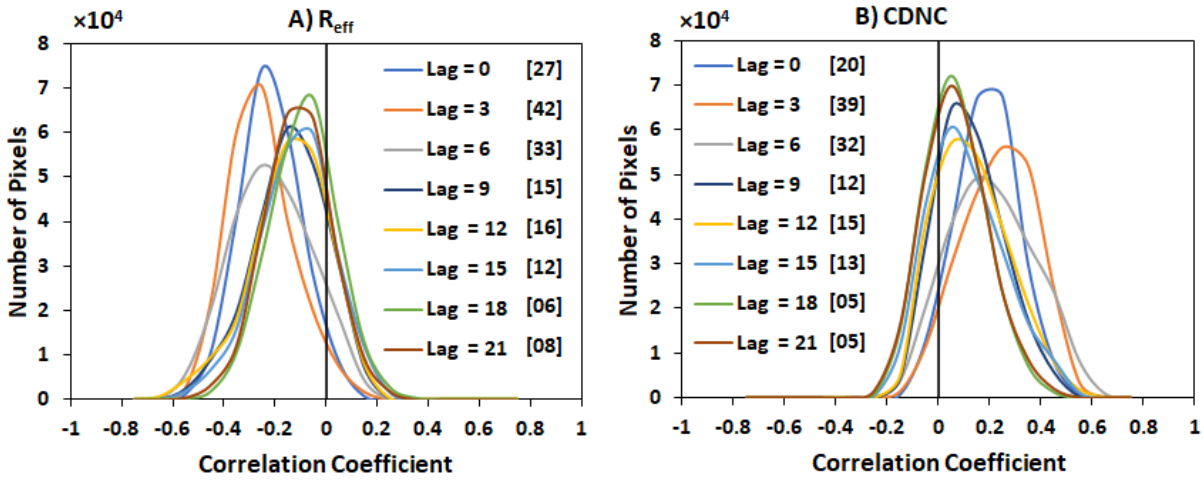

Figure 7.4: Correlation coefficient frequency distributions for R_{eff} and CDNC in the identified box at different time-lags from 0 to 21 days. The percentages of the number of pixels with negative (positive) significant correlation in that region for R_{eff} (CDNC) are inserted.

The reported correlations (CHL vs. R_{eff} & CHL vs. CDNC) are driven by the seasonal variability of the considered parameters, as shown in Table 7.1. We evidence that, although the majority of cases is representative of summer season (24 cases), the database covers all the seasons, with 9 cases in both winter and autumn and 10 cases in spring. Table 7.1 shows that seasons of enhanced sea surface CHL (spring and summer) are also characterized by low R_{eff} and by high CDNC. Typical low biological activity conditions, as observed during this study for the eastern NA Ocean, are characterized by surface CHL in the range of 0.13 – 0.40 mg m^{-3} (min – max over the box in Figure 7.2) during winter season. These conditions are typically associated with R_{eff} and CDNC ranging between 9.6 – 13.2 µm and 16.8 – 86.3 cm^{-3}, respectively. Conversely, the peak of biological productivity was represented by CHL between 0.33 and 0.93 mg m^{-3} in summer. During these periods, R_{eff} and CDNC ranged 5.4 – 14.2 µm and 14.9 – 213.3 cm^{-3}. In summary, within the fluctuation of the average CHL from winter (0.21 [median 0.20]) mg m^{-3} to summer (0.49 [median 0.47]) mg m^{-3}, CDNC increase from 40 [median 28.5] cm^{-3} to 80.6 [median 54.2] cm^{-3}. Conversely, R_{eff} diminishes from 12.1 [median 12.5] to 10.3 [median 10.8].

Table 7.1: Seasonal statistics of CHL, R_{eff} and CDNC.

	Winter	Spring	Summer	Autumn
Variable	**Mean [Median] (Min – Max)**			
CHL [mg m^{-3}]	0.21 [0.20] (0.13 – 0.40)	0.35 [0.34] (0.14 – 0.72)	0.49 [0.47] (0.33 – 0.93)	0.31 [0.30] (0.18 – 0.54)
R_{eff} [µm]	12.1 [12.5] (9.6 – 13.2)	10.2 [11.1] (7.1 – 12.7)	10.3 [10.8] (5.4 – 14.2)	10.8 [11.1] (7.2 – 14.5)
CDNC [cm^{-3}]	40 [28.5] (16.8 – 86.3)	77.7 [56.8] (16.4 – 159.8)	80.6 [54.2] (14.9 – 213.3)	61.6 [41.4] (10.9 – 149.4)

Note: The CHL statistics are obtained from daily mean data (2009-2015) within the outlined black box region in Figure 7.2. CDNC and R_{eff} statistics are obtained from the considered 52 cloud cases. The difference between Winter and Summer is statistically significant ($p < 0.05$) for all the reported variables.

The concurrent seasonality between CHL and cloud microphysical properties can be explained by one of the following hypotheses. **(1)** Cloud microphysical properties are influenced by phytoplankton activity through its effect on marine aerosol properties (Ayers and Cainey, 2007; Charlson et al., 1987; Gantt et al., 2012; Li et al., 2016; McCoy et al., 2015; Meskhidze and Nenes, 2006, 2010; O'Dowd et al., 2004; Sorooshian et al., 2009; Thomas et al., 2010; Zhang and Du, 2017). **(2)** The correlation between cloud properties and CHL is only apparent and not causal, as both variables are influenced by the seasonal evolution of meteorological parameters (Klein and Hartmann, 1993; Miller and Yuter, 2008).

In order to further investigate the possible physical meaning of the observed correlations, we extended the analysis to in-situ measured particle number concentration. We have selected the particle number concentration in the CCN relevant size range (40 – 300 nm); within this size range particles are large enough to take up water vapour and serve as nuclei for cloud droplet formation in MBL (Quinn and Bates, 2011). Aerosol number concentration (hereafter denoted by N_a) exhibits seasonal variations ranges from 111.9 [median 79.1] cm^{-3} during winter to 339.4 [median 319.1] cm^{-3} in summer. Although N_a is not available for all cloud cases, because of occasional down time of the SMPS, we report that N_a shares the same seasonal trend as cloud microphysical parameters.

N_a is positively correlated with CHL in the identified oceanic region, as shown in Figure 7.5 and presents a similar spatio-temporal pattern and time-lag dependency of the correlation as CDNC and R_{eff} (Figure 7.2 and Figure 7.3). This finding suggests that the observed correlation between cloud microphysical properties and CHL may indeed represent a real cause-effect link between marine biological activity and cloud properties, modulated by the influence that phytoplankton activity exerts on marine aerosol concentration.

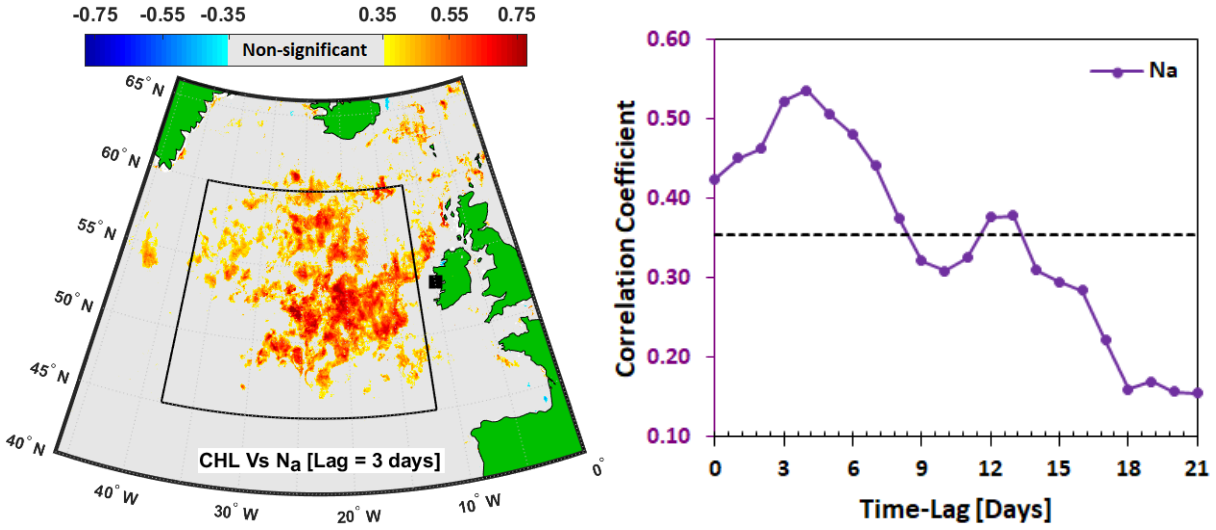

Figure 7.5: **Left)** Spatial distributions of correlation coefficients between N_a measured at MHD and CHL over the NA Ocean for 3-day time-lag. **Right)** Correlation coefficients as a function of the time-lag between mean CHL within the identified box region and N_a.

7.2 Aerosol-Cloud Interaction

R_{eff}–N_a and CDNC–N_a relationships are presented in Figure 7.6A. In general, R_{eff} (CDNC) decreases (increases) with increasing N_a concentration. From the linear regression, it can be inferred that variations in aerosol concentrations can describe up to 27% (44%) of the R_{eff} (CDNC) variance. These results agree with the recent findings by Rosenfeld et al. (2019), who concluded that the variability in aerosol concentration can explain ~ 40% of the variability of the cloud fraction of oceanic low-level clouds over the Southern Ocean. Although the data scattering is evident, the two regressions are statistically significant ($p < 0.05$). The data scatter can reasonably be attributed to the fact that in-situ ground level particle number measurements are compared with remote sensing cloud data.

Even though significant efforts have been made over the past decades to understand aerosol-cloud interactions, the overall scientific understanding is still limited. The quantification of cloud microphysical response to aerosol loading has been previously attempted by using the quantitative aerosol-cloud interaction (ACI) index (Koike et al., 2019; McComiskey and Feingold, 2012; Zhao et al., 2012). Some literature names it first indirect effect (FIE) index. The ACI index can be calculated for both R_{eff} and CDNC as:

$$\mathrm{ACI_r} = -\frac{d\ln(\mathrm{R_{eff}})}{d\ln(\mathrm{N_a})}, \text{at constant LWC}$$

$$\mathrm{ACI_n} = \frac{1}{3}\frac{d\ln(\mathrm{CDNC})}{d\ln(\mathrm{N_a})}, \text{at constant LWC}$$

Both ACI_r and ACI_n emphasize the microphysical response of the cloud by reflecting the relative change in the mean layer of R_{eff} and CDNC to the relative change in the aerosol loading. The ACI values range from 0 to 0.33 where the lower boundary implies no change in cloud microphysical properties with aerosol variation and the upper boundary suggests a linear relation. Recently, the ACI indices (or the slopes of the relationships between aerosols and clouds) were used to assess the ability of general circulation models to represent aerosol-cloud interactions by comparing the slopes between observations and numerical model calculations (Duan et al., 2019; Liu et al., 2020b; Zhao et al., 2012).

The ACI must be calculated and compared at constant LWC, due to the dependence of R_{eff} and CDNC on LWC. In this study, we use three LWC bins classified as Low, Medium, and High, using the one-third and two-third percentiles as threshold values. The LWC bins are < 0.186 gm m^{-3} (n = 10), 0.186 – 0.278 gm m^{-3} (n = 12), and > 0.278 gm m^{-3} (n = 14).

R_{eff}–N_a and CDNC–N_a relationships, grouped for homogeneous LWC classes, are presented in Figure 7.6 B & C, respectively. Both ACI_r and ACI_n values from the three LWC bins show a generally increasing trend with increasing LWC from low to medium and then a sharp decline at high LWC. The higher ACI levels at medium LWC show that clouds are more sensitive to aerosol number concentration when there is a moderate amount of liquid water in the atmosphere. When LWC rises, there is increased activity of collision-coalescence within the cloud resulting in a reduction of CDNC. This leads in part to cloud microphysical sensitivity damping, as demonstrated by decreased ACI (McComiskey et al., 2009).

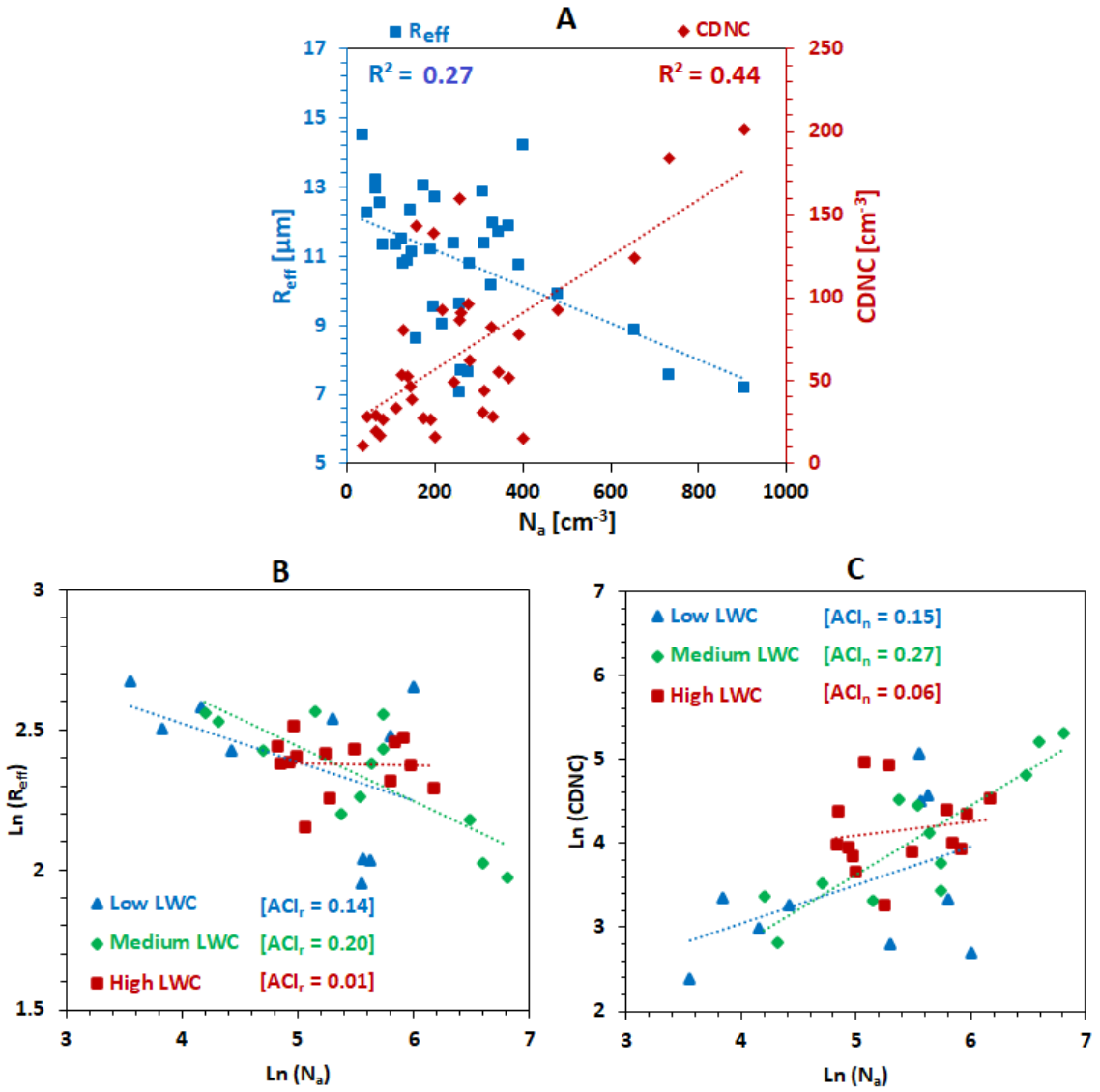

Figure 7.6: **A)** Scatter plot between N_a and R_{eff} / CDNC, **B)** ACI_r derived from R_{eff} to N_a and **C)** ACI_n derived from CDNC to N_a at three LWC bins classified as LWC < third percentile (blue), one-third percentile < LWC < two-third percentile (green) and LWC > two-third percentile (red).

The ACI values show that stratiform clouds observed at MHD are moderate to highly sensitive to aerosol number concentration variations, in medium and low LWC conditions. The range of ACI_r values observed (0.01 – 0.20) and the mean value of 0.12 ± 0.10 are consistent with previous ACI_r findings using ground-based measurements. For instance, Kim et al. (2008) found similar declining microphysical activity with higher liquid water path (LWP) represented by ACI_r values ranging from 0.04 to 0.17 from a triennial analysis (1999-2001). The ACI_r values between 0.02 and 0.19 were derived from an intensive operation period during May 2003 at a continental site of United States (Feingold et al., 2003) and around 0.10 – 0.19 based on in-

situ aircraft observations in September 2015 over Hebei, China (Zhao et al., 2018). By considering in-situ ground-based remote sensing for stratiform clouds, the ACI_r values ranged from 0.05 to 0.16 at the California coast (McComiskey et al., 2009) and from 0.13 to 0.19 in the Arctic regions (Garrett et al., 2004).

ACI_r and ACI_n behaviors are consistent. ACI_n ranged from 0.06 at high LWC to 0.27 at medium LWC, with 0.16 ± 0.11 as a mean value. A similarly intermediate value for ACI_n (0.22 ± 0.03) was found in clean air Arctic summer conditions (Koike et al., 2019).

In summary, the microphysical properties of marine stratiform clouds advected over MHD respond from moderately to strongly (at low and medium LWC conditions) to changes in aerosol number concentration below the cloud. This result is in line with other studies conducted at different locations, as evidenced above.

7.3 Relating Cloud Properties to Meteorology

Because of the substantial effect of meteorological conditions on cloud formation and characteristics, we investigated the relationship between the main meteorological variables extracted from ECMWF ERA5 (0.25° × 0.25° spatial resolution) over the Eastern NA domain and the properties of the selected clean marine cloud cases.

The air temperature at 2m above sea level (T) and sea surface temperature (SST) were chosen as representative for thermal heating and the relative humidity (RH) was chosen as representative of water vapor abundance in the atmosphere. To represent the atmospheric thermodynamic and dynamic conditions, the lower tropospheric stability (LTS) parameter and the pressure vertical velocity (PVV) were utilized, respectively.

The LTS, an indicator for air convection, is calculated as the potential temperature difference between 1000 hPa and 850 hPa, which reflects thermal (in)stability in the sub-cloud layer: the higher the LTS, the more unstable the atmosphere. For the studied cloud cases, the LTS ranges from –1.5 to 10.4 °C. Positive values of LTS account for 95.7% of the data points, indicating a dominant thermal instability for the selected cloud cases. Klein and Hartmann (1993) showed that each 1 °C increase of LTS leads to a 6% increase of marine stratocumulus cloud fraction at 5 different oceanic regions.

The pressure vertical velocity (PVV; Pa s^{-1}) is the speed at which the air travels up or down. Negative values of PVV imply upward motion (ascent areas), while positive values represent downward motion (subsidence). In general, the vertical upward motion favors the cloud formation, enhancing aerosol indirect effect and cloud thickness (Jones et al., 2009; Liu et al., 2020a).

The correlation coefficients between the 52 clean marine cloud properties (47 days) and the meteorological parameters are listed in Table 7.2, together with the maximum correlation coefficients observed between cloud properties and CHL/ N_a in the evidenced box region.

Table 7.2: Correlation coefficients between clean marine cloud data measured at MHD and meteorological variables over the coordinates (50° – 55° N and 10° – 15° W), 5° latitude/longitude around MHD. Correlations with CHL and N_a were added for comparison.

Variable	T	SST	RH	PVV	LTS	CHL	N_a
R_{eff}	−0.32*	−0.28**	−0.12	−0.25**	−0.13	−0.45*	−0.54*
CDNC	0.24	0. 19	0.06	0.20	0.26**	0.43*	0.69*
LWC	−0.05	−0.10	0.19	−0.05	−0.07	−0.07	−0.05
Albedo	0.05	−0.05	0.46*	−0.03	−0.35*	−0.07	−0.14
|Albedo|	−0.01	−0.14	0.54*	0.11	−0.32*	−0.01	0.12
COD	0.11	0.01	0.40*	−0.05	−0.25**	0.01	−0.15
|COD|	0.06	−0.06	0.52*	0.05	−0.28**	0.03	−0.01
H_{base}	0.03	0.14	−0.73*	0.02	0.75*	0.23	0.48*
H_{top}	0.07	0.18	−0.74*	−0.03	0.74*	0.21	0.42*
H_{thick}	0.13	0.10	0.15	−0.19	−0.21	−0.13	−0.35**

Note: * significant correlation at the level of $p < 0.05$ and ** significant correlation at the level of 0.1

It can be seen from the table, that cloud microphysical properties (R_{eff} and CDNC) are mainly controlled by CHL (proxy of the oceanic biological activity) and aerosol number concentration, with a minor contribution from T and/or SST (which both tend to covariate with marine biological activity). Conversely, Cloud macrophysical (H_{base}, H_{top} and H_{thick}) and optical properties (COD and albedo) are influenced mainly by meteorological conditions such as RH, LTS and PVV, with no apparent contribution from either temperature or biological

activity. Increased RH (more water available in the atmosphere) is associated with low H_{base} and H_{top} values, due to rapid particle activation, as well as to enhanced cloud albedo and COD.

The PVV-R_{eff} correlation is at the edge of the significance level ($p < 0.1$), nevertheless it may suggest some impact of the vertical air motion on cloud activation, with an effect on cloud microphysical properties.

The parameters most influenced by LTS are cloud base and top heights, which tend to increase in unstable conditions (deeper boundary layer). The finding is consistent with the observational study of Wood and Bretherton (2006) and modeling study of Bretherton et al. (2013). An interesting result is that LTS does not directly control the microphysical properties of the cloud, but the correlations R_{eff} vs. CHL and CDNC vs. CHL are strengthened with increasing LTS (strong vertical mixing due to thermal instability). The R^2 value of CHL-R_{eff} relationship moves from 0.14 (non-significant) to 0.26 (significant at $p < 0.05$) and R^2 value of CHL-CDNC relationship pass from 0.08 to 0.27, with moving from less to more unstable conditions. These numbers were obtained by classifying the data into two subsets which were categorized by low and high LTS, using the median value as the threshold.

The above results are consistent with those inferred from satellite observations of marine stratiform clouds in the Southern Ocean (Rosenfeld et al., 2019), which showed that aerosol number concentration mainly affects cloud microphysical properties, while meteorological conditions have a higher effect on cloud geometric thickness. Rosenfeld et al. (2019) proposed an approach to quantify the dependency of cloud reflectivity on CDNC. The method separates the aerosol effect on clouds from the meteorology effect, sorting the clouds by their thickness.

Even though CHL patterns have no apparent effect on cloud albedo, the normalized albedo (albedo/ cloud thickness) is increased with enhanced CDNC and reduced R_{eff}. The correlation between CDNC (R_{eff}) and normalized albedo is significant ($p < 0.05$) and equal to 0.54 (–0.36). This highlights the link between microphysical cloud properties and albedo, as expected from theory (Twomey, 1974; Twomey et al., 1984). This relation can only be seen if the cloud thickness effect, which affects the total cloud albedo and which appears to be mainly driven by meteorology, is excluded. This shows that meteorology has a strong impact on cloud albedo, notwithstanding the well-known relation between microphysical properties and cloud reflectivity. Aerosol-cloud interactions are complex and there is already literature showing limited albedo response to changes in microphysical parameters. For example, using monthly

satellite measurements, the cloud albedo induced by the impact of aerosol on CDNC and R_{eff}, is found not to dominate (Bender et al., 2016).

The LWC is considered the most important microphysical parameter in controlling cloud albedo (Frey et al., 2017; Liu et al., 2020b) and our results confirm this finding. Our data shows that LWC can describe up to 52% of the albedo variance. In essence, cloud albedo is primarily influenced by LWC while CHL/ aerosol number controls cloud initiation/ formation and its microphysical characteristics (CDNC and R_{eff}). The relation between R_{eff} (CDNC) and normalized albedo proves that there is a certain contribution to the cloud albedo from phytoplankton-driven aerosol number, even though it is probably less important than the contribution from meteorology.

Finally, to better evaluate which parameter is more important for R_{eff} , biological activity or air temperature (the two parameters that showed a significant correlation with R_{eff}), a two-dimensional linear regression of R_{eff} as a function of CHL and T as average values over the identified box was performed and the results are reported in Table 7.3. The regression shows that 20% of the R_{eff} variance could be interpreted by CHL and T patterns, of which 15% is contributed by CHL and 5% by the air temperature.

Table 7.3: Two-dimensional linear regression of R_{eff} as a function of CHL and T spatial averages.

	Total R^2	RMS error	Normalized Contribution to R^2	
			CHL	**T**
R_{eff}	0.20	2 µm	0.15	0.05

Note. The contribution to R^2 for each of the independent variables is the decrease in total R^2 with that variable omitted. The sums of individual contributions of R^2 are adjusted to equal the total R^2.

Further confirmation of the importance of oceanic biological activity over meteorology as for cloud microphysical properties was obtained by analyzing the dependency of R_{eff} on CHL and T when the other parameter is nearly constant. In Figure 7.7, the dataset is divided into 3 homogeneous groups based on percentiles to check whether CHL is more significant than T in determining the observed R_{eff} seasonal variations. Briefly, the 47 days are divided into sub-groups characterized by quasi-homogeneous temperature (Low, Medium, and High). The

correlation coefficient between CHL and R_{eff} had been calculated for each sub-group. A significant negative correlation ($p < 0.05$), in the CHL-R_{eff} relationship, is observed for categories "low T" and "medium T", while at "high T", the correlation is non-significant. When we apply the opposite analysis (testing R_{eff}-T correlation in quasi-homogeneous CHL groups), we never get a significant correlation.

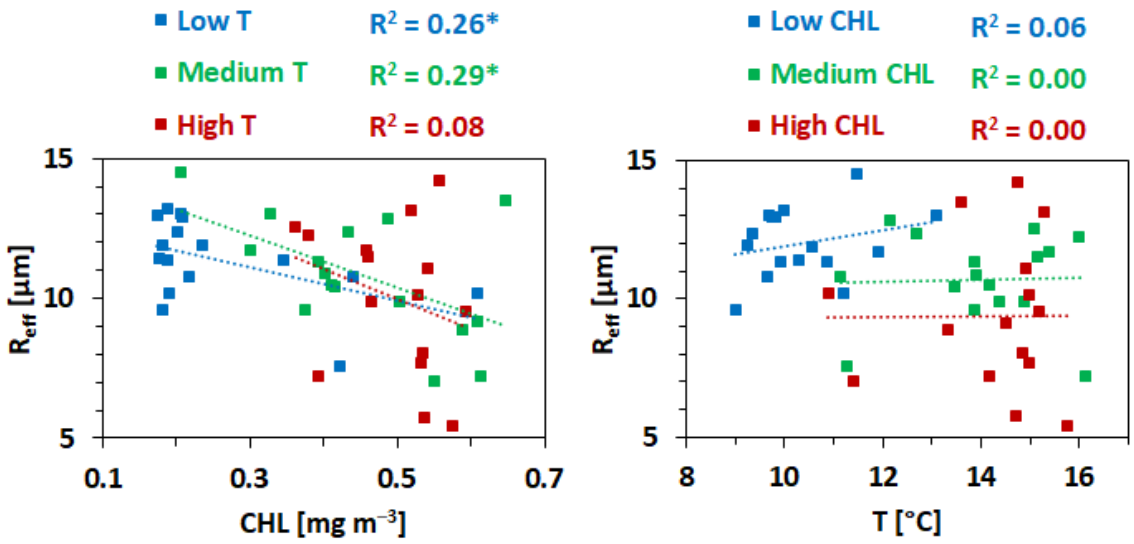

Figure 7.7: Left) scatterplot showing the relation between CHL and R_{eff} at nearly homogenous T. Right) scatterplot showing the relation between T and R_{eff} at nearly homogenous CHL. * represents significant correlation at 95% confidence interval.

In conclusion, even binning the data for homogeneous air temperature conditions, the R_{eff} (and CDNC) dependency on CHL patterns is maintained. Conversely, the dependency of R_{eff} (CDNC) on T is lost when analyzing subsets of data characterized by constant CHL levels. This shows that the observed relation between cloud microphysical properties and T is mainly indirect, likely caused by the covariance between surface CHL and T, due to the well-known effect of temperature (and solar radiation) on marine biological activity.

7.4 Discussion

The present Chapter evidences the effect of phytoplankton activity on cloud properties over the eastern NA Ocean, deploying a unique dataset of multi-year (2009-2015) remote sensing cloud observations. Our data show that phytoplankton activity affects marine cloud microphysical properties, diminishing R_{eff} and enhancing CDNC. This occurs because

phytoplankton activity controls the concentration of aerosol particles in the unperturbed marine boundary layer, as emerges from this Dissertation and several previous studies. Supporting these findings, the aerosol-cloud-interaction index analysis shows that marine stratiform clouds observed at MHD are moderately to highly sensitive to aerosol number concentration variations, in medium and low LWC conditions.

Conversely, the effect of biological activity is not evident on other parameters, as H_{base} and H_{top}, H_{thick} and cloud reflectivity, which appear mainly controlled by meteorological conditions. Our data suggest that meteorology is very important in determining the overall cloud albedo. Anyhow, when the meteorology effect is minimized by sorting the cloud cases according to cloud thickness, CDNC and R_{eff} effect on cloud albedo is evident.

Within the range of variability of our dataset, passing from low to high biological activity conditions (winter to summer) induces an increase in surface CHL of ~ 2.4 times in seawaters facing MHD, a consequent doubling in CDNC and a decrease of R_{eff} of ~ 14%. Similarly, observations in the Southern Ocean show that ocean biology can double the CDNC over biologically productive waters in summer, with respect to unproductive waters. It was calculated that such a change in CDNC can cause a net reflection in shortwave radiation between –4 and –6 W m^{-2} as annual average, exceeding –10 W m^{-2} in summer (McCoy et al., 2015). Meskhidze and Nenes (2006) reported a similar doubling in CDNC over a blooming area of the Southern Ocean with respect to no blooming regions, in this case associated with a larger reduction of the effective radius (~ 30%); such variation in cloud microphysical properties was estimated to cause a strong cooling reaching –15 W m^{-2} (Meskhidze and Nenes, 2006). These values are comparable to the annual mean radiative forcing from aerosol-cloud interaction downwind of highly polluted regions as simulated in global circulation models (Bian and Prather, 2002; Jones et al., 1994; Menon et al., 2002; Rap et al., 2013; Zelinka et al., 2014). Further studies in the Southern Ocean quantified the effect of secondary sulfate emissions on the annual mean reflected shortwave radiation to be –9.32 W m^{-2} (Thomas et al., 2010), as a result of 15-18% reduction in R_{eff}. To this same seasonal cycle of R_{eff} over the Southern Ocean, McCoy et al. (2014) attributed a difference in the reflection of the shortwave radiation of up to −8 W m^{-2}.

To quantify the net radiative effect due the observed winter-summer variation in cloud radiative properties is beyond our possibilities at present; nevertheless, the above comparison

with previous studies, reporting similar differences in CDNC and R_{eff}, suggests that it may be not negligible.

Furthermore, we can assume an effect of plankton activity on cloud lifetime (2nd aerosol indirect effect). Enhancement of CHL and aerosol number tend to increase CDNC and decrease the size of the cloud droplets, leading to a suppression of precipitating droplets, which leaves more water in liquid-phase clouds for longer periods. Precipitation is considered as strongly suppressed when R_{eff} does not exceed 12–14 μm in marine low clouds (Fan et al., 2020; Freud and Rosenfeld, 2012). This effect is even more difficult to quantify and further studies would be needed to address this point.

Finally, one can argue that the radiative balance over the NA is dominated by anthropogenic emissions, considering that clean marine conditions are rare (Hamilton et al., 2014). Preissler et al. (2016) discussed an extended version of this same cloud dataset, comprising also samples collected under continental and anthropogenic influence. They reported an enhancement of CDNC by 2.7 times and a 20% reduction in R_{eff}, passing from unperturbed marine clouds to polluted conditions, which is not far from the impact of passing from low to high biological activity, in clean marine conditions. These findings suggest that the impact of phytoplankton activity on cloud properties may be comparable with that of anthropogenic and continental aerosols over the Eastern NA Ocean, even though we recognize that further studies would be necessary to address this point more quantitatively.

The present study is the first to report direct observations of the impact of the oceanic biota on the aerosol-cloud-climate system over the NA Ocean, using long-term data. This contributes to a better understanding of the natural climate system and confirms the possibility of feedback mechanisms involving climate regulation by phytoplankton (Charlson et al., 1987). Carslaw et al. (2013) pointed out that an important fraction of the uncertainty associated to aerosol-cloud interactions, in climate models, is related to our limits in the understanding of the natural climate system. Considering this, the present study provides and important piece of information that can contribute to the development of an improved generation of climate and Earth System Models.

8. General Discussion and Conclusions

Accurate climate change predictions require the understanding of a wide range of ocean-atmosphere interactions. One of the most intriguing questions in climate studies is the coupling between marine biota and aerosol/ cloud properties and the sensitivity of the climate system to feedback mechanisms resulting from these interactions. Achieving a better understanding of this issue may increase our understanding of the complex nature of the natural climate system. This Dissertation aims to shed light on the role of oceanic biological activity in modulating the chemical and physical properties of marine aerosol and, ultimately, its impact on clouds. To achieve this aim, an approach based on back-trajectory analysis, spatio-temporal correlation analysis between in-situ aerosol/ cloud observations and high-resolution satellite ocean color data and source region location models was applied in three contrasting marine environments, in the Northern hemisphere, characterized by different marine ecosystems, aerosol loads, meteorological conditions and seasonalities.

In-situ measurements from the North East Atlantic Ocean (MHD), the central Mediterranean Sea (CGR) and the Arctic Ocean (GVB), were studied, providing insights into the physico-chemical properties of marine aerosol and the related cloud characteristics. For the Eastern North Atlantic Ocean, we employed nine years (2009-2017) of submicron aerosol chemical composition measurements and six years of particle size distribution and ground-based remote sensing cloud observations (February 2009 – January 2015) at MHD. In addition, data from an intensive campaign (30 July – 21 September 2015) at MHD station were used to investigate short term relations between marine aerosol and phytoplankton activity. An intensive aerosol characterization campaign (07 – 25 April 2016) at CGR station was used to investigate the atmospheric concentration of submicron MSA over the Mediterranean Sea, in relation to CHL patterns. Finally, INP concentrations measured at GVB (Svalbard) during two intensive field campaigns (spring: 17 April – 02 May; summer: 11 – 27 July) in 2018 were used to assess the impact of the Arctic marine ecosystem on this important atmospheric component. The long-term measurements provided a valuable resource, being the datasets representative of a wide range of atmospheric and ocean conditions and allowing robust statistics. On the other hand, the short-term campaigns allowed extending the range of observed aerosol parameters to other climate-relevant properties, as CCN and INP

concentrations, which are not all available as long-term data, and to other locations, so far less characterized from the phytoplankton-aerosol interactions point of view (Mediterranean and Arctic). The different datasets present a wide range of aerosol and cloud properties in different ecosystems and spanning various extents of time to elucidate the relationship between the oceanic biota and marine aerosol/cloud properties from multiyear to short time scales (~ 1-2 month). All the data have been selected to be representative of marine air masses, limiting to a minimum any anthropogenic input.

The long-term measurements of submicron marine biogenic aerosol chemical components at MHD exhibit seasonal variations, linked to oceanic biological activity across the NA Ocean. In general, marine aerosol in the NA Ocean is characterized by two distinct seasons (winter and summer) with transition periods presenting intermediate characteristics. In winter (characterized by low oceanic biological activity, indicated by low surface chlorophyll concentration), the atmospheric concentrations of marine biogenic aerosol components are at their yearly minimum; in summer (high biological activity and high chlorophyll), the concentration of biogenic marine aerosol components is maximized. Our analysis shows that the seasonality of marine aerosol chemical composition cannot be explained by the air mass origin, suggesting an impact of biological activity on marine aerosol concentration and composition. The Sea region directly to the West of MHD station, roughly within 45° − 60° N and 12° − 38° W, was identified as the main source of biogenic aerosol reaching the station over the investigated period (2009-2017).

CHL in the NA exhibits different cycles from annual (the dominant one) to monthly and, possibly, sub-monthly. The annual cycle of the CHL is driven by meteorological parameters, primarily solar radiation, which modifies the sea surface and air temperatures and has a direct effect on phytoplankton growth. In parallel, meteorology also affects concentrations of aerosols by increasing the release of gases from the sea surface and their oxidation rates in the atmosphere, during the seasons characterized by high solar radiation. Therefore, in the annual cycle of marine aerosol composition, the impact of phytoplanktonic activity and meteorology are intertwined and it is difficult to deconvolute one contribution from the other. For this reason, we extended the analysis into seasonal scales. Our results evidence a relationship between aerosol chemical composition and CHL patterns also at sub-yearly (seasonal) scale with the exception of winter. In winter, the missing correlation is probably

caused by a combination of factors, like the low level of phytoplankton emissions but also a higher noise in atmospheric measurements, which are close to the detection limit. These findings further support the hypothesis that oceanic biological activity is a major driver of marine aerosol chemical composition.

To further investigate the relation linking marine aerosol properties to phytoplankton activity, we focused our analysis on shorter time scales (~ 1-2 months). The value of short-time scale case studies is that the impact of meteorology can be more readily distinguished from that of biology, enabling a process-level understanding of the relationship between phytoplankton behavior and marine aerosol properties.

The analysis of the data collected during the intensive campaign performed at MHD in late summer 2015 showed a clear lagged correlation between all the main aerosol physicochemical properties and surface CHL. These spatial and temporal relationships demonstrate that the marine biota influences aerosol properties under a variety of aspects, from chemical composition to number concentration and size distribution, up to the most cloud-relevant properties (CCN and INP concentration). Furthermore, during the study period, CHL was the most influential parameter, explaining the majority of the observed variance in aerosol properties, while a lower contribution from meteorological parameters was observed. Consequently, the oceanic biological activity resulted the strongest driver of marine aerosol properties over the NA Ocean, at least in the conditions represented by the studied intensive campaign. Furthermore, the main source of biogenic marine aerosols reaching MHD during the study period (47° – 57° N and 14° – 30° W) is consistent with the results obtained from the multi-year chemical composition dataset. Another potential source region was identified between the Eastern coast of Greenland and Iceland. This latter source region was not highlighted by the multi-year CHL correlations, suggesting that the influence of this region may be lower in other periods of the year or not always as important in different years.

The same combined approach was applied on the Mediterranean Sea domain, to investigate the relationship between marine biological activity and biogenic aerosol production. In detail, this study was based on intensive measurements of MSA atmospheric concentration, the only available tracer of marine biogenic aerosol available in the polluted Mediterranean atmosphere. Our analysis evidenced that the most probable source of MSA over the Western Mediterranean, during spring 2016, was located roughly between 37° and

39° N and between 02° and 10 °E (SW Mediterranean Sea, between Sardinia and the Algerian coast). The identified source area did not coincide with the most biologically productive sea area during the measurement period, which is located across the Ligurian Sea and Gulf of Lion. The reasons why the blooming NW portion of the Mediterranean Sea was not contributing significantly to the aerosol burden observed at CGR may be biotic (different phytoplankton types or stress conditions) or abiotic factors (SST), which may also be intertwined in determining the observed effect. It is reasonable to assume that the identified source region was probably also associated to the production of nss-sulfate, which shares the same precursor and formation routes with MSA and, possibly, of secondary organic aerosols from the processing of biogenic volatile organic compounds released from the sea surface. Although it has been shown in the literature that the yearly cycle of surface CHL, in the Mediterranean Sea, is not in phase with the atmospheric concentration of aerosol MSA, the present work shows that CHL can be used to evidence a relationship between phytoplankton activity and MSA concentration, on short time scales.

Analyzing of INP concentrations measured at Ny-Ålesund (Svalbard), during spring and summer 2018, and ground conditions during the passage of the sampled air masses suggests that the summertime INP population over the Arctic may be contributed by local sources, both of terrestrial and marine origin. Our analysis suggests that, outside the major terrestrial inputs, the Arctic marine biota may have a role in regulating the atmospheric concentration of INPs, during the summer season. Given the limited number of INP samples available for the analysis, further studies are required to confirm this outcome and to obtain a more quantitative understanding of the role of the marine biota as a source of INPs and the relative importance of marine vs. terrestrial INP sources over the Arctic.

Importantly, by deploying a unique dataset of multi-year (2009-2015) remote sensing cloud observations, the effect of phytoplankton activity on cloud properties over the eastern NA Ocean was evidenced. Phytoplankton activity affects marine cloud microphysical properties, diminishing Reff (–14%) and enhancing CDNC (+90%), by enhancing the aerosol number concentration in summertime with respect to quiescent winter conditions, in unperturbed marine air masses. Supporting these findings, the analysis of the aerosol-cloud interaction index showed that marine stratiform clouds observed at MHD are moderately to highly sensitive to aerosol number concentration variations, in medium and low LWC

conditions. Conversely, other parameters, as cloud base and top, cloud thickness and optical properties resulted more influenced by meteorological variables than by biological activity. In agreement with previous studies, our data suggest that meteorology is very important in determining the overall cloud albedo, nevertheless, the effect of variations in CDNC and R_{eff} on cloud albedo can be appreciated when the meteorology effect is minimized, sorting the cloud cases according to cloud thickness. This evidences the role of phytoplankton-driven particle number concentration on the overall cloud radiative properties over the NA Ocean, which may be not dominant with respect to the effect of meteorology but that cannot be entirely dismissed. Further studies would be necessary to assess quantitatively the cloud radiative effect resulting from the marine biota influence. Nevertheless, our considerations, based on comparison with the literature, suggest that it may be not negligible or even comparable to the forcing exerted by anthropogenic aerosols over the NA ocean.

As an overall conclusion, this work shows that a relation between marine aerosol properties and the patterns of marine biological activity can be observed on different time scales and in contrasting environments (Mediterranean: scarcely productive; NA Ocean: intense seasonal blooming; Arctic: covered by ice most of the year). Our results evidence that phytoplankton activity impacts marine aerosol properties such as chemical composition, aerosol number concentration, size distribution and cloud relevant properties, exerting an observable effect even on clouds themselves (at least over the NA Ocean).

Even though we can provide a clear evidence that phytoplankton activity impacts the production of SMA, reasonably by providing precursors that degas from the sea surface to the atmosphere, it is more difficult to draw a firm conclusion on the impact of phytoplankton activity on the chemical composition of sea-spray aerosol. This mainly because we lacked a clear tracer of primary marine organic aerosol. On this regard, we highlight that our analyses linked the ice nucleating properties of marine aerosol to CHL patterns in two different environments (NA Ocean and Arctic). Considering that the ability to nucleate ice has always been attributed, so far, to primary marine organic aerosol and never to secondary, this can be considered an indirect proof of the fact that phytoplankton activity is able to influence the properties of primary marine aerosol also. This also highlights the potentially important role that primary marine organic aerosol may exert on the climate system as even small variations

in the INP concentration may determine disproportionately high variations in cloud albedo, given the impact that ice formation have on cloud radiative properties.

In the studied short-term campaigns, the correlation between marine aerosol properties and satellite tracers of oceanic biological activity is maximized when an appropriate time-lag is considered. The understanding of the time-lag between CHL patterns and the evolution of marine aerosol properties is not only a technical issue; it may improve the current capacity of using CHL as a predictive variable of marine aerosol properties, in regional and global atmospheric models. The time-lag likely represents the time scale of the biochemical processes responsible for the production of transferable organic matter (in the case of primary) or gaseous precursors (for secondary) in the seawater, after the phytoplankton growing phase. Indeed, while the surface CHL tracks the growing phase of algal blooms, the release of phytoplankton exudates occurs, mainly, at a later stage, during the senescence/demise phase. Our analysis shows that, in multi-year observations, where the correlation is mainly driven by the annual cycle of CHL, there is no sharp dependence of the correlation coefficient (CHL vs. aerosol/ cloud) on the time-lag, and hence it is of limited value to consider the time-lag for applications over such long-time scales. Conversely, considering data on a short time scale (~ 1-2 months) it is evident that the correlation between CHL and aerosol properties is strongly dependent on the delay time considered between the two time-series. This implies that applications at short time scales (as models used to investigate variations in aerosol properties on the daily to weekly time scale) must consider an appropriate delay time between CHL patterns and the consequent evolution of marine aerosol properties. The three short campaigns analyzed in the present Dissertation show significantly improved correlation with delay time ranging between about one to ca. three weeks. In summary, processes occurring now in the seawater will influence the atmospheric composition in one to three weeks. The discrepancy in the obtained max-correlation time-lags in the different studied environments may be due to a number of still unknown factors; this suggests that further studies are needed to better assess the time-lag issue.

To conclude, this work contributes to fill the current knowledge gap on the dynamics of phytoplankton-aerosol-cloud interactions in different environments. Achieving a better characterization of the time and space relationships linking marine biological activity to marine aerosol composition and properties may significantly impact our future capability of

predicting the chemical composition of the marine atmosphere, both at regional and global scale. Our results contribute to a better understanding of the natural climate system, and to evidence potential feedback mechanisms, which may result in fundamental importance to reduce the uncertainty of future climate predictions.

Bibliography

[1]. Aamaas, B., Berntsen, T.K., Fuglestvedt, J.S., Shine, K.P., Collins, W.J., Regional temperature change potentials for short-lived climate forcers based on radiative forcing from multiple models, *Atmospheric Chemistry and Physics* **17**(2017), pp. 10795-10809.

[2]. Albrecht, B.A., AEROSOLS, CLOUD MICROPHYSICS, AND FRACTIONAL CLOUDINESS, *Science* **245**(1989), pp. 1227-1230.

[3]. Allan, J.D. *et al.*, Quantitative sampling using an Aerodyne aerosol mass spectrometer - 1. Techniques of data interpretation and error analysis, *Journal of Geophysical Research-Atmospheres* **108**(2003).

[4]. Allan, J.D. *et al.*, Iodine observed in new particle formation events in the Arctic atmosphere during ACCACIA, *Atmospheric Chemistry and Physics* **15**(2015), pp. 5599-5609.

[5]. Andersen, H., Cermak, J., Fuchs, J., Knutti, R., Lohmann, U., Understanding the drivers of marine liquid-water cloud occurrence and properties with global observations using neural networks, *Atmospheric Chemistry and Physics* **17**(2017), pp. 9535-9546.

[6]. Andreae, M.O., OCEAN-ATMOSPHERE INTERACTIONS IN THE GLOBAL BIOGEOCHEMICAL SULFUR CYCLE, *Marine Chemistry* **30**(1990), pp. 1-29.

[7]. Andreae, M.O., Elbert, W., Demora, S.J., BIOGENIC SULFUR EMISSIONS AND AEROSOLS OVER THE TROPICAL SOUTH-ATLANTIC .3. ATMOSPHERIC DIMETHYLSULFIDE, AEROSOLS AND CLOUD CONDENSATION NUCLEI, *Journal of Geophysical Research-Atmospheres* **100**(1995), pp. 11335-11356.

[8]. Andreas, E.L., SEA SPRAY AND THE TURBULENT AIR-SEA HEAT FLUXES, *Journal of Geophysical Research-Oceans* **97**(1992), pp. 11429-11441.

[9]. Arsene, C., Barnes, I., Becker, K.H., FT-IR product study of the photo-oxidation of dimethyl sulfide: Temperature and O-2 partial pressure dependence, *Physical Chemistry Chemical Physics* **1**(1999), pp. 5463-5470.

[10]. Ayers, G.P., Cainey, J.M., The CLAW hypothesis: a review of the major developments, *Environmental Chemistry* **4**(2007), pp. 366-374.

[11]. Ayers, G.P., Cainey, J.M., Gillett, R.W., Ivey, J.P., Atmospheric sulphur and cloud condensation nuclei in marine air in the Southern Hemisphere, *Philosophical Transactions of the Royal Society B-Biological Sciences* **352**(1997), pp. 203-211.

[12]. Ayers, G.P., Gras, J.L., SEASONAL RELATIONSHIP BETWEEN CLOUD CONDENSATION NUCLEI AND AEROSOL METHANESULFONATE IN MARINE AIR, *Nature* **353**(1991), pp. 834-835.

[13]. Baek, B.H., Aneja, V.P., Tong, Q.S., Chemical coupling between ammonia, acid gases, and fine particles, *Environmental Pollution* **129**(2004), pp. 89-98.

[14]. Bahreini, R. *et al.*, Organic aerosol formation in urban and industrial plumes near Houston and Dallas, Texas, *Journal of Geophysical Research-Atmospheres* **114**(2009).

[15]. Bardouki, H. *et al.*, Gaseous (DMS, MSA, SO2, H2SO4 and DMSO) and particulate (sulfate and methanesulfonate) sulfur species over the northeastern coast of Crete, *Atmospheric Chemistry and Physics* **3**(2003), pp. 1871-1886.

[16]. Barnes, I., Becker, K.H., Patroescu, I., FTIR product study of the OH initiated oxidation of dimethyl sulphide: Observation of carbonyl sulphide and dimethyl sulphoxide, *Atmospheric Environment* **30**(1996), pp. 1805-1814.

[17]. Barnes, I., Hjorth, J., Mihalopoulos, N., Dimethyl sulfide and dimethyl sulfoxide and their oxidation in the atmosphere, *Chemical Reviews* **106**(2006), pp. 940-975.

[18]. Basterretxea, G., Font-Munoz, J.S., Salgado-Hernanz, P.M., Arrieta, J., Hernandez-Carrasco, I., Patterns of chlorophyll interannual variability in Mediterranean biogeographical regions, *Remote Sensing of Environment* **215**(2018), pp. 7-17.

[19]. Bates, T.S. *et al.*, Aerosol direct radiative effects over the northwest Atlantic, northwest Pacific, and North Indian Oceans: estimates based on in-situ chemical and optical measurements and chemical transport modeling, *Atmospheric Chemistry and Physics* **6**(2006), pp. 1657-1732.

[20]. Bates, T.S. *et al.*, Variability in Marine Plankton Ecosystems Are Not Observed in Freshly Emitted Sea Spray Aerosol Over the North Atlantic Ocean, *Geophysical Research Letters* **47**(2020).

[21]. Bauer, S.E. *et al.*, Nitrate aerosols today and in 2030: a global simulation including aerosols and tropospheric ozone, *Atmospheric Chemistry and Physics* **7**(2007), pp. 5043-5059.

[22]. Becagli, S. *et al.*, Relationship between methanesulfonate (MS-) in atmospheric particulate and remotely sensed phytoplankton activity in oligo-mesotrophic central Mediterranean Sea, *Atmospheric Environment* **79**(2013), pp. 681-688.

[23]. Behrenfeld, M.J., Boss, E., Siegel, D.A., Shea, D.M., Carbon-based ocean productivity and phytoplankton physiology from space, *Global Biogeochemical Cycles* **19**(2005).

[24]. Bellacicco, M. *et al.*, Global Distribution of Non-algal Particles From Ocean Color Data and Implications for Phytoplankton Biomass Detection, *Geophysical Research Letters* **45**(2018), pp. 7672-7682.

[25]. Bellacicco, M., Volpe, G., Colella, S., Pitarch, J., Santoleri, R., Influence of photoacclimation on the phytoplankton seasonal cycle in the Mediterranean Sea as seen by satellite, *Remote Sensing of Environment* **184**(2016), pp. 595-604.

[26]. Belosi, F. *et al.*, Ground level ice nuclei particle measurements including Saharan dust events at a Po Valley rural site (San Pietro Capofiume, Italy), *Atmospheric Research* **186**(2017), pp. 116-126.

[27]. Bender, F.A.M., Engstrom, A., Karlsson, J., Factors Controlling Cloud Albedo in Marine Subtropical Stratocumulus Regions in Climate Models and Satellite Observations, *Journal of Climate* **29**(2016), pp. 3559-3587.

[28]. Bian, H.S., Prather, M.J., Fast-J2: Accurate simulation of stratospheric photolysis in global chemical models, *Journal of Atmospheric Chemistry* **41**(2002), pp. 281-296.

[29]. Bigg, E.K., ICE NUCLEUS CONCENTRATIONS IN REMOTE AREAS, *Journal of the Atmospheric Sciences* **30**(1973), pp. 1153-1157.

[30]. Bigg, E.K., Ice forming nuclei in the high Arctic, *Tellus Series B-Chemical and Physical Meteorology* **48**(1996), pp. 223-233.

[31]. Bigg, E.K., Leck, C., Cloud-active particles over the central Arctic Ocean, *Journal of Geophysical Research-Atmospheres* **106**(2001), pp. 32155-32166.

[32]. Bigg, E.K., Mossop, S.C., Meade, R.T., Thorndike, N.S.C., The measurements of Ice Nuclei concentration by means of Millipore filters. Journal of applied meteorology (1963), pp. 266-269.

[33]. Blanchard, D.C., The electrification of the atmosphere by particles from bubbles in the sea, *Progress in Oceanography* **1**(1963), pp. 73-202.

[34]. Borys, R.D., The effects of long-range transport of air pollutants on Arctic cloud-active aerosol. *Atmospheric Science*, Colorado State University, Fort Collins, Colorado, USA (1983), p. 367.

[35]. Borys, R.D., STUDIES OF ICE NUCLEATION BY ARCTIC AEROSOL ON AGASP-II, *Journal of Atmospheric Chemistry* **9**(1989), pp. 169-185.

[36]. Boucher, O. *et al.*, DMS atmospheric concentrations and sulphate aerosol indirect radiative forcing: a sensitivity study to the DMS source representation and oxidation, *Atmospheric Chemistry and Physics* **3**(2003), pp. 49-65.

[37]. Boucher, O. *et al.*, Clouds and Aerosols. In: Climate Change 2013: The Physical Science Basis. Contribution of Working Group I to the Fifth Assessment Report of the Intergovernmental Panel on Climate Change [Stocker, T.F., D. Qin, G.-K. Plattner, M. Tignor, S.K. Allen, J. Boschung, A. Nauels, Y. Xia, V. Bex and P.M. Midgley (eds.)]. Cambridge University Press, Cambridge, United Kingdom and New York, NY, USA. (2013).

[38]. Bove, M.C. *et al.*, PM10 source apportionment applying PMF and chemical tracer analysis to ship-borne measurements in the Western Mediterranean, *Atmospheric Environment* **125**(2016), pp. 140-151.

[39]. Breon, F.M., Climate - How do aerosols affect cloudiness and climate?, *Science* **313**(2006), pp. 623-624.

[40]. Bretherton, C.S., Blossey, P.N., Jones, C.R., Mechanisms of marine low cloud sensitivity to idealized climate perturbations: A single-LES exploration extending the CGILS cases, *Journal of Advances in Modeling Earth Systems* **5**(2013), pp. 316-337.

[41]. Brooks, S.D., Thornton, D.C.O., Marine Aerosols and Clouds, *Annual Review of Marine Science, Vol 10* **10**(2018), pp. 289-313.

[42]. Burrows, S.M., Hoose, C., Poschl, U., Lawrence, M.G., Ice nuclei in marine air: biogenic particles or dust?, *Atmospheric Chemistry and Physics* **13**(2013), pp. 245-267.

[43]. Burrows, S.M. *et al.*, A physically based framework for modeling the organic fractionation of sea spray aerosol from bubble film Langmuir equilibria, *Atmospheric Chemistry and Physics* **14**(2014), pp. 13601-13629.

[44]. Bycenkiene, S., Dudoitis, V., Ulevicius, V., The Use of Trajectory Cluster Analysis to Evaluate the Long-Range Transport of Black Carbon Aerosol in the South-Eastern Baltic Region, *Advances in Meteorology*(2014).

[45]. C3S, C.C.C.S., ERA5: Fifth generation of ECMWF atmospheric reanalyses of the global climate . Copernicus Climate Change Service Climate Data Store (CDS), d*ate of access* . https://cds.climate.copernicus.eu/cdsapp#!/home. (2017).

[46]. Canagaratna, M.R. *et al.*, Chemical and microphysical characterization of ambient aerosols with the aerodyne aerosol mass spectrometer, *Mass Spectrometry Reviews* **26**(2007), pp. 185-222.

[47]. Carslaw, K.S. *et al.*, A review of natural aerosol interactions and feedbacks within the Earth system, *Atmospheric Chemistry and Physics* **10**(2010), pp. 1701-1737.

[48]. Carslaw, K.S. *et al.*, Large contribution of natural aerosols to uncertainty in indirect forcing, *Nature* **503**(2013), pp. 67-+.

[49]. Cavalli, F. *et al.*, Advances in characterization of size-resolved organic matter in marine aerosol over the North Atlantic, *Journal of Geophysical Research-Atmospheres* **109**(2004).

[50]. Ceburnis, D. *et al.*, Quantification of the carbonaceous matter origin in submicron marine aerosol by C-13 and C-14 isotope analysis, *Atmospheric Chemistry and Physics* **11**(2011), pp. 8593-8606.

[51]. Chang, R.Y.W. *et al.*, Aerosol composition and sources in the central Arctic Ocean during ASCOS, *Atmospheric Chemistry and Physics* **11**(2011), pp. 10619-10636.

[52]. Charlson, R.J., Lovelock, J.E., Andreae, M.O., Warren, S.G., OCEANIC PHYTOPLANKTON, ATMOSPHERIC SULFUR, CLOUD ALBEDO AND CLIMATE, *Nature* **326**(1987), pp. 655-661.

[53]. Chen, Q.J., Sherwen, T., Evans, M., Alexander, B., DMS oxidation and sulfur aerosol formation in the marine troposphere: a focus on reactive halogen and multiphase chemistry, *Atmospheric Chemistry and Physics* **18**(2018), pp. 13617-13637.

[54]. Choi, Y.S., Lindzen, R.S., Ho, C.H., Kim, J., Space observations of cold-cloud phase change, *Proceedings of the National Academy of Sciences of the United States of America* **107**(2010), pp. 11211-11216.

[55]. Cochran, R.E. *et al.*, Molecular Diversity of Sea Spray Aerosol Particles: Impact of Ocean Biology on Particle Composition and Hygroscopicity, *Chem* **2**(2017a), pp. 655-667.

[56]. Cochran, R.E., Ryder, O.S., Grassian, V.H., Prather, K.A., Sea Spray Aerosol: The Chemical Link between the Oceans, Atmosphere, and Climate, *Accounts of Chemical Research* **50**(2017b), pp. 599-604.

[57]. Collins, D.B. *et al.*, Impact of marine biogeochemistry on the chemical mixing state and cloud forming ability of nascent sea spray aerosol, *Journal of Geophysical Research-Atmospheres* **118**(2013a), pp. 8553-8565.

[58]. Collins, W.J. *et al.*, Global and regional temperature-change potentials for near-term climate forcers, *Atmospheric Chemistry and Physics* **13**(2013b), pp. 2471-2485.

[59]. Conen, F., Morris, C.E., Leifeld, J., Yakutin, M.V., Alewell, C., Biological residues define the ice nucleation properties of soil dust, *Atmospheric Chemistry and Physics* **11**(2011), pp. 9643-9648.

[60]. Conen, F., Stopelli, E., Zimmermann, L., Clues that decaying leaves enrich Arctic air with ice nucleating particles, *Atmospheric Environment* **129**(2016), pp. 91-94.

[61]. Costa, A. *et al.*, Classification of Arctic, midlatitude and tropical clouds in the mixed-phase temperature regime, *Atmospheric Chemistry and Physics* **17**(2017), pp. 12219-12238.

[62]. Creamean, J.M. *et al.*, Marine and terrestrial influences on ice nucleating particles during continuous springtime measurements in an Arctic oilfield location, *Atmospheric Chemistry and Physics* **18**(2018), pp. 18023-18042.

[63]. Crewell, S., Lohnert, U., Accuracy of cloud liquid water path from ground-based microwave radiometry - 2. Sensor accuracy and synergy, *Radio Science* **38**(2003).

[64]. Cristofanelli, P. *et al.*, Investigation of reactive gases and methane variability in the coastal boundary layer of the central Mediterranean basin, *Elementa-Science of the Anthropocene* **5**(2017), pp. 1-21.

[65]. Cristofanelli, P. *et al.*, New "Smart" Systems for Atmospheric Aerosol and Reactive Gas Sampling in Ambient Air, *Sensors* **18**(2018).

[66]. Crocker, D.R. *et al.*, Biological Influence on delta C-13 and Organic Composition of Nascent Sea Spray Aerosol, *Acs Earth and Space Chemistry* **4**(2020), pp. 1686-1699.

[67]. Croft, B. *et al.*, Factors controlling marine aerosol size distributions and their climate effects over the northwest Atlantic Ocean region, *Atmospheric Chemistry and Physics* **21**(2021), pp. 1889-1916.

[68]. D'Alimonte, D., Melin, F., Zibordi, G., Berthon, J.F., Use of the novelty detection technique to identify the range of applicability of empirical ocean color algorithms, *Ieee Transactions on Geoscience and Remote Sensing* **41**(2003), pp. 2833-2843.

[69]. D'Ortenzio, F., d'Alcala, M.R., On the trophic regimes of the Mediterranean Sea: a satellite analysis, *Biogeosciences* **6**(2009), pp. 139-148.

[70]. Dall'Olmo, G., Boss, E., Behrenfeld, M.J., Westberry, T.K., Particulate optical scattering coefficients along an Atlantic Meridional Transect, *Optics Express* **20**(2012), pp. 21532-21551.

[71]. Dall'Olmo, G., Westberry, T.K., Behrenfeld, M.J., Boss, E., Slade, W.H., Significant contribution of large particles to optical backscattering in the open ocean, *Biogeosciences* **6**(2009), pp. 947-967.

[72]. Dall'Osto, M. *et al.*, Simultaneous Detection of Alkylamines in the Surface Ocean and Atmosphere of the Antarctic Sympagic Environment, *Acs Earth and Space Chemistry* **3**(2019), pp. 854-+.

[73]. Dall'Osto, M. *et al.*, Arctic sea ice melt leads to atmospheric new particle formation, *Scientific Reports* **7**(2017a).

[74]. Dall'Osto, M. *et al.*, Aerosol properties associated with air masses arriving into the North East Atlantic during the 2008 Mace Head EUCAARI intensive observing period: an overview, *Atmospheric Chemistry and Physics* **10**(2010), pp. 8413-8435.

[75]. Dall'Osto, M. *et al.*, Regions of open water and melting sea ice drive new particle formation in North East Greenland, *Scientific Reports* **8**(2018).

[76]. Dall'Osto, M. *et al.*, Antarctic sea ice region as a source of biogenic organic nitrogen in aerosols, *Scientific Reports* **7**(2017b).

[77]. DeCarlo, P.F. *et al.*, Field-deployable, high-resolution, time-of-flight aerosol mass spectrometer, *Analytical Chemistry* **78**(2006), pp. 8281-8289.

[78]. Decesari, S. *et al.*, Shipborne measurements of Antarctic submicron organic aerosols: an NMR perspective linking multiple sources and bioregions, *Atmospheric Chemistry and Physics* **20**(2020), pp. 4193-4207.

[79]. DeMott, P.J. *et al.*, Sea spray aerosol as a unique source of ice nucleating particles, *Proceedings of the National Academy of Sciences of the United States of America* **113**(2016), pp. 5797-5803.

[80]. DeMott, P.J. *et al.*, The Fifth International Workshop on Ice Nucleation phase 2 (FIN-02): laboratory intercomparison of ice nucleation measurements, *Atmospheric Measurement Techniques* **11**(2018), pp. 6231-6257.

[81]. DeMott, P.J. *et al.*, Predicting global atmospheric ice nuclei distributions and their impacts on climate, *Proceedings of the National Academy of Sciences of the United States of America* **107**(2010), pp. 11217-11222.

[82]. Dorling, S.R., Davies, T.D., Pierce, C.E., CLUSTER-ANALYSIS - A TECHNIQUE FOR ESTIMATING THE SYNOPTIC METEOROLOGICAL CONTROLS ON AIR AND PRECIPITATION CHEMISTRY - METHOD AND APPLICATIONS, *Atmospheric Environment Part a-General Topics* **26**(1992), pp. 2575-2581.

[83]. Duan, Y.J., Petters, M.D., Barros, A.P., Understanding aerosol-cloud interactions through modeling the development of orographic cumulus congestus during IPHEx, *Atmospheric Chemistry and Physics* **19**(2019), pp. 1413-1437.

[84]. Dusek, U. *et al.*, Size matters more than chemistry for cloud-nucleating ability of aerosol particles, *Science* **312**(2006), pp. 1375-1378.

[85]. El Hourany, R. *et al.*, Phytoplankton Diversity in the Mediterranean Sea From Satellite Data Using Self-Organizing Maps. Journal of Geophysical Research: Oceans (2019).

[86]. Facchini, M.C. *et al.*, Important Source of Marine Secondary Organic Aerosol from Biogenic Amines, *Environmental Science & Technology* **42**(2008), pp. 9116-9121.

[87]. Falkowski, P.G. *et al.*, NATURAL VERSUS ANTHROPOGENIC FACTORS AFFECTING LOW-LEVEL CLOUD ALBEDO OVER THE NORTH-ATLANTIC, *Science* **256**(1992), pp. 1311-1313.

[88]. Fan, C.X. *et al.*, Strong Precipitation Suppression by Aerosols in Marine Low Clouds, *Geophysical Research Letters* **47**(2020).

[89]. Fanourgakis, G.S. *et al.*, Evaluation of global simulations of aerosol particle and cloud condensation nuclei number, with implications for cloud droplet formation, *Atmospheric Chemistry and Physics* **19**(2019), pp. 8591-8617.

[90]. Feingold, G., Eberhard, W.L., Veron, D.E., Previdi, M., First measurements of the Twomey indirect effect using ground-based remote sensors, *Geophysical Research Letters* **30**(2003).

[91]. Fiore, A.M., Naik, V., Leibensperger, E.M., Air Quality and Climate Connections, *Journal of the Air & Waste Management Association* **65**(2015), pp. 645-685.

[92]. Fitzgerald, J.W., MARINE AEROSOLS - A REVIEW, *Atmospheric Environment Part a-General Topics* **25**(1991), pp. 533-545.

[93]. Fossum, K.N. *et al.*, Summertime Primary and Secondary Contributions to Southern Ocean Cloud Condensation Nuclei, *Scientific Reports* **8**(2018).

[94]. Freud, E., Rosenfeld, D., Linear relation between convective cloud drop number concentration and depth for rain initiation, *Journal of Geophysical Research-Atmospheres* **117**(2012).

[95]. Frey, L., Bender, F.A.M., Svensson, G., Cloud albedo changes in response to anthropogenic sulfate and non-sulfate aerosol forcings in CMIP5 models, *Atmospheric Chemistry and Physics* **17**(2017), pp. 9145-9162.

[96]. Friedland, K.D. *et al.*, Seasonal phytoplankton blooms in the North Atlantic linked to the overwintering strategies of copepods, *Elementa-Science of the Anthropocene* **4**(2016), pp. 1-19.

[97]. Frohlich-Nowoisky, J. *et al.*, Ice nucleation activity in the widespread soil fungus Mortierella alpina, *Biogeosciences* **12**(2015), pp. 1057-1071.

[98]. Fuentes, E., Coe, H., Green, D., McFiggans, G., On the impacts of phytoplankton-derived organic matter on the properties of the primary marine aerosol - Part 2: Composition, hygroscopicity and cloud condensation activity, *Atmospheric Chemistry and Physics* **11**(2011), pp. 2585-2602.

[99]. Gali, M. *et al.*, Diel patterns of oceanic dimethylsulfide (DMS) cycling: Microbial and physical drivers, *Global Biogeochemical Cycles* **27**(2013), pp. 620-636.

[100]. Gantt, B., Meskhidze, N., The physical and chemical characteristics of marine primary organic aerosol: a review, *Atmospheric Chemistry and Physics* **13**(2013), pp. 3979-3996.

[101]. Gantt, B. *et al.*, Wind speed dependent size-resolved parameterization for the organic mass fraction of sea spray aerosol, *Atmospheric Chemistry and Physics* **11**(2011), pp. 8777-8790.

[102]. Gantt, B. *et al.*, Global distribution and climate forcing of marine organic aerosol - Part 2: Effects on cloud properties and radiative forcing, *Atmospheric Chemistry and Physics* **12**(2012), pp. 6555-6563.

[103]. Garrett, T.J., Zhao, C., Dong, X., Mace, G.G., Hobbs, P.V., Effects of varying aerosol regimes on low-level Arctic stratus, *Geophysical Research Letters* **31**(2004).

[104]. Giardi, F. *et al.*, Size distribution and ion composition of aerosol collected at Ny-lesund in the spring-summer field campaign 2013, *Rendiconti Lincei-Scienze Fisiche E Naturali* **27**(2016), pp. 47-58.

[105]. Gondwe, M., Krol, M., Gieskes, W., Klaassen, W., de Baar, H., The contribution of ocean-leaving DMS to the global atmospheric burdens of DMS, MSA, SO2, and NSS SO4=, *Global Biogeochemical Cycles* **17**(2003).

[106]. Grigas, T. *et al.*, Sophisticated Clean Air Strategies Required to Mitigate Against Particulate Organic Pollution, *Scientific Reports* **7**(2017).

[107]. Halsey, K.H., Jones, B.M., Phytoplankton Strategies for Photosynthetic Energy Allocation, *Annual Review of Marine Science, Vol 7* **7**(2015), pp. 265-297.

[108]. Hamilton, D.S. *et al.*, Occurrence of pristine aerosol environments on a polluted planet, *Proceedings of the National Academy of Sciences of the United States of America* **111**(2014), pp. 18466-18471.

[109]. Hartmann, M. *et al.*, Variation of Ice Nucleating Particles in the European Arctic Over the Last Centuries, *Geophysical Research Letters* **46**(2019), pp. 4007-4016.

[110]. Hasenecz, E.S. *et al.*, Marine Bacteria Affect Saccharide Enrichment in Sea Spray Aerosol during a Phytoplankton Bloom, *Acs Earth and Space Chemistry* **4**(2020), pp. 1638-1649.

[111]. Heese, B., Flentje, H., Althausen, D., Ansmann, A., Frey, S., Ceilometer lidar comparison: backscatter coefficient retrieval and signal-to-noise ratio determination, *Atmospheric Measurement Techniques* **3**(2010), pp. 1763-1770.

[112]. Hegg, D.A., Dependence of marine stratocumulus formation on aerosols, *Geophysical Research Letters* **26**(1999), pp. 1429-1432.

[113]. Hegg, D.A., Ferek, R.J., Hobbs, P.V., Radke, L.F., DIMETHYL SULFIDE AND CLOUD CONDENSATION NUCLEUS CORRELATIONS IN THE NORTHEAST PACIFIC-OCEAN, *Journal of Geophysical Research-Atmospheres* **96**(1991), pp. 13189-13191.

[114]. Heidam, N.Z., Wahlin, P., Christensen, J.H., Tropospheric gases and aerosols in northeast Greenland, *Journal of the Atmospheric Sciences* **56**(1999), pp. 261-278.

[115]. Heintzenberg, J., Covert, D.C., Van Dingenen, R., Size distribution and chemical composition of marine aerosols: a compilation and review, *Tellus Series B-Chemical and Physical Meteorology* **52**(2000), pp. 1104-1122.

[116]. Helfrich, S.R., McNamara, D., Ramsay, B.H., Baldwin, T., Kasheta, T., Enhancements to, and forthcoming developments in the Interactive Multisensor Snow and Ice Mapping System (IMS), *Hydrological Processes* **21**(2007), pp. 1576-1586.

[117]. Hezel, P.J. *et al.*, Modeled methanesulfonic acid (MSA) deposition in Antarctica and its relationship to sea ice, *Journal of Geophysical Research-Atmospheres* **116**(2011).

[118]. Hill, R.W., White, B.A., Cottrell, M.T., Dacey, J.W.H., Virus-mediated total release of dimethylsulfoniopropionate from marine phytoplankton: a potential climate process, *Aquatic Microbial Ecology* **14**(1998), pp. 1-6.

[119]. Hiranuma, N. *et al.*, A comprehensive characterization of ice nucleation by three different types of cellulose particles immersed in water, *Atmospheric Chemistry and Physics* **19**(2019), pp. 4823-4849.

[120]. Hoose, C., Mohler, O., Heterogeneous ice nucleation on atmospheric aerosols: a review of results from laboratory experiments, *Atmospheric Chemistry and Physics* **12**(2012), pp. 9817-9854.

[121]. Hoppel, W.A., Fitzgerald, J.W., Frick, G.M., Larson, R.E., Mack, E.J., AEROSOL SIZE DISTRIBUTIONS AND OPTICAL-PROPERTIES FOUND IN THE MARINE BOUNDARY-LAYER OVER THE ATLANTIC-OCEAN, *Journal of Geophysical Research-Atmospheres* **95**(1990), pp. 3659-3686.

[122]. Hoppel, W.A., Frick, G.M., Fitzgerald, J., Larson, R.E., MARINE BOUNDARY-LAYER MEASUREMENTS OF NEW PARTICLE FORMATION AND THE EFFECTS NONPRECIPITATING CLOUDS HAVE ON AEROSOL-SIZE DISTRIBUTION, *Journal of Geophysical Research-Atmospheres* **99**(1994), pp. 14443-14459.

[123]. Hoppel, W.A., Frick, G.M., Fitzgerald, J.W., Deducing droplet concentration and supersaturation in marine boundary layer clouds from surface aerosol measurements, *Journal of Geophysical Research-Atmospheres* **101**(1996), pp. 26553-26565.

[124]. Hoppel, W.A., Frick, G.M., Larson, R.E., EFFECT OF NONPRECIPITATING CLOUDS ON THE AEROSOL SIZE DISTRIBUTION IN THE MARINE BOUNDARY-LAYER, *Geophysical Research Letters* **13**(1986), pp. 125-128.

[125]. Hsu, Y.K., Holsen, T.M., Hopke, P.K., Comparison of hybrid receptor models to locate PCB sources in Chicago, *Atmospheric Environment* **37**(2003), pp. 545-562.

[126]. Hudson, J.G. *et al.*, Cloud condensation nuclei and ship tracks, *Journal of the Atmospheric Sciences* **57**(2000), pp. 2696-2706.

[127]. Huntzicker, J.J., Cary, R.A., Ling, C.S., NEUTRALIZATION OF SULFURIC-ACID AEROSOL BY AMMONIA, *Environmental Science & Technology* **14**(1980), pp. 819-824.

[128]. Illingworth, A.J. *et al.*, Cloudnet - Continuous evaluation of cloud profiles in seven operational models using ground-based observations, *Bulletin of the American Meteorological Society* **88**(2007), pp. 883-+.

[129]. Irish, V.E. *et al.*, Ice nucleating particles in the marine boundary layer in the Canadian Arctic during summer 2014, *Atmospheric Chemistry and Physics* **19**(2019), pp. 1027-1039.

[130]. Janssen, R.H.H. *et al.*, Estimating seasonal variations in cloud droplet number concentration over the boreal forest from satellite observations, *Atmospheric Chemistry and Physics* **11**(2011), pp. 7701-7713.

[131]. Jeong, U. *et al.*, Estimation of the contributions of long range transported aerosol in East Asia to carbonaceous aerosol and PM concentrations in Seoul, Korea using highly time resolved measurements: a PSCF model approach, *Journal of Environmental Monitoring* **13**(2011), pp. 1905-1918.

[132]. Jimenez, J.L. *et al.*, Ambient aerosol sampling using the Aerodyne Aerosol Mass Spectrometer, *Journal of Geophysical Research-Atmospheres* **108**(2003).

[133]. Jones, A., Roberts, D.L., Slingo, A., A CLIMATE MODEL STUDY OF INDIRECT RADIATIVE FORCING BY ANTHROPOGENIC SULFATE AEROSOLS, *Nature* **370**(1994), pp. 450-453.

[134]. Jones, T.A., Christopher, S.A., Quaas, J., A six year satellite-based assessment of the regional variations in aerosol indirect effects, *Atmospheric Chemistry and Physics* **9**(2009), pp. 4091-4114.

[135]. Kaku, K.C. *et al.*, Organics in the Northeastern Pacific and their impacts on aerosol hygroscopicity in the subsaturated and supersaturated regimes, *Atmospheric Chemistry and Physics* **6**(2006), pp. 4101-4115.

[136]. Kanji, Z.A. *et al.*, Overview of Ice Nucleating Particles, *Ice Formation and Evolution in Clouds and Precipitation: Measurement and Modeling Challenges* **58**(2017).

[137]. Karaca, F., Anil, I., Alagha, O., Long-range potential source contributions of episodic aerosol events to PM10 profile of a megacity, *Atmospheric Environment* **43**(2009), pp. 5713-5722.

[138]. Kasparian, J. *et al.*, Assessing the Dynamics of Organic Aerosols over the North Atlantic Ocean, *Scientific Reports* **7**(2017).

[139]. Keene, W.C. *et al.*, Factors That Modulate Properties of Primary Marine Aerosol Generated From Ambient Seawater on Ships at Sea, *Journal of Geophysical Research-Atmospheres* **122**(2017), pp. 11961-11990.

[140]. Keene, W.C. *et al.*, Chemical and physical characteristics of nascent aerosols produced by bursting bubbles at a model air-sea interface, *Journal of Geophysical Research-Atmospheres* **112**(2007).

[141]. Keller, M.D., Bellows, W.K., Guillard, R.R.L., DIMETHYL SULFIDE PRODUCTION IN MARINE-PHYTOPLANKTON, *Acs Symposium Series* **393**(1989), pp. 167-182.

[142]. Kieber, D.J. *et al.*, Coupled ocean-atmosphere loss of marine refractory dissolved organic carbon, *Geophysical Research Letters* **43**(2016), pp. 2765-2772.

[143]. Kim, A.H., Yum, S.S., Lee, H., Chang, D.Y., Shim, S., Polar Cooling Effect Due to Increase of Phytoplankton and Dimethyl-Sulfide Emission, *Atmosphere* **9**(2018).

[144]. Kim, B.G., Miller, M.A., Schwartz, S.E., Liu, Y.G., Min, Q.L., The role of adiabaticity in the aerosol first indirect effect, *Journal of Geophysical Research-Atmospheres* **113**(2008).

[145]. Kleefeld, C. *et al.*, Relative contribution of submicron and supermicron particles to aerosol light scattering in the marine boundary layer, *Journal of Geophysical Research-Atmospheres* **107**(2002).

[146]. Klein, S.A., Hartmann, D.L., THE SEASONAL CYCLE OF LOW STRATIFORM CLOUDS, *Journal of Climate* **6**(1993), pp. 1587-1606.

[147]. Kloster, S. *et al.*, DMS cycle in the marine ocean-atmosphere system - a global model study, *Biogeosciences* **3**(2006), pp. 29-51.

[148]. Kocak, M., Kubilay, N., Mihalopoulos, N., Ionic composition of lower tropospheric aerosols at a Northeastern Mediterranean site: implications regarding sources and long-range transport, *Atmospheric Environment* **38**(2004), pp. 2067-2077.

[149]. Kogan, Z.N., Kogan, Y.L., Lilly, D.K., Evaluation of sulfate aerosols indirect effect in marine stratocumulus clouds using observation-derived cloud climatology, *Geophysical Research Letters* **23**(1996), pp. 1937-1940.

[150]. Koike, M. *et al.*, Year-Round In Situ Measurements of Arctic Low-Level Clouds: Microphysical Properties and Their Relationships With Aerosols, *Journal of Geophysical Research-Atmospheres* **124**(2019), pp. 1798-1822.

[151]. Korhonen, H., Carslaw, K.S., Spracklen, D.V., Mann, G.W., Woodhouse, M.T., Influence of oceanic dimethyl sulfide emissions on cloud condensation nuclei concentrations and seasonality over the remote Southern Hemisphere oceans: A global model study, *Journal of Geophysical Research-Atmospheres* **113**(2008).

[152]. Korolev, A., Limitations of the wegener-bergeron-findeisen mechanism in the evolution of mixed-phase clouds, *Journal of the Atmospheric Sciences* **64**(2007), pp. 3372-3375.

[153]. Korolev, A., Field, P.R., The effect of dynamics on mixed-phase clouds: Theoretical considerations, *Journal of the Atmospheric Sciences* **65**(2008), pp. 66-86.

[154]. Kouvarakis, G., Mihalopoulos, N., Seasonal variation of dimethylsulfide in the gas phase and of methanesulfonate and non-sea-salt sulfate in the aerosols phase in the Eastern Mediterranean atmosphere, *Atmospheric Environment* **36**(2002), pp. 929-938.

[155]. Kwint, R.L.J., Kramer, K.J.M., DIMETHYLSULFIDE PRODUCTION BY PLANKTON COMMUNITIES, *Marine Ecology Progress Series* **121**(1995), pp. 227-237.

[156]. Köhler, H., The nucleus in and the growth of hygroscopic droplets. Transactions of the Faraday Society (1936), pp. 1152-1161.

[157]. Lacour, L., Claustre, H., Prieur, L., D'Ortenzio, F., Phytoplankton biomass cycles in the North Atlantic subpolar gyre: A similar mechanism for two different blooms in the Labrador Sea, *Geophysical Research Letters* **42**(2015), pp. 5403-5410.

[158]. Lana, A., Simo, R., Vallina, S.M., Dachs, J., Potential for a biogenic influence on cloud microphysics over the ocean: a correlation study with satellite-derived data, *Atmospheric Chemistry and Physics* **12**(2012), pp. 7977-7993.

[159]. Lance, S., Nenes, A., Rissman, T.A., Chemical and dynamical effects on cloud droplet number: Implications for estimates of the aerosol indirect effect, *Journal of Geophysical Research-Atmospheres* **109**(2004).

[160]. Lange, R., Dall'Osto, M., Wex, H., Skov, H., Massling, A., Large Summer Contribution of Organic Biogenic Aerosols to Arctic Cloud Condensation Nuclei, *Geophysical Research Letters* **46**(2019), pp. 11500-11509.

[161]. Langmann, B., Scannell, C., O'Dowd, C., New Directions: Organic matter contribution to marine aerosols and cloud condensation nuclei, *Atmospheric Environment* **42**(2008), pp. 7821-7822.

[162]. Laroche, D. *et al.*, DMSP synthesis and exudation in phytoplankton: a modeling approach, *Marine Ecology Progress Series* **180**(1999), pp. 37-49.

[163]. Lau, K.M., Wu, H.T., Warm rain processes over tropical oceans and climate implications, *Geophysical Research Letters* **30**(2003).

[164]. Lavigne, H. *et al.*, Enhancing the comprehension of mixed layer depth control on the Mediterranean phytoplankton phenology, *Journal of Geophysical Research-Oceans* **118**(2013), pp. 3416-3430.

[165]. Leaitch, W.R. *et al.*, Physical and chemical observations in marine stratus during the 1993 North Atlantic Regional Experiment: Factors controlling cloud droplet number concentrations, *Journal of Geophysical Research-Atmospheres* **101**(1996), pp. 29123-29135.

[166]. Lee, C. *et al.*, Advancing Model Systems for Fundamental Laboratory Studies of Sea Spray Aerosol Using the Microbial Loop, *Journal of Physical Chemistry A* **119**(2015), pp. 8860-8870.

[167]. Lee, Z., Update of the Quasi-Analytical Algorithm (QAA_v6) http://www.ioccg.org/groups/Software_OCA/QAA_v6_2014209.pdf. (2014).

[168]. Lee, Z.P., Carder, K.L., Arnone, R.A., Deriving inherent optical properties from water color: a multiband quasi-analytical algorithm for optically deep waters, *Applied Optics* **41**(2002), pp. 5755-5772.

[169]. Lehahn, Y. *et al.*, Decoupling Physical from Biological Processes to Assess the Impact of Viruses on a Mesoscale Algal Bloom, *Current Biology* **24**(2014), pp. 2041-2046.

[170]. Li, S.M., Barrie, L.A., Toom, D., Seasonal variations of methanesulfonate, non-sea-salt sulfate, and sulfur dioxide at three sites in Canada, *Journal of Geophysical Research-Atmospheres* **101**(1996), pp. 4165-4173.

[171]. Li, Z., Xue, H.W., Chen, J.P., Wang, W.C., Meteorological and Aerosol Effects on Marine Stratocumulus, *Journal of the Atmospheric Sciences* **73**(2016), pp. 807-820.

[172]. Liou, K.N., Ou, S.C., THE ROLE OF CLOUD MICROPHYSICAL PROCESSES IN CLIMATE - AN ASSESSMENT FROM A ONE-DIMENSIONAL PERSPECTIVE, *Journal of Geophysical Research-Atmospheres* **94**(1989), pp. 8599-8607.

[173]. Liu, J.J., Li, Z.Q., Aerosol properties and their influences on low warm clouds during the Two-Column Aerosol Project, *Atmospheric Chemistry and Physics* **19**(2019), pp. 9515-9529.

[174]. Liu, J.J., Li, Z.Q., Cribb, M., Response of Marine Boundary Layer Cloud Properties to Aerosol Perturbations Associated with Meteorological Conditions from the 19-Month AMF-Azores Campaign, *Journal of the Atmospheric Sciences* **73**(2016), pp. 4253-4268.

[175]. Liu, T.Q. *et al.*, Effect of aerosols on the macro- and micro-physical properties of warm clouds in the Beijing-Tianjin-Hebei region, *Science of the Total Environment* **720**(2020a).

[176]. Liu, Z. *et al.*, Evaluation of Cloud and Precipitation Response to Aerosols in WRF-Chem With Satellite Observations, *Journal of Geophysical Research-Atmospheres* **125**(2020b).

[177]. Loeb, N.G., Schuster, G.L., An observational study of the relationship between cloud, aerosol and meteorology in broken low-level cloud conditions, *Journal of Geophysical Research-Atmospheres* **113**(2008).

[178]. Lohmann, U., Feichter, J., Global indirect aerosol effects: a review, *Atmospheric Chemistry and Physics* **5**(2005), pp. 715-737.

[179]. Lohmann, U., Leck, C., Importance of submicron surface-active organic aerosols for pristine Arctic clouds, *Tellus Series B-Chemical and Physical Meteorology* **57**(2005), pp. 261-268.

[180]. Lohnert, U., Crewell, S., Accuracy of cloud liquid water path from ground-based microwave radiometry - 1. Dependency on cloud model statistics, *Radio Science* **38**(2003).

[181]. Lohnert, U., Turner, D.D., Crewell, S., Ground-Based Temperature and Humidity Profiling Using Spectral Infrared and Microwave Observations. Part I: Simulated Retrieval Performance in Clear-Sky Conditions, *Journal of Applied Meteorology and Climatology* **48**(2009), pp. 1017-1032.

[182]. Lowe, S.J. *et al.*, Key drivers of cloud response to surface-active organics, *Nature Communications* **10**(2019).

[183]. Lupi, A. *et al.*, Multi-seasonal ultrafine aerosol particle number concentration measurements at the Gruvebadet observatory, Ny-lesund, Svalbard Islands, *Rendiconti Lincei-Scienze Fisiche E Naturali* **27**(2016), pp. 59-71.

[184]. Mahmood, R., von Salzen, K., Norman, A.L., Gali, M., Levasseur, M., Sensitivity of Arctic sulfate aerosol and clouds to changes in future surface seawater dimethylsulfide concentrations, *Atmospheric Chemistry and Physics* **19**(2019), pp. 6419-6435.

[185]. Marti, J.J. *et al.*, H2SO4 vapor pressure of sulfuric acid and ammonium sulfate solutions, *Journal of Geophysical Research-Atmospheres* **102**(1997), pp. 3725-3735.

[186]. Martinez, E., Antoine, D., D'Ortenzio, F., Montegut, C.D., Phytoplankton spring and fall blooms in the North Atlantic in the 1980s and 2000s, *Journal of Geophysical Research-Oceans* **116**(2011).

[187]. Martucci, G. *et al.*, Comparison of In-Situ, Satellite and Ground-Based Remote Sensing Retrievals of Liquid Cloud Microphysics During MACLOUD. *19th International Conference on Nucleation and Atmospheric Aerosols (ICNAA)*, Colorado State Univ, Ctr Arts, Fort Collins, CO (2013), pp. 828-831.

[188]. Martucci, G., Milroy, C., O'Dowd, C.D., Detection of Cloud-Base Height Using Jenoptik CHM15K and Vaisala CL31 Ceilometers, *Journal of Atmospheric and Oceanic Technology* **27**(2010), pp. 305-318.

[189]. Martucci, G., O'Dowd, C.D., Ground-based retrieval of continental and marine warm cloud microphysics, *Atmospheric Measurement Techniques* **4**(2011), pp. 2749-2765.

[190]. Masiol, M., Squizzato, S., Cheng, M.D., Rich, D.Q., Hopke, P.K., Differential Probability Functions for Investigating Long-term Changes in Local and Regional Air Pollution Sources, *Aerosol and Air Quality Research* **19**(2019), pp. 724-736.

[191]. Mason, R.H. *et al.*, Size-resolved measurements of ice-nucleating particles at six locations in North America and one in Europe, *Atmospheric Chemistry and Physics* **16**(2016), pp. 1637-1651.

[192]. Matrai, P.A., Vernet, M., Dynamics of the vernal bloom in the marginal ice zone of the Barents Sea: Dimethyl sulfide and dimethylsulfoniopropionate budgets, *Journal of Geophysical Research-Oceans* **102**(1997), pp. 22965-22979.

[193]. Mayer, K.J. *et al.*, Secondary Marine Aerosol Plays a Dominant Role over Primary Sea Spray Aerosol in Cloud Formation, *Acs Central Science* **6**(2020), pp. 2259-2266.

[194]. Mazzola, M., Viola, A.P., Lanconelli, C., Vitale, V., Atmospheric observations at the Amundsen-Nobile Climate Change Tower in Ny-lesund, Svalbard, *Rendiconti Lincei-Scienze Fisiche E Naturali* **27**(2016), pp. 7-18.

[195]. McCluskey, C.S. *et al.*, Observations of Ice Nucleating Particles Over Southern Ocean Waters, *Geophysical Research Letters* **45**(2018a), pp. 11989-11997.

[196]. McCluskey, C.S. *et al.*, A Dynamic Link between Ice Nucleating Particles Released in Nascent Sea Spray Aerosol and Oceanic Biological Activity during Two Mesocosm Experiments, *Journal of the Atmospheric Sciences* **74**(2017), pp. 151-166.

[197]. McCluskey, C.S. *et al.*, A Mesocosm Double Feature: Insights into the Chemical Makeup of Marine Ice Nucleating Particles, *Journal of the Atmospheric Sciences* **75**(2018b), pp. 2405-2423.

[198]. McCluskey, C.S. *et al.*, Marine and Terrestrial Organic Ice-Nucleating Particles in Pristine Marine to Continentally Influenced Northeast Atlantic Air Masses, *Journal of Geophysical Research-Atmospheres* **123**(2018c), pp. 6196-6212.

[199]. McComiskey, A., Feingold, G., The scale problem in quantifying aerosol indirect effects, *Atmospheric Chemistry and Physics* **12**(2012), pp. 1031-1049.

[200]. McComiskey, A. *et al.*, An assessment of aerosol-cloud interactions in marine stratus clouds based on surface remote sensing, *Journal of Geophysical Research-Atmospheres* **114**(2009).

[201]. McCoy, D.T. *et al.*, Natural aerosols explain seasonal and spatial patterns of Southern Ocean cloud albedo, *Science Advances* **1**(2015).

[202]. McCoy, D.T., Hartmann, D.L., Grosvenor, D.P., Observed Southern Ocean Cloud Properties and Shortwave Reflection. Part I: Calculation of SW Flux from Observed Cloud Properties, *Journal of Climate* **27**(2014), pp. 8836-8857.

[203]. McKinley, G.A., Ritzer, A.L., Lovenduski, N.S., Mechanisms of northern North Atlantic biomass variability, *Biogeosciences* **15**(2018), pp. 6049-6066.

[204]. McParland, E.L., Levine, N.M., The role of differential DMSP production and community composition in predicting variability of global surface DMSP concentrations, *Limnology and Oceanography* **64**(2019), pp. 757-773.

[205]. Melchionna, S., Bauer, M., Peters, G., A new algorithm for the extraction of cloud parameters using multipeak analysis of cloud radar data - First application and preliminary results, *Meteorologische Zeitschrift* **17**(2008), pp. 613-620.

[206]. Menon, S., Del Genio, A.D., Koch, D., Tselioudis, G., GCM Simulations of the aerosol indirect effect: Sensitivity to cloud parameterization and aerosol burden, *Journal of the Atmospheric Sciences* **59**(2002), pp. 692-713.

[207]. Meskhidze, N., Nenes, A., Phytoplankton and cloudiness in the Southern Ocean, *Science* **314**(2006), pp. 1419-1423.

[208]. Meskhidze, N., Nenes, A., Effects of Ocean Ecosystem on Marine Aerosol-Cloud Interaction, *Advances in Meteorology*(2010).

[209]. Meskhidze, N. *et al.*, Global distribution and climate forcing of marine organic aerosol: 1. Model improvements and evaluation, *Atmospheric Chemistry and Physics* **11**(2011), pp. 11689-11705.

[210]. Middlebrook, A.M., Bahreini, R., Jimenez, J.L., Canagaratna, M.R., Evaluation of Composition-Dependent Collection Efficiencies for the Aerodyne Aerosol Mass Spectrometer using Field Data, *Aerosol Science and Technology* **46**(2012), pp. 258-271.

[211]. Mihalopoulos, N., Kerminen, V.M., Kanakidou, M., Berresheim, H., Sciare, J., Formation of particulate sulfur species (sulfate and methanesulfonate) during summer over the Eastern Mediterranean: A modelling approach, *Atmospheric Environment* **41**(2007), pp. 6860-6871.

[212]. Mihalopoulos, N., Stephanou, E., Kanakidou, M., Pilitsidis, S., Bousquet, P., Tropospheric aerosol ionic composition in the Eastern Mediterranean region, *Tellus Series B-Chemical and Physical Meteorology* **49**(1997), pp. 314-326.

[213]. Miller, M.A., Yuter, S.E., Lack of correlation between chlorophyll a and cloud droplet effective radius in shallow marine clouds, *Geophysical Research Letters* **35**(2008).

[214]. Miyazaki, Y., Kawamura, K., Sawano, M., Size distributions and chemical characterization of water-soluble organic aerosols over the western North Pacific in summer, *Journal of Geophysical Research-Atmospheres* **115**(2010).

[215]. Miyazaki, Y. *et al.*, New index of organic mass enrichment in sea spray aerosols linked with senescent status in marine phytoplankton, *Scientific Reports* **10**(2020).

[216]. Monahan, E.C., Fairall, C.W., Davidson, K.L., Boyle, P.J., OBSERVED INTERRELATIONS BETWEEN 10M WINDS, OCEAN WHITECAPS AND MARINE AEROSOLS, *Quarterly Journal of the Royal Meteorological Society* **109**(1983), pp. 379-392.

[217]. Mukai, H., Yokouchi, Y., Suzuki, M., SEASONAL-VARIATION OF METHANESULFONIC-ACID IN THE ATMOSPHERE OVER THE OKI ISLANDS IN THE SEA OF JAPAN, *Atmospheric Environment* **29**(1995), pp. 1637-1648.

[218]. Murphy, D.M. *et al.*, Influence of sea-salt on aerosol radiative properties in the Southern Ocean marine boundary layer, *Nature* **392**(1998), pp. 62-65.

[219]. Murray, B.J., Cracking the problem of ice nucleation, *Science* **355**(2017), pp. 346-347.

[220]. Murray, B.J., Carslaw, K.S., Field, P.R., Opinion: Cloud-phase climate feedback and the importance of ice-nucleating particles, *Atmospheric Chemistry and Physics* **21**(2021), pp. 665-679.

[221]. Murray, B.J., O'Sullivan, D., Atkinson, J.D., Webb, M.E., Ice nucleation by particles immersed in supercooled cloud droplets, *Chemical Society Reviews* **41**(2012), pp. 6519-6554.

[222]. Myhre, G. *et al.*, Anthropogenic and Natural Radiative Forcing. In: Climate Change 2013: The Physical Science Basis. Contribution of Working Group I to the Fifth Assessment Report of the Intergovernmental Panel on Climate Change [Stocker, T.F., D. Qin, G.K. Plattner, M. Tignor, S.K. Allen, J. Boschung, A. Nauels, Y. Xia, V. Bex and P.M. Midgley (eds.)]. Cambridge University Press, Cambridge, United Kingdom and New York, NY, USA (2013).

[223]. Myhre, G. *et al.*, Aerosol-cloud interaction inferred from MODIS satellite data and global aerosol models, *Atmospheric Chemistry and Physics* **7**(2007), pp. 3081-3101.

[224]. National Ice-Center, U.S., *IMS Daily Northern Hemisphere Snow and Ice Analysis at 1 km, 4 km, and 24 km Resolutions, Version 1. updated daily*, Boulder , Colorado USA. NSIDC: National Snow and Ice Data Center (2008).

[225]. Navarro, G., Alvain, S., Vantrepotte, V., Huertas, I.E., Identification of dominant phytoplankton functional types in the Mediterranean Sea based on a regionalized remote sensing approach, *Remote Sensing of Environment* **152**(2014), pp. 557-575.

[226]. O'Dowd, C. *et al.*, Connecting marine productivity to sea-spray via nanoscale biological processes: Phytoplankton Dance or Death Disco?, *Scientific Reports* **5**(2015).

[227]. O'Dowd, C. *et al.*, Do anthropogenic, continental or coastal aerosol sources impact on a marine aerosol signature at Mace Head?, *Atmospheric Chemistry and Physics* **14**(2014), pp. 10687-10704.

[228]. O'Dowd, C.D. *et al.*, Biogenically driven organic contribution to marine aerosol, *Nature* **431**(2004), pp. 676-680.

[229]. O'Dowd, C.D. *et al.*, Marine aerosol formation from biogenic iodine emissions, *Nature* **417**(2002), pp. 632-636.

[230]. O'Dowd, C.D. *et al.*, A combined organic-inorganic sea-spray source function, *Geophysical Research Letters* **35**(2008).

[231]. O'Dowd, C.D., Lowe, J.A., Smith, M.H., Kaye, A.D., The relative importance of non-sea-salt sulphate and sea-salt aerosol to the marine cloud condensation nuclei population: An improved multi-component aerosol-cloud droplet parametrization, *Quarterly Journal of the Royal Meteorological Society* **125**(1999), pp. 1295-1313.

[232]. O'Sullivan, D. *et al.*, Ice nucleation by fertile soil dusts: relative importance of mineral and biogenic components, *Atmospheric Chemistry and Physics* **14**(2014), pp. 1853-1867.

[233]. O'Sullivan, D. *et al.*, The relevance of nanoscale biological fragments for ice nucleation in clouds, *Scientific Reports* **5**(2015).

[234]. Orellana, M.V., Matrai, P.A., Janer, M., Rauschenberg, C.D., DIMETHYLSULFONIOPROPIONATE STORAGE IN PHAEOCYSTIS (PRYMNESIOPHYCEAE) SECRETORY VESICLES, *Journal of Phycology* **47**(2011), pp. 112-117.

[235]. Ovadnevaite, J. *et al.*, On the effect of wind speed on submicron sea salt mass concentrations and source fluxes, *Journal of Geophysical Research-Atmospheres* **117**(2012).

[236]. Ovadnevaite, J. *et al.*, Submicron NE Atlantic marine aerosol chemical composition and abundance: Seasonal trends and air mass categorization, *Journal of Geophysical Research-Atmospheres* **119**(2014), pp. 11850-11863.

[237]. Ovadnevaite, J. *et al.*, Primary marine organic aerosol: A dichotomy of low hygroscopicity and high CCN activity, *Geophysical Research Letters* **38**(2011a).

[238]. Ovadnevaite, J. *et al.*, Detecting high contributions of primary organic matter to marine aerosol: A case study, *Geophysical Research Letters* **38**(2011b).

[239]. Ovadnevaite, J. *et al.*, Surface tension prevails over solute effect in organic-influenced cloud droplet activation, *Nature* **546**(2017), pp. 637-641.

[240]. Pathak, R.K., Wu, W.S., Wang, T., Summertime PM2.5 ionic species in four major cities of China: nitrate formation in an ammonia-deficient atmosphere, *Atmospheric Chemistry and Physics* **9**(2009), pp. 1711-1722.

[241]. Pitarch, J. *et al.*, Retrieval of Particulate Backscattering Using Field and Satellite Radiometry: Assessment of the QAA Algorithm, *Remote Sensing* **12**(2020).

[242]. Polissar, A.V., Hopke, P.K., Harris, J.M., Source regions for atmospheric aerosol measured at Barrow, Alaska, *Environmental Science & Technology* **35**(2001), pp. 4214-4226.

[243]. Prather, K.A. *et al.*, Bringing the ocean into the laboratory to probe the chemical complexity of sea spray aerosol, *Proceedings of the National Academy of Sciences of the United States of America* **110**(2013), pp. 7550-7555.

[244]. Preissler, J. *et al.*, Six years of surface remote sensing of stratiform warm clouds in marine and continental air over Mace Head, Ireland, *Journal of Geophysical Research-Atmospheres* **121**(2016), pp. 14538-14557.

[245]. Prenni, A.J. *et al.*, Can ice-nucleating aerosols affect arctic seasonal climate?, *Bulletin of the American Meteorological Society* **88**(2007), pp. 541-+.

[246]. Quinn, P.K., Bates, T.S., The case against climate regulation via oceanic phytoplankton sulphur emissions, *Nature* **480**(2011), pp. 51-56.

[247]. Quinn, P.K. *et al.*, Contribution of sea surface carbon pool to organic matter enrichment in sea spray aerosol, *Nature Geoscience* **7**(2014), pp. 228-232.

[248]. Quinn, P.K., Charlson, R.J., Zoller, W.H., Ammonia, the dominant base in the remote marine troposphere: a review. Tellus B: Chemical and Physical Meteorology (1987), pp. 413-425.

[249]. Quinn, P.K., Coffman, D.J., Johnson, J.E., Upchurch, L.M., Bates, T.S., Small fraction of marine cloud condensation nuclei made up of sea spray aerosol, *Nature Geoscience* **10**(2017), pp. 674-+.

[250]. Quinn, P.K., Collins, D.B., Grassian, V.H., Prather, K.A., Bates, T.S., Chemistry and Related Properties of Freshly Emitted Sea Spray Aerosol, *Chemical Reviews* **115**(2015), pp. 4383-4399.

[251]. Rap, A. *et al.*, Natural aerosol direct and indirect radiative effects, *Geophysical Research Letters* **40**(2013), pp. 3297-3301.

[252]. Reade, L., Jennings, S.G., McSweeney, G., Cloud condensation nuclei measurements at Mace Head, Ireland, over the period 1994-2002, *Atmospheric Research* **82**(2006), pp. 610-621.

[253]. Rinaldi, M. *et al.*, Evidence of a natural marine source of oxalic acid and a possible link to glyoxal, *Journal of Geophysical Research-Atmospheres* **116**(2011).

[254]. Rinaldi, M. *et al.*, Primary and Secondary Organic Marine Aerosol and Oceanic Biological Activity: Recent Results and New Perspectives for Future Studies, *Advances in Meteorology*(2010).

[255]. Rinaldi, M. *et al.*, On the representativeness of coastal aerosol studies to open ocean studies: Mace Head - a case study, *Atmospheric Chemistry and Physics* **9**(2009), pp. 9635-9646.

[256]. Rinaldi, M. *et al.*, Is chlorophyll-a the best surrogate for organic matter enrichment in submicron primary marine aerosol?, *Journal of Geophysical Research-Atmospheres* **118**(2013), pp. 4964-4973.

[257]. Rinaldi, M. *et al.*, Ground level ice nucleating particles measurements at Capo Granitola, a Mediterranean coastal site, *Atmospheric Research* **219**(2019), pp. 57-64.

[258]. Rinaldi, M. *et al.*, Contribution of Water-Soluble Organic Matter from Multiple Marine Geographic Eco-Regions to Aerosols around Antarctica, *Environmental Science & Technology* **54**(2020), pp. 7807-7817.

[259]. Roberts, G., Mauger, G., Hadley, O., Ramanathan, V., North American and Asian aerosols over the eastern Pacific Ocean and their role in regulating cloud condensation nuclei, *Journal of Geophysical Research-Atmospheres* **111**(2006).

[260]. Roberts, G.C., Nenes, A., A continuous-flow streamwise thermal-gradient CCN chamber for atmospheric measurements, *Aerosol Science and Technology* **39**(2005), pp. 206-221.

[261]. Rolph, G., Stein, A., Stunder, B., Real-time Environmental Applications and Display sYstem: READY, *Environmental Modelling & Software* **95**(2017), pp. 210-228.

[262]. Rosenfeld, D. *et al.*, Aerosol-driven droplet concentrations dominate coverage and water of oceanic low-level clouds, *Science* **363**(2019), pp. 599-+.

[263]. Ruehl, C.R., Davies, J.F., Wilson, K.R., An interfacial mechanism for cloud droplet formation on organic aerosols, *Science* **351**(2016), pp. 1447-1450.

[264]. Russell, L.M., Hawkins, L.N., Frossard, A.A., Quinn, P.K., Bates, T.S., Carbohydrate-like composition of submicron atmospheric particles and their production from ocean bubble bursting, *Proceedings of the National Academy of Sciences of the United States of America* **107**(2010), pp. 6652-6657.

[265]. Salgado-Hernanz, P.M., Racault, M.F., Font-Muñoz, J.S., Basterretxea, G., Trends in phytoplankton phenology in the Mediterranean Sea based on ocean-colour remote sensing, *Remote Sensing of Environment* ***221***(2019), pp. 50-64.

[266]. Saltzman, E.S., Marine Aerosols, *Surface Ocean--Lower Atmosphere Processes* **187**(2009), pp. 17-35.

[267]. Sammartino, M., Di Cicco, A., Marullo, S., Santoleri, R., Spatio-temporal variability of micro-, nano- and pico-phytoplankton in the Mediterranean Sea from satellite ocean colour data of SeaWiFS, *Ocean Science* **11**(2015), pp. 759-778.

[268]. Sanchez, K.J. *et al.*, Substantial Seasonal Contribution of Observed Biogenic Sulfate Particles to Cloud Condensation Nuclei, *Scientific Reports* **8**(2018).

[269]. Sanchez, K.J. *et al.*, Top-down and bottom-up aerosol-cloud closure: towards understanding sources of uncertainty in deriving cloud shortwave radiative flux, *Atmospheric Chemistry and Physics* **17**(2017), pp. 9797-9814.

[270]. Santachiara, G., Di Matteo, L., Prodi, F., Belosi, F., Atmospheric particles acting as Ice Forming Nuclei in different size ranges, *Atmospheric Research* **96**(2010), pp. 266-272.

[271]. Santl-Temkiv, T. *et al.*, Biogenic Sources of Ice Nucleating Particles at the High Arctic Site Villum Research Station, *Environmental Science & Technology* **53**(2019), pp. 10580-10590.

[272]. Sato, Y., Suzuki, K., How do aerosols affect cloudiness?, *Science* **363**(2019), pp. 580-+.

[273]. Savoie, D.L., Prospero, J.M., COMPARISON OF OCEANIC AND CONTINENTAL SOURCES OF NON-SEA-SALT SULFATE OVER THE PACIFIC-OCEAN, *Nature* **339**(1989), pp. 685-687.

[274]. Schembari, C. *et al.*, Source apportionment of PM10 in the Western Mediterranean based on observations from a cruise ship, *Atmospheric Environment* **98**(2014), pp. 510-518.

[275]. Schnell, R.C., Vali, G., BIOGENIC ICE NUCLEI .1. TERRESTRIAL AND MARINE SOURCES, *Journal of the Atmospheric Sciences* **33**(1976), pp. 1554-1564.

[276]. Sciare, J. *et al.*, Long-term observations of carbonaceous aerosols in the Austral Ocean atmosphere: Evidence of a biogenic marine organic source, *Journal of Geophysical Research-Atmospheres* **114**(2009).

[277]. Sellegri, K. *et al.*, Surface ocean microbiota determine cloud precursors, *Scientific Reports* **11**(2021).

[278]. Sellegri, K. *et al.*, Evidence of atmospheric nanoparticle formation from emissions of marine microorganisms, *Geophysical Research Letters* **43**(2016), pp. 6596-6603.

[279]. Shaw, G.E., BIO-CONTROLLED THERMOSTASIS INVOLVING THE SULFUR CYCLE, *Climatic Change* **5**(1983), pp. 297-303.

[280]. Shaw, G.E., The arctic haze phenomenon, *Bulletin of the American Meteorological Society* **76**(1995), pp. 2403-2413.

[281]. Shupe, M.D., Matrosov, S.Y., Uttal, T., Arctic mixed-phase cloud properties derived from surface-based sensors at SHEBA, *Journal of the Atmospheric Sciences* **63**(2006), pp. 697-711.

[282]. Shupe, M.D. *et al.*, Clouds at Arctic Atmospheric Observatories. Part I: Occurrence and Macrophysical Properties, *Journal of Applied Meteorology and Climatology* **50**(2011), pp. 626-644.

[283]. Si, M. *et al.*, Ice-nucleating ability of aerosol particles and possible sources at three coastal marine sites, *Atmospheric Chemistry and Physics* **18**(2018), pp. 15669-15685.

[284]. Sinclair, K. *et al.*, Observations of Aerosol-Cloud Interactions During the North Atlantic Aerosol and Marine Ecosystem Study, *Geophysical Research Letters* **47**(2020).

[285]. Slingo, A., SENSITIVITY OF THE EARTHS RADIATION BUDGET TO CHANGES IN LOW CLOUDS, *Nature* **343**(1990), pp. 49-51.

[286]. Sorooshian, A. *et al.*, On the link between ocean biota emissions, aerosol, and maritime clouds: Airborne, ground, and satellite measurements off the coast of California, *Global Biogeochemical Cycles* **23**(2009).

[287]. Stein, A.F. *et al.*, NOAA'S HYSPLIT ATMOSPHERIC TRANSPORT AND DISPERSION MODELING SYSTEM, *Bulletin of the American Meteorological Society* **96**(2015), pp. 2059-2077.

[288]. Stevens, B., Feingold, G., Untangling aerosol effects on clouds and precipitation in a buffered system, *Nature* **461**(2009), pp. 607-613.

[289]. Stocker, T.F. *et al.*, Climate change 2013: The physical science basis." C*ontribution of working group I to the fifth assessment report of the intergovernmental panel on climate change*". Cambridge University Press (2013).

[290]. Stockwell, W.R. *et al.*, The Treasure Valley secondary aerosol study II: modeling of the formation of inorganic secondary aerosols and precursors for southwestern Idaho, *Atmospheric Environment* **37**(2003), pp. 525-534.

[291]. Stohl, A., Characteristics of atmospheric transport into the Arctic troposphere, *Journal of Geophysical Research-Atmospheres* **111**(2006).

[292]. Tesson, S.V.M., Santl-Temkiv, T., Ice Nucleation Activity and Aeolian Dispersal Success in Airborne and Aquatic Microalgae, *Frontiers in Microbiology* **9**(2018).

[293]. Thomas, M.A. *et al.*, Quantification of DMS aerosol-cloud-climate interactions using the ECHAM5-HAMMOZ model in a current climate scenario, *Atmospheric Chemistry and Physics* **10**(2010), pp. 7425-7438.

[294]. Tobo, Y. *et al.*, Glacially sourced dust as a potentially significant source of ice nucleating particles, *Nature Geoscience* **12**(2019), pp. 253-+.

[295]. Toll, V., Christensen, M., Quaas, J., Bellouin, N., Weak average liquid-cloud-water response to anthropogenic aerosols, *Nature* **572**(2019), pp. 51-+.

[296]. Toole, D.A., Siegel, D.A., Light-driven cycling of dimethylsulfide (DMS) in the Sargasso Sea: Closing the loop, *Geophysical Research Letters* **31**(2004).

[297]. Tripathi, O.P. *et al.*, Statistical analysis of eight surface ozone measurement series for various sites in Ireland, *Journal of Geophysical Research-Atmospheres* **115**(2010).

[298]. Tsigaridis, K., Koch, D., Menon, S., Uncertainties and importance of sea spray composition on aerosol direct and indirect effects, *Journal of Geophysical Research-Atmospheres* **118**(2013), pp. 220-235.

[299]. Twohy, C.H., Anderson, J.R., Droplet nuclei in non-precipitating clouds: composition and size matter, *Environmental Research Letters* **3**(2008).

[300]. Twomey, S., Pollution and the Planetary Albedo, *Atmospheric Environment* **8**(1974), pp. 1251-1256.

[301]. Twomey, S.A., Piepgrass, M., Wolfe, T.L., An assessment of the impact of pollution on global cloud albedo, *Tellus Series B-Chemical and Physical Meteorology* **36**(1984), pp. 356-366.

[302]. Udisti, R. *et al.*, Sulfate source apportionment in the Ny-Alesund (Svalbard Islands) Arctic aerosol, *Rendiconti Lincei-Scienze Fisiche E Naturali* **27**(2016), pp. 85-94.

[303]. Urbanski, S.P., Stickel, R.E., Wine, P.H., Mechanistic and kinetic study of the gas-phase reaction of hydroxyl radical with dimethyl sulfoxide, *Journal of Physical Chemistry A* **102**(1998), pp. 10522-10529.

[304]. Vaishya, A., Jennings, S.G., O'Dowd, C., Wind-driven influences on aerosol light scattering in north-east Atlantic air, *Geophysical Research Letters* **39**(2012).

[305]. Vali, G., ICE NUCLEATION WORKSHOP, 1975 LARAMIE, WYOMING, 19 MAY - 6 JUNE 1975, *Bulletin of the American Meteorological Society* **56**(1975), pp. 1180-1184.

[306]. Vali, G., DeMott, P.J., Mohler, O., Whale, T.F., Technical Note: A proposal for ice nucleation terminology, *Atmospheric Chemistry and Physics* **15**(2015), pp. 10263-10270.

[307]. Vallina, S.M., Simo, R., Strong relationship between DMS and the solar radiation dose over the global surface ocean, *Science* **315**(2007), pp. 506-508.

[308]. Vallina, S.M., Simo, R., Gasso, S., What controls CCN seasonality in the Southern Ocean? A statistical analysis based on satellite-derived chlorophyll and CCN and model-estimated OH radical and rainfall, *Global Biogeochemical Cycles* **20**(2006).

[309]. Vergara-Temprado, J. *et al.*, Contribution of feldspar and marine organic aerosols to global ice nucleating particle concentrations, *Atmospheric Chemistry and Physics* **17**(2017), pp. 3637-3658.

[310]. Vignati, E. *et al.*, Global scale emission and distribution of sea-spray aerosol: Sea-salt and organic enrichment, *Atmospheric Environment* **44**(2010), pp. 670-677.

[311]. Volpe, G., Buongiorno Nardelli, B., Cipollini, P., Santoleri, R., Robinson, I.S., Seasonal to interannual phytoplankton response to physical processes in the Mediterranean Sea from satellite observations, *Remote Sensing of Environment* **117**(2012), pp. 223-235.

[312]. Volpe, G. *et al.*, The colour of the Mediterranean Sea: Global versus regional bio-optical algorithms evaluation and implication for satellite chlorophyll estimates, *Remote Sensing of Environment* **107**(2007), pp. 625-638.

[313]. Wang, X.F. *et al.*, Microbial Control of Sea Spray Aerosol Composition: A Tale of Two Blooms, *Acs Central Science* **1**(2015), pp. 124-131.

[314]. Watts, S.F., Brimblecombe, P., Watson, A.J., Methanesulphonic acid, dimethyl sulphoxide and dimethyl sulphone in aerosols, *Atmospheric Environment. Part A. General Topics* **24**(1990), pp. 353-359.

[315]. Westberry, T., Behrenfeld, M.J., Siegel, D.A., Boss, E., Carbon-based primary productivity modeling with vertically resolved photoacclimation, *Global Biogeochemical Cycles* **22**(2008).

[316]. Westberry, T.K., Dall'Olmo, G., Boss, E., Behrenfeld, M.J., Moutin, T., Coherence of particulate beam attenuation and backscattering coefficients in diverse open ocean environments, *Optics Express* **18**(2010), pp. 15419-15425.

[317]. Westervelt, D.M., Moore, R.H., Nenes, A., Adams, P.J., Effect of primary organic sea spray emissions on cloud condensation nuclei concentrations, *Atmospheric Chemistry and Physics* **12**(2012), pp. 89-101.

[318]. Wex, H. *et al.*, Aerosol arriving on the Caribbean island of Barbados: physical properties and origin, *Atmospheric Chemistry and Physics* **16**(2016), pp. 14107-14130.

[319]. Wex, H. *et al.*, Annual variability of ice-nucleating particle concentrations at different Arctic locations, *Atmospheric Chemistry and Physics* **19**(2019), pp. 5293-5311.

[320]. Wiedensohler, A. *et al.*, Mobility particle size spectrometers: harmonization of technical standards and data structure to facilitate high quality long-term observations of atmospheric particle number size distributions, *Atmospheric Measurement Techniques* **5**(2012), pp. 657-685.

[321]. Wiedensohler, A. *et al.*, Mobility particle size spectrometers: Calibration procedures and measurement uncertainties, *Aerosol Science and Technology* **52**(2018), pp. 146-164.

[322]. Wilbourn, E.K. *et al.*, Ice Nucleation by Marine Aerosols Over the North Atlantic Ocean in Late Spring, *Journal of Geophysical Research-Atmospheres* **125**(2020).

[323]. Wilson, T.W. *et al.*, A marine biogenic source of atmospheric ice-nucleating particles, *Nature* **525**(2015), pp. 234-+.

[324]. Wolfe, G.V., Steinke, M., Grazing-activated production of dimethyl sulfide (DMS) by two clones of Emiliania huxleyi, *Limnology and Oceanography* **41**(1996), pp. 1151-1160.

[325]. Wood, R., Bretherton, C.S., On the relationship between stratiform low cloud cover and lower-tropospheric stability, *Journal of Climate* **19**(2006), pp. 6425-6432.

[326]. Woodhouse, M.T. *et al.*, Low sensitivity of cloud condensation nuclei to changes in the sea-air flux of dimethyl-sulphide, *Atmospheric Chemistry and Physics* **10**(2010), pp. 7545-7559.

[327]. Woolf, D.K., Bowyer, P.A., Monahan, E.C., DISCRIMINATING BETWEEN THE FILM DROPS AND JET DROPS PRODUCED BY A SIMULATED WHITECAP, *Journal of Geophysical Research-Oceans* **92**(1987), pp. 5142-5150.

[328]. Yoon, Y.J. *et al.*, Seasonal characteristics of the physicochemical properties of North Atlantic marine atmospheric aerosols, *Journal of Geophysical Research-Atmospheres* **112**(2007).

[329]. Zelinka, M.D., Andrews, T., Forster, P.M., Taylor, K.E., Quantifying components of aerosol-cloud-radiation interactions in climate models, *Journal of Geophysical Research-Atmospheres* **119**(2014), pp. 7599-7615.

[330]. Zhang, F.F., Du, J.Z., How to Change the Chemical Composition of Sea Spray Aerosol via Marine Bloom, *Chem* **2**(2017), pp. 610-612.

[331]. Zhao, C.F. *et al.*, Aerosol first indirect effects on non-precipitating low-level liquid cloud properties as simulated by CAM5 at ARM sites, *Geophysical Research Letters* **39**(2012).

[332]. Zhao, C.F. *et al.*, Negative Aerosol-Cloud r(e) Relationship From Aircraft Observations Over Hebei, China, *Earth and Space Science* **5**(2018), pp. 19-29.

[333]. Zhuang, G.C., Yang, G.P., Yu, J.A., Gao, Y.A., Production of DMS and DMSP in different physiological stages and salinity conditions in two marine algae, *Chinese Journal of Oceanology and Limnology* **29**(2011), pp. 369-377.

[334]. Zorn, S.R., Drewnick, F., Schott, M., Hoffmann, T., Borrmann, S., Characterization of the South Atlantic marine boundary layer aerosol using an aerodyne aerosol mass spectrometer, *Atmospheric Chemistry and Physics* **8**(2008), pp. 4711-4728.

APPENDIX

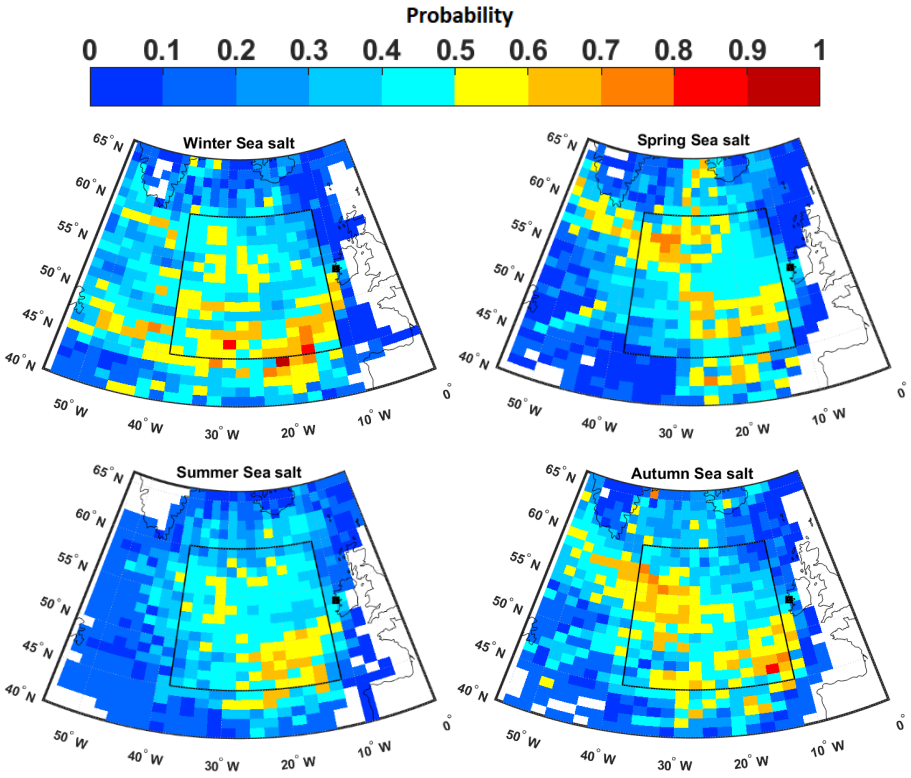

Figure S1: Seasonal PSCF distributions for sea salt considering clean marine air masses arrived at MHD during 2009-2017. The sources of high concentrations are defined above the median values.

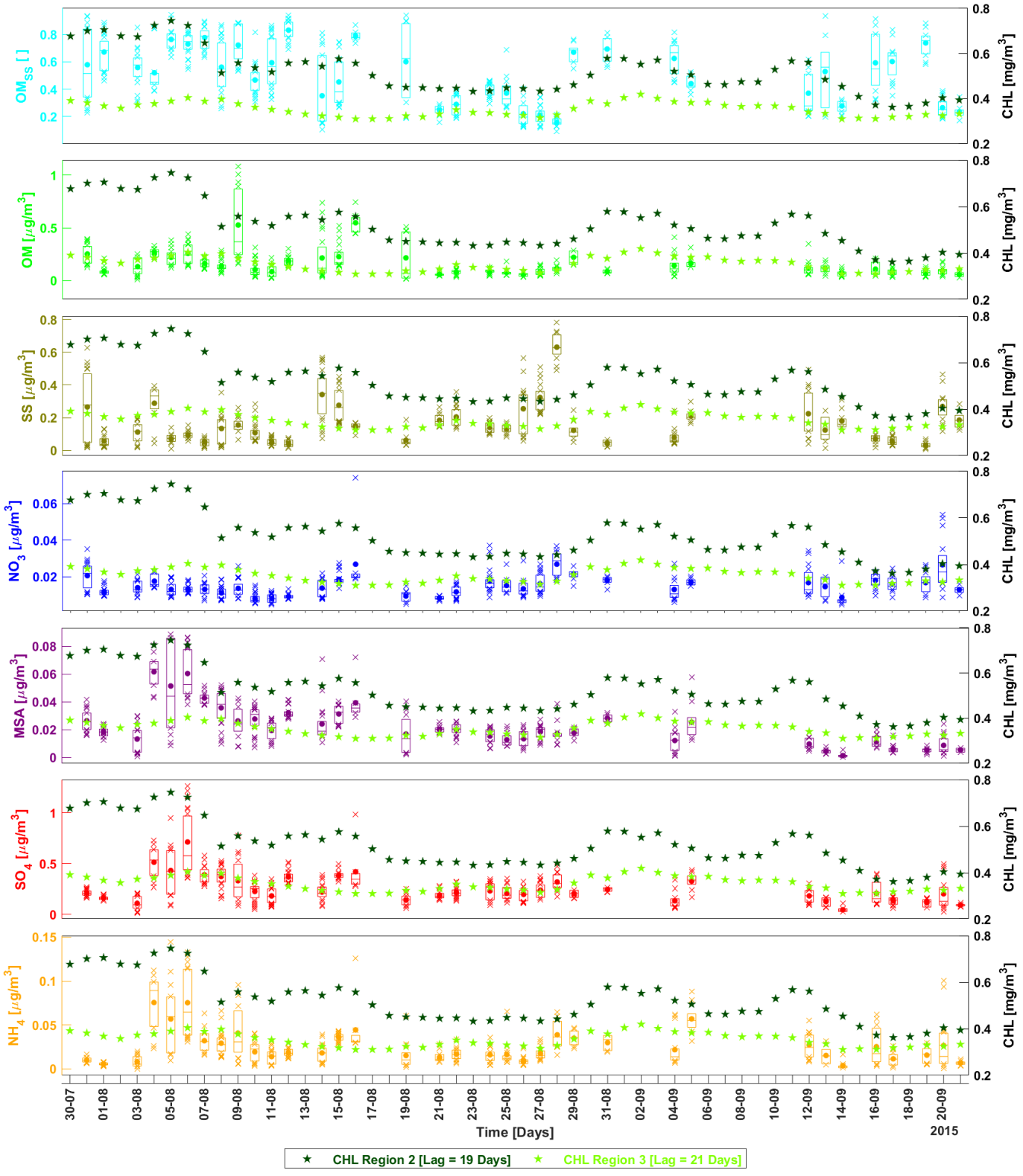

Figure S2: Daily concentrations of aerosol chemical components at MHD. On each box, that represents a day, the central mark indicates the median and the bottom (top) edges of the box indicate the 25th (75th) percentiles. The symbols "×" show points exceeding the interquartile range. The dot symbol represents the daily mean. Only days with clean marine conditions are shown. Daily mean lagged CHL over Regions 2 and 3 are inserted as strike symbols. The time-lag that maximizes correlation coefficient within the two regions are considered.

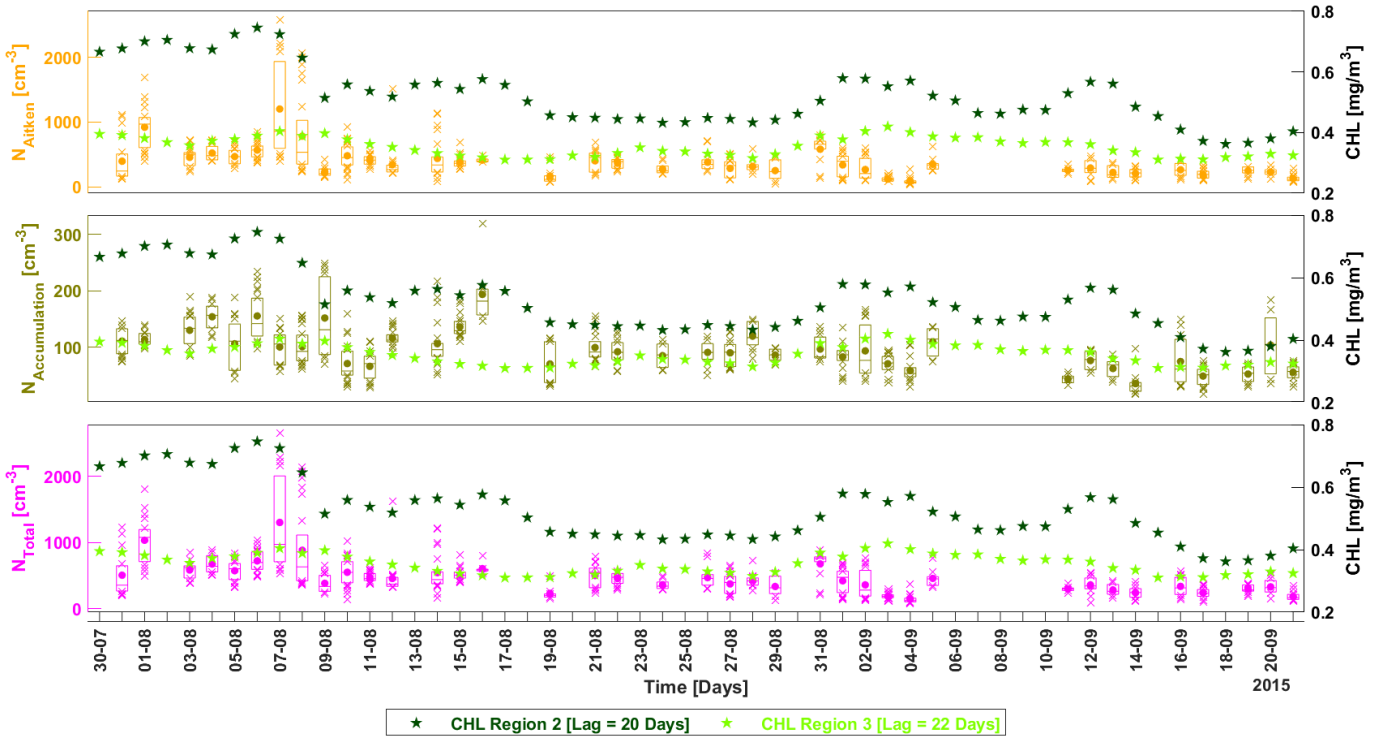

Figure S3: Same as Figure S2, but for daily particle number concentrations.

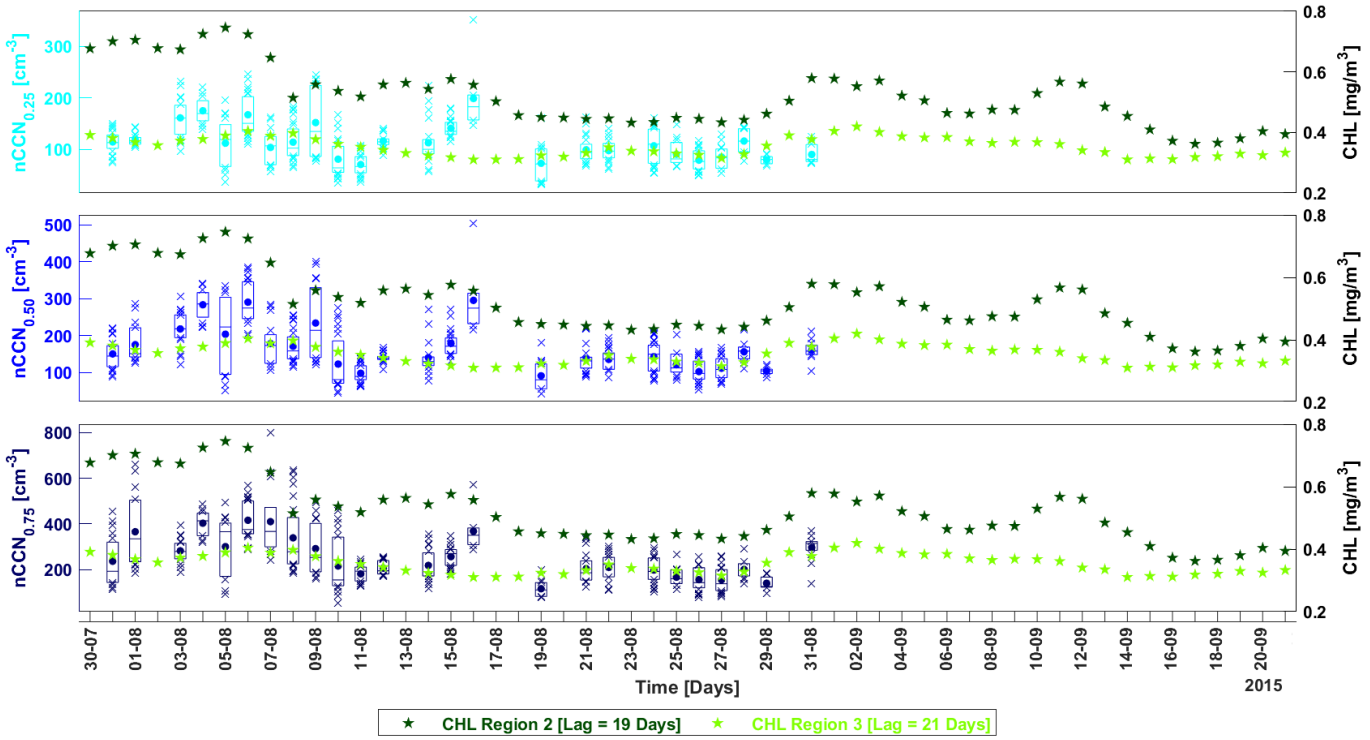

Figure S4: Same as Figure S2, but for daily CCN number concentrations.

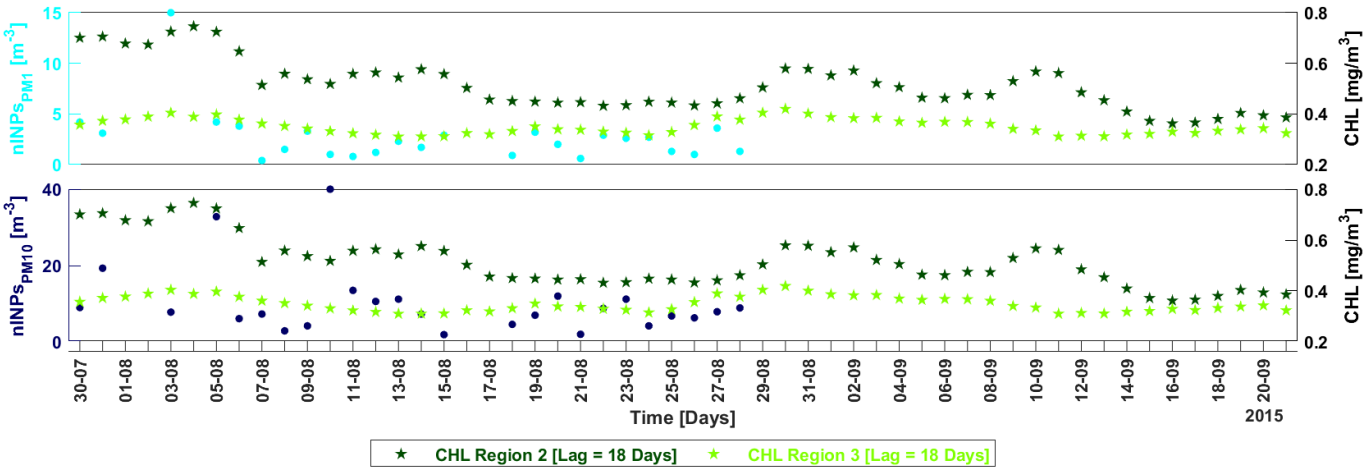

Figure S5: Daily clean samples of *n*INP concentration at MHD. Daily mean lagged CHL over Regions 2 and 3 are inserted as strike symbols. The time-lags that maximize the correlation coefficient in the two regions are considered.

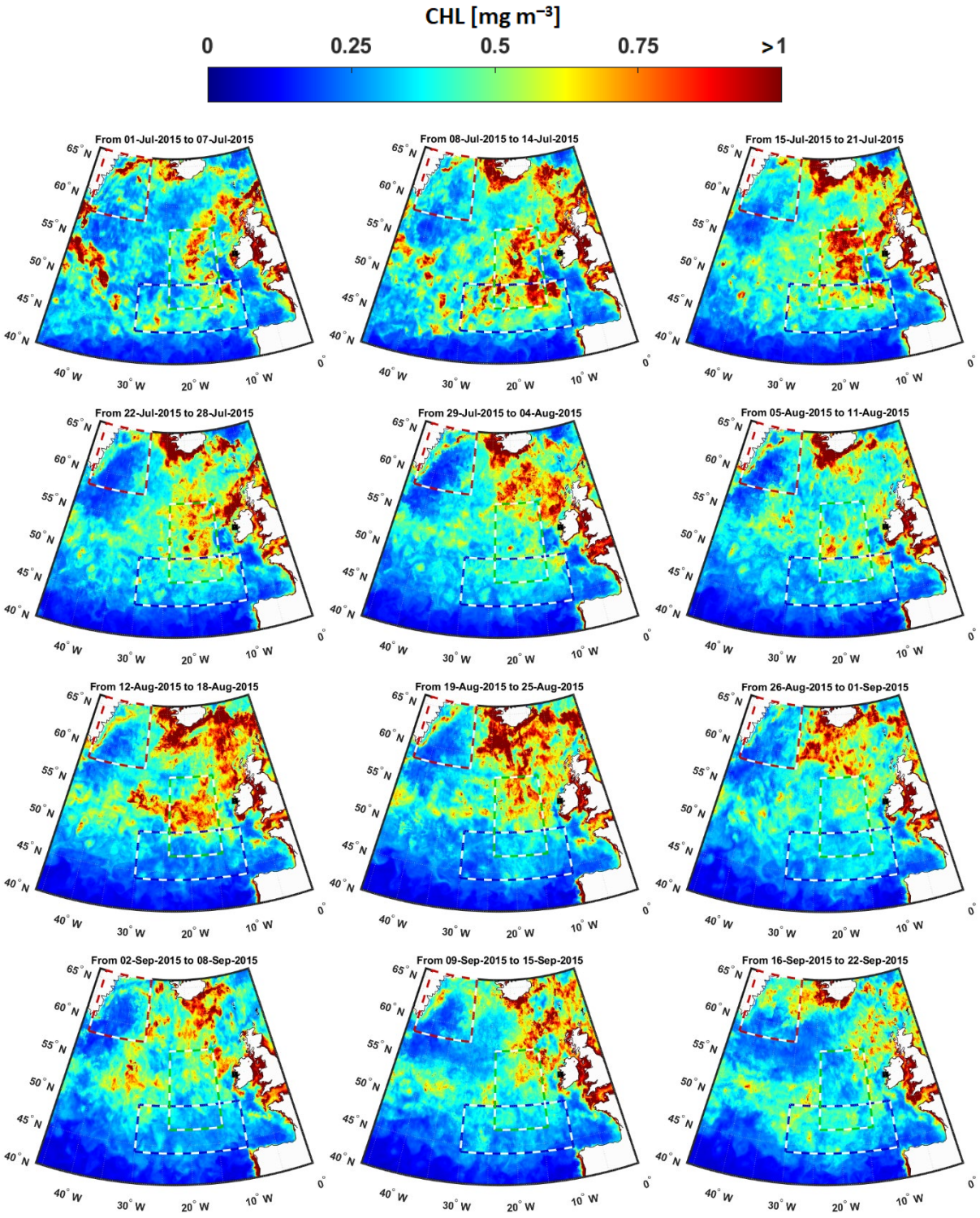

Figure S6: Spatial distributions of weekly mean CHL over the NA Ocean during July-September 2015. The dashed blue, green, and red boxes represent the regions of interest. The spatial resolution of CHL is ~ 4×4 km.

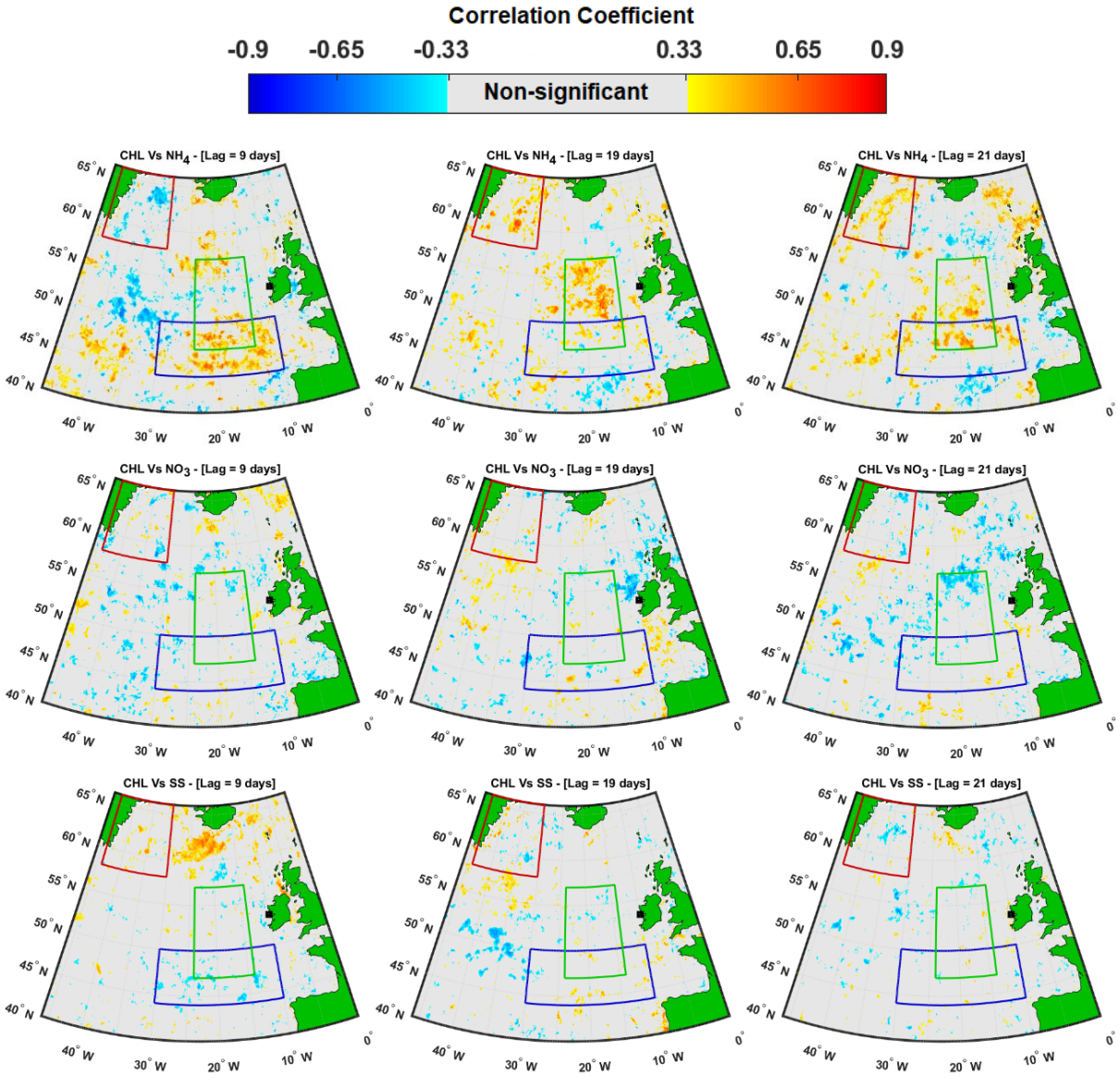

Figure S7: Examples of correlation coefficients between ammonia, nitrate and sea salt measured at MHD and CHL over the NA Ocean for 9 days (left), 19 days (middle), and 22 days (right) time-lags, considering only clean marine air masses. The grey color represents non-significant correlation coefficients at 95% confidence level, the black square corresponds to MHD station and the regions of interests are shown as blue, green, and red boxes.

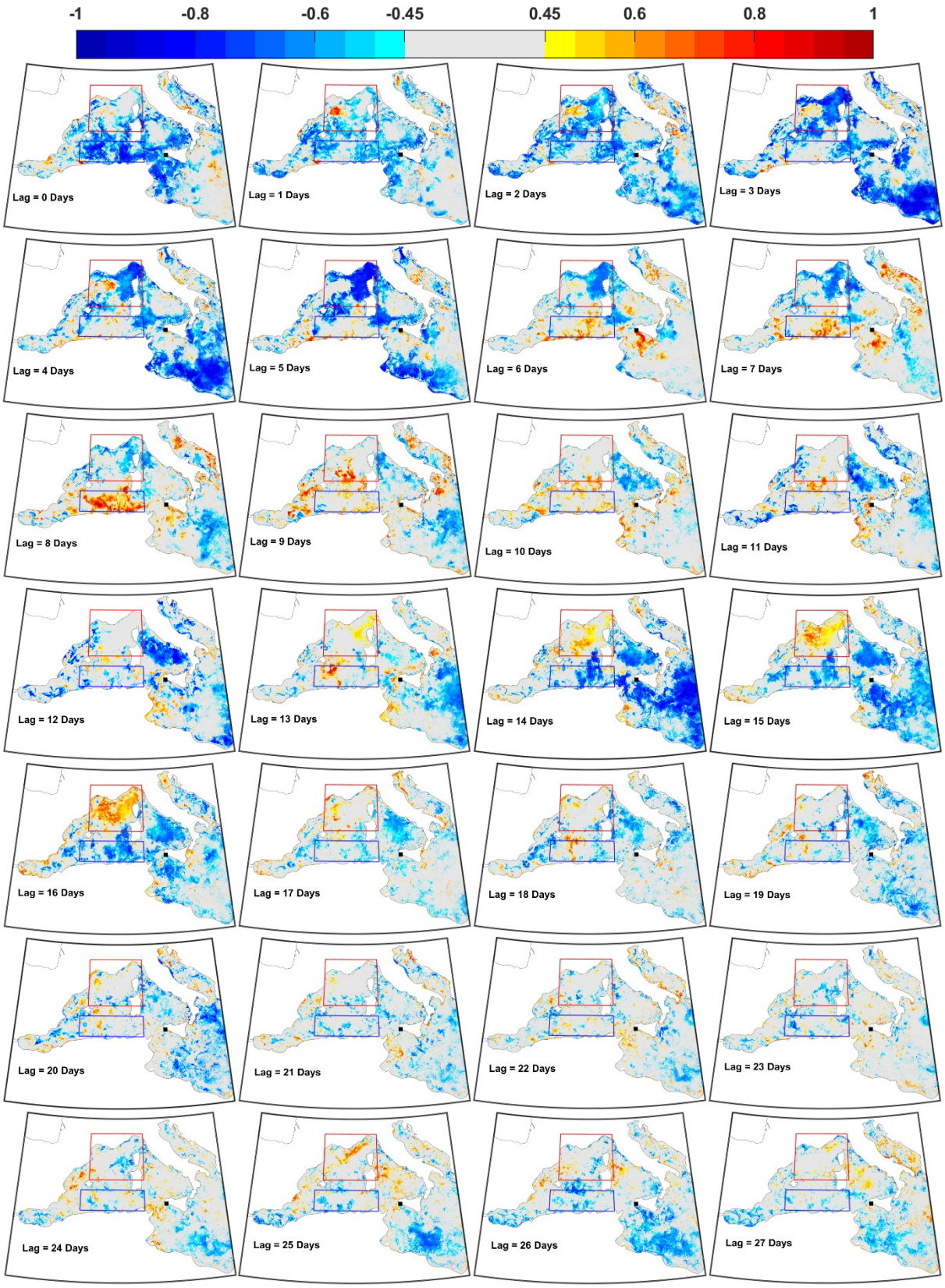

Figure S8: Spatial distributions of the correlation coefficient between MSA measured at CGR and CHL over the Mediterranean Sea at different time-lags from 0 to 27 days. The grey color represents non-significant correlation coefficients at 95% confidence level. The black square corresponds to CGR station.

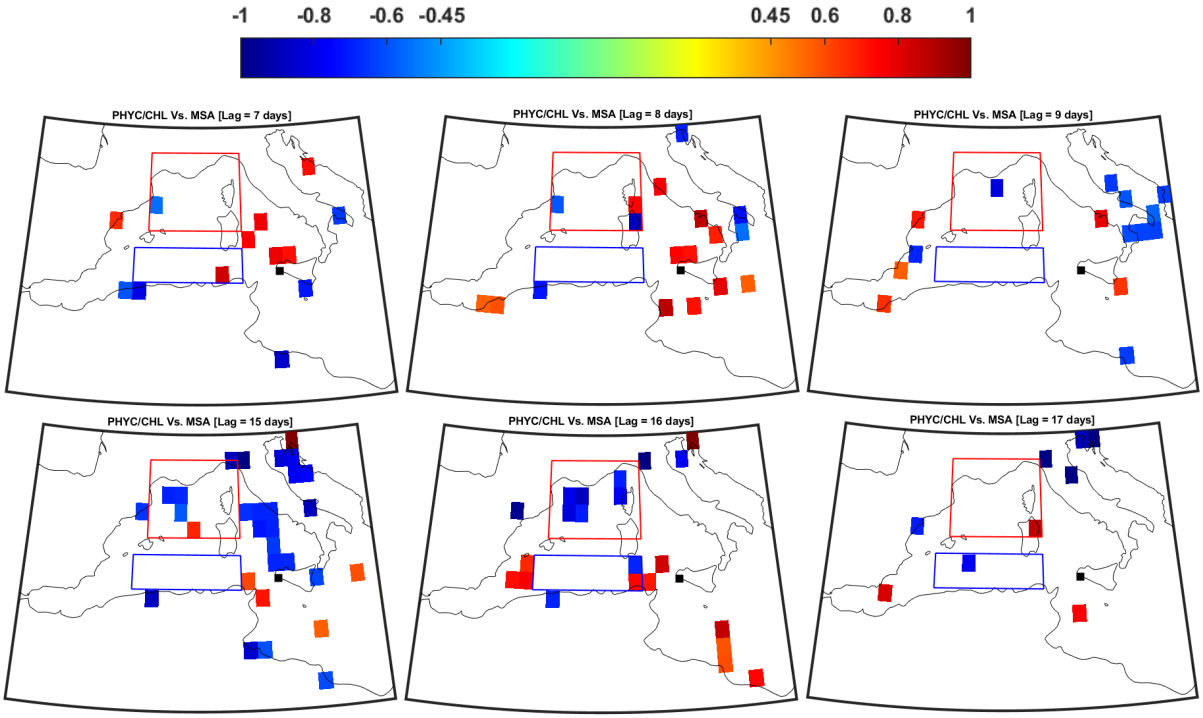

Figure S9: Examples of spatial distributions of the correlation coefficient between PHYC: CHL ratio over the Mediterranean Sea and MSA measured at CGR. Only significant correlations ($p < 0.05$) are presented. The black square corresponds to CGR station.

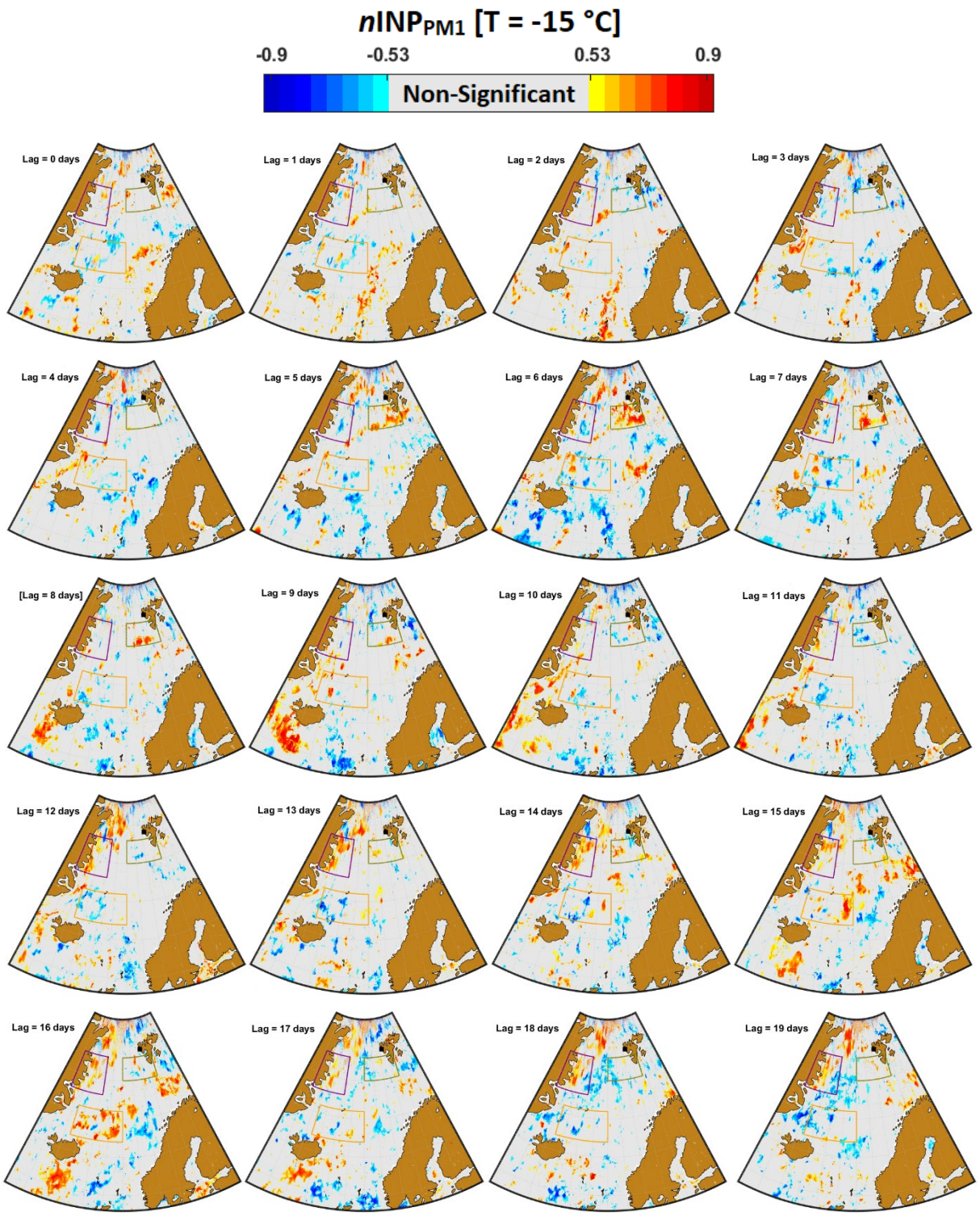

Figure S10: Spatial distributions of the correlation coefficient between $n\mathrm{INP}_{\mathrm{PM1}}$ at T = –15 °C sampled at GVB (represented by the black square) in Summer 2018 and CHL over the Arctic Ocean at different time-lags from 0 to 27 days. The grey color represents non-significant correlation coefficients ($p < 0.05$). Regions of interest are shown as Olivo (Region 1), dark Purple (Region 2) and Orange (Region 3) boxes.

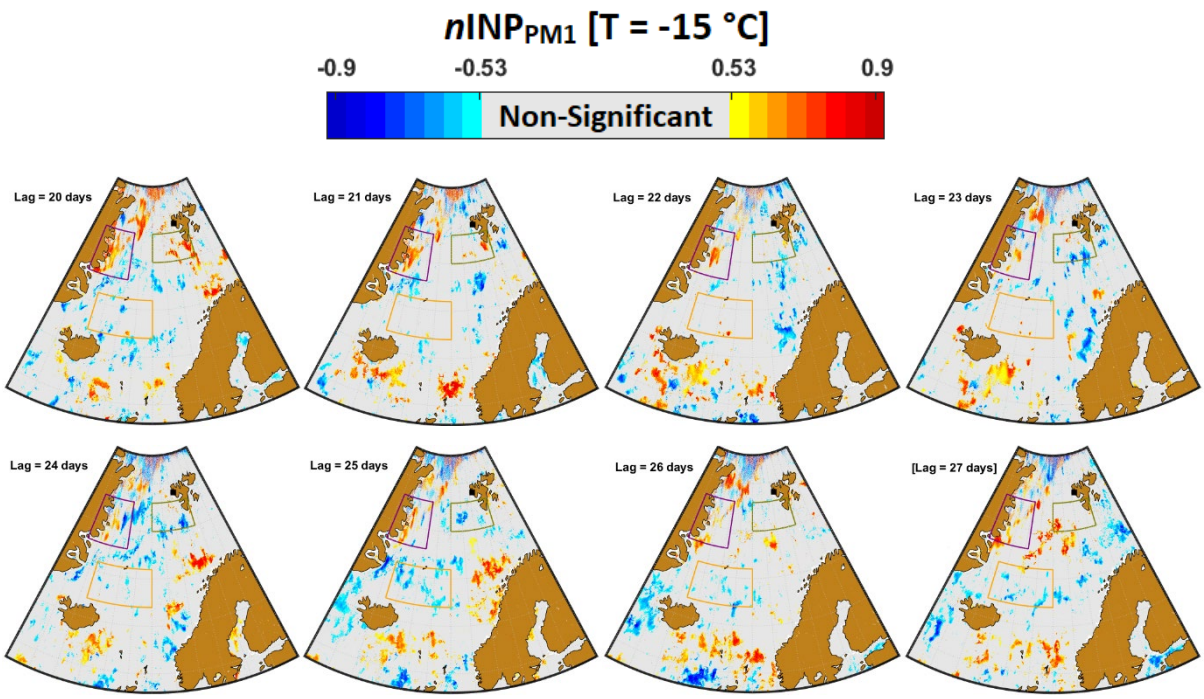

Figure S10: Continued.

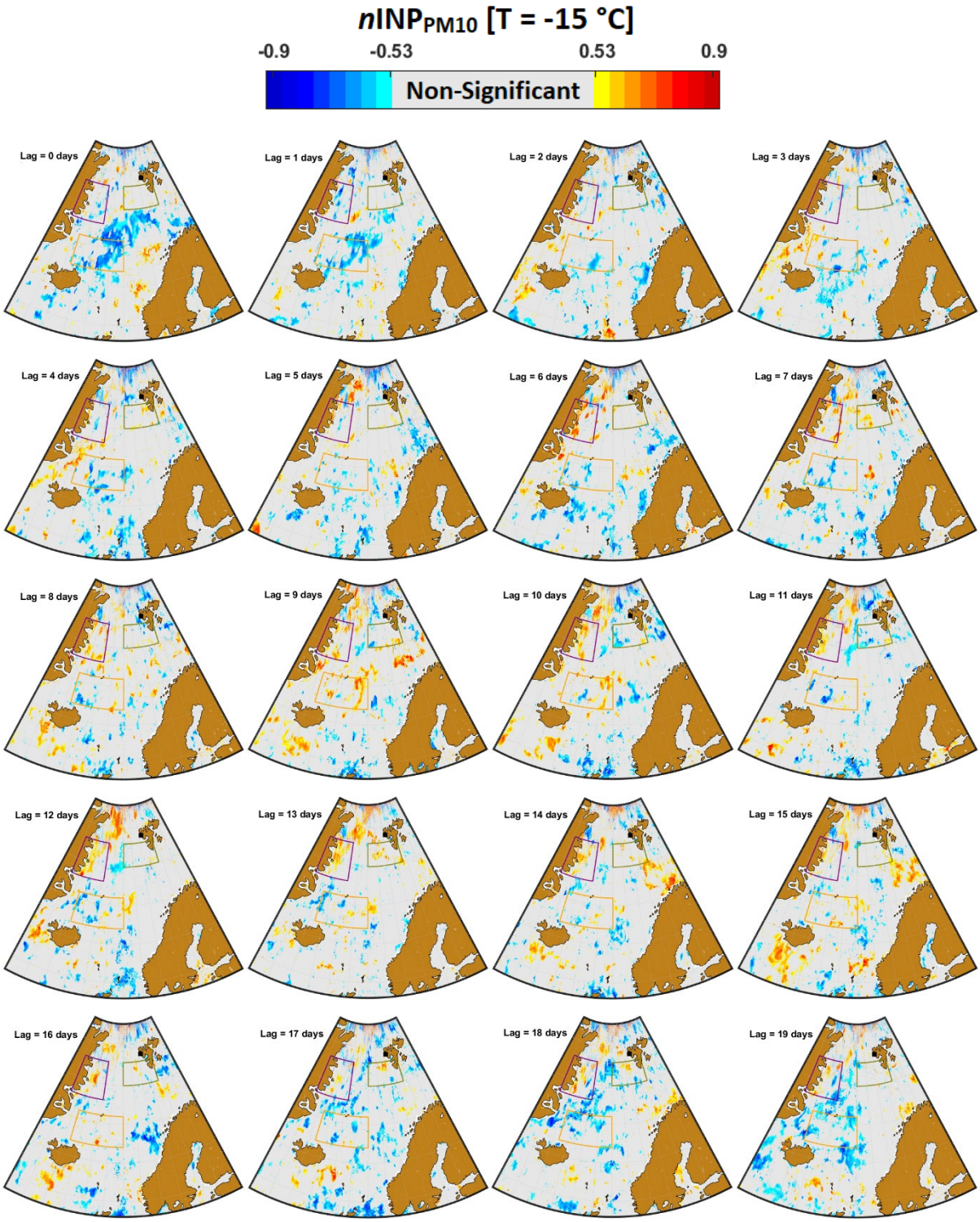

Figure S11: Spatial distribution of the correlation coefficient between $n\text{INP}_{PM10}$ at T = –15 °C sampled at GVB (represented by the black square) in Summer 2018 and CHL over the Arctic Ocean at different time-lags from 0 to 27 days. The grey color represents non-significant correlation coefficients ($p < 0.05$).

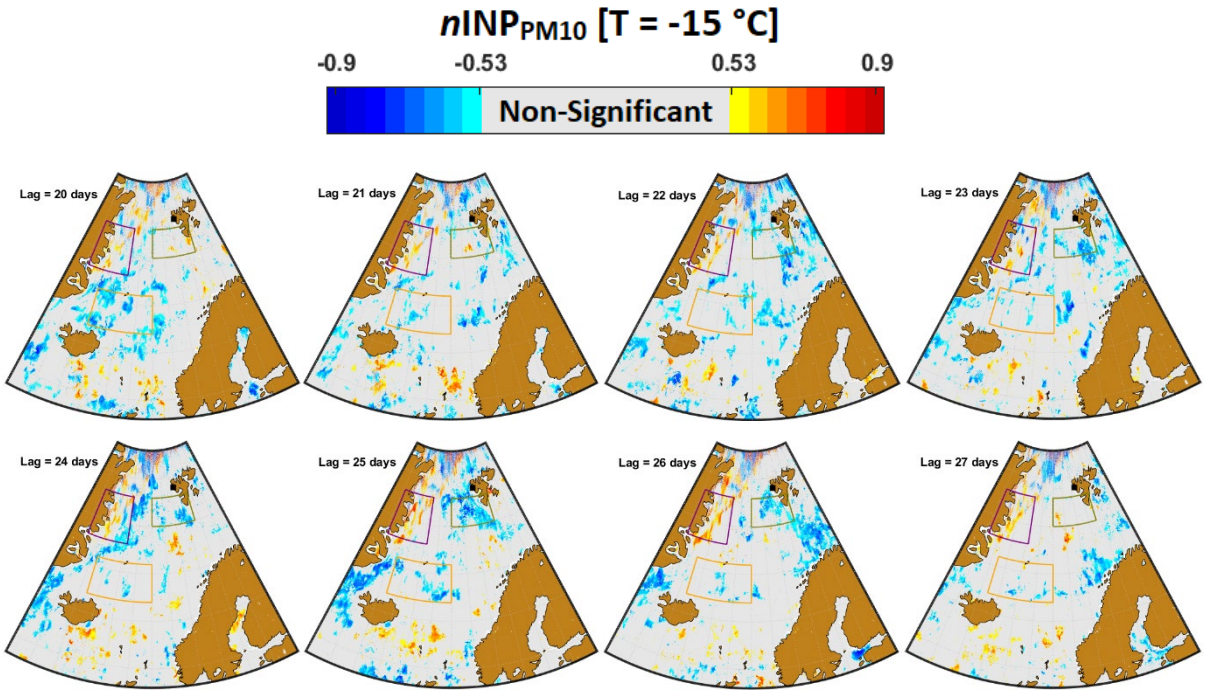

Figure S11: Continued.

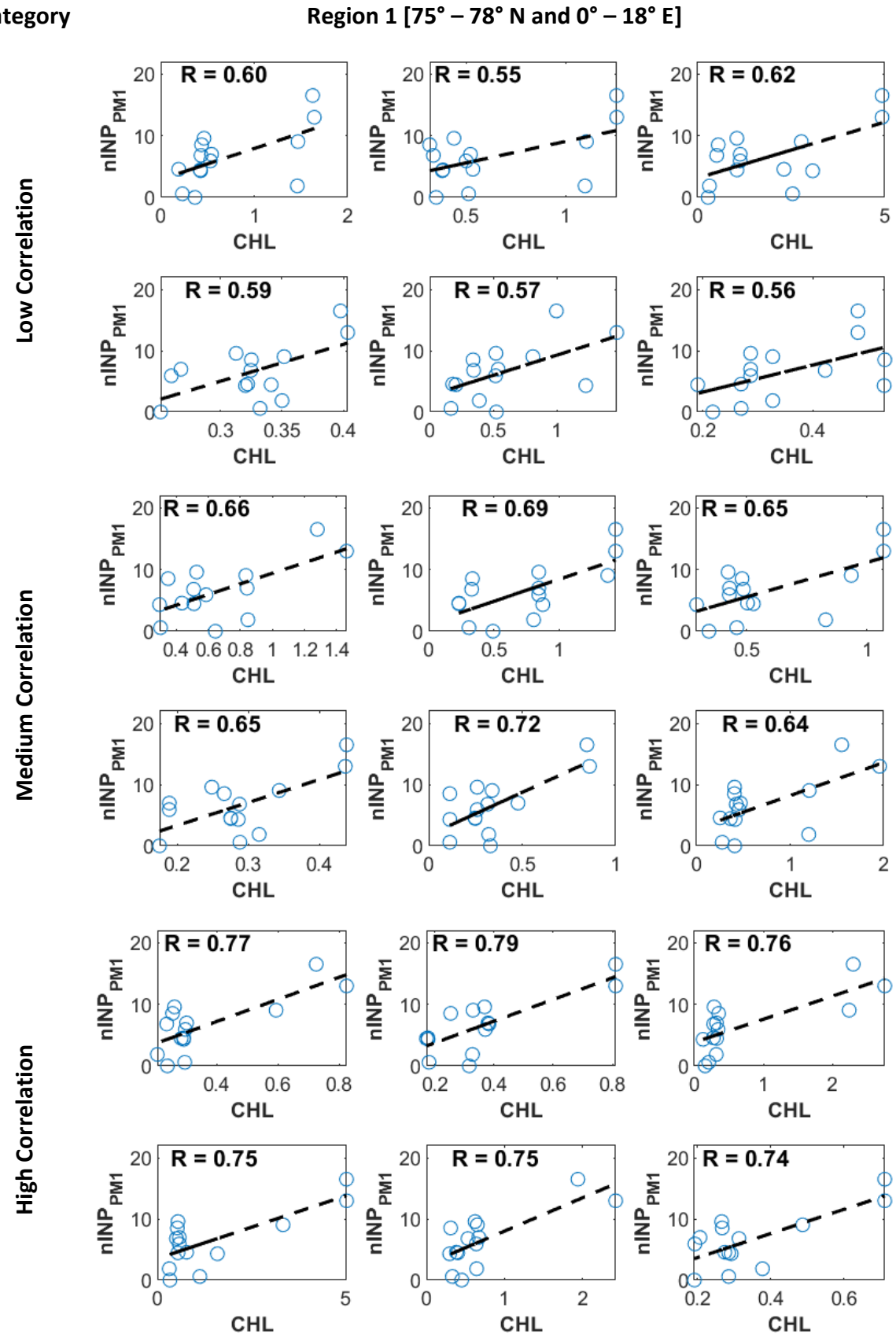

Figure S12: Scatter plots between *n*INP$_{PM1}$ sampled at GVB and CHL at pixels selected randomly within Region 1.

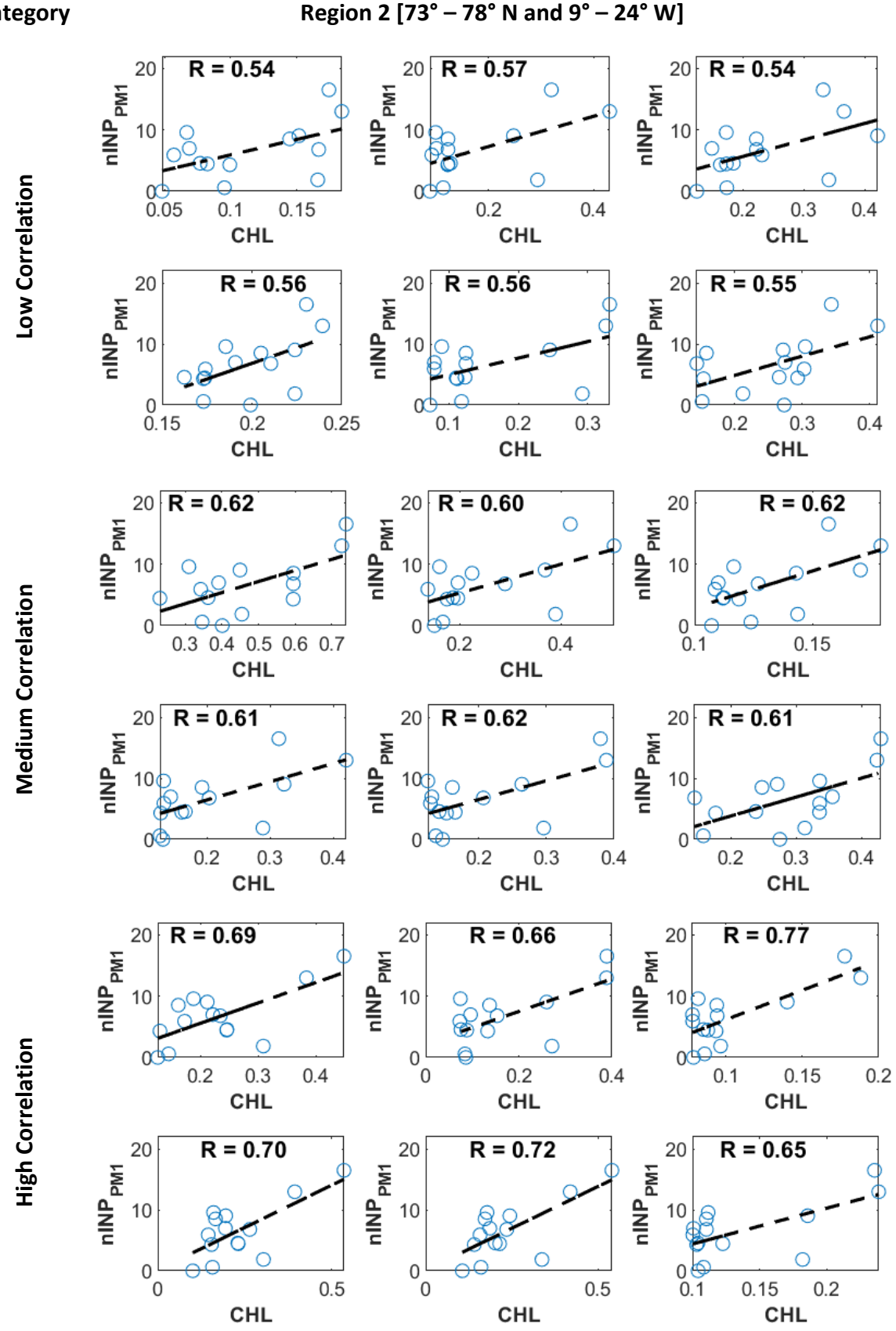

Figure S13: Same as Figure S12, but for Region 2.

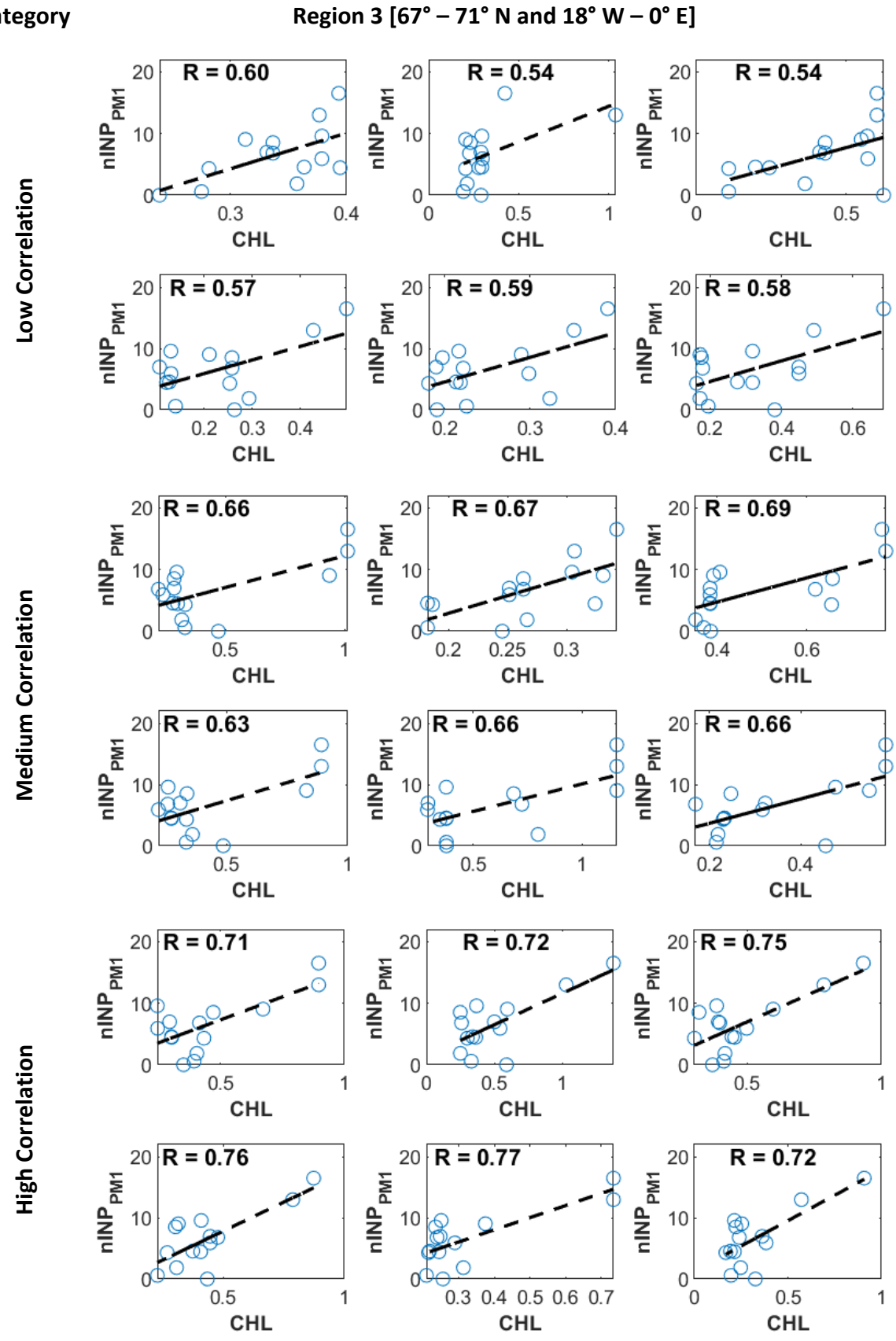

Figure S14: Same as Figure S12, but for Region 3.

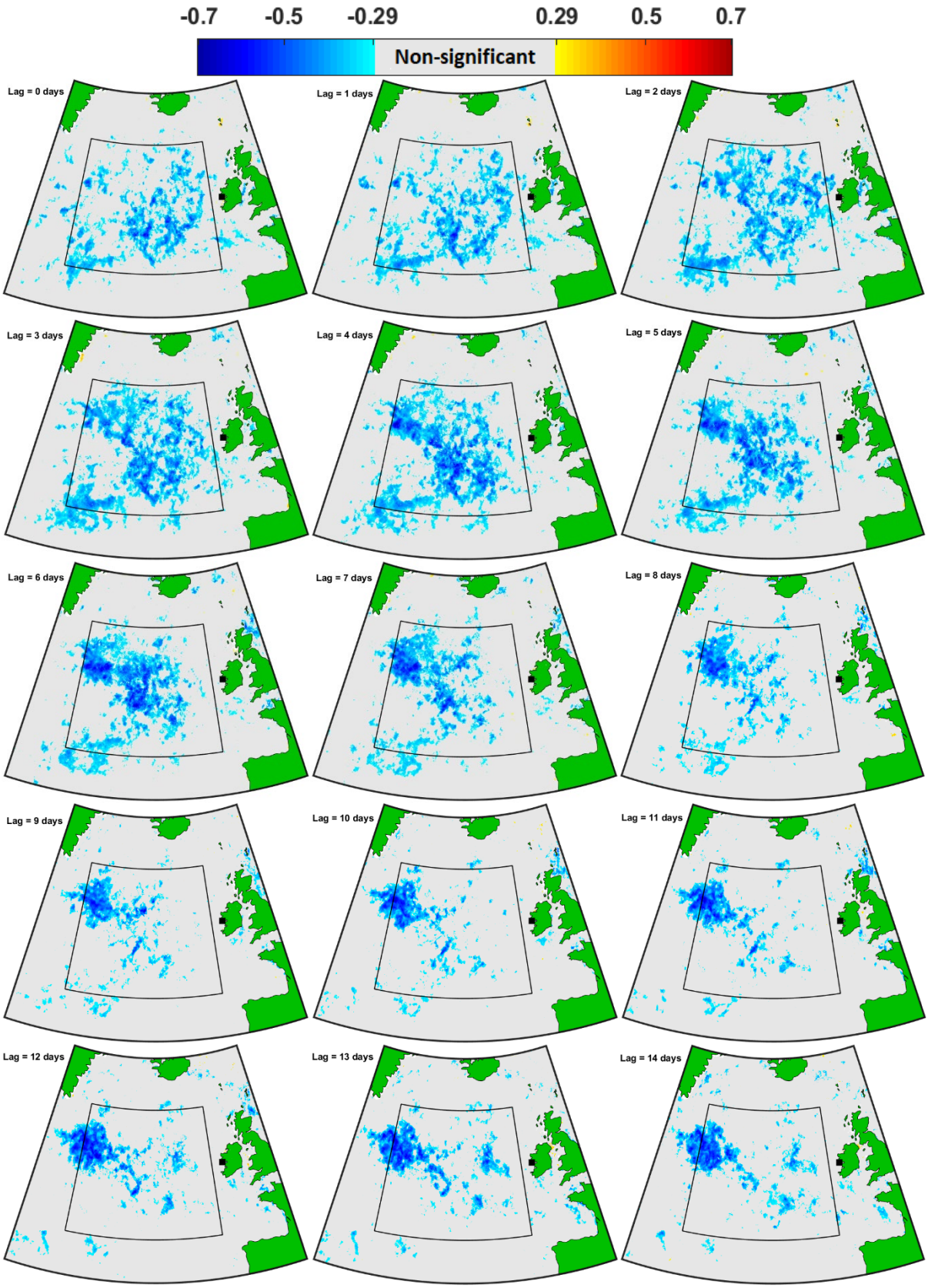

Figure S15: Spatial distributions of correlation coefficients between R_{eff} measured at MHD and CHL over the NA Ocean at different time-lags from 0 to 20 days. The grey color represents non-significant correlation coefficients at 95% confidence level, the black square corresponds to MHD station.

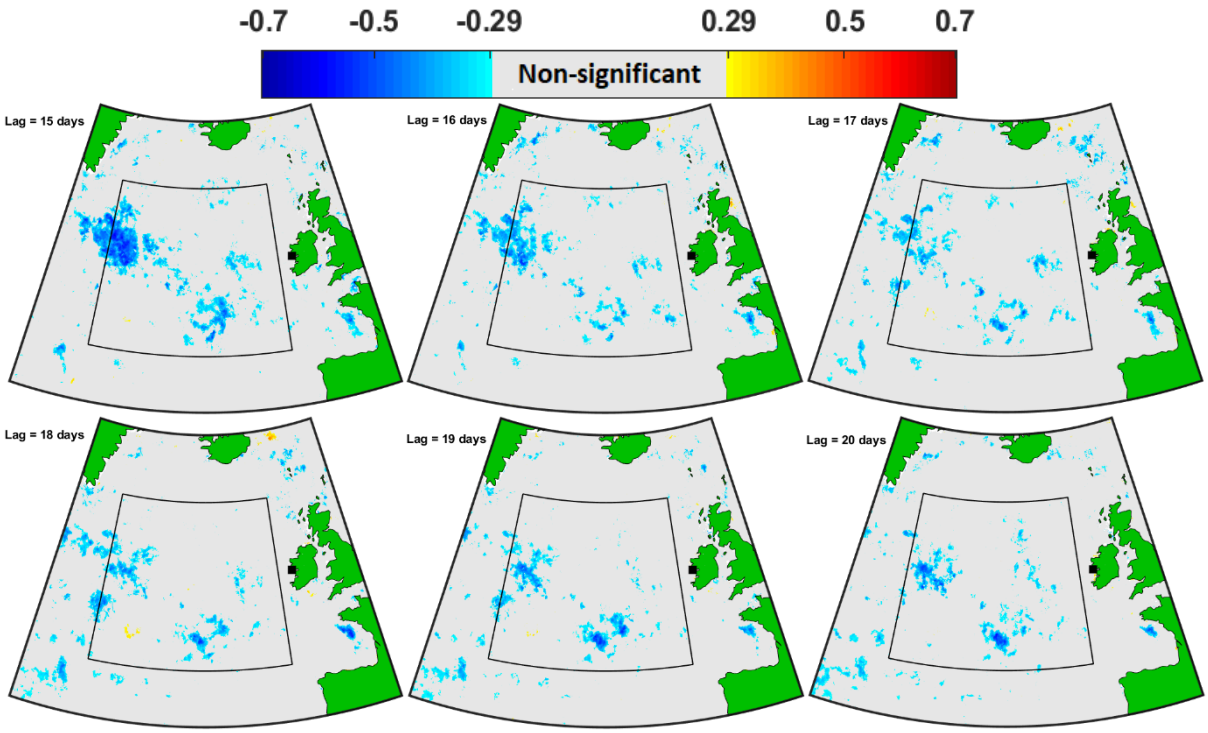

Figure S15: Continued.

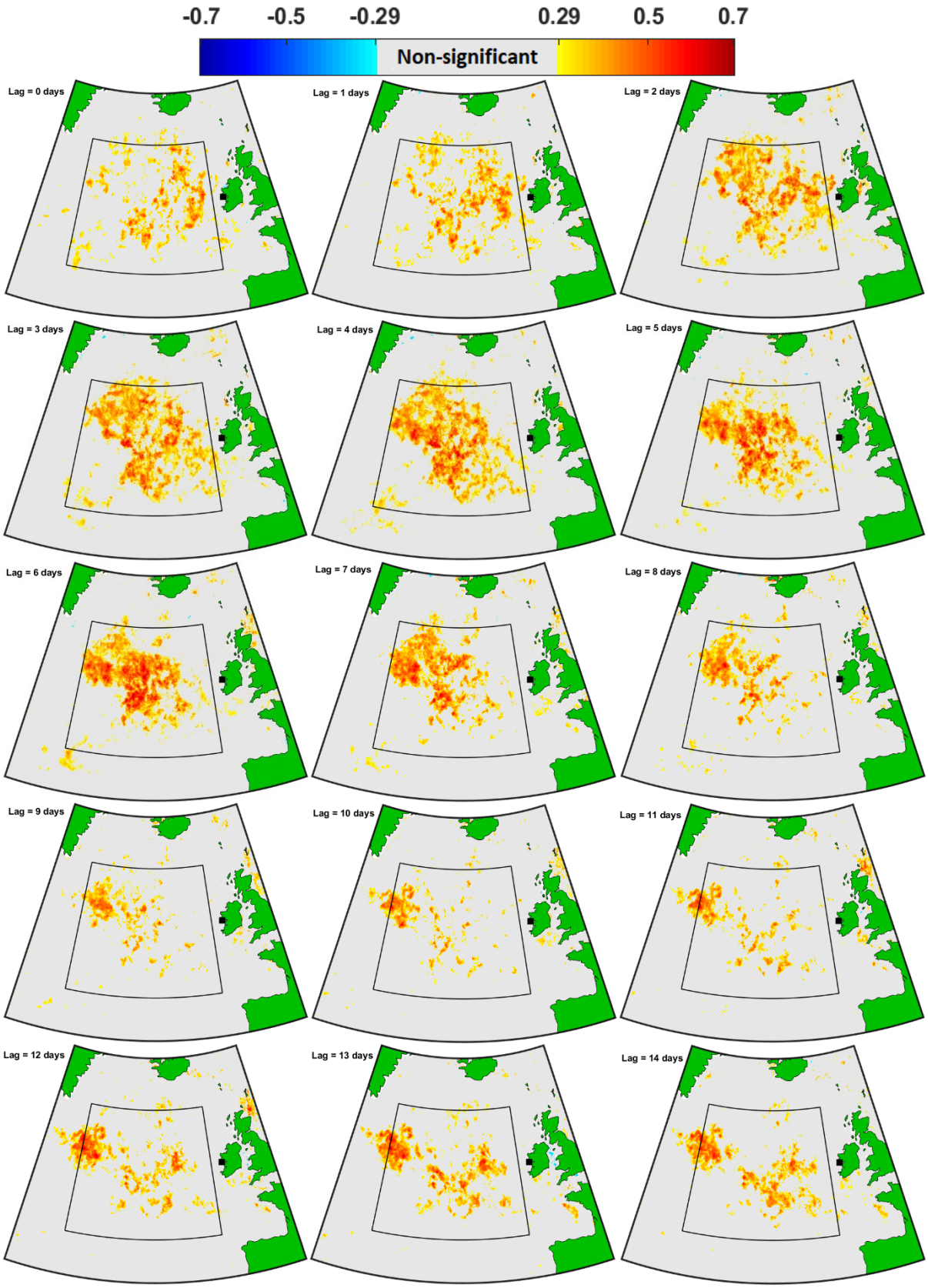

Figure S16: Same as Figure S15, but for CDNC.

-0.7 -0.5 -0.29 0.29 0.5 0.7
Non-significant

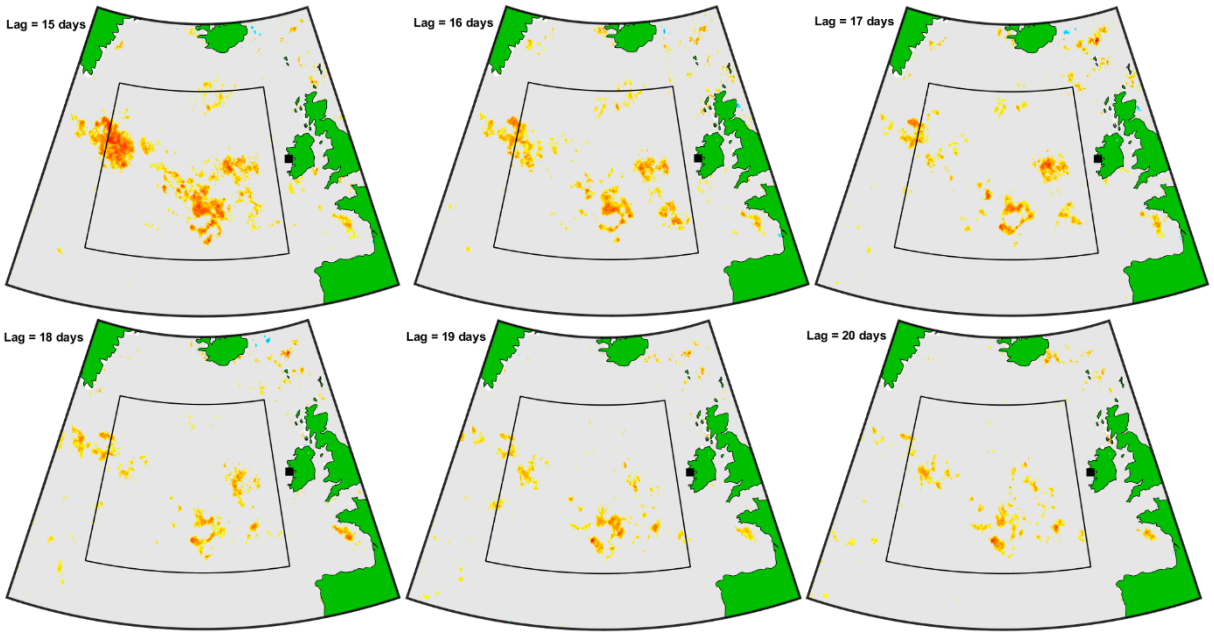

Figure S16: Continued.